VELOCITY AUGMENTATION OF A SUPERSONIC SOURCE AND THE PRODUCTION OF SLOW, COLD, MOLECULAR BEAMS

A Dissertation

by

LES STERLING SHEFFIELD

Submitted to the Office of Graduate and Professional Studies of
Texas A&M University
In partial fulfillment of the requirements for the degree of

DOCTOR OF PHILOSOPHY

Chair of Committee,	Igor Lyuksyutov
Committee Members,	Dudley Herschbach
	Donald Naugle
	Simon North
Head of Department,	George Welch

May 2015

Major Subject: Physics

ABSTRACT

In this thesis I describe the second generation of a rotating supersonic beam source. The purpose of this device is to produce velocity augmented molecular beams for use with scattering experiments or subsequent slowing methods. The beam emerges from a nozzle inserted at the tip of a hollow aluminum rotor which can be spun at high speeds in either the forward or backwards direction. The forward direction mode increases the laboratory frame velocity distribution of the emitted beam and the backward direction mode decreases this velocity distribution.

Both rotor modes are analyzed theoretically and experimentally within the text. I introduce a pulsed gas inlet system for the rotating source as well as cryocooling of the vacuum chamber. This new version provides moderately intense beams of slow molecules, containing $\sim 10^{12}$ molecules at lab speeds as low as 35 m/s, and very intense beams of fast molecules, containing $\sim 10^{15}$ molecules at 400 m/s. Beams of any molecule available in gas phase can be produced utilizing this system. For collision experiments, the ability to scan the velocity utilizing the rotating source is very advantageous when using two merged beams. If the two velocities can be closely matched, very low relative collision energies can be produced without making either beam slow.

NOMENCLATURE

L	Mean Free Path
Θ	Collision Frequency
P	Pressure
S	Pumping Speed
T	Temperature
d	Orifice Diameter
ℓ	Distance to Detector
A_{det}	Detector Area
θ_{noz}	Nozzle Spread
Δt	Pulse Duration
d_{dk}	Skimmer Diameter
ℓ_{sk}	Distance to Skimmer
v	Velocity
$\bar{v}$	Average Velocity
α	Most Probably Velocity
m	Molecular Mass
T_o	Reservoir Temperature
k	Boltzmann Constant
n_o	Reservoir Number Density
Ω	Collision Integral
C_6	Van Der Waals Coefficient

γ	Poisson Coefficient
σ	Orifice Area
ω	Solid Angle
θ	Beam Angle
x	Speed Ratio
I	Beam Intensity
E	Energy
U_i	Internal Energy State
P_i	Pressure State
V_i	Volume State
v_i	Flow Velocity
N_A	Avogadro's Number
H_i	Enthalpy State
ΔH_v	Enthalpy of Vaporization
C_p	Isobaric Heat Capacity
R	Gas Constant
v_∞	Maximum Terminal Velocity
R_{noz}	Nozzle Radius
a	Sudden Freeze Model Parameter (SFMP) 1: Multiplier
b	SFMP 2: Cosine Exponential
θ_o	SFMP 3: Limiting Angle
d	SFMP 4: Distance to Focus

N_f	Total Collisions
z_f	Freezing Surface
Ξ	Source Parameter
$T_{\parallel}$	Parallel Temperature
$T_{\perp}$	Transverse Temperature
$E_{\parallel}$	Parallel Energy
$E_{\perp}$	Transverse Energy
Λ	Energy Transfer Coefficient
K	Thermal Conduction Model Parameter 1
τ	Thermal Conduction Model Parameter 2
λ_o	Thermal Conduction Model Parameter 3
z_o	Thermal Conduction Model Parameter 4
$\dot{N}$	Nozzle Flow Rate
κ	Peaking Factor
T_t	Triple Point Temperature
T_b	Boiling Point Temperature
T_c	Critical Temperature
P_t	Triple Point Pressure
P_c	Critical Pressure
$\Delta_v H_b$	Vaporization Enthalpy
$\Delta_v H_t$	Vaporization Enthalpy
F_C	Centrifugal Force

V_C	Centrifugal Potential
ω	Rotational Frequency
R	Rotor Length
V_R	Rotor Velocity
V_e	Expansion Force
L_n	Nozzle Location
d	Length to Clear Rotor Path
ϕ_{sw}	Swatting Angle
u_{min}	Minimum Velocity
ϕ	Rotor Angle
ϕ_1	Initial Detector Exposure
ϕ_2	Full Detector Exposure Start
ϕ_3	Full Detector Exposure Finish
ϕ_4	Final Detector Exposure
$\Delta\phi$	Angular Width of Detector Exposure
X	Nozzle Frame Velocity
V	Lab Frame Velocity
D	Number Density
$\bar{F}$	Total Flux
σ	Nozzle Throat Area
σ_s	Skimmer Area
Ω_s	Skimmer Solid Angle
L_s	Distance to Skimmer

τ	Pulse Duration
U	Nozzle Frame Flow Velocity
Δv	Nozzle Frame Velocity Spread
w	Final Lab Frame Velocity
Q	Interaction Coefficient
ρ_{bk}	Density of Background Gas
u	Final Lab Frame Velocity
S	Scattering Cross Section
S_{lim}	Scattering Cross Section Limit
u_{rel}	Relative Velocity
u_{beam}	Final Lab Frame Velocity
u_{bk}	Background Velocity
φ	Scattering Ratio
Δv_L	Local Velocity Spread
X	Final Lab Frame Velocity
Δt	Pulse Duration
τ	Time of Flight
E_R	Relative Kinetic Energy
μ	Reduced Mass
θ	Intersection Angle
ΔE_R	Energy Spread
y	Augmentation Magnitude
z	Augmentation Ratio

TABLE OF CONTENTS

Page

Page

LIST OF FIGURES

Page

Page

Page

Page

Page

LIST OF TABLES

Page

Page

1. INTRODUCTION

"Born in leaks, the original sin in vacuum technology, molecular beams are collimated wisps of molecules traversing the chambered void that is their theatre (...). On stage for only milliseconds between their entrances and exits, they have captivated an ever growing audience by the variety and range of their repertoire." [1]

Some of the first molecular beam experiments were undertaken by Otto Stern soon after Dunoyer proved in 1911 that molecules traversing a region of vacuum travel in straight lines. Sterns' initial efforts were to verify the velocity distribution of a beam expanding into the vacuum as predicted by the Maxwell-Boltzmann distribution. His approach included a revolving platform that obtained a peripheral velocity of a mere $15\ \mathrm{m/s}$. In the time since these initial explorations molecular beams have transformed into a vibrant field of study and an indispensable tool for studying the physical world. It is somewhat fitting that a hundred years after Stern some experimental efforts still involve the concept of a rotating source to augment the velocity distribution of the emitted beam.

In the years after Stern, both chemists and physicists pursued the development of atomic and molecular beams. These researchers continuously increased the supply pressure behind their beam sources to attain a corresponding increase in the intensity of the output signal. These efforts were initially hindered by other experimental parameters, namely the chamber pressure where the experiments were taking place. To maintain the ballistic trajectories of a 'Molecular Ray' from the source to the detector requires the mean free path in the chamber must be larger than the length traversed by the beam. Maintaining this large mean free path while increasing the supply pressure required either the development of a high speed valve or an increased pumping capacity in the attached vacuum system. Both

methods are used in modern beam techniques[2] but in the early 1900's it was the widespread adoption of the oil diffusion pump[3] which brought pressures of 10^{-6} Torr and pumping speeds up to 5,000 L/s.

With this new era of vacuum pumps researchers can extend the supply pressures behind their beam sources to much higher regimes. At some point, the mean free path of the gas in the nozzle itself will be comparable to the nozzle diameter. This means collisions will occur in the throat of the nozzle, or orifice, that effect the properties of the expanding jet. The first design study to consider such effects was performed by Kontrowitz and Grey in 1951[4]. They predicted an increase in beam intensity of ~ 75 over previous works. The experimental realization of the supersonic nozzle by Becker and Bier[5], and the realization of the pulsed beam by Hagena and coworkers[6] immediately followed this work.

These pioneers, the sources that were built, the analysis techniques developed, and the discoveries they claimed all helped define molecular beam experiments as they are understood today. The current applicability of pulsed nozzle sources extends across many disciplines of science from chemistry to physics, and from engineering to material science. Each field has benefited from the use of such an intense, well collimated beam of atoms or molecules with a narrow velocity distribution. This wide range of applicability means that any fundamental improvement or further development of molecular beam sources can be understood and applied in many different scientific arenas.

The focus of this thesis will be on the detailed analysis and further improvement of a novel method to mechanically augment the flow velocity of a supersonic beam. It will consist of a design study on each critical component in the beam system and establish the critical factors involved with each. The ancestral device was developed by Gupta and

Herschbach between 1999 and 2001 [7-9]. The emphasis of this research, as before, will be on understanding the effects that prevent creating and/or measuring very slow, cold beams. In this context "slowing" refers to the molecular velocity, characterized by the most probable velocity, and "cooling" refers to reducing the width of the velocity spread, characterized by temperature. If the molecules are in equilibrium, these two characteristics are related, but this is seldom the case in beam experiments.

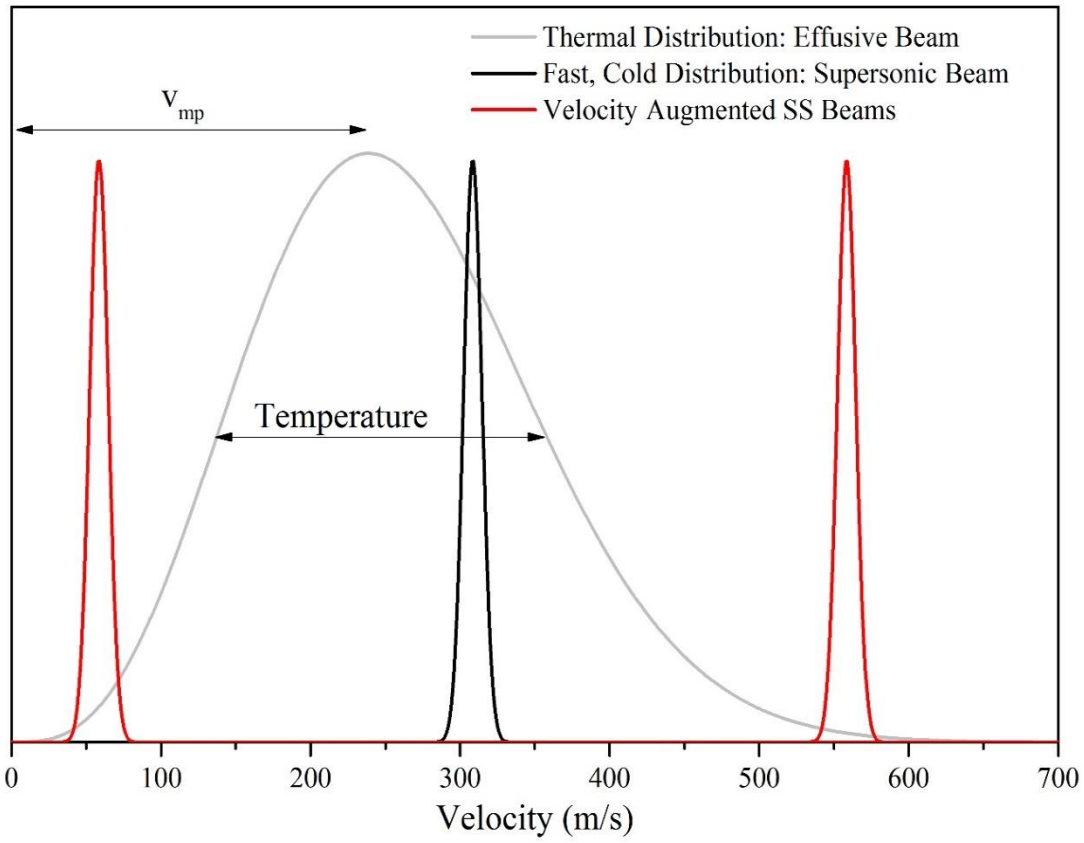

Figure 1 - 1: Schematic of Thesis Objective

As is shown in Figure 1-1, and will be discussed in Section 2, the beams produced by a supersonic expansion are very cold but also travel at a significantly higher most probable

velocity. The work contained in this thesis attempts to combine the cooling effect of a supersonic nozzle expansion with a means to directly cancel this increased average velocity. I hope that this research fosters the development of the field of ultracold molecular physics.

1.1 Motivation

Over the past decade much effort has been devoted to bringing chemists and physicists beyond the "alkali age" by developing means with which to cool preexisting molecules. Currently the only method of producing molecules in ultracold temperatures is to induce the formation of alkali dimers from a precooled dilute atomic gas. As can be seen from the analogy with Bose Einstein Condensation (BEC) there is no single method to cool an ensemble from room temperature to the nanokelvin achieved in their setup. Instead there are several cooling methods applied in sequence to an ensemble to subsequently increase its density and decrease its temperature. It makes sense that the first application of the rotating source be to simply slow gasses to allow for effective trapping. Once the molecules are trapped they can most likely be evaporatively cooled[10]. Since evaporative cooling is a process which removes particles from the ensemble the size of the initial cloud is very important. If a large enough cloud is evaporatively cooled the temperature can be brought down sufficiently low, and a condensate will form. This molecular BEC will have drastically different properties than its atomic predecessors.

Ultracold chemistry is the study of collisions that occur at very low energy. These collisions exhibit different effects due to the quantum nature of the interaction. The long range attractive forces between molecules can be studied in this way. Such low energy can be achieved by merging two fast beams along the same beam path and allowing them to

interact [11]. In the merged beams case the velocity augmentation properties of the rotating source will prove very valuable.

The low energy threshhold for a conventional crossed beam experiment is determined by cooling both of the supersonic nozzles and seeding the reactant in a heavier carrier gas. This cooling slows the beam and narrows the velocity distribution. The seeding slows down the most probable velocity of the beam, but reduces the density of the reactant proportionally. In fact both of these methods are available to the rotating source and should be pursued if the slowest beams are needed.

Slow atomic and molecular beams allow for a much longer time of flight. This means any optical techniques which are limited by the interrogation time of the beam can be improved by simply slowing the beam down. This increased interrogation time will correspond to a subsequent increase in frequency resolution.

The large deBroglie wavelength of slow, cold molecules can interfere with a physical grating similar to the atomic interferometer[12]. These interference patterns will be much more dynamic due to the extra degrees of freedom in the molecular system. By initially orienting the beam with an electromagnetic field and then changing the orientation these degrees of freedom can be isolated and studied.

Manipulation of molecular beams by electromagnetic fields always conserves energy and the kinetic energy of the beam is proportional to the square of the velocity. This makes a slow beam much easier to control than a room temperature supersonic expansion. This is a primary advantage over other techniques attempting to slow beams using such inhomogenous fields. By utilizing the rotor as a source for a Zeeman or Stark decelerator all the benefitial

properties of the rotating source would effect the results of the electromagnetic slowing schemes. By starting with a pre-slowed ensemble the fields can be made much smaller, or molecules can be studied that interact weakly with electromagnetic fields.

The centrifugal force that acts inside the rotor as it spins at high frequencies can produce extremely high pressures behind the nozzle. These high source pressures do not burden the pumping system as the same amount of gas is pulsed into the rotor for each beam. The produced beam will contain dimers, trimers, and larger clusters depending on the pressure. Modeling this condensation in a supersonic beam is difficult and would benefit from the study of a system which can explore such high pressures.

1.2 Outline of Thesis

Section 2 presents the theoretical framework of molecular beams and how they are extended naturally to the supersonic regime and easily applied to a counter rotating source. Section 3 represents the construction and development of the slow molecular beams experiment. This includes all iterations of the rotor apparatus, the detector design, and the many auxiliary systems required for the successful measurement of slow, cold beams. Section 4 presents the results and thorough analysis of the velocity distributions attained by the equipment described in Section 3. Where appropriate material was diverted to the Appendices for the ease of reading.

2. THEORY

In this section I review the basic theory behind stationary molecular beam sources. I focus initially on the Sudden Freeze Model (SFM) due to its simplicity and wide range of applicability. The Thermal Conduction Model (TCM) improves upon the SFM by including realistic intermolecular potentials as well as other features that are described in Section 2.3. To complete the discussion of stationary molecular beam sources the aggregation state of the source gas and completely expanded beam is included by using the thermodynamic equation of state. Finally, I describe the rotating source and apply all the concepts developed previously to understanding its peculiarities.

2.1 Atomic and Molecular Beams

Stationary molecular beams are perhaps one of the most useful tools available to the experimental science community. They can be produced in a wide variety of ways [13] from laser ablation to alkali ovens but this thesis will focus on supersonic and effusive molecular beams. These sources are produced, as is seen in Figure 2-1, by conecting a gas reservoir to a vacuum chamber through a small orifice. As gas flows through the orifice a beam is formed. If the mean free path of the gas is much larger than the diameter of the orifice then an effusive beam is formed. Alternately, if the mean free path is much smaller than the orifice then a supersonic beam is formed. Thus our treatment of beam sources will begin with these relevant parameters.

The mean free path, L, of the molecules in the reservoir [14] is related to their collision frequency, Θ by

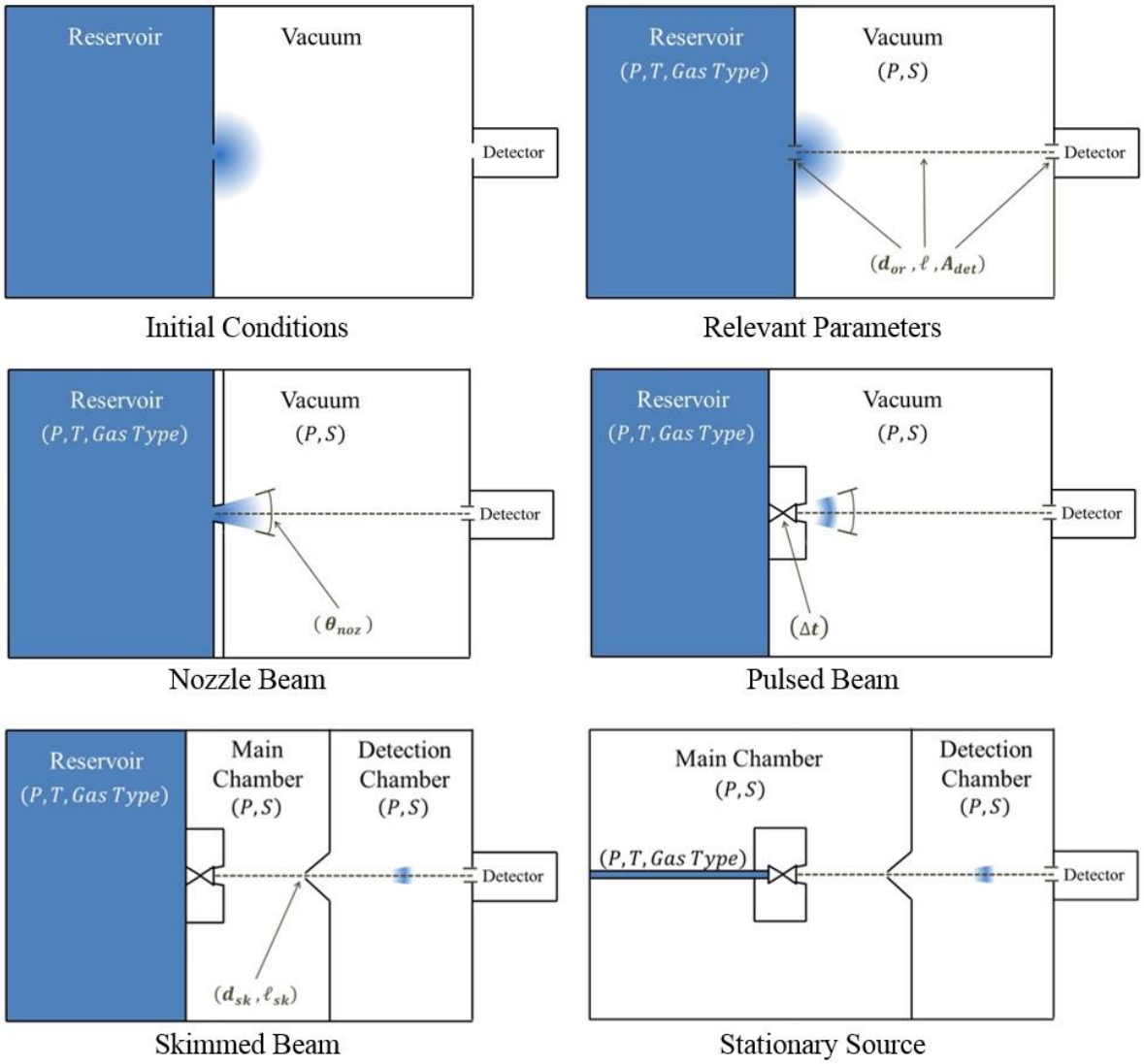

Figure 2 - 1: Beam Types and Parameters

$$\bar{v} = \Theta L \tag{2.1}$$

where the average speed of a molecule, $\bar{v}$, for a gas in equilibrium is given by

$$\bar{v} = \int_0^\infty v f(v) dv \tag{2.2}$$

For a normalized Maxwell-Boltzman velocity distribution we have

$$f(v) = \frac{4}{\sqrt{\pi}} \frac{1}{\alpha^3} v^2 e^{-\frac{v^2}{\alpha^2}} \tag{2.3}$$

where α is the most probably velocity in the reservoir. It is defined using the molecules mass, m, the temperature of the reservoir, T_o, and Boltzmann's constant, k, by

$$\alpha = \sqrt{\frac{2kT_o}{m}} \tag{2.4}$$

Now integrating Eqn 2.2 returns an average speed of

$$\bar{v} = \frac{2}{\sqrt{\pi}} \alpha \tag{2.5}$$

The collision frequency is given by [15]

$$\Theta = 2 n_o \Omega \tag{2.6}$$

where n_o is the number density in the reservoir and Ω is a species-dependent integral that depends primarily on the C_6 Van der Waals coefficient [16]

$$\Omega = 2.99 \alpha \sqrt[3]{\frac{C_6}{kT_o}} \tag{2.7}$$

This takes into account the relative velocity of the species that are interacting. As this relative velocity increases the colliding molecules probe more deeply into the intermolecular

Molecules	**Mass**	$\boldsymbol{\gamma}$	$\boldsymbol{\alpha(m/s)}$	$\boldsymbol{C_6(10^{-77}Jm^6)}$
He	4	$5/3$	1117	0.014 [17]
Ne	20	$5/3$	499	0.060 [17]
Ar	40	$5/3$	353	0.622 [17]
Kr	84	$5/3$	244	1.25 [17]
Xe	131	$5/3$	195	2.59 [17]
H_2	2	$7/5$	1572	0.014 [17]
N_2	28	$7/5$	422	0.694 [17]
O_2	32	$7/5$	395	0.488 [17]
CH_4	16	$9/7$	558	1.43[18]
CH_3F	34	1.278[19]	383	6.98[18]
SF_6	146	1.094 [19]	185	7.86[18]

Table 2 - 1: Molecular Constants at 300 Kelvin

potential U(r). This reduces the overall cross section for collisions and is an improvement to the hard sphere treatment of particle interactions.

Solving Equation 2.1 for the mean free path yields

$$L = \frac{1}{2.99 n_o \sqrt{\pi}} \sqrt[3]{\frac{kT_o}{C_6}} \tag{2.8}$$

Table 2.1 lists the appropriate molecular constants used throughout these calculations for a selection of gases at $T_o = 300K$. Figure 2-2 shows how the mean free path is effected by the reservoir pressure. The gases chosen for analysis in this section are not all inclusive but are merely chosen to highlight the effects of mass and Poisson coefficient, γ, on the resulting beam properties.

2.1.1 Effusive Beams

Effusive beams are produced when the reservoir pressure is so low that the mean free path, L, of the gas is larger than the diameter of the orifice, d. In this situation, the distribution of gas velocities produced in the molecular beam directly reflect the conditions in the reservoir. There are no interspecies collisions that take place near the orifice or nozzle throat. The properties of the beam that will be discussed are the velocity distribution, angular distribution, and the intensity.

For a reservoir with number density, n_o, and velocity distribution, $f(v)$, the number of molecules that make it through an orifice element, $d\sigma$, in a period of time, dt, is

$$dN = n_o f(v) \frac{d\omega}{4\pi} v cos(\theta) d\sigma dt dv \tag{2.9}$$

where $d\omega$ is the solid angle into which the molecules are expanding. For an ideal gas the

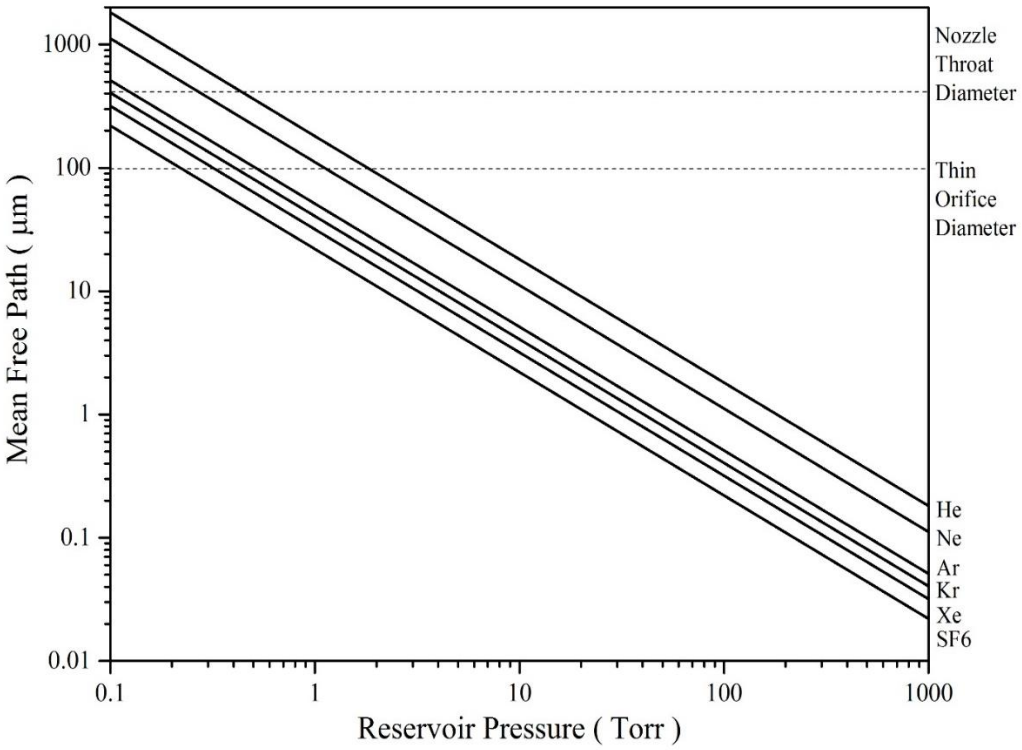

Figure 2 - 2: Mean Free Path

Maxwell-Boltzman distribution, shown in Eqn 2.3, only depends on the most probable velocity in the reservoir, α. Utilizing a reduced velocity, $x = v/\alpha$, to simplify the expression for the MB distribution,

$$f(x)dx = \frac{4}{\sqrt{\pi}}\, x^2 e^{x^2} dx \tag{2.10}$$

and then restating the Eqn 2.9 as the rate at which molecules escape through the orifice

$$\frac{dN}{dt}(x,\theta) = \frac{n_o d\sigma}{\pi^{3/2}} \alpha x^3 e^{x^2} dx\, cos(\theta)\, d\omega \tag{2.11}$$

A further simplifcation comes by considering the size of the orifice as very small compared to the distances at which the beam will be measured. In this case instead of having to integrate over the orifice area to determine the flux for the entire source, a substitution of $d\sigma \rightarrow \sigma$ will suffice.

Now the particle flux, into the angle $d\omega$, is given by the expression

$$I(x,\theta)d\omega = \frac{dN}{dt}(x,\theta) \tag{2.12}$$

which is shown in Eqn 2.11. The flux velocity distribution is

$$f(x) = 2x^3 e^{-x^2} \tag{2.13}$$

which is shown for the rare gases in Figure 2-3. These distributions are calculated for a single temperature, $300\ K$, and show the dependence that the most probable velocity has on the mass of the gas species in use.

To obtain the particle flux the velocity distribution must integrated. This was done in the preceding section in order to calculate the average speed of a molecule in equilibrium, $\bar{v}$, and is recounted here

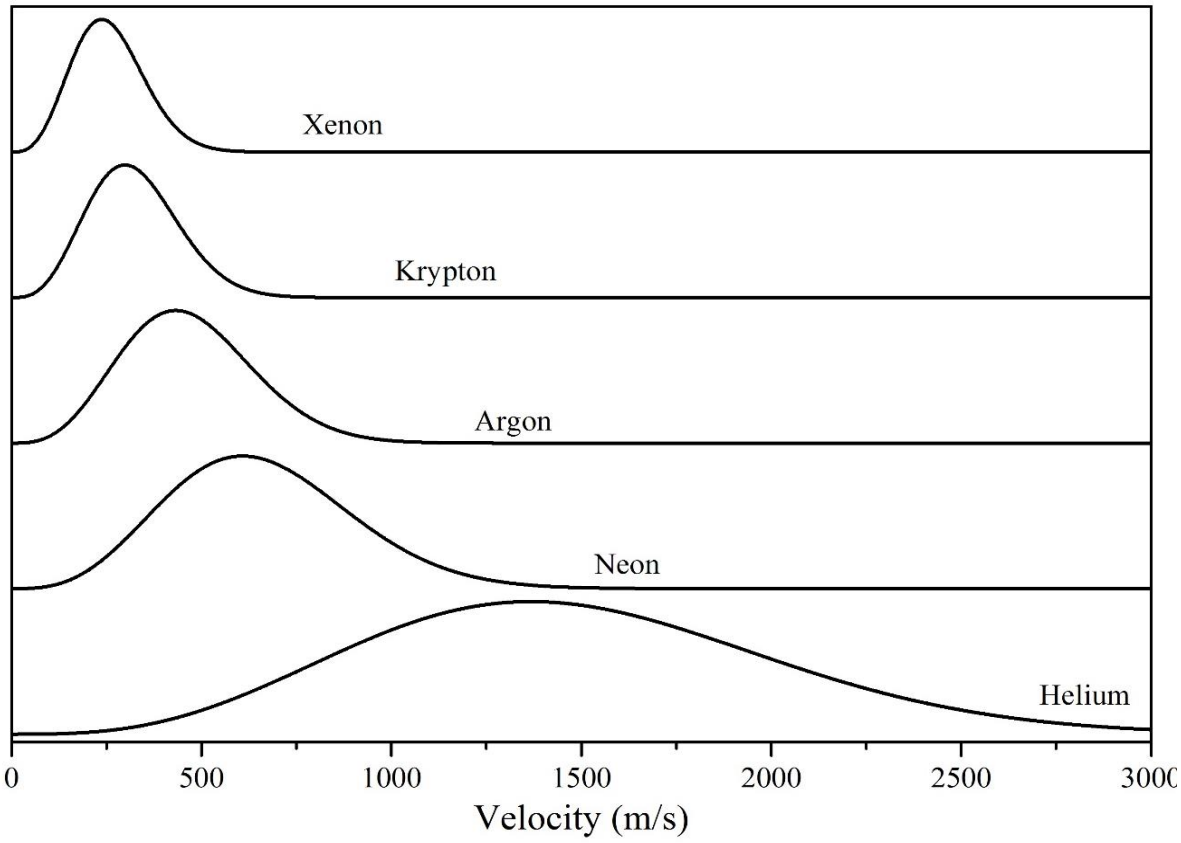

Figure 2 - 3: Effusive Velocity Distributions

$$\bar{v} = \frac{2}{\sqrt{\pi}}\alpha \tag{2.14}$$

This integration removes the velocity dependence from the intensity function, which becomes

$$I(\theta)d\omega = \frac{n_o \bar{v}\sigma}{4\pi} cos\theta d\omega \tag{2.15}$$

If the flux is needed for the entire orifice the forward hemisphere can be integrated over

$$\int cos(\theta)d\omega = \int_{-\pi/2}^{\pi/2} cos\theta d\theta \int_0^{\pi} d\phi = 2\pi \tag{2.16}$$

and the resulting intensity pertains to the entire beam

$$I = \frac{n_o \bar{v}\sigma}{4} \tag{2.17}$$

Angles can be inserted into Eqn 2.15 to determine the intensity in that direction. For example the forward direction corresponds to $\theta = 0$ and $\cos\theta = 1$ which returns an intensity of

$$I(0) = \frac{n_o \bar{v}\sigma}{4\pi} \tag{2.18}$$

When experimental parameters are recorded they very rarely utilize n_o but instead work with pressure, temperature, and a gas type. A working formula for these constants, some of which are described in Table 2-2, will be useful later. It utilizes the ideal gas law, Eqn 2.4, and Eqn 2.14 to solve for intensity as given in Eqn 2.18.

$$I(0) = \left(\frac{P}{kT_o}\right)\left(\frac{2}{\sqrt{\pi}}\sqrt{\frac{2kT_o}{m}}\right)\frac{\sigma}{4\pi} = \frac{P\sigma}{\sqrt{2\pi^3 mkT_o}} = 1.118 \times 10^{22}\ \frac{P\sigma}{\sqrt{mT_o}} \tag{2.19}$$

Parameter	**Value**
Reservoir Pressure	3 Torr
Reservoir Temperature	300 K
Mass (Xenon Gas)	131 amu
Orifice Area ($10\mu m$ aperture)	7.85E-7 cm^2
Centerline Intensity (Eqn 2.19)	1.33E14 atoms/sec

Table 2 - 2: Typical Effusive Parameters

Where the units for pressure are Torr, temperatures are in Kelvin, masses are in units of AMU, and the orifice area is in cm^2.

It is worth noting the ratio between the values of total effusing intensity, Eqn 2.17, to forward centerline intensity, 2.18. For a detector that has an area A, and a distance ℓ, this ratio is $A/\pi\ell^2$. For our typical experiment $A = 7mm^2$, $R = 120mm$, and the ratio of intensities is around 1.5×10^{-4}. This means that a very small fraction of the total gas is being sampled, and that the intensity measured at the detector should correspond very well with the calculated centerline intensity.

2.1.2 Supersonic Beams

In stark contrast to effusive beams, the regime of the supersonic beam is entered when the mean free path in the reservoir is much smaller than the size of the orifice. In this situation the calculations pertaining to an effusive source are no longer applicable and in fact the situation becomes much harder to predict beforehand. The difficulty arises due to the highly non-equilibrium dynamics that occur when flow transitions from a hydrodynamic state with many collisions, to a ballistic expansion where no collisions occur. Two approaches will be discussed in the following text: the sudden freeze model and the thermal conduction model.

Since detailed knowledge of the expansion dynamics are often not known, the initial and final states of the gas are considered independently. This is a macroscopic approach and does not consider the fine details of the expansion. It requires many approximations and these will be reviewed in detail because they define the models regions of applicability. The initial state is considered to be the thermodynamic state of the fluid within the reservoir and is denoted by index O. The final state is the completely expanded beam at a large distance

from the source and is denoted by index 1. Applying the conservation of energy to these two states we obtain

$$\langle E \rangle = U_o + P_o V_o + \frac{N_A m \langle v_o \rangle^2}{2} = U_1 + P_1 V_1 + \frac{N_A m \langle v_1 \rangle^2}{2} \tag{2.20}$$

where it is shown that the total energy contains an internal energy component, U_i, which corresponds to the random translational and internal components of the ensemble. The next term, $P_i V_i$, is the pressure-volume work for a fixed pressure P and a change in volume V. Finally the kinetic energy term contains the Avogadro constant, $N_A = 6.022 \times 10^{23}\ mol^{-1}$, and the kinetic energy for the center of mass motion of molecules, with mass m, moving with a mean velocity $\langle v_i \rangle$. Now considering the enthalpy as

$$H \equiv U + PV \tag{2.21}$$

This allows us to solve Eqn 2.20 for the final flow velocity

$$\langle v_1 \rangle = \sqrt{\frac{2(H_o - H_1)}{N_A m}} \tag{2.22}$$

This neglects the center-of-mass motion of the fluid in the reservoir, v_o. For a fast pulsed valve, such as the type used in this research, the fraction of particles leaving the reservoir during a single pulse is very small, and this approximation is valid[20].

The maximum flow velocity that is achieved in a supersonic beam, as seen in Eqn 2.22, occurs when there is the largest change in the enthalpy between the initial and final states. This change in enthalpic state

$$\Delta H = H_o - H_1 \tag{2.23}$$

may or may not include the enthalpy of vaporization, ΔH_v. The phase change occurs in the working fluid during the expansion where dimers, trimers, and higher order clusters begin to form. This condensation effects the beam considerably. It proves that the terminal velocity of a supersonic beam is determined, not only by the pressure and temperature of the source, but by the initial and final aggregation states. A supersonic beam which is cold and condensed is expected to be much faster than one which is cold and gaseous, assuming the same initial thermodynamic state for both beams.

Instead of having to address the appropriate selection of H_o and H_1, the enthalpies are transformed using the isobaric (constant pressure), molar heat capacity

$$C_p = \left(\frac{\partial H}{\partial T}\right)_P \tag{2.24}$$

Now assuming that the specific heat itself does not depend on pressure or temperature, the change in enthalpy caused by an adiabatic expansion, $H_o - H_1$, is described by a proportional change in temperature

$$H_o - H_1 = C_p(T_o - T_1) \tag{2.25}$$

Where T_o is the temperature of the reservoir, and T_1 is the temperature of the expanded jet. By combining Eqn 2.22 with Eqn 2.25 the terminal velocity of the supersonic beam can be described by the formula

$$\langle v_1 \rangle = \sqrt{\frac{2C_p(T_o - T_1)}{N_A m}} \tag{2.26}$$

This is only valid for an ideal gas that does not undergo any condensation during its expansion. The use of C_p as a constant value through the temperature range $\Delta T = T_o - T_1$

turns out to be a major simplification of the actual system. Even for argon and helium, which are usually considered ideal gasses, the heat capacities can change by a factor of 4 at temperatures below 300K[21, 22]. The use of C_p as a constant value also prevents any accurate description of the system as it undergoes a first order phase transition[23].

Instead of using the isobar heat capacity itself, a great improvement on Eqn 2.26 can be attained by the substitution

$$C_p = C_v + R \tag{2.27}$$

Where the constant volume molar heat capacity, C_v, and the gas constant, R, are used. Again, the use of a heat capacity greatly increases error in the terminal velocities calculated for real gases at high pressures. To correct for these errors the Poisson Coefficient, γ, listed in Table 2-1, is used.

$$\gamma = \frac{C_p}{C_v} \quad , \quad C_p = \frac{\gamma}{\gamma - 1} R \tag{2.28}$$

In this case the pressure and temperature variations in the specific heats partially cancel each other out. This prevents the direct use of either of the specific heats in the characteristic equation for the mean flow velocity, which becomes

$$\langle v_1 \rangle = \sqrt{\frac{\gamma}{\gamma - 1} \frac{2R(T_o - T_1)}{N_A m}} \tag{2.29}$$

In the limiting case of a vanishing beam temperature, $T_o \gg T_1$, and the maximum terminal velocity is achieved[23]

$$\langle v_\infty \rangle = \sqrt{\frac{\gamma}{\gamma - 1} \frac{2RT_o}{N_A m}} \tag{2.30}$$

For an ideal monatomic gas $\gamma = 5/3$ and the terminal velocity is

$$\langle v_\infty \rangle = \sqrt{\frac{5kT_o}{m}} \tag{2.31}$$

It must be noted that this terminal velocity does not depend on the pressure in the reservoir but only the temperature. It also does not depend on any particle property other than mass. Thus it is applicable to ideal monatomic gasses only.

Sudden-Freeze Model

Any successful description of the measurable parameters in a supersonic expansion must somehow address the transitions[16] from hydrodynamic flow, where there are many collisions, to inertial behavior, where there are few collisions, and into the kinetic regime, where there are no collisions at all. In the Sudden-Freeze Model[15] these transitions occur at fixed distances from the sonic plane of the nozzle, as seen in Figure 2-4.The transition from hydrodynamic to inertial occurs at a distance, d, from the sonic plane, and beyond this point the expansion proceeds along the streamlines as shown. The density distribution from this source is given as

$$n(r,\theta) = a^2 n_o \left(\frac{R_n}{r}\right)^2 \cos^b\left(\frac{\pi}{2}\frac{\theta}{\theta_o}\right) \tag{2.32}$$

where r is the distance downstream from the sonic plane of the nozzle and θ is the angle with respect to the z-axis, as shown in Figure 2-4. The experimental parameters n_o, R_n, and θ_o are the reservoir density, radius of the throat, and angular spread of the nozzle respectively. The free parameters a, b, and θ_o are shown in Table 2-3 as a function of the Poisson coefficient.

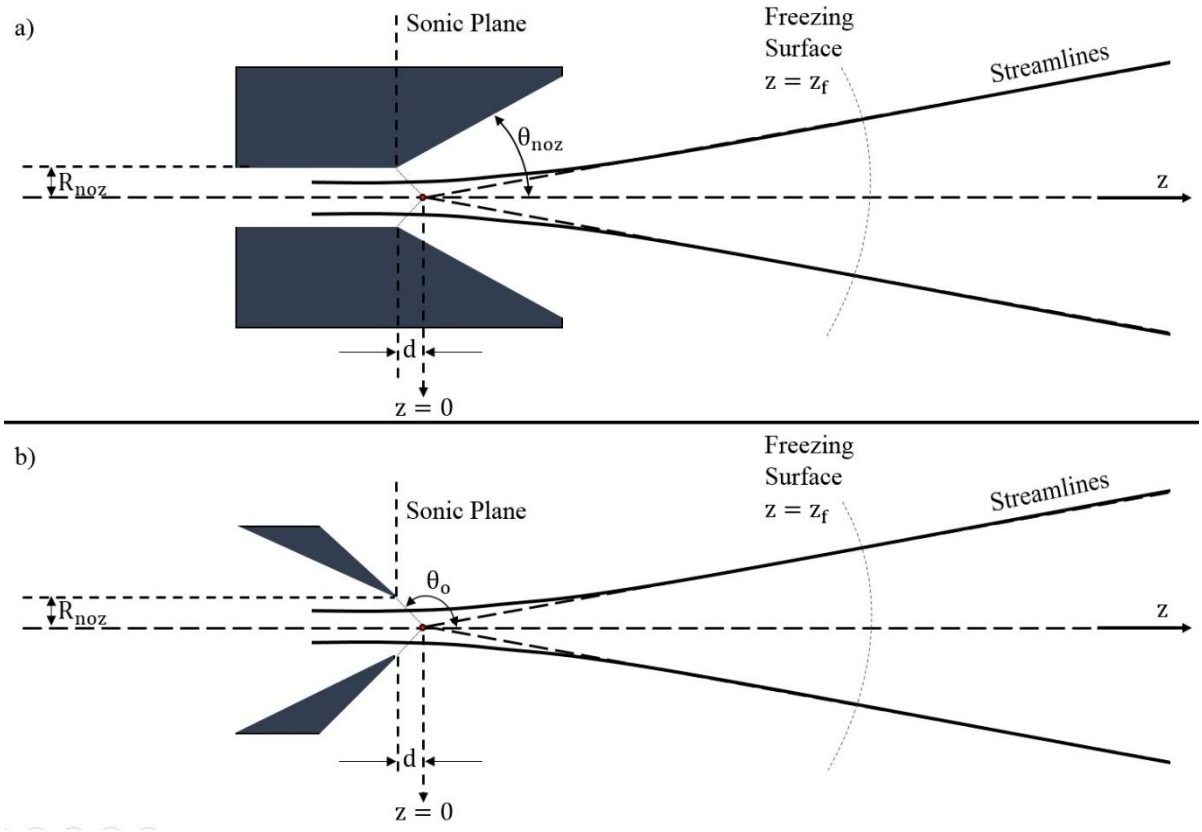

Figure 2 - 4: Supersonic Expansion Parameters

$\boldsymbol{\gamma}$	$5/3$	$7/5$	$9/7$
$\boldsymbol{a}$	0.802	0.591	0.490
$\boldsymbol{b}$	3	4.32	5.47
$\boldsymbol{\theta_o}$	$\pi/2$	2.28	2.87
$\boldsymbol{d/R_n}$	2	0.85	3.62

Table 2 - 3: Sudden-Freeze Model Parameters

The values shown in Table 2-3 for θ_o are determined by the Prandtl-Meyer relation. This relation describes the angles through which a flow can turn during an expansion and is usually expressed in terms of the Mach number for the flow, or by the Poisson coefficient, as

$$\theta_o = \frac{\pi}{2}\left(\sqrt{\frac{\gamma+1}{\gamma-1}} - 1\right) \tag{2.33}$$

Strictly speaking θ_o is the angle that the outer streamline makes with the z-axis, shown in Figure 2-5 as a function of rotor angle. For the values of a and b show in Table 2-3 the standard conservation laws are applied across the sonic plane and the equations generated by that analysis are solved numberically. For the number density, flow velocity, pressure, and temperature of the ensemble at the sonic plane

$$n_1 = n_o\left(\frac{2}{\gamma+1}\right)^{\frac{1}{\gamma-1}} \tag{2.34}$$

$$u_1 = \alpha\sqrt{\frac{\gamma}{\gamma+1}} \tag{2.35}$$

$$p_1 = n_1 k T_1 \tag{2.36}$$

$$T_1 = T_o\left(\frac{2}{\gamma+1}\right) \tag{2.37}$$

For the conservation of mass and axial momentum we have the initial equations

$$m\left(n_1 u_1(\pi R_n^2)\right) = m\int_0^{\theta_o} f(n(r,\theta),u)2\pi r^2 \sin(\theta)d\theta \tag{2.38}$$

$$\left((mu_1)n_1 u_1 + p_1\right)(\pi R_n^2) = m\int_0^{\theta_o}\left(u\cos(\theta)\right)f(n(r,\theta),u)2\pi r^2 \sin(\theta)d\theta \tag{2.39}$$

Which can be transformed by utilizing Eqn 2.34 through Eqn 2.37. This results in two equations

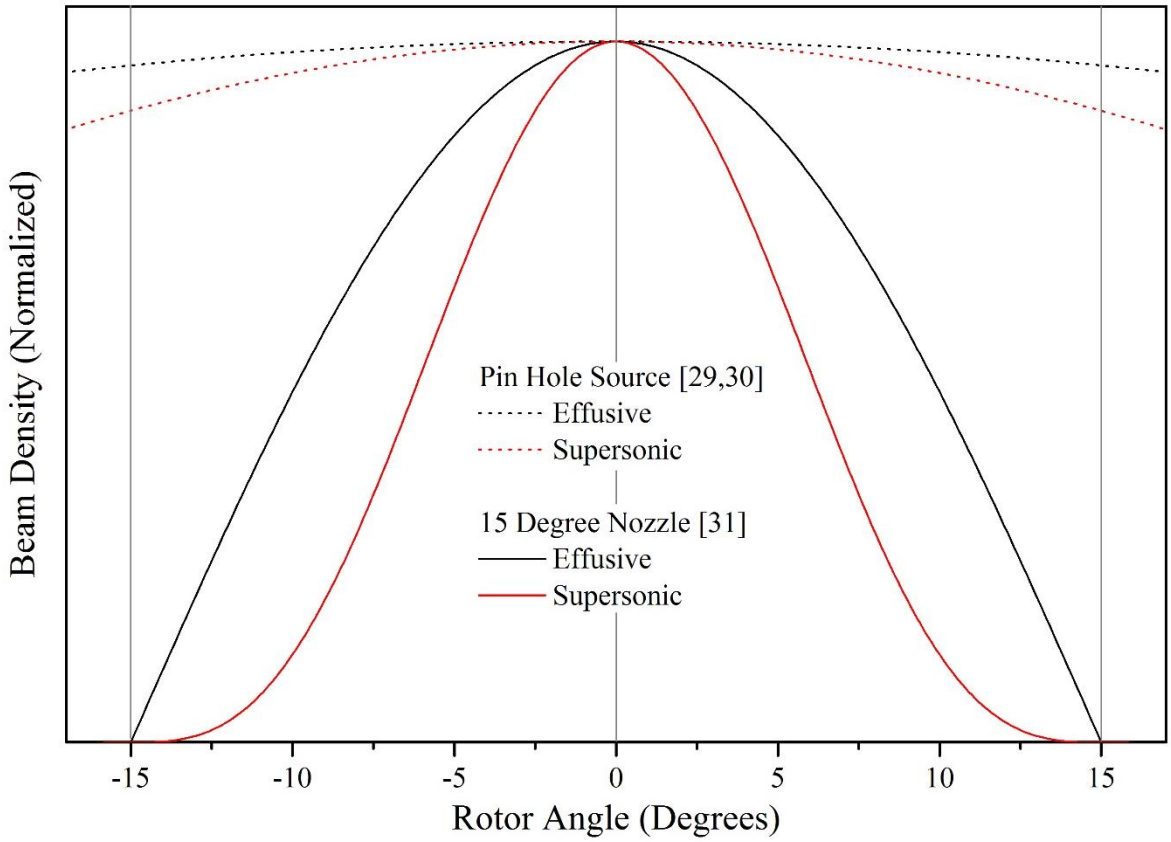

Figure 2 - 5: Angular Distributions with Conical Nozzle

$$\pi\left(\frac{2}{\gamma+1}\right)^{\frac{1}{\gamma-1}} = \int_0^{\theta_o} 2\pi \sin(\theta)\cos^b\left(\frac{\pi}{2}\frac{\theta}{\theta_o}\right) d\theta \tag{2.40}$$

$$\pi\left(\frac{2}{\gamma+1}\right)^{\frac{1}{\gamma-1}}\left(\frac{\gamma-1}{1}\right) = \int_0^{\theta_o} 2\pi \sin(\theta)\cos^b\left(\frac{\pi}{2}\frac{\theta}{\theta_o}\right)\cos(\theta)\, d\theta \tag{2.41}$$

that are solved numerically[16] for the case of an ideal atomic, diatomic, and triatomic gases.

These are only valid for the inertial region but act as a guide to setting up the equations governing beam behavior in the kinetic region. The name of the model, Sudden-Freeze, adequately describes how this transition is treated theoretically. It is assumed to occur at a specific location downstream of the nozzle called the 'Freezing Surface'.

The position of this plane is determined solely by the condition that the remaining collisions that occur beyond z_f be some small fixed number,N_F, which is estimated by

$$N_F = \int_{z_f}^{\infty} \Theta(z)\frac{dz}{u} \tag{2.42}$$

Where $\Theta(z)$ is the collision frequency described in Eqn 2.6. In order to solve for the location of the freezing surface a scale length, z_{ref}, and an a-dimensional source parameter, Ξ, are needed.

$$z_{ref} = aR_n \tag{2.43}$$

$$\Xi = 3.189\sqrt{\frac{\gamma-1}{\gamma}}\, z_{ref} n_o \left(\frac{C_6}{kT_o}\right)^{\frac{1}{3}} \tag{2.44}$$

Notice that both the scale length and a-dimensional source parameter are defined by model parameters (a), experimental dimensions (R_n), source conditions (n_o, T_o), and species-

dependent properties (γ, C_6). With these in hand, the position of the freezing surface can be estimated by

$$\frac{z_f}{z_{ref}} = \left(\frac{1.875\Xi}{N_F}\right)^{\frac{3}{\gamma+2}} \tag{2.45}$$

In the inertial regime the beam is assumed to be in full thermal equilibrium. This means the temperature can be expressed by

$$T(z) = T_o\left(\frac{z}{z_{ref}}\right)^{-2(\gamma-1)} \tag{2.46}$$

which describes the general reduction in temperature that occurs as the distance to the nozzle increases. This behavior is due to the fact that collisions tend to reduce the velocity differences between the molecules. This type of cooling is limited to the inertial regime and the temperature approaches a final finite value. This value can be in the mK range for typical beam conditions. However, beyond the intertial regime where there are very few collisions the behavior of the temperature can no longer be described by a single temperature. Instead a parrallel temperature, $T_{\parallel}$, and an orthogonal temperature, $T_{\perp}$, are introduced to describe the two distributions.

The Sudden-Freeze Model addresses the lack of subsequent cooling collisions by introducing a "freezing surface". The translational nonequilibrium that occurs in the kinetic regime allows two distinct equations to represent the seperate degrees of freedom. The parallel temperature for any distance beyond the freezing surface yields the same value

$$T_{\parallel}(z) = T\left(z_f\right) \tag{2.47}$$

The perpendicular temperature of the beam in the kinetic regime behaves differently to the temperature in the inertial regime and the parallel temperature. It is given by

$$T_{\perp}(z) = T(z_f)\left(\frac{z}{z_f}\right)^{-2} \tag{2.48}$$

and this cooling is the result of the beam distributing itself according to its orthogonal velocity. In the absence of collisions, any atom or molecule with small $u_{\perp}$ remain near the jet axis. With increasing distance from the nozzle, the $u_{\perp}$ distributions within a fixed volume element decrease, leading to the term "geometric cooling".

By combining Eqn 2.45 and 2.46 a final parallel temperature can be estimated.

$$T_{\parallel} = T_o\left(\frac{1.875\Xi}{N_F}\right)^{\frac{-6(\gamma-1)}{\gamma+2}} \tag{2.49}$$

This parallel temperature manifests itself in the velocity spread of the emitted beam, as shown in Figure 1-1. This drastically lower temperature is the result of converting the thermal energy of the reservoir into the directional kinetic energy of the expanded jet. As the final velocity of the beam increases the temperature decreases. To estimate a final flow velocity in this case we recall Eqn 2.29 and 2.30

$$u = \sqrt{\frac{\gamma}{\gamma-1}\frac{2R(T_o-T)}{N_A}} \qquad , \qquad u_{\infty} = \sqrt{\frac{\gamma}{\gamma-1}\frac{2RT_o}{N_A}} \tag{2.50}$$

These are manipulated to form

$$u = u_{\infty}\sqrt{1-\frac{T}{T_o}} \tag{2.51}$$

Which can utilize Eqn 2.49 directly to form a final flow velocity

$$u = u_\infty \sqrt{1 - \left(\frac{1.875\Xi}{N_F}\right)^{\frac{-6(\gamma-1)}{\gamma+2}}} \tag{2.52}$$

The Sudden-Freeze Model is compared with other theoretical models as well as experimental data[16] to determine $N_F \sim 2.14$ for a monatomic gas. It must be remembered, that although Eqn 2.52 looks simple the a-dimensional source parameter is defined by model parameters (a), experimental dimensions (R_n), source conditions (n_o, T_o), and species-dependent properties (γ, C_6).

If the species is not a monatomic gas there are internal temperatures corresponding to each active vibrational and rotational degrees of freedom (DOF) of the molecule. The Sudden- Freeze Model assumes these DOF are in equilibrium with one another during the inertial region of the expansion. As the beam ventures into the kinetic region each of the modes freezes out at a different location. This is easily incorporated into the Sudden Freeze Model by assigning different values of N_F for each internal degrees of freedom. The ordering of the surfaces relates to the efficiency of energy transfer between the modes and the translational degree of freedom. Since vibration couples the weakest to translation the ordering is $N_F^{vib} > N_F^{rot} > N_F$. This effects the final parallel translational temperature of the beam as well as the temperatures which correspond to rotation and vibration. Typical beam temperatures for polyatomic gases are $T_{vib} \sim 5T_{rot}$, and $T_{rot} \sim 5T_{\parallel}$ [24, 25].

Thermal Conduction Model

C.W. Beijerinck and N.F. Verster [16] attempt to improve on the Sudden Freeze Model by re-examining the temperature evolution in the kinetic regime. Instead of assuming two

independent temperatures the Thermal Conduction Model establishes two energy reservoirs that can interact. These are the reservoir of parallel energy

$$E_{\parallel} = \frac{m}{2}\sum v_z^2 \tag{2.53}$$

and the reservoir of orthogonal energy

$$E_{\perp} = \frac{m}{2}\sum\left(v_x^2 + v_y^2\right) \tag{2.54}$$

Where the summations are over all the atoms in the expansion. Collisions determine the energy transfer between the two reservoirs. The two distinct temperatures used to describe the energy distributions above obey a set of coupled differential equations

$$\frac{dT_{\perp}}{dz} = -\frac{2T_{\perp}}{z} + \frac{1}{2}\Lambda(z)(T_{\parallel} - T_{\perp}) \tag{2.55}$$

$$\frac{dT_{\parallel}}{dz} = -\frac{1}{2}\Lambda(z)(T_{\parallel} - T_{\perp}) \tag{2.56}$$

$$\Lambda(z) = \frac{16}{15} n \frac{\Omega(T)}{u_{\infty}} \tag{2.57}$$

where the coefficient $\Lambda(z)$ takes into consideration the energy transfer between the two reservoirs. Here $n = n(z)$ is the number density and u_{∞} is the terminal velocity of the beam. Ω is a species-dependent integral, described in Eqn 2.7, that depends primarily on the C_6 Van der Waals coefficient [16]. For use in calculating Ω the temperature used is simply the average of the two reservoirs: $T = (1/3)(T_{\parallel} + 2T_{\perp})$.

The cooling that is described as "geometric" in the Sudden Freeze Model can be seen in the first term of Eqn 2.55. In the limiting case of no thermal conduction between the two reservoirs: $\Lambda(z) = 0$, $T_{\parallel} = const$, and $T_{\perp} \propto z^{-2}$. In this case the Sudden Freeze Model is

recovered. In the limiting case where the two reservoirs have perfect conduction: $\Lambda(z) = \infty$, and $T_{\parallel} = T_{\perp} \propto z^{-4/3}$. Explicit formulations of $\Lambda(z)$ for realistic intermolecular potentials can be found [16, 26] in literature. Only a summarization will be contained here and then the working formulas which will be used for the rest of this thesis are presented in Table 2-5.

The Thermal Conduction Model relates the final translational temperature of the beam to the parameters in the reservoir by utilizing a product, $\lambda_o z_o$, which is essentially an inverse Knudsen number. The Knudsen number is a dimensionless parameter that represents the ratio of the mean free path, λ, to a characteristic length scale of the system.

γ	5/3	7/5	8/6
K	2.0	1.35	1.08
τ	1.151	1.266	1.258

Table 2 - 4: Thermal Conduction Model Parameters

$$\frac{T_o}{T_{\parallel}} = \frac{1}{\tau}(\lambda_o z_o)^{12/11} \tag{2.58}$$

$$\lambda_o = 1.564\sqrt{\frac{\gamma-1}{\gamma}}\left(\frac{3C_6}{kT_o}\right)^{1/3} n_o \tag{2.59}$$

$$z_o = R_n\sqrt{K}\left[\sqrt{\frac{\gamma-1}{\gamma+1}}\left(\frac{2}{\gamma+1}\right)^{1/(\gamma-1)}\right]^{1/2} \tag{2.60}$$

Molecule	$\boldsymbol{\gamma}$	**Working Formula**
He	$5/3$	$T_{\parallel} = \left(\frac{T_o}{6.1}\right)(P_o d)^{-12/11}$
Ne	$5/3$	$T_{\parallel} = \left(\frac{T_o}{10.4}\right)(P_o d)^{-12/11}$
Ar	$5/3$	$T_{\parallel} = \left(\frac{T_o}{24.3}\right)(P_o d)^{-12/11}$
Kr	$5/3$	$T_{\parallel} = \left(\frac{T_o}{31.2}\right)(P_o d)^{-12/11}$
Xe	$5/3$	$T_{\parallel} = \left(\frac{T_o}{40.8}\right)(P_o d)^{-12/11}$
O_2	$7/5$	$T_{\parallel} = \left(\frac{T_o}{6.1}\right)(P_o d)^{-0.706}$
SF_6	$8/6$	$T_{\parallel} = \left(\frac{T_o}{1.5}\right)(P_o d)^{-12/11}$
	1.094	$T_{\parallel} = \left(\frac{T_o}{6.7}\right)(P_o d)^{-12/11}$

Table 2 - 5: Thermal Conduction Model Working Formulas

The constants K and τ are given in Table 2-4 as a function of the Poisson coefficient. These are used to formulate a set of working equations[7], shown in Table 2-5, that are presented using the reservoir pressure, P_o, reservoir temperature, T_o, and the nozzle diameter, $d = 2R_n$. The reservoir pressure, P_o, is measured in units of Torr, and the nozzle diameter is measured in cm. This parallel temperature is used along with Eqn 2.51 to solve for the final flow velocity of the beam.

For most calculations presented in this thesis, the working formulas presented in Table 2-5 are used. This is due to the fact that the Sudden Freeze model tends to overestimate the parallel temperatures of the beam. While the Thermal Conduction Model improves upon this estimation by including realistic intermolecular potentials and thermal conduction due to collisions that occur throughout the expansion. Figure 2-6 shows how u/u_∞ and $T_\parallel$ change as a function of $P_o d$, the reservoir pressure and source diameter, measured in $torr\ cm$. While the temperature varies slowly as the source conditions change the terminal velocity approaches its asymptotic value very quickly. Molecules behave in a similar manner to atoms but the cooling is less efficient. The velocity distributions of xenon and sulfure hexafloride (SF6) are shown as a function of $P_o d$ in Figure 2-7. The disparity is due to the fact that each energy mode in SF6 has an associated temperature and thermal distribution which evolves throughout the expansion. This evolution always impacts the final parallel temperature of the beam.

The Thermal Conduction Model applies correction terms to the terminal velocities and parallel beam temperatures. The flow rate for a nozzle operating in the supersonic regime can be estimated by using Eqn 2.34 and 2.35 from the Sudden Freeze Model.

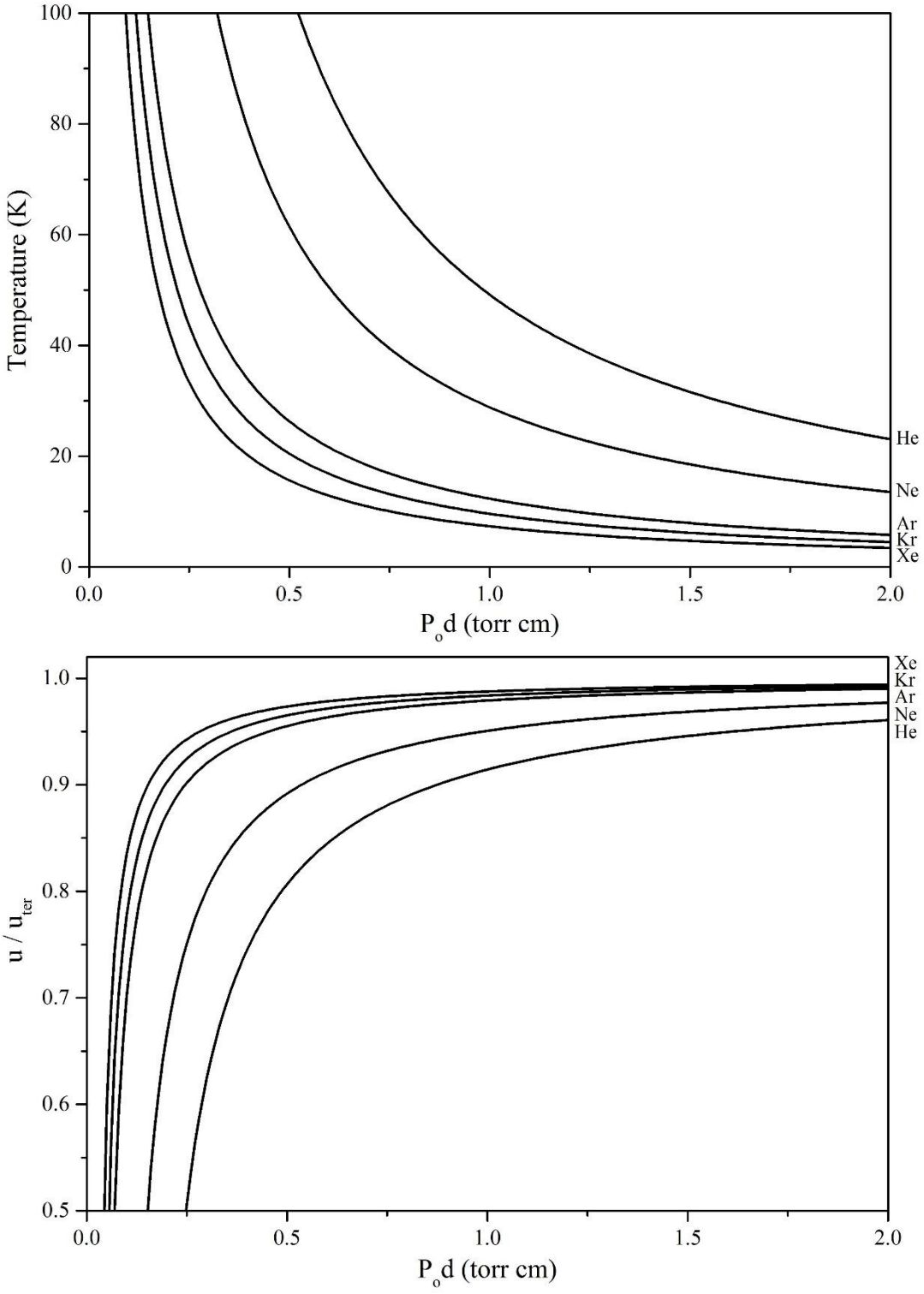

Figure 2 - 6: Supersonic Beam Parameters – Rare Gases

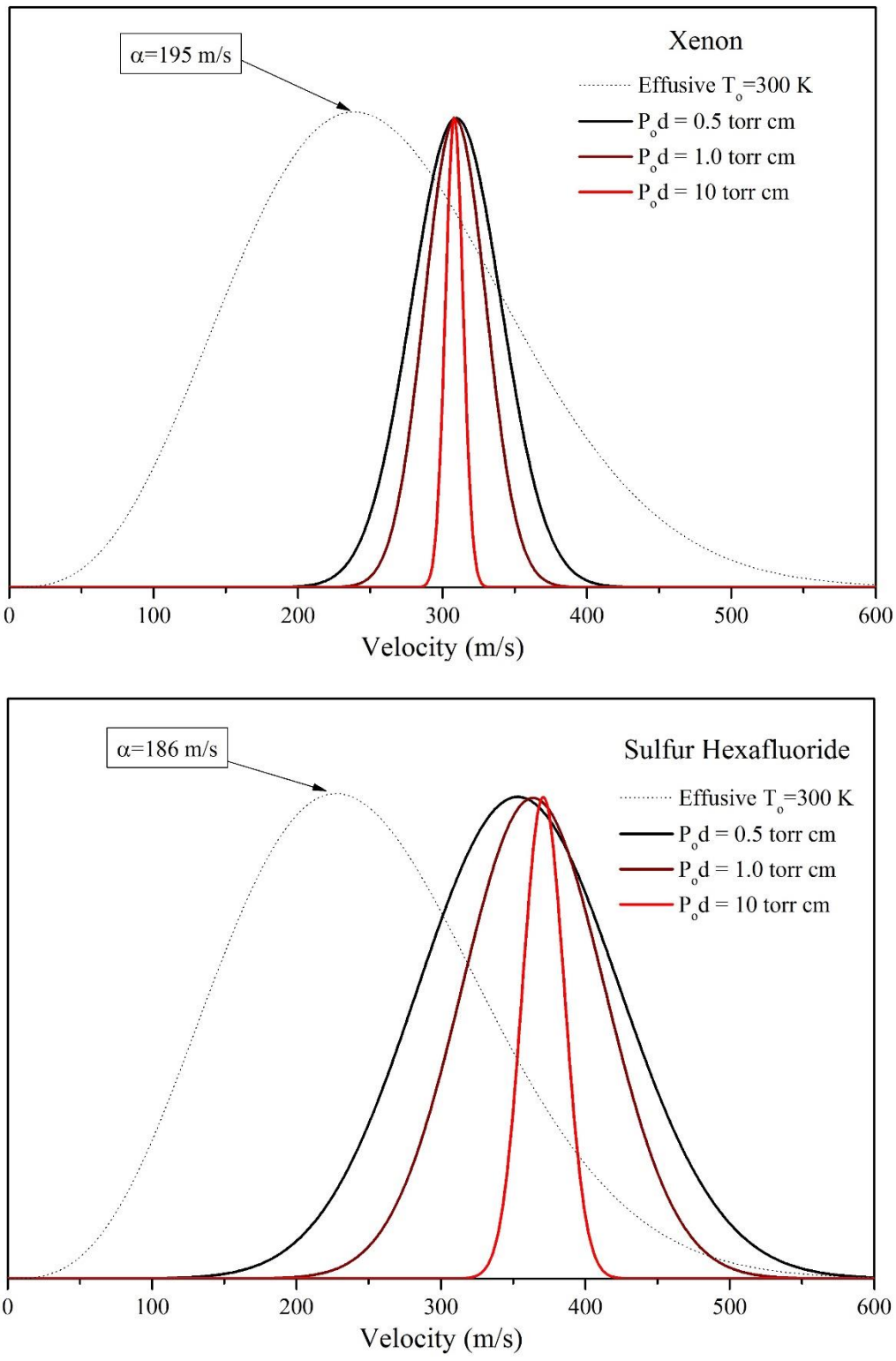

Figure 2 - 7: Supersonic Beam Parameters - Velocity Distributions

$$\dot{N} = u_1 n_1 (\pi R_n^2) \tag{2.61}$$

$$\dot{N} = (\pi R_n^2) n_o \alpha f(\gamma) \tag{2.62}$$

$$f(\gamma) = \sqrt{\frac{\gamma}{\gamma+1}} \left(\frac{2}{\gamma+1}\right)^{1/(\gamma-1)} \tag{2.63}$$

Where all parameters have been defined previously. These equations are used to estimate the emission along the symmetry axis of the beam by using an a-dimensional peaking factor, κ, which is

$$\kappa = \pi \frac{I(0)}{\dot{N}} \quad , \quad I(0) = \frac{\kappa \dot{N}}{\pi} \tag{2.64}$$

For an effusive source Eqn 2.17 and 2.18 are used in Eqn 2.64 and result in $\kappa = 1$. In the case of a convergent nozzle operating in the supersonic regime Eqn 2.32 is used to estimate centerline intensity as

$$I(0) = n(z) z^2 u = a^2 n_o R_n^2 u_\infty \tag{2.65}$$

Now this can be combined with Eqn 2.62 to obtain

$$\kappa = \pi \frac{a^2 n_o R_n^2 u_\infty}{(\pi R_n^2) n_o \alpha f(\gamma)} \tag{2.66}$$

$$\kappa = \frac{a^2}{f(\gamma)} \sqrt{\frac{\gamma}{\gamma-1}} \tag{2.67}$$

For the case of a monatomic gas in a convergent nozzle this returns $\kappa = 2$. So the large on-axis intensity for a convergent nozzle is a result of the large value of $\dot{N}$ and not due to the forward peaking of the beam. Such a large value of $\dot{N}$ is possible due to the high pumping speed used for supersonic beams versus that utilized in an effusive source.

To extend this analysis to cases where the aggregation state of the source gas is considered a free parameter the Thermodynamic Equation of State can be applied. This approach is different than any previously described because it doesn't attempt to explain the transition through the different density regimes, but instead only attempts to define the initial and final states of the ensemble.

Thermodynamic Equations of State

The primary advantage of using Eqn 2.68 for beam characterization is its simplicity. It allows the researcher to estimate, within a small window of applicability, the terminal flow velocity of a supersonic beam given a characteristic temperature and gas type.

$$\langle v_\infty \rangle = \sqrt{\frac{\gamma}{\gamma-1}\frac{2RT_o}{N_A m}} \tag{2.68}$$

Unfortunately it fails at higher pressures and lower temperatures. This can be seen by direct observation of helium [27-30] and hydrogen [31] beams at cryogenic conditions, in carbon dioxide beams [32, 33] in supercritical conditions, and even in rare gas beams [34] at high densities. These experiments show that an appropriate method for characterizing a beam source must take into consideration cluster formation and treat the system as a real fluid instead of an ideal perfect gas.

For real gases, liquids, and supercritical fluids, the general method of employing realistic enthalpies as in Eqn 2.22, may be used to characterize the beam properties. In order to calculate these enthalpies an equation of state (EOS) for the fluid system must be used. This equation is a multiparameter description of all experimental results for a particular fluid[35]. They are available for the rare gases [21, 22, 36, 37] and for many other gases as

Species	**Triple Point Temp.**	**Critical Temp.**	**Triple Point Press.**	**Critical Press.**	**Vaporization Enthalpy**	**Vaporization Enthalpy**
	$T_t(K)$	$T_c(K)$	$P_t(MPa)$	$P_c(MPa)$	$\Delta_v H_t(kJ/mol)$	$\Delta_v H_b(kJ/mol)$
He[22]	2.18	5.20	4.86	0.227	0.093	0.083
Ne[36]	24.56	44.49	43.37	2.679	1.778	1.730
Ar[21]	83.81	150.69	68.89	4.863	6.540	6.437
Kr[37]	115.78	209.48	73.53	5.525	9.084	8.971
Xe[37]	161.41	289.73	81.77	5.842	12.657	12.550

Table 2 - 6: Relevant Thermodynamic Properties for Rare Gases

well. This approach allows for the inclusion of all three aggregation states: the gaseous, liquid, and supercritical. It includes the liquid-gas phase transition as well as the critical point. It cannot however describe any solid clusters, so the triple point temperature is the lower bound of its applicability. This does not provide a strict limitation on the application of this method. Several relevant parameters for the stable rare gases are given in Table 2-6. Frequently the EOS is expressed in terms of the Helmholtz energy, A, which is

$$A \equiv U - TS \tag{2.69}$$

Where S is the molar entropy. This transformation allows all the relevant thermodynamic properties to be assessed by partial derivatives of A. The molar enthalpy becomes

$$H \equiv A + TS + PV \tag{2.70}$$

and several other relations can be defined as well.

$$S = -\left(\frac{\partial A}{\partial T}\right)_V \quad , \quad P = -\left(\frac{\partial A}{\partial V}\right)_T \tag{2.71}$$

In order to estimate the Poisson coefficient, as used in Eqn 2.29, the following derivatives

$$C_V = \left(\frac{\partial U}{\partial T}\right)_V \quad , \quad U = A - \left(\frac{\partial A}{\partial T}\right)_V \tag{2.72}$$

are used in conjunction with Eqn 2.28. This analysis reveals the different dependence of the enthalpy and Poisson coefficient on the reservoir temperature and pressure. The Poisson coefficient is remarkably stable over the entire pressure and temperature range. Only deviating from the familiar $\gamma = 5/3$ near the critical point. In this region the value of the Poisson coefficient rises quickly and easily reaches a value of 5 or greater. The enthalpy on the other hand increases linearly with respect to temperature and is not significantly effected

by a change in pressure. The only noticeable feature in the enthalpy response to changes in reservoir pressure and temperature correspond to the liquid-vapor phase boundary where the rate of change increases considerably. This lack of features is what allows the enthalpy to be used to describe other parameters so readily.

2.2 Rotating Beam Source

As mentioned in the introduction, the purpose of this study is to understand how a high speed rotating source augments the characteristics of a supersonic beam as they are described by the previous sections of this section. The analysis is based on the experimental configuration shown in Figure 2-8. This figure shows the rotor mounted on a high speed motor capable of forward and backward motion and frequencies up to 400 Hz. The rotor is hollow and contains convergent-divergent nozzle at the very tip which emits a supersonic beam orthogonal to the body of the rotor. Prior to cycling the solenoid valve, the rotor and the gas feed system are assumed to be at the pressure measured on the main chamber ionization gauge. As the valve transitions through its opening and closing phases the rotor fills to a maximum pressure and then drains through the nozzle and feed system leaks. Once per rotation the nozzle lines up with a skimmer mounted on the chamber wall and a profile of the emerging beam is incident upon a detector. This profile is what will be used in Section 4 to identify the unique characteristics of the rotating source in different directions and at different frequencies.

Upon reaching very high peripheral velocities of the rotor several effects must be considered. First is the enhancement of the input pressure due to the centrifugal force acting on the gas molecules inside the rotor. Next the gate function of the rotor is considered for

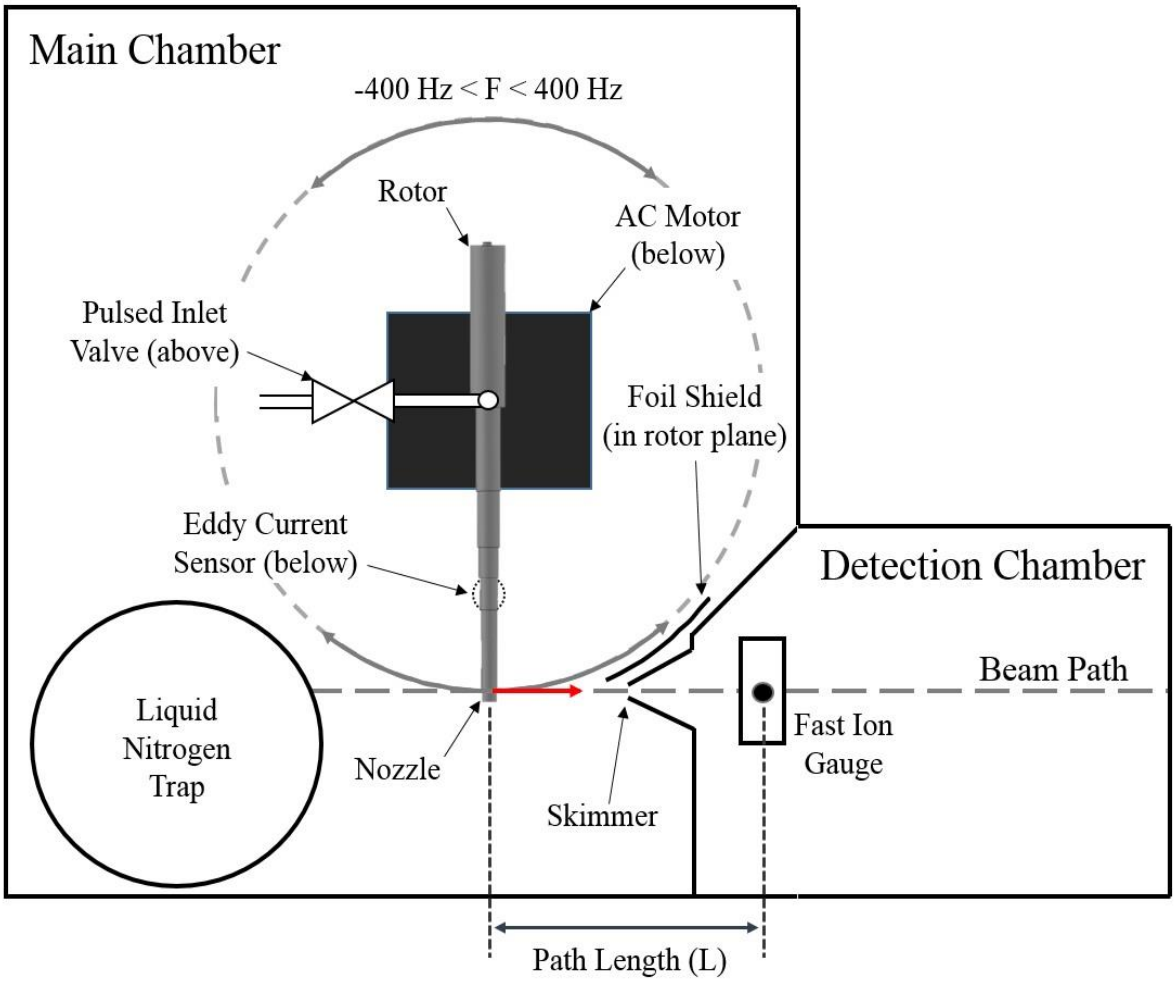

Figure 2 - 8: Experimental Configuration

different skimmer sizes. Finally, the vectorial addition of the tip velocity, V_{rot}, with the molecular beam velocity, X, is considered. The velocity augmentation and density enhancement are verified for different types of gases as well.

2.2.1 Centrifugal Enhancement

The intial condition of the rotor prior to cycling the solenoid valve is expected to be identical to the rest of the main chamber. Once the valve is cycled the pressure inside the rotor grows to a maximum and then the pressures re-equilibrate prior to the next pulse. The evolution of this maximum value depends directly on the angular velocity, ω, of the rotor. The centrifugal force, F_c, is

$$F_c = m\omega^2 R \tag{2.73}$$

Where R is the length of the rotor and m is the mass of gas species being used. Integrating this over R returns the potential energy, V_c, experienced by the molecules inside the rotor

$$V_c = -\frac{m\omega^2 R^2}{2} = -\frac{mV_R^2}{2} \tag{2.74}$$

Which depends on the peripheral velocity of the rotor squared. This potential can be used with Boltzmann's law to describe the number density inside the rotor as

$$n = n_o e^{-V/kt} \tag{2.75}$$

$$n = n_o e^{mV_R^2/2kt} \tag{2.76}$$

With the gas density behind the nozzle growing exponentially as the velocity of the rotor is increased. This growth means that the beam formed by the nozzle can have a drastically higher pressure than the reservoir pressure supplied by the inlet valve. Figure 2-9 shows this

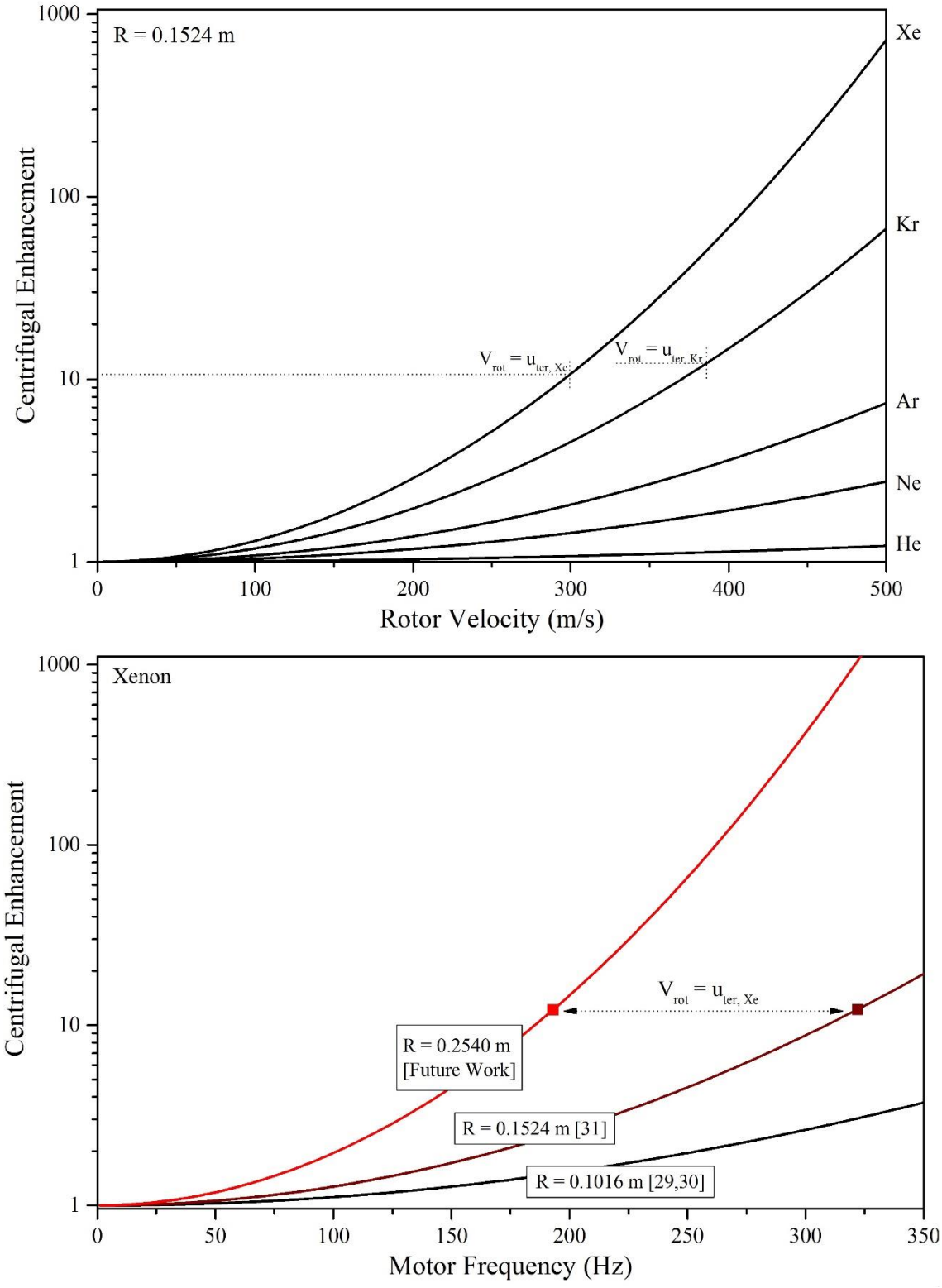

Figure 2 - 9: Centrifugal Enhancement Term

enhancement factor as a function of the rotor velocity for the rare gases. This effect occurs regardless of the direction of rotation. For the backwards direction, however, the rotor velocity cannot exceed the terminal velocity of the supersonic beam. In the forwards direction there is no such limit, and it is worth noting that the enhancement term for xenon grows to over 1000 for a modest rotor velocity of 500 m/s. This is why such high source pressures were considered in Section 2.1.

For expansions that occur at such high effective reservoir pressures the mean free path near the sonic plane is much smaller than the throat of the nozzle. This means the equilibrium assumed by the Boltzmann law extends beyond the rotor itself. It becomes insignificant at the same distance that rethermalizing collisions in the expansion cease. To understand the impact that such a force has on the beam a simple comparison can be made between the expansion force and the centrifugal force[7].

$$F_e = ma = m\frac{dv}{dt} \tag{2.77}$$

During a supersonic expansion the molecules are accelerated essentially from rest to the terminal velocity within one nozzle diameter

$$dv = u - 0 = u \tag{2.78}$$

$$dt = \frac{dl}{u/2} \tag{2.79}$$

Where the average velocity is used in the denominator Eqn 2.86, and the distance in which the acceleration occurs is $dl = 2R_n$.[38] This returns an expansion force

$$F_e = \frac{mu^2}{4R_n} \tag{2.80}$$

Name	Gupta, et. al.[8, 9]	Sheffield, et. al.[39]	Future Work
Rotor Length, R	$0.1016\ m$	$0.1524\ m$	$0.2540\ m$
Nozzle Radius, R_n	$5E-5\ m$	$2.54E-4\ m$	$5E-4\ m$
Force Ratio, F_e/F_c	500	150	262

Table 2 - 7: Experimental Parameters for Force Comparison

Which can be compared with the centrifugal force for the situation when $u = V_{rot}$

$$F_c = \frac{mu^2}{R} \tag{2.81}$$

The ratio of these two forces,

$$\frac{F_e}{F_c} = \frac{R}{4R_n} \tag{2.82}$$

is given in Table 2-7 for the original version of the rotating source, the current version, and a proposed rotor design for future research. Even though the expansion force is 150 times larger than the centrifugal force it can still effect the final transverse velocity and angular density distribution of the beam. Since the centrifugal force only occurs in the transverse direction it should have no effect on the longitudinal velocity component of the beam. The force ratio is used to determine the amount of transverse velocity that is imparted on the completely expanded jet

$$u_\perp = u\left(\frac{R}{4R_n}\right) \tag{2.83}$$

For the current design $u_\perp = u/150$ and the transverse velocity imparted by the centrifugal force acting throughout the expansion can be neglected for all except the slowest beams. For very slow beams the final lab frame velocity is often below 50 m/s. For xenon gas the terminal beam velocity in the rotor frame of reference is above 300 m/s. This returns a transverse velocity component of at least 2 m/s which grows as slower beams are pursued.

2.2.2 Swatting

The next situation analyzed involves the limiting case where molecules emitted from the rotor are collected by the rotor tip on the subsequent rotation[7]. This section defines a lower

limit on final velocity of the slowed beam. When the rotor is used to accelerate the supersonic beam swatting does not occur and the fundamental lower limit of the final velocity can be estimated as the rotor tip velocity. It will become obvious however, that the lower limit of measured beams does not yet approach the fundamental limit imposed by swatting.

For a rotor of length R the nozzle cannot be placed at the absolute edge of the rotor. It is instead placed a distance, L_n, from the point of rotation. These two parameters, as can be seen in Figure 2-10, define the minimum distance that a molecule must travel the distance

$$d = \sqrt{R^2 - L_n^2} \tag{2.84}$$

To clear the path of the rotor before its next rotation. The time it takes for the rotor to perform one full rotation minus the angle ϕ_{sw} depends on the angular frequency of the rotor, ω

$$\tau_{r,sw} = (2\pi - \phi_{sw})\omega^{-1} \tag{2.85}$$

The angle ϕ_{sw} is defined, as is seen in Figure 2-10, by

$$\phi_{sw} = \cos^{-1}\left(\frac{L_n}{R}\right) \tag{2.86}$$

The fundamental limit, u_{min}, occurs when the time it takes for the rotor to subtend $360 - \phi_{sw}$ degrees is the same time it takes for the molecules to travel the distance d.

$$\tau_{r,sw} = \frac{d}{u_{min}} \tag{2.87}$$

$$u_{min} = \frac{\omega\sqrt{R^2 - L_n^2}}{\left(2\pi - \cos^{-1}\left(\frac{L_n}{R}\right)\right)} \tag{2.88}$$

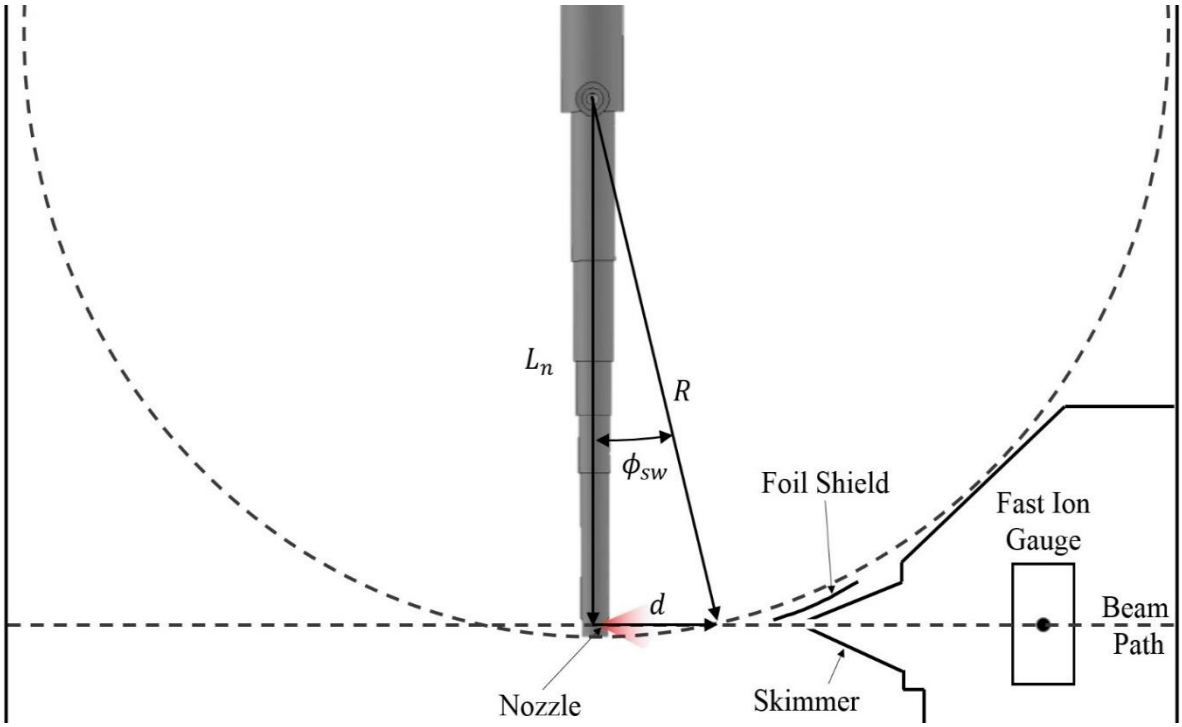

Figure 2 - 10: Experimental Parameters - Swatting Limit

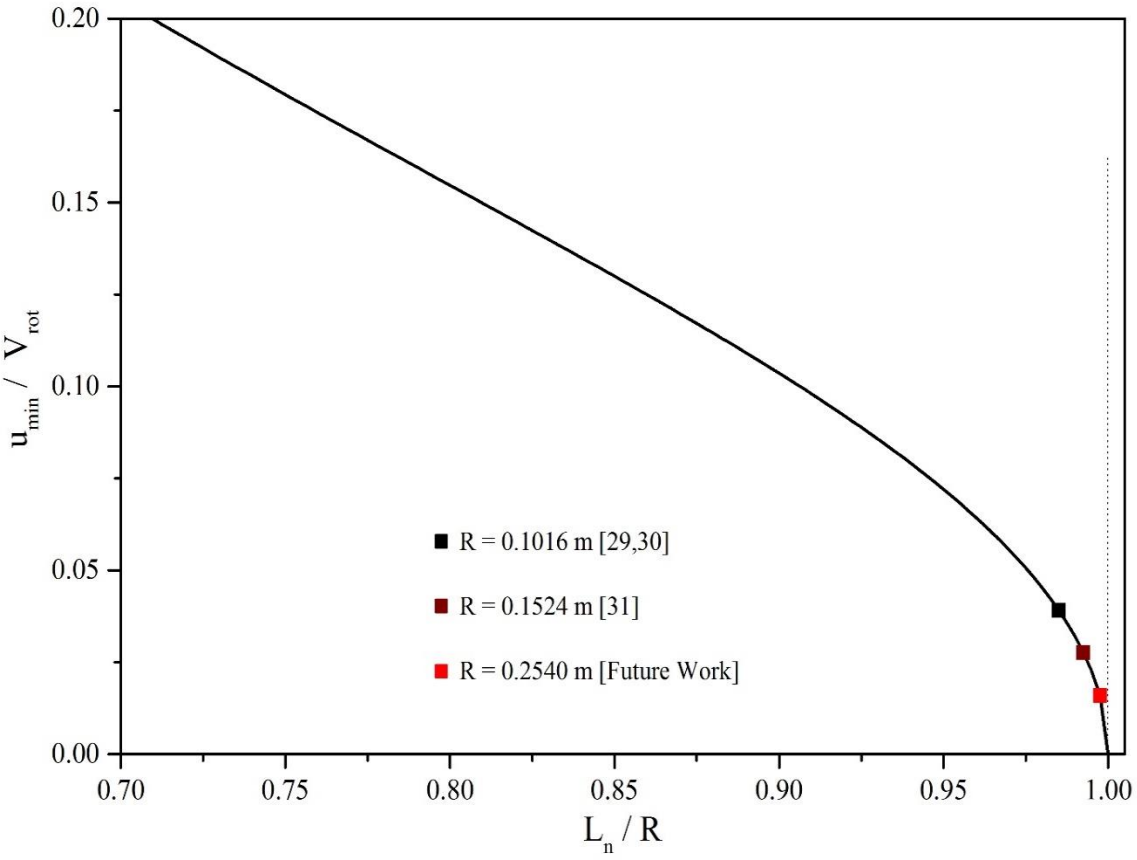

Figure 2 - 11: Minimum Beam Velocity - Swatting Limit

This can be simplified by using the linear velocity of the rotor, $V_{rot} = \omega L_n$, and results can be understood as a ratio of velocities. This ratio is shown in Figure 2-11, with each iteration of the rotor describing a point on this function of L_n/R

$$\frac{u_{min}}{V_{rot}} = \frac{\sqrt{\left(\frac{R}{L_n}\right)^2 - 1}}{\left(2\pi - \cos^{-1}\left(\frac{L_n}{R}\right)\right)} \tag{2.89}$$

$$(2\pi - \phi_{sw})\omega^{-1} = \frac{\sqrt{R^2 - L_n^2}}{u_{min}} \tag{2.90}$$

Name	Gupta, et. al.[8, 9]	Sheffield, et. al.[39]	Future Work
Rotor Length, R	$0.1016\ m$	$0.1524\ m$	$0.2540\ m$
Distance to Nozzle, L_n	$0.099\ m$	$0.1499\ m$	$0.2527\ m$
Velocity Ratio, u_{min}/V_{rot}	0.038	0.030	0.016

Table 2 - 8: Experimental Parameters for Swatting Comparison

Future work, as shown in Figure 2-8, can move the nozzle considerably closer to the tip of the rotor. This alteration subsequently reduces the limiting velocity by almost a factor of 2.

This fundamental limit can be extended upon by considering not only swatting by the rotor but also scattering by gas emitted from the rotor. Instead of traveling through vacuum straight through the skimmer, the beam, or part of the beam, is scattered by gas from the

subsequent rotation. Before considering this case the peak shape for an individual pulse is discussed for the rotating source.

2.2.3 Relevant Angles

Due to the use of many different rotors and skimmers, one cannot assume that the rotor fires molecules only from the "shooting" position, $\phi = 0$. Such a perspective leads to large errors in the interpretation of the rotor augmented beams. Instead, the rotor is assumed to emit molecules from a range of angles that ultimately pass through the skimmer and into the detection region. This analysis critically depends on the assumption that the rotor is perfectly aligned/oriented with the skimmer and detector when $\phi = 0$. The angles, both forward and back from $\phi = 0$, are determined by the detector line-of-sight (LOS). The detector LOS, as seen in Figure 2-12, consists of two lines that intersect at the inner edge of the skimmer. One line, LOS_1, corresponds to the point at which molecules begin traveling from the nozzle to the detector. The other line, LOS_2, corresponds to the point at which the entire detection region is exposed to the nozzle.

As can be seen in Figure 2-12, the detector LOS is determined by the distance to the skimmer L_{sk} which is 60 mm, as well as the distance to the detector L_{det} which is 120mm. The radius of the skimmer, R_{sk}, varies between 0.5, 1.5, or 2.5 mm. The width of the detection region in the y-direction, called R_{det} in this calculation, stays at 3mm. The detector LOS are defined by two points (x_1, y_1) and (x_2, y_2), each described in Table 2-9. The points of intersection for either of the detector LOS and the circular path of the nozzle with radius L_n, centered at zero, is[40]

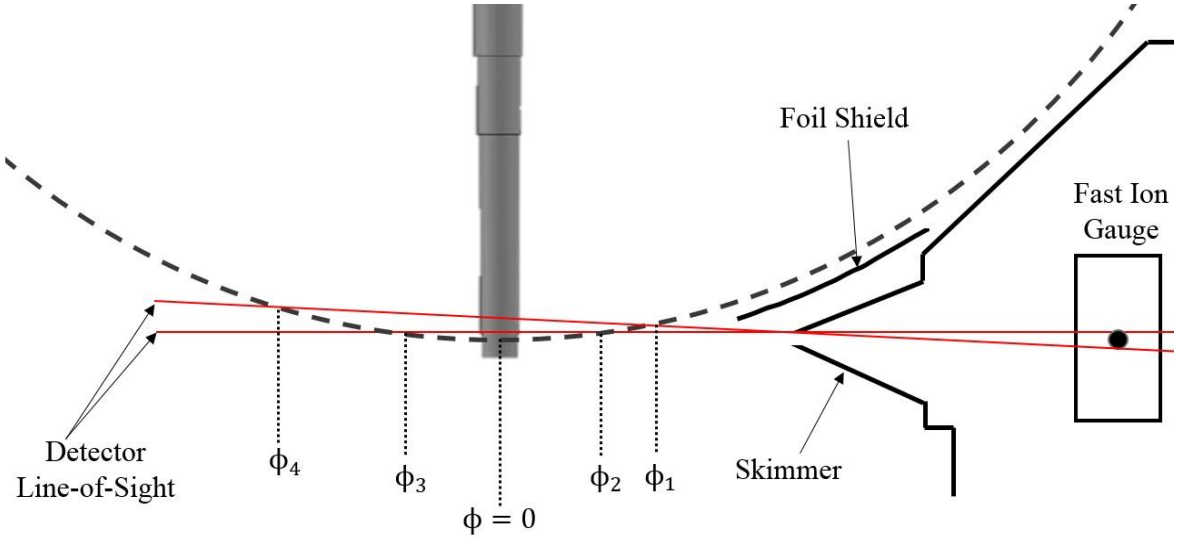

Figure 2 - 12: Detector Line-of-Sight

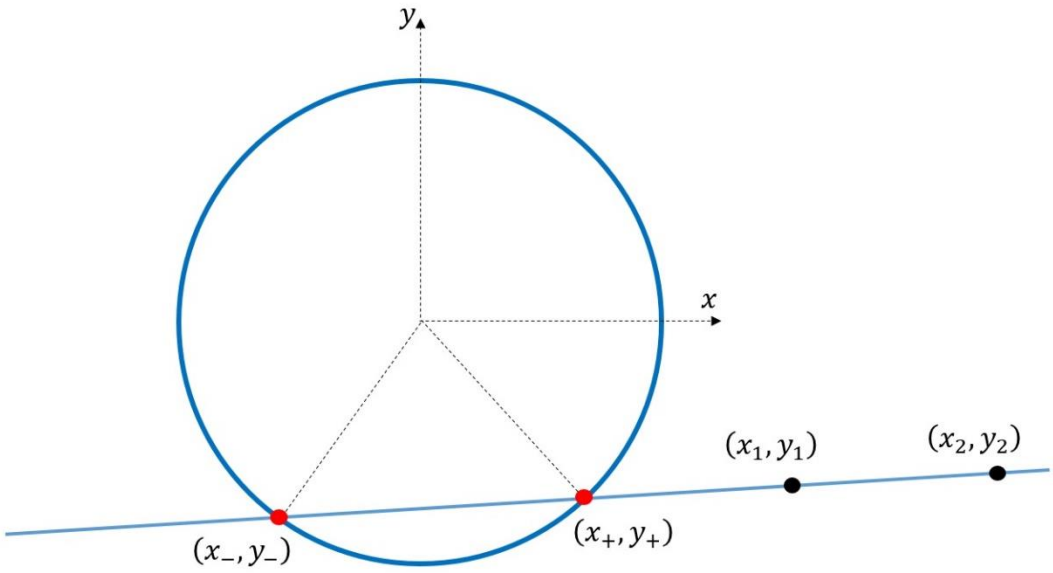

Figure 2 - 13: Detector Line-of-Sight Schematic

$$d_x = x_2 - x_1 \tag{2.91}$$

$$d_y = y_2 - y_1 \tag{2.92}$$

$$d_r = \sqrt{d_y^2 + d_x^2} \tag{2.93}$$

$$D = \begin{vmatrix} x_1 & x_2 \\ y_1 & y_2 \end{vmatrix} = x_1 y_2 - x_2 y_1 \tag{2.94}$$

The points of intersection, shown in Figure 2-13, are

$$x_{\pm} = \frac{D d_y \pm sgn(d_y) d_x \sqrt{r^2 d_r^2 - D^2}}{d_r^2} \tag{2.95}$$

$$y_{\pm} = \frac{-D d_x \pm |d_x| \sqrt{r^2 d_r^2 - D^2}}{d_r^2} \tag{2.96}$$

And the function $sgn(d_y)$ is

$$sgn(d_y) = \begin{cases} -1 & \text{for } d_y < 0 \\ 1 & \text{otherwise} \end{cases} \tag{2.97}$$

For both of the detector LOS lines the values for (x_1, y_1) are the same. As is shown in Table 2-9 there are 2 different values for y_2 which produce the 4 critical angles

$$\phi_{i,\pm} = \left(\frac{360}{2\pi}\right) \arctan\left(\left|\frac{x_{,\pm}}{y_{i,\pm}}\right|\right) \tag{2.98}$$

Where the subsript i represents the two different detector LOSs, and the subscript $\pm$ represents the two different intersections that occur between a line and a circle. The data shown in Figure 2-14 represents the 4 critical angle values that determine the shape of the detected beam as a function of skimmer radius. For some values of the skimmer radius the rotor augmented beam does not illuminate the entire detection region. Thus the angles

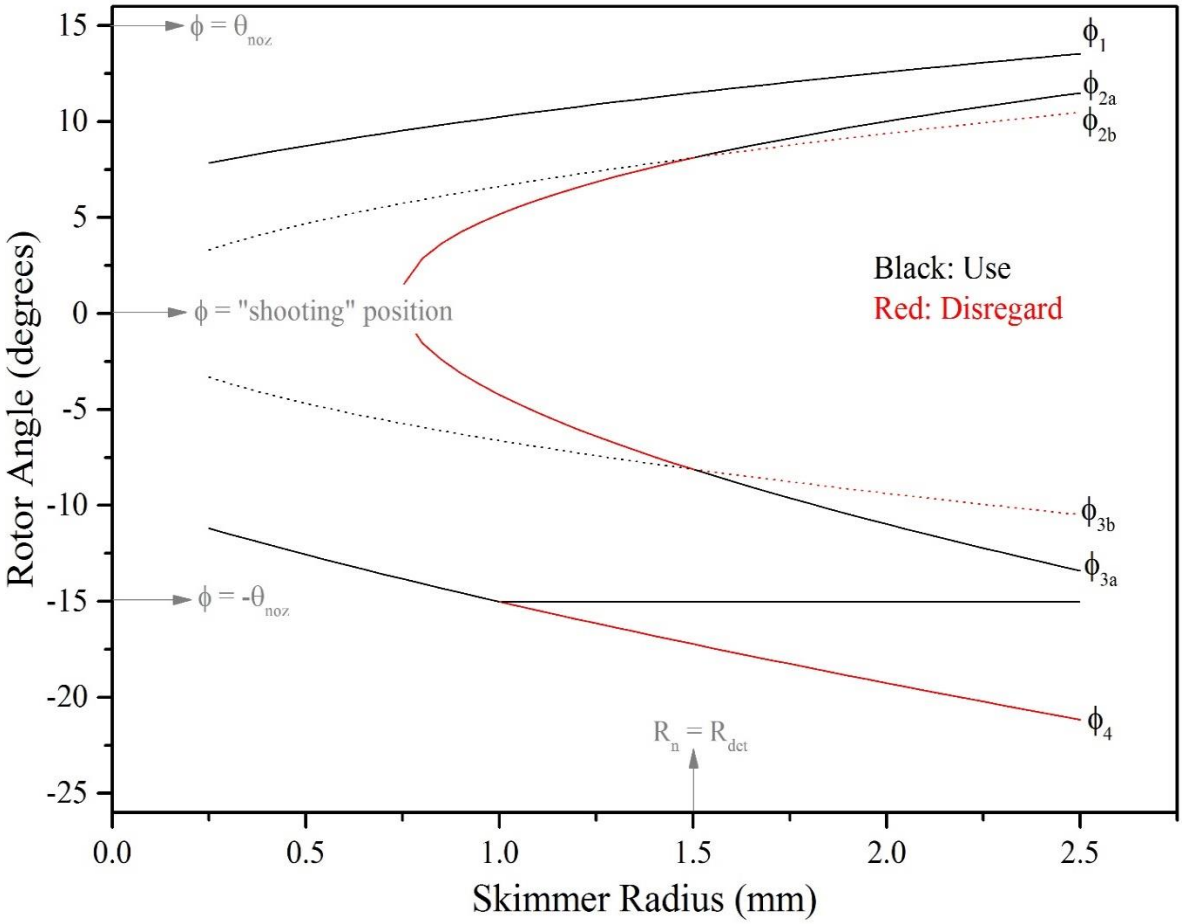

Figure 2 - 14: Relevant Rotor Angles vs Skimmer Radius

Angle	LOS	x_1	y_1	x_2	y_2	$(x_{+/-}, y_{+/-})$
ϕ_1	LOS_1	L_{sk}	$-L_n + R_{sk}$	L_{det}	$-L_n - R_{det}$	(x_+, y_+)
ϕ_2	LOS_2	L_{sk}	$-L_n + R_{sk}$	L_{det}	$-L_n + R_{det}$	$(x_+, y_\pm)$
ϕ_3	LOS_2	L_{sk}	$-L_n + R_{sk}$	L_{det}	$-L_n + R_{det}$	(x_-, y_-)
ϕ_4	LOS_1	L_{sk}	$-L_n + R_{sk}$	L_{det}	$-L_n - R_{det}$	(x_-, y_-)

Table 2 - 9: Detector Line of Sight

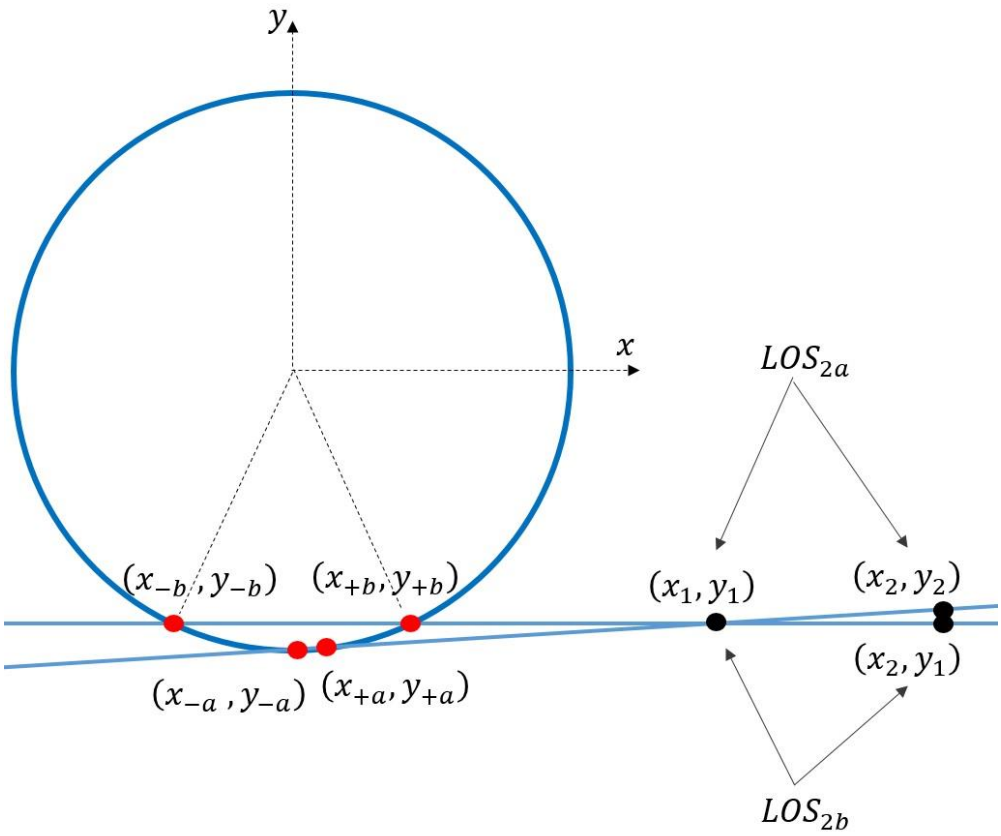

Figure 2 - 15: Detector LOS 2a and 2b

ϕ_2, and ϕ_3 approach zero. For this situation, the angular region of maximum density is estimated by replacing the definition of LOS_2 with $y_2 = -L_n + R_{det}$. This makes a straight line with respect to the inner edge of skimmer, (x_1, y_1), as is shown in Figure 2-15.

Another correction that must be implemented takes into consideration the limited angular spread of the beam due to the nozzle. Since the nozzle restricts any gas from expanding at angles beyond it, the rotor angle can be restricted by that limitation as well. This takes into account the fact that the nozzle is oriented 90° from the point of rotation and thus $\phi = \theta$. For the duration of a pulse from the rotating source use the time spent with the detector fully illuminated

$$\Delta\phi = (\phi_{2*} - \phi_{3*})F^{-1} \tag{2.99}$$

A first order approximation of the FWHM uses the midpoint between ϕ_1 and ϕ_2, and the midpoint between ϕ_3 and ϕ_4.

$$FWHM = \left[\frac{(\phi_1 - \phi_{2*})}{2} - \frac{(\phi_{4*} - \phi_{3*})}{2}\right] F^{-1} \tag{2.100}$$

Where the subsript $*$ represents chosing the correct value for that angle after the two corrections are imposed, as shown in Figure 2-14.

2.2.4 Kinematic Analysis: Effusive Beams

As the rotor moves through the relevant angles discussed in the previous section a small part of the beam will make it through the skimmer and into the detection region. In an effusive beam the velocity of the molecules, $\boldsymbol{X}$, is determined by the temperature of the reservoir and the mass of the gas species being used. For rotating beams the reservoir becomes the rotor and the temperature used to determine $\boldsymbol{X}$ is the rotor temperature. For an effusive beam there

are no collisions near the nozzle but there are enough collisions that occur inside the rotor to thermalize the gas with its temperature.

The components of the molecular velocity in cartesian coordinates are

$$\boldsymbol{X} = \left(X_x, X_y, X_z\right) \tag{2.101}$$

which is defined in the frame of the rotor. To extend this to the lab frame we must add the peripheral velocity of the nozzle, $\boldsymbol{V_{rot}}$,

$$\boldsymbol{V} = \boldsymbol{X} + \boldsymbol{V_{rot}} \tag{2.102}$$

where $\boldsymbol{V}$ is the lab velocity of the rotor augmented beam. $\boldsymbol{V_{rot}}$ is dependent only on the length of the rotor and the frequency of the motor, F. It is defined in the lab frame as

$$\boldsymbol{V_{rot}} = 2\pi L_n F = 0.94|F|\ m/s \tag{2.103}$$

This turns out to be $0.94|F|\ m/s$ for $L_n = 5.9"$. This value, even though it is the nozzle velocity, will be referred to as the rotor velocity for the remainder of the text. The rotor velocity can be positive or negative depending on the direction of rotation. In this section the rotor will only be considered in the "shooting" position, where $\phi = 0$, and $\boldsymbol{V_{rot}}$ points directly at the skimmer.

The flux of molecules emitted from the nozzle, as described in 2.1.1, is

$$F(X)dX = CXe^{-(X/\alpha)^2} dX_x dX_y dX_z \tag{2.104}$$

where C is a constant that depends only on the reservoir temperature, and the exponential term is the Boltzman probability of finding a molecule of speed X in a thermally equilibrated gas at temperature T. The volume element $dX_x dX_y dX_z$ in velocity space represents

molecules with velocities in the range $X_i \rightarrow X_i + dX_i$ where $i = x, y, z$. To transform 2.104 into the lab frame we begin with the solid angle element

$$\Omega = \frac{dX_x dX_y}{X_z^2} \tag{2.105}$$

which is defined in the lab frame. The final velocity of the beam is not X_z, but is V, such that the volume element and flux become [41]

$$dX_x dX_y dX_z = \Omega \mathrm{V}^2 dV \tag{2.106}$$

$$F(V)dV = C\mathrm{V}^2(V - V_{rot})e^{-((V-V_{rot})/\alpha)^2}dV \tag{2.107}$$

where all the constants have been grouped into C. The equation for flux reduces to the stationary form when $V_{rot} = 0$.

For beams that have a very large $V_{\parallel}$ the entire distribution of $V_{\perp}$ may make it through the skimmer[15]. In this case the flux equation no longer contains the V^2 term, which enters as a Jacobian element in Eqn 2.110. The focus of this thesis however is on slow molecular beams, and this means that only a small portion of molecules will meet the conditions

$$V_{\perp} < \mathrm{f}\, V_{\parallel} \qquad \text{(f is a small constant)} \tag{2.108}$$

Allowing them to pass through the skimmer into the detection region. As the rotor acts to remove considerable portions of $V_{\parallel}$ the range of $V_{\perp}$ that pass the skimmer into the detection region are reduced as well. It is important to note that the V^2 term represents simple geometric attenuation of the beam flux and becomes a real problem as $V \rightarrow 0$.

The flux is transformed into a number density, $D(V)dV$ by dividing through by V

$$D(V)dV = CV(V - V_{rot})e^{-((V-V_{rot})/\alpha)^2}dV \tag{2.109}$$

and this number density should be transformed into a time based distribution to facilitate the direct comparison with experiment. This requires explicit definition of the velocity and its differential as

$$V = \frac{L}{t} \tag{2.110}$$

$$dV = -\frac{L}{t^2} dt \tag{2.111}$$

Where L is the distance to the detector, as seen in Figure 2-7, and t is the time-of-flight required for the molecule to traverse L. Now the time based flux distribution is

$$F(t)dt = F(V)dV \tag{2.112}$$

$$F(t) = F\left(\frac{L}{t}\right)\frac{dV}{dt} \tag{2.113}$$

$$F(t) = \frac{C}{t}\left(\frac{L}{t}\right)^3 \left(\frac{L}{t} - V_{rot}\right) e^{-\left(\left(\frac{L}{t} - V_{rot}\right)/\alpha\right)^2} \tag{2.114}$$

and the number density distribution is

$$D(t) = \frac{C}{t}\left(\frac{L}{t}\right)^2 \left(\frac{L}{t} - V_{rot}\right) e^{-\left(\left(\frac{L}{t} - V_{rot}\right)/\alpha\right)^2} \tag{2.115}$$

The constant C must be determined in the absence of the rotor. In the case of a stationary rotor at $\phi = 0$ the flux reduces to

$$F(V)dV = C\mathrm{V}^3 e^{-(V/\alpha)^2} dV \tag{2.116}$$

Where the total flux, $\bar{F}$, in $molecules/sec\ m^2$ is obtained by integrating the flux distribution over all possible velocities

$$\bar{F} = C\int_0^\infty \mathrm{V}^3 e^{-(V/\alpha)^2} dV \tag{2.117}$$

yet this integral does not have an analytic solution. Instead, the total flux is converted to centerline intensity, $I(0)$,

$$I(0) = \frac{\sigma_S}{\Omega_s}\bar{F} \qquad \text{in } molecules/sec\ sr \tag{2.118}$$

Where σ_S is the cross sectional area of the skimmer, and Ω_s is the solid angle subtended by the skimmer. Since the distance to the skimmer, L_s, is large compared to other characteristic lengths in the effusive beam system, $\sigma_S \sim \Omega_s L_s^2$ and the centerline intensity becomes

$$I(0) = L_s^2\bar{F} \qquad \text{in } molecules/sec\ sr \tag{2.119}$$

which can be equated to the value derived in Section 2.1.1

$$I(0) = \frac{n_o\bar{v}\sigma}{4\pi} = \frac{n_o\alpha\sigma}{2\pi^{3/2}} \tag{2.120}$$

To obtain

$$L_s^2 C \int_0^\infty \mathrm{V}^3 e^{-(V/\alpha)^2} dV = \frac{n_o\alpha\sigma}{2\pi^{3/2}} \tag{2.121}$$

$$C = \frac{n_o\alpha\sigma}{2\pi^{3/2}L_s^2}\left(\int_0^\infty \mathrm{V}^3 e^{-(V/\alpha)^2} dV\right)^{-1} \tag{2.122}$$

and returns a form that can be evaluated numerically. With the rotor spinning at frequency F the number of molecules that pass into the skimmer can be determined by[9]

$$N_P = \tau\sigma_s \int F(V)dV \tag{2.123}$$

where τ, the pulse duration, is estimated using the angles determined in the previous section

$$\Delta\phi = (\phi_2 - \phi_3) \tag{2.124}$$

$$\tau = \frac{\Delta\phi}{2\pi F} \tag{2.125}$$

The flux distribution in Eqn 2.120 pertains to the rotating source and the velocity integration has limits of $u_{swat} \rightarrow \infty$ for the slowing direction, and $V_{rot} \rightarrow \infty$ for the speeding direction.

$$N_P = \tau\sigma_s \left(\frac{n_o \alpha \sigma}{2\pi^{3/2} L_s^2}\right) \frac{\int_{V_{min}}^{\infty} \mathrm{V}^2 (V - V_{rot}) e^{-((V - V_{rot})/\alpha)^2} dV}{\int_0^{\infty} \mathrm{V}^3 e^{-(V/\alpha)^2} dV} \tag{2.126}$$

The intensity of the velocity augmented effusive beam that makes it through the skimmer and into the detection region is the product of

$$I = \omega N_P \tag{2.127}$$

where ω is the rotors angular velocity. Typical values for each of these parameters are given in Table 2-10, and Figure 2-16 shows how the intensity varies as a function of V_{rot} for an effusive xenon beam. Mathematica 10 was used to evaluate all the integrals contained in 2.126. The programs written for use with Mathematica are contained in Appendix C for the effusive system and the supersonic case. It is important to note that the angular velocity term from Eqn 2.127 cancels with the angular velocity term contained in the definition of the pulse width. This means that the results of the integrals calculated in the Appendices dictate the behavior of the beam intensity.

2.2.5 Kinematic Analysis: Supersonic Beams

In considering the free expansion of a supersonic beam from a rotating source we use of the same flux equation but shift the molecular velocity, **X**, by the flow velocity, **U**. The parallel temperature, as described in Section 2.1.2 is used to determine the width of the shifted Boltzman distribution.

$$\boldsymbol{X} \rightarrow \boldsymbol{X} - \boldsymbol{U} \tag{2.128}$$

Symbol	Name	Value	Units
F	Rotor Frequency	$0 \rightarrow \pm 300$	sec^{-1}
ω	Angular Velocity	$2\pi F$	sec^{-1}
V_{rot}	Rotor Velocity	$L_n \omega$	m/s
L_n	Distance: nozzle to gas feed	0.15	$meters$
α	Characteristic velocity	195	m/s
τ	Pulse duration	$\Delta\phi\omega^{-1}$	$seconds$
$\Delta\phi$	Total acceptance angle	14	$degrees$
n_o	Reservoir density (0.2 torr)	$6.43E15$	cm^{-3}
σ	Nozzle area	$1.3E-3$	cm^2
σ_s	Skimmer area	$7.9E-3$	cm^2
L_s	Distance to detector	12	cm

Table 2 - 10: Relevant Parameters for Intensity Calculation (Effusive)

$$\boldsymbol{U} = \sqrt{\frac{2kT_o}{m}}\sqrt{\frac{\gamma}{\gamma-1}}\sqrt{1-\frac{T_{\|}}{T_o}} \tag{2.129}$$

$$\boldsymbol{\alpha} \rightarrow \Delta v \tag{2.130}$$

$$\Delta v = \sqrt{\frac{2kT_{\|}}{m}} \tag{2.131}$$

Now the flux equation can be rewritten to describe a supersonic flux distribution in the frame of the nozzle.

$$F(X)dX = CXe^{-((X-U)/\Delta v)^2}dX_x dX_y dX_z \tag{2.132}$$

The constant C is different from the effusive case and will be considered after the time based number density has been formulated. The above flux distribution must be transformed into the laboratory frame and include the velocity augmentation of the rotor tip

$$F(V)dV = CV^2(V - V_{rot})e^{-((V-w)/\Delta v)^2}dV \tag{2.133}$$

Where the flow velocity of the supersonic expansion has been combined with the velocity of the rotor to create, w, the effective flow velocity in the lab frame along the centerline of the beam.

$$w = U + V_{rot} \tag{2.134}$$

The lab frame flux distribution in Equn 2.137 is converted to a density distribution

$$D(V)dV = CV(V - V_{rot})e^{-((V-w)/\Delta v)^2}dV \tag{2.135}$$

This density distribution should be expressed in the time domain using

$$D(t) = D\left(\frac{L}{t}\right)\frac{dV}{dt} = D\left(\frac{L}{t}\right)\frac{-L}{t^2} \tag{2.136}$$

$$D(t) = \frac{C}{t}\left(\frac{L}{t}\right)^2 \left(\frac{L}{t} - V_{rot}\right) e^{-\left(\left(\frac{L}{t} - w\right)/\Delta v\right)^2} dV \tag{2.137}$$

Once again the problem becomes finding a suitable value for the constant C. First set the rotor velocity to zero, and then integrate the flux distribution over all possible velocities to obtain, $\bar{F}$, the total flux

$$\bar{F} = C \int V^3 e^{-((V-U)/\Delta v)^2} dV \tag{2.138}$$

Where U is the supersonic flow velocity in the nozzle frame. Once again this integral does not have an analytic solution. Instead, the total flux is converted to centerline intensity, $I(0)$,

$$I(0) = \frac{\sigma_S}{\Omega_s}\bar{F} \qquad \text{in } molecules/sec\ sr \tag{2.139}$$

Where σ_S is the cross sectional area of the skimmer, and Ω_s is the solid angle subtended by the skimmer. Since the distance to the skimmer, L_s, is large compared to other characteristic lengths in the effusive beam system, $\sigma_S \sim \Omega_s L_s^2$ and the centerline intensity becomes

$$I(0) = L_s^2 \bar{F} \qquad \text{in } molecules/sec\ sr \tag{2.140}$$

which is equated to the intensity derived in Section 2.1.2.

$$I(0) = \frac{\kappa}{\pi}\dot{N} = \frac{\kappa}{\pi}(\pi R_n^2)\alpha n_o f(\gamma) \tag{2.141}$$

$$f(\gamma) = \sqrt{\frac{\gamma}{\gamma-1}}\left(\frac{2}{\gamma+1}\right)^{1/(\gamma-1)} \tag{2.142}$$

This allows us to solve for the constant C.

$$\frac{\kappa}{\pi}(\pi R_n^2)\alpha n_o f(\gamma) = L_s^2 C \int V^3 e^{-((V-U)/\Delta v)^2} dV \tag{2.143}$$

$$C = \kappa\alpha n_o \left(\frac{R_n}{L_s}\right)^2 f(\gamma)\left(\int V^3 e^{-((V-U)/\Delta v)^2} dV\right)^{-1} \tag{2.144}$$

This returns a form similar to the effusive case, except for the displacement of the Boltzman distribution by the flow velocity of the expansion, and a narrowing of its width due to cooling that occurs during the expansion.

With the rotor spinning at an angular frequency ω the number of molecules that pass into the skimmer can be determined by[9]

$$N_P = \tau\sigma_s \int F(V)dV \tag{2.145}$$

where τ, the pulse duration, is estimated using the angles determined in the Section 2.3.3. It should be stated in terms of the rotor velocity

$$\Delta\phi = \phi_2 - \phi_3 \tag{2.146}$$

$$\tau = \frac{\Delta\phi}{\omega} = \Delta\phi \frac{L_n}{V_{rot}} \tag{2.147}$$

And this is considered to be similar in both directions. For situations where the rotor is accelerating/decelerating the molecular beam the number of molecules per pulse attains a subscript sp/sl for speeding/slowing. The two cases must be seperated at this point due to different limits of integration.

$$N_{P,sp} = \tau\sigma_s C \int_{V_{rot}}^{\infty} V^2(V - V_{rot})e^{-((V-w)/\Delta v)^2}dV \tag{2.148}$$

$$N_{P,sl} = \tau\sigma_s C \int_{V_{sw}}^{\infty} V^2(V - V_{rot})e^{-((V-w)/\Delta v)^2}dV \tag{2.149}$$

With the appropriate valuesfor the constant C can be substituted into 2.149 to produce

$$N_{P,i} = \tau\sigma_s \kappa\alpha n_o \left(\frac{R_n}{L_s}\right)^2 f(\gamma) \frac{\int_{V_i}^{\infty} V^2(V-V_{rot})e^{-((V-w)/\Delta v)^2}dV}{\int_0^{\infty} V^3 e^{-((V-U)/\Delta v)^2}dV} \tag{2.150}$$

Symbol	Name	Value	Units
L_n	Distance: Nozzle to gas feed	0.15	$meters$
V_{rot}	Rotor Velocity	$2\pi L_n F$	m/s
V_i	Integration Lower Bound (speeding)	V_{rot}	m/s
α	Characteristic Velocity	195	m/s
U	Supersonic Flow Velocity	305	m/s
Δv	Supersonic Velocity Spread	12.7	m/s
w	SS Flow Velocity and Rotor Velocity	$V_{rot} + 305$	m/s
τ	Pulse Duration	$\Delta\phi/F$	$seconds$
$\Delta\phi$	Total Acceptance Angle	$14/360$	constant
κ	Peaking Factor	2	constant
n_o	Reservoir Density (100 torr)	$3.22E18$	cm^{-3}
R_n	Nozzle Radius	0.0254	cm
σ_s	Skimmer Area ($r_s = 0.15\ cm$)	$7.9E-3$	cm^2
L_s	Distance to Detector	12	cm
γ	Poisson Coefficient (atomic)	$5/3$	constant

Table 2 - 11: Relevant Parameters for Intensity Calculation (Supersonic)

Where i can stand for sp/sl with lower integration limit V_{rot}/V_{sw}. The intensity of the velocity augmented supersonic beam that makes it through the skimmer and into the detection region is the product

$$I = \omega N_{P,i} \tag{2.151}$$

$$I_{P,i}(F) = 2\pi F\tau\sigma_s\kappa\alpha n_o \left(\frac{R_n}{L_s}\right)^2 \sqrt{\frac{\gamma}{\gamma-1}}\left(\frac{2}{\gamma+1}\right)^{1/(\gamma-1)} \frac{\int_{V_i}^{\infty} V^2(V-V_{rot})e^{-((V-w)/\Delta v)^2}dV}{\int_0^{\infty} V^3 e^{-((V-U)/\Delta v)^2}dV} \tag{2.152}$$

$$I_{P,i}(F) = \left(15.5E15\,\frac{molecules}{sec}\right)\frac{\int_{V_i}^{\infty} V^2(V-V_{rot})e^{-((V-w)/\Delta v)^2}dV}{\int_0^{\infty} V^3 e^{-((V-U)/\Delta v)^2}dV} \tag{2.153}$$

Typical values for each of these parameters are given in Table 2-11, and Figure 2-16 shows how the intensity varies as a function of V_{rot} for a supersonic xenon beam. The integrals contained in Eqn 2.153 for the forward direction, backward direction, and denominator are evaluated using Mathematica 10. The code is contained in Appendix C.

2.3 Beam Scattering

After the analysis of the rotor mounted supersonic nozzle it becomes important to analyze the impact that the background gas has on the velocity augmented beam. Unlike conventional sources the rotor mounted beam must travel through a considerable amount of space before passing through the skimmer and into the detection region. Several sections of Section 3 are devoted to ways in which to minimize this scattering. The amount of scattering that occurs will depend[7] on the density of background gases, ρ_{bk}, the distance to the detector, ℓ, the velocity of the beam, u, and the scattering cross-section, S. Since the removal of beam particles is considered uniform throughout the length of the beam it satisfies

$$\frac{dI}{dz} = -QI \tag{2.154}$$

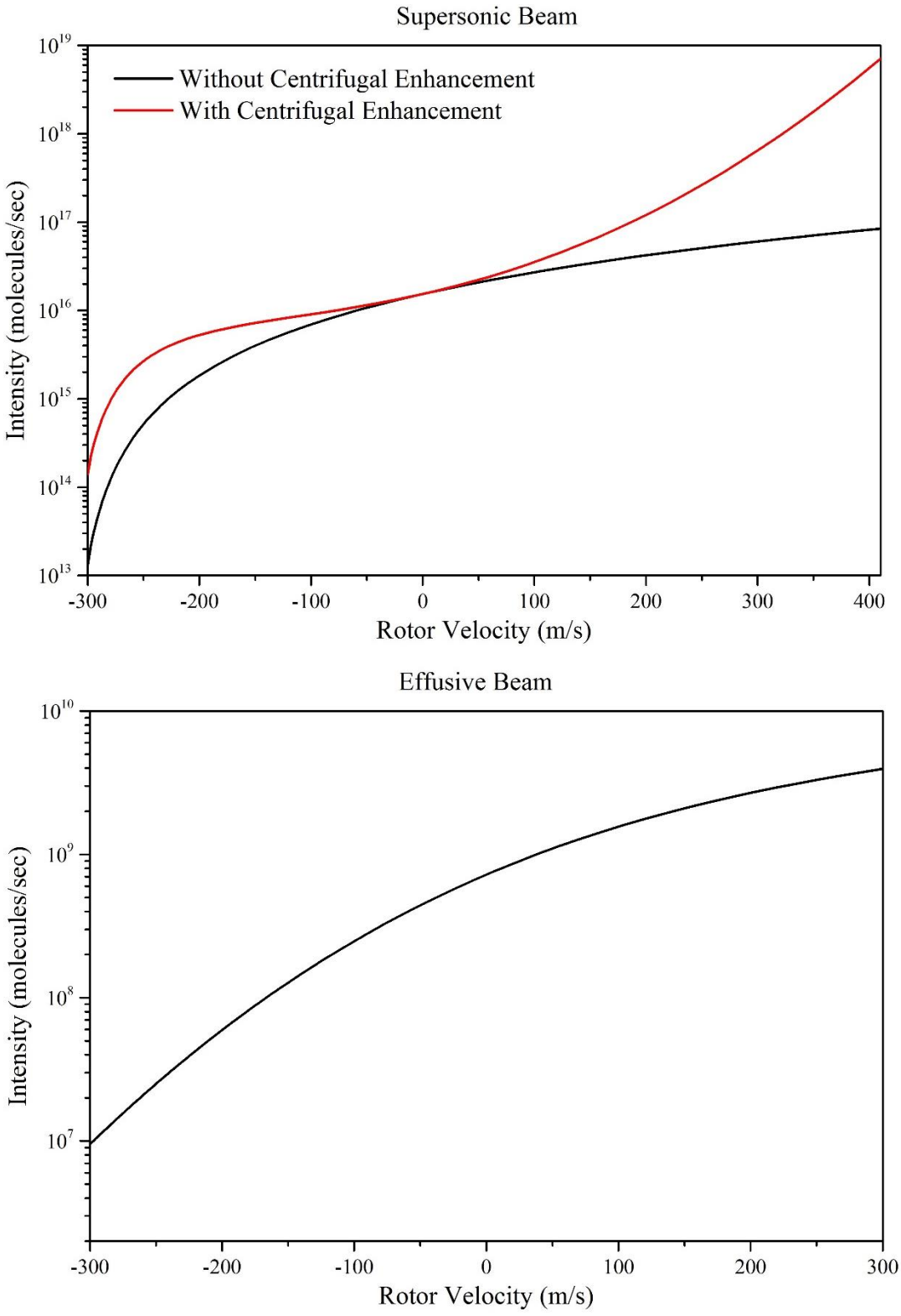

Figure 2 - 16: Calculated Intensity Distributions for Rotating Source

Where Q is a dimensionless interaction coefficient that takes the form

$$Q = \frac{\Theta \ell}{u} \tag{2.155}$$

Where ℓ/u represents the amount of time it takes the beam to reach the detector, and Θ is the scattering rate which assumes every scattering event removes particles from the beam. Thus, the fraction of molecules that remain in the beam is described by

$$\frac{n(\ell)}{n_o} = e^{-\frac{\Theta \ell}{u}} \tag{2.156}$$

With a rate that is most easily described[1, 2] using a reduced beam velocity $x = u/\alpha$

$$\Theta = \frac{\rho_{bk} S \alpha}{\sqrt{\pi}} \left[e^{-x^2} + \left(2x + \frac{1}{X} \right) \int_0^x e^{-y^2} dy \right] \tag{2.157}$$

Now for a Lennard-Jones 6-12 potential an upper limit can be placed on value of the mutual collision cross section [41]

$$S_{lim} \cong 2\pi \left(\frac{C_6}{h v_{rel}} \right)^{2/5} \propto v_{rel}^{-2/5} \tag{2.158}$$

By using a relative velocity term, v_{rel}, the Van der Waals coefficient, C_6, and Planks constant, h. The relative velocity term is [14]

$$v_{rel} = \frac{1}{6 v_1 v_2} [(v_1 + v_2)^3 - |v_1 - v_2|] \tag{2.159}$$

Where the molecular beam velocity, $v_1 = u_{beam}$, is compared to the velocity of the background gas, $v_2 = u_{bk}$. Here I assume u_{bk} to be its most probable value $\alpha = \sqrt{2kT_o/m}$. The actual value is much smaller than this limiting case. It is determined experimentally by changing the background pressure in the chamber containing the source and analyzing the subsequent change in measured density. This experiment was performed for a very early

version of the rotating source[41] as well as the rotor developed by Gupta and Herschbach[7, 9]. They found that for a Xe beam traveling through a chamber containing Xe gas that the actual scattering rate is 60% of the limiting case.

For the setup currently in use $\ell \cong 11cm$ which is only possible due to the custom detection enclosure outlined in Figure 3-3. The beam traverses the main chamber for 6cm before going through the skimmer and into the detection chamber. In this region the background pressures are typically

$$P_{bk} = \begin{cases} 0 < \ell < 6cm & P_{bk} < 10^{-7} Torr \\ 6cm < \ell < 12cm & P_{bk} < 10^{-8} Torr \end{cases} \tag{2.160}$$

These values, shown in Figure 2-17, are a large improvement over previous versions of the rotating source experiment due to the installation of several large liquid nitrogen traps, and the introduction of a pulsed valve to supply the rotor with gas. The changes emphasize the focus shifting from verification of supersonic beam properties to the measurement of a very slow and cold pulse. The verification of the beam properties can be done at moderate beam velocities, and subsequently moderate scattering. While the production of slow pulses will require measuring very low velocity beams which are more susceptible to scattering.

Using the formulas for the flux, density, and number/pulse presented in previous sections the scattering due to background gases can be taken into consideration.

$$\varphi = e^{-\frac{\Theta \ell}{u}} \tag{2.161}$$

$$F = \varphi F_o \tag{2.162}$$

$$D = \varphi D_o \tag{2.163}$$

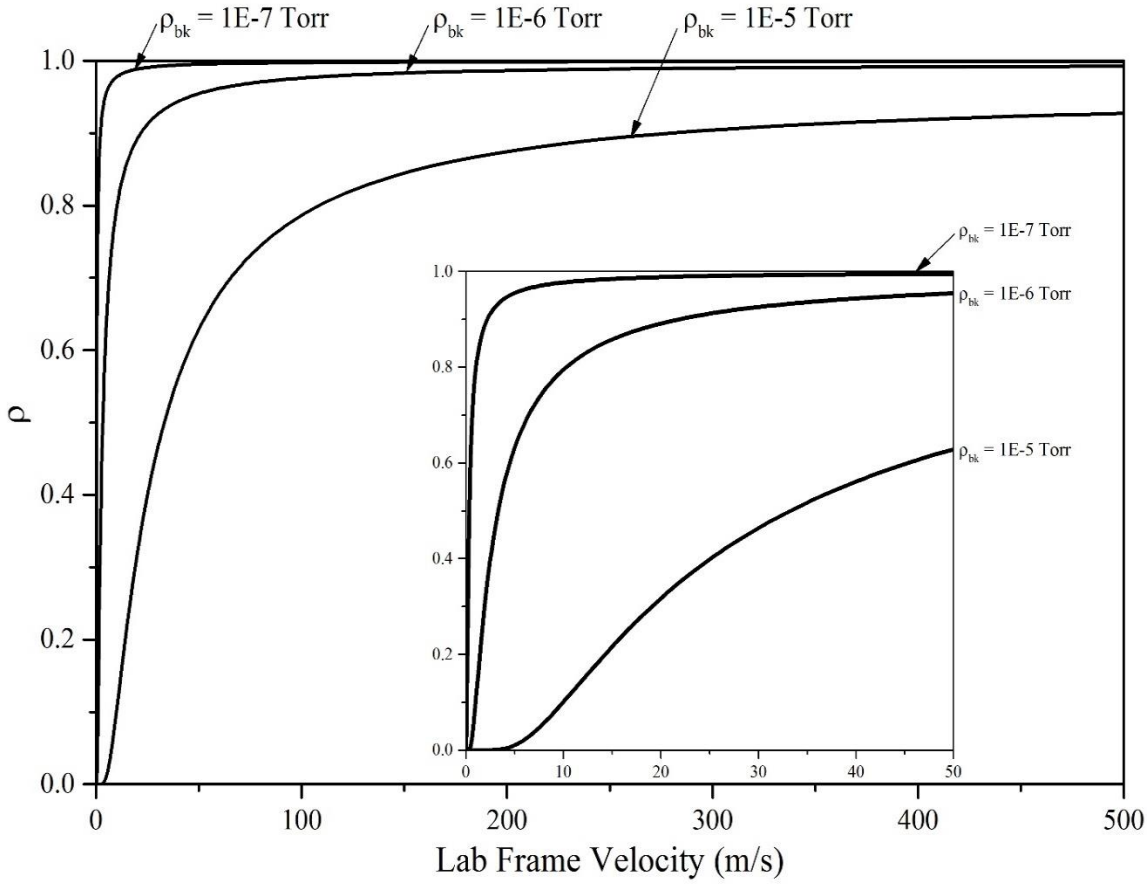

Figure 2 - 17: Fraction of Xe Atoms Remaining

$$N_P = \varphi N_{Po} \tag{2.164}$$

This correction term can be applied directly to the time of flight distribution.

2.4 Beam Merging

Utilizing the velocity augmented beam in a collision experiment can greatly extend the attainable energy range of the resulting collisions. Standard beam techniques either change the seeding ratio to effect the final supersonic flow velocity or change the temperature of the nozzle through which the beam is expanding. The seeding ratio changes the intensity of the target molecule in the beam, and the temperature of the nozzle also effects the velocity dispersion of the beam. The rotating source provides a cleaner and faster way to achieve this same goal without augmenting the intensity of the source or temperature of the nozzle.

In this section the attainable energy range and the energy resolution of a merged beam experiment will be developed along similar lines to Wei, Lyuksyutov, and Herschbach[42]. This method utilizes the velocity distribution of the rotating source and the velocity distribution produced by a traditional stationary supersonic beam. Each of the energy parameters $\langle E_r \rangle$ and ΔE_r are evaluated for different values of the velocity dispersion in the two colliding beams.

The velocity dispersions explored in this section are an order of magnitude smaller than previous estimates. This is due to recent work[43] which describes a method for achieving lower collision energies and better energy resolution than ever before. The technique utilizes a fast action valve to generate very short gas pulses. The beam seperates itself with respect to velocity as it flies across the chamber. This means faster particles

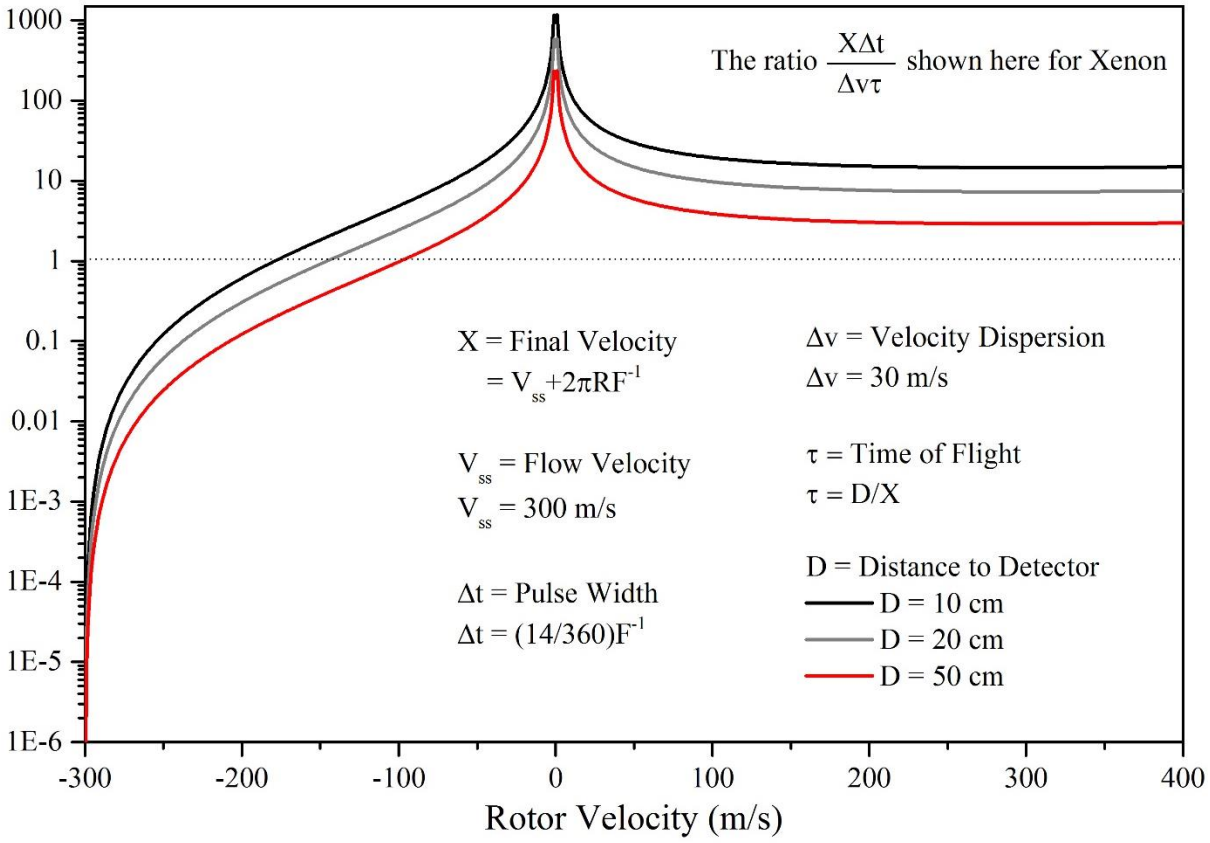

Figure 2 - 18: Requirement for Significant Velocity Dispersion

generally arrive at the detector first and slower particles last. By utilizing only a portion of this beam, after it has had a chance to longitudinally spread apart, a much lower collision energy and energy resolution are attainable. This technique requires a very fast detection technique and would benefit even further from improvements in this arena. The impetus of the approach is that with such a small detection window there is a need to define a 'local' velocity dispersion, Δv_L. The value of this local velocity dispersion evolves as the beam spreads longitudinally over the course of its flight.

$$\Delta v_L^2 = \frac{(X\Delta t\Delta v)^2}{\Delta v^2\tau + X^2\Delta t^2} \tag{2.165}$$

Where X is the rotor augmented flow velocity, Δv is the velocity dispersion, Δt is the FWHM of the valve opening time, and τ is the actual time of flight. It is due to this progress that velocity dispersion values 0.1%, 0.2%, and 1% will be used in this section. It must be noted that these smaller velocity dispersions require

$$X * \Delta t \ll \Delta v * \tau \tag{2.166}$$

to be valid. This condition is not always achieved in the rotating source experiment because the pulse width is inversely proportional to the rotor frequencies. In fact, slow rotational frequencies create essentially continuous beam conditions for several microseconds. In the continuous regime the local velocity dispersion is identical to the beam velocity dispersion. This effect is shown in Figure 2-18 which determines the region of applicability for the rotating source. This region can be expanded if the rotor source is chopped using a mechanical chopper. Without special preparation the lower dispersion values are only applicable for a beam that has a very long time of flight and short temporal width.

For two beams with velocity V_1 and V_2 that collide at an angle θ the relative kinetic energy of the collision is

$$E_r = \frac{1}{2}\mu(V_1^2 + V_2^2 - 2V_1V_2\cos(\theta)) \tag{2.167}$$

where μ is the reduced mass. In the case of merged beams $\theta \to 0$ and the cosine term becomes unity. This situation produced the lowest collision energy for two beams that have a constant lab frame velocity. The average energy is estimated utilizing the two velocity distributions of the collision

$$\langle E_r \rangle = \frac{1}{2}\mu(\langle V_1^2 \rangle + \langle V_2^2 \rangle - 2\langle V_1 \rangle \langle V_2 \rangle \cos(\theta)) \tag{2.168}$$

and the rms spread is

$$\Delta E_r = \sqrt{\langle E_r^2 \rangle - \langle E_r \rangle^2} \tag{2.169}$$

Which requires evaluating the distribution averages for velocity, seen above as $\langle V^k \rangle$, up to $k = 4$. These velocity distributions are described in Section 2.1.2 for a supersonic source

$$F(V) = V^3 e^{-((V-u)/\Delta v)^2} \tag{2.170}$$

and Section 2.3.6 for a rotating source

$$F(V) = V^2(V - V_{rot})e^{-((V-w)/\Delta v)^2} \tag{2.171}$$

Both of these distributions will be used to produce analytic forms of the integrals involved in the energy resolution estimation. These analytic forms are given in terms of

$$x = \Delta v/u \tag{2.172}$$

which is the ratio of the velocity dispersion to the flow velocity. In addition to x, it is useful to define two additional parameters to describe the effect of the rotor velocity. The parameter

$$y = w/u \tag{2.173}$$

represents the ratio of the final augmented velocity to the flow velocity. For the stationary source this parameter is equal to 1 since there is no rotor velocity. The parameter

$$z = V_{rot}/u = y - 1 \tag{2.174}$$

represents the ratio of the rotor velocity to the flow velocity. When the rotor is spun in the forward direction $z > 0$, and when the rotor is spun in the backwards direction $z < 0$.

Now that x, y, and z have been defined the integration over the velocity distributions can be performed as in [42]. This integration results in an expression in terms of P_n functions

$$\langle (V/u)^k \rangle = \frac{P_{k+3}(x,y,z) - zP_{k+2}(x,y,z)}{P_3(x,y,z) - zP_2(x,y,z)} \quad , \quad \text{Rotating Beam} \tag{2.175}$$

$$\langle (V/u)^k \rangle = P_{k+3}(x,1)/P_3(x,1) \quad , \quad \text{Stationary Beam} \tag{2.176}$$

Where the stationary source has substituted in for the approriate value of y and z. The P_n functions are given in terms of A_n functions which are shown in Table 2-12.

$$P_n(x,y,z) \approx \frac{\sqrt{\pi}}{8} A_n(x,y) \quad , \quad \text{Rotating Beam} \tag{2.177}$$

$$P_n(x,1) = \frac{\sqrt{\pi}}{8} A_n(x,1) \quad , \quad \text{Stationary Beam} \tag{2.178}$$

n	$\boldsymbol{A_n(x,y)}$
2	$4(2y^2 + x^2)x$
3	$4(2y^2 + 3x^2)xy$
4	$2(4y^4 + 12x^2y^2 + 3x^4)x$
5	$2(4y^4 + 20x^2y^2 + 15x^4)xy$
6	$(8y^6 + 60x^2y^4 + 90x^4y^2 + 15x^6)x$
7	$(8y^6 + 84x^2y^4 + 210x^4y^2 + 105x^6)xy$

Table 2 - 12: Approximate Integrals for Velocity Averages

The A_n functions allow for a simplified expression for the integration over the velocity distributions

$$\langle (V/u)^k \rangle = \frac{A_{k+3}(x,y) - zA_{k+2}(x,y)}{A_3(x,y) - zA_2(x,y)} \quad , \quad \text{Rotating Beam} \tag{2.179}$$

$$\langle (V/u)^k \rangle = A_{k+3}(x,1)/A_3(x,1) \quad , \quad \text{Stationary Beam} \tag{2.180}$$

As an example of how these equations can be used consider a single stationary supersonic beam. Its kinetic energy is

$$\langle E_{BK} \rangle = \frac{1}{2} m \langle u^2 \rangle = \frac{1}{2} m u^2 \langle (V/u)^2 \rangle = \frac{1}{2} m u^2 (P_5(x,1)/P_3(x,1)) \tag{2.181}$$

$$\langle E_{BK} \rangle = \frac{1}{2} m u^2 (A_5(x,1)/A_3(x,1)) = \frac{1}{2} m u^2 \frac{\left(4+20x^2+15x^4\right)}{(4+6x^2)} \tag{2.182}$$

Where the dependence is explicit in the mass m. The flow velocity of the gas u and the velocity dispersion Δv are both contained in the dimensionless variable x. Finally, information about the distribution function $F(V)$ of the supersonic beam is contained in the A_n functions.

Likewise, the rms spread of a single stationary supersonic beam is a function of the mass, m, the flow velocity, u, and the velocity dispersion, Δv, of the beam. Once again the A_n functions are a function of the dimensionless variable x.

$$\Delta E_{BK} = [\langle E_{BK}^2 \rangle - \langle E_{BK} \rangle^2]^{\frac{1}{2}} = \frac{1}{2} m u^2 [P_7/P_3 - (P_5/P_3)^2]^{\frac{1}{2}} \tag{2.183}$$

$$\Delta E_{BK} = \frac{1}{2} m u^2 [A_7/A_3 - (A_5/A_3)^2]^{\frac{1}{2}} \tag{2.184}$$

For a pair of merged beams the energy contribution from the rotating source must be evaluated for several different rotor frequencies. This is because the rotor can be stationary

producing a standard velocity distribution, or it can also be spun slowly or quickly in either direction to speed or slow the beam. Note that this augmentation does not reduce the velocity spread! The values for x,y, and z are shown in Table 2-13 for the various rotor directions.

The ordinate energy scale E_R^o is used as a reference to establish how small the merged beam collisions can become. In the case of two supersonic beams $E_R^o = \frac{\mu}{2}(u_1^2 + u_2^2)$ represents the collision energy of beams crossed at a 90 degree angle. In the merged beam scenario described below $\theta = 1°$ will be used and $\cos\theta \to 1$. The average energy in a merged beam is

$$\langle E_r \rangle / E_R^o = \left(\frac{a^2}{1+a^2}\right)\langle v_1^2\rangle + \left(\frac{1}{1+a^2}\right)\langle v_2^2\rangle - 2\left(\frac{a}{1+a^2}\right)\langle v_1\rangle\langle v_2\rangle \tag{2.185}$$

Where $a = u_2/u_1$ is the ratio of velocities. This is shown Figure 2-19. The $\langle v_i^k \rangle$ terms are dimensionless functions of (x, y, z) and are shown in Table 2-13. Likewise the rms spread is

$$\Delta E_R / E_R^o = [A - B + C]^{1/2} \tag{2.186}$$

with

$$A = \left(\frac{1}{1+a^2}\right)^2 [\langle v_1^4\rangle - \langle v_1^2\rangle^2] + a^4\left(\frac{1}{1+a^2}\right)^2 [\langle v_2^4\rangle - \langle v_2^2\rangle^2] \tag{2.187}$$

$$\frac{B}{4a\left(\frac{1}{1+a^2}\right)^2} = [\langle v_1^3\rangle - \langle v_1\rangle\langle v_1^2\rangle]\langle v_2\rangle + 4a^3\left(\frac{1}{1+a^2}\right)^2 [\langle v_2^3\rangle - \langle v_2\rangle\langle v_2^2\rangle]\langle v_1\rangle \tag{2.188}$$

$$C = 4a^2\left(\frac{1}{1+a^2}\right)^2 [\langle v_1^2\rangle\langle v_2^2\rangle - \langle v_1\rangle^2\langle v_2\rangle^2] \tag{2.189}$$

Direction	**Speed**	x	y	z	$\langle v_i \rangle$	$\langle v_i^2 \rangle$	$\langle v_i^3 \rangle$	$\langle v_i^4 \rangle$
Slowing	Fast	0.01	$1/2$	$-1/2$	0.50025	0.2503	0.12526	0.0627
Slowing	Slow	0.01	$4/5$	$-1/5$	0.80017	0.64033	0.51246	0.41015
Speeding	Slow	0.01	$5/4$	$1/4$	1.25013	1.56287	1.95392	2.44289
Speeding	Fast	0.01	2	1	2.0001	4.00045	8.0015	16.0044
Slowing	Fast	0.002	$1/2$	$-1/2$	0.50001	0.25001	0.12501	0.06251
Slowing	Slow	0.002	$4/5$	$-1/5$	0.80001	0.64001	0.51202	0.40962
Speeding	Slow	0.002	$5/4$	$1/4$	1.25001	1.56251	1.95316	2.44147
Speeding	Fast	0.002	2	1	2	4.00002	8.00006	16.00018
Slowing	Fast	0.001	$1/2$	$-1/2$	0.5	0.25	0.125	0.0625
Slowing	Slow	0.001	$4/5$	$-1/5$	0.8	0.64	0.512	0.40961
Speeding	Slow	0.001	$5/4$	$1/4$	1.25	1.5625	1.95313	2.44142
Speeding	Fast	0.001	2	1	2	4	8.00001	16.00004

Table 2 - 13: Averages over Velocity Distributions

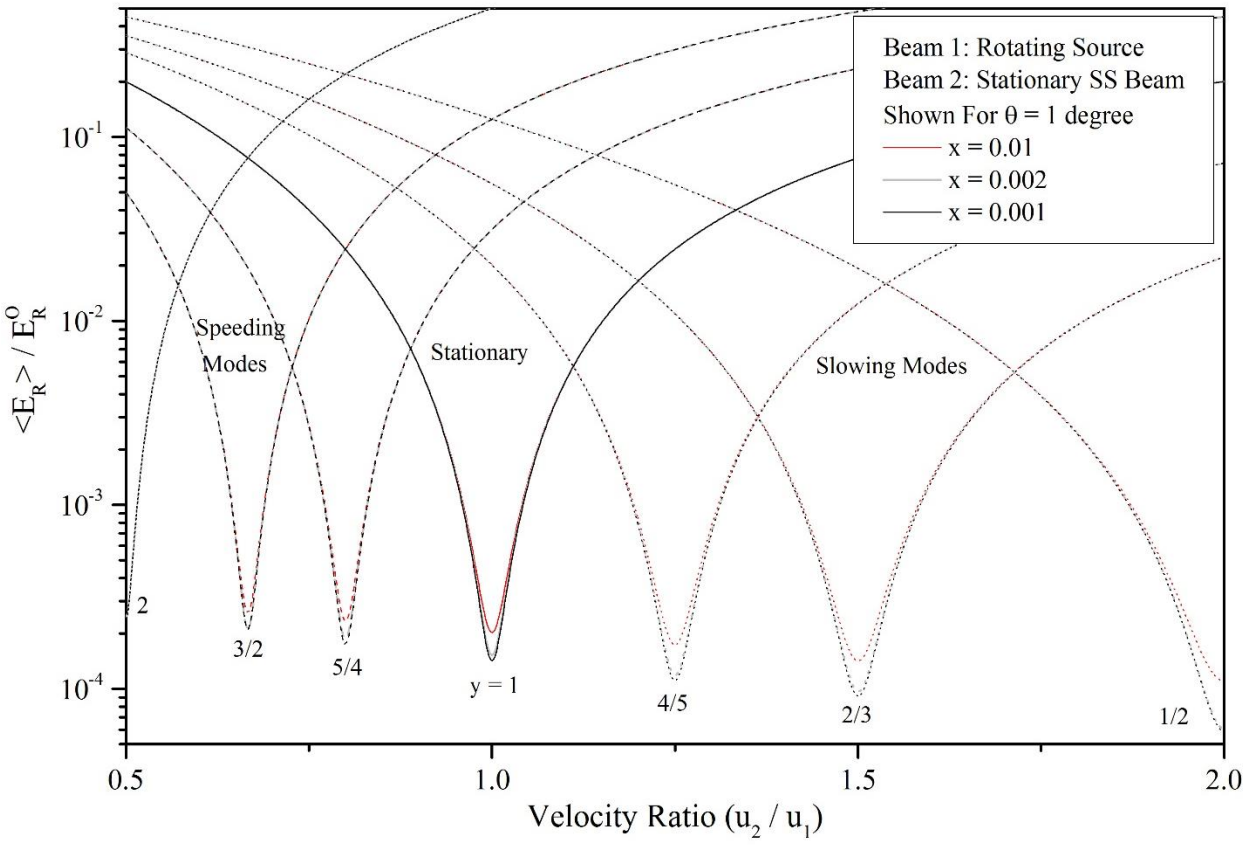

Figure 2 - 19: Averaged Relative Kinetic Energy

3. EXPERIMENT

3.1 High Vacuum System

The vacuum chambers currently in use have been operational since 2008. The pumping systems have been run continuously over these past 5+ years and consist of one 5000 l/s NHS 10" diffusion pump in the main chamber, and a smaller 800 l/s Edwards 8" diffusion pump installed in the detection chamber. These pumps use a stream of oil vapor to direct the chamber gases into the throat of the foreline system[3, 44] and were named because of the fact that gases cannot diffuse back from this stream of oil and remain in the chamber. To prevent any of this oil vapor from back streaming into the chamber there are liquid nitrogen cooled baffles installed between the diffusion pumps and the chamber.

The main chamber, seen in Figure 3-1, is made from six stainless steel plates welded together to make a cube. It houses all of our beam sources, several large liquid nitrogen (LN2) traps, and the 10" diffusion pump. The LN2 traps are accessed through several ports on the top flange and when filled improve the absolute pressure by an order of magnitude as well as drastically improve the pumping speed for condensable gases. The front flange contains a Bayard-Alpert ion gauge to measure high-vacuum pressures, and a thermocouple gauge to measure low-vacuum pressures. The chamber is vented by unplugging a 1/8" quick connect coupling installed on the top flange. Also installed in the top flange is a custom made rotatable feedthrough that controls the position of the aluminum foil shield while the chamber is closed and the system is under vacuum.

Several 1/4" quick connect (QC) feedthroughs mounted on the left flange allow for both water and gas to be supplied via tubing into the main chamber. The gas is supplied

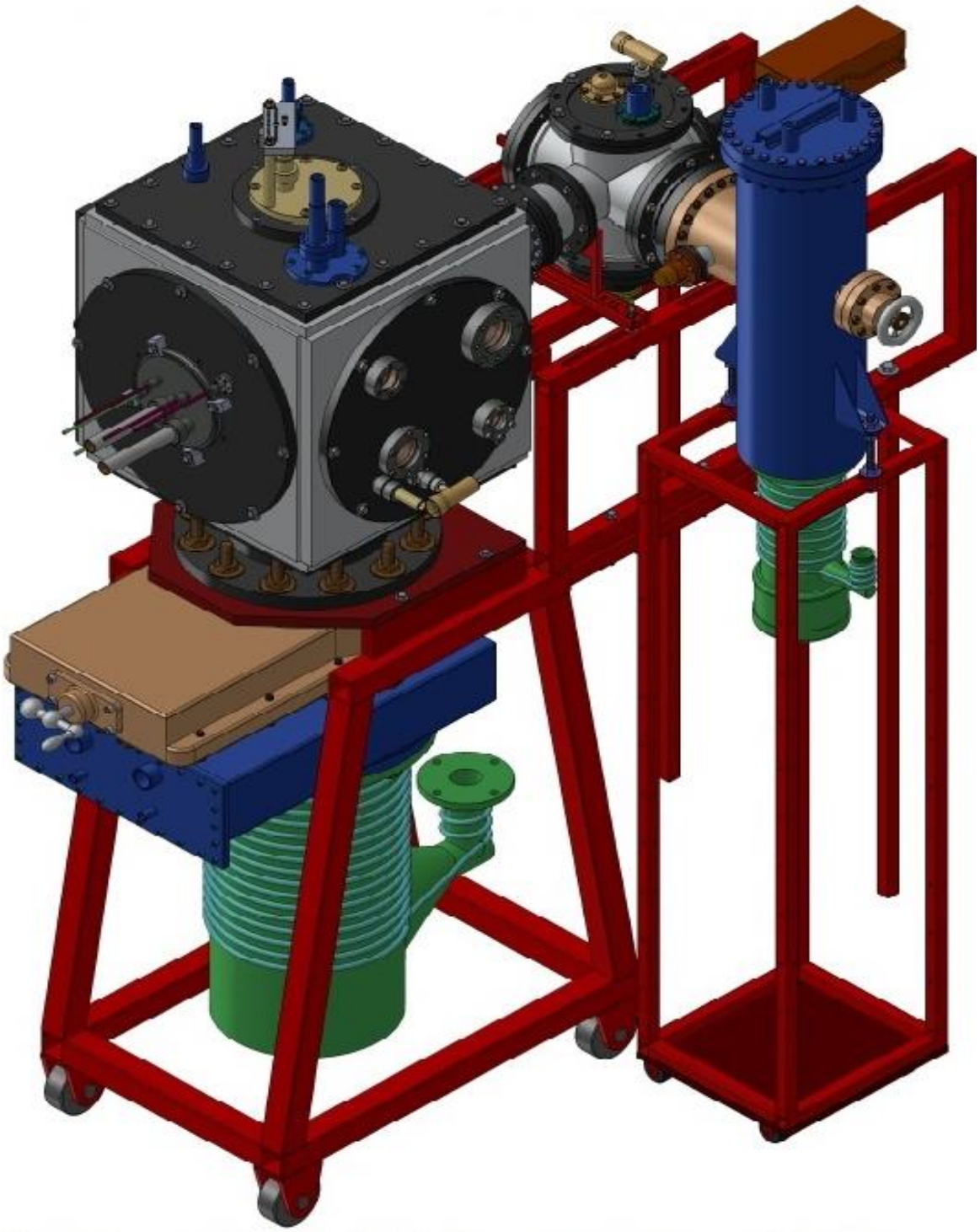

Figure 3 - 1: The Vacuum System

directly to the inlet port of the valves via stainless steel tubing and sections of flexible stainless steel bellows. Water is circulated through a copper plate that is coupled directly to the motor for heat removal. A 1/4" QC coupling is mounted directly in the beam path, allowing us to place a molecular beam source outside the chamber and seal the QC coupling on the nozzle extending from the outlet port of the source. The left flange also houses a 1" port that feeds to the fore line system and allows us to evacuate all chambers to a rough vacuum before opening the isolation valves for the diffusion pumps.

Optical feedthroughs on the front flange allow the user to verify no obstructions exist in the path of the rotor; both before it is started and while in operation. The rotor will be damaged beyond repair if any obstruction were left in place due to the high peripheral velocities it attains and the tight limit that vibration places on our rotor balance. Rotor vibration is kept at a strict minimum because all equipment is mechanically coupled by the chamber itself. Only once has the rotor been replaced due to damage sustained from a falling bolt as in Figure 3-2. These optical feedthroughs allow direct access to the beam path for the laser induced fluorescence reactive scattering experiment discussed in Appendices 9.1.

A 12" × 15" breadboard is mounted directly above the throat of the diffusion pump in the main chamber. It is mounted on Teflon[45] spacers to prevent vibrations from being transmitted from the board to the frame and all other equipment. The breadboard allows for easy mounting of all the molecular beam sources and rapid alignment along the beam path.

The detection chamber is made completely of stainless steel and houses both the beam detectors and the sample holder. This chamber is equipped with an 8" diffusion pump and its own ion gauge for pressure measurements. The two chambers are separated by an aperture which defines the beam path i.e. line of sight between source and detector. This

Figure 3 - 2: Impacted Rotor

aperture limits the conductance between the two chambers and makes it possible to differentially pump the detection chamber to much lower pressures, at least one order of magnitude, than the main chamber. The set of apertures, called skimmers, span a range of diameters from 1 mm to 5 mm. If the entire skimmer is removed the two chamber pressures are essentially coupled and the pressure readings in each chamber are similar. The distance between the source and skimmer is a vital parameter[15] due to the large pressure difference between the chambers and to minimize this distance we have modified the right flange extensively as seen in Figure 3-3. The original skimmer mount, seen in Figure 3-3a, had an inner diameter of 1.5", which limited the overall pump out time of the system, and the clearance between the rotor and the skimmer was around 2". After modifying the beam out flange we have a much larger inner diameter of 4" bore that allowed us to design and install an improved system with the following advantages:

1) The system is made completely of stainless steel, except for the base plate seen in Figures 3-3b, 3-3c, 3-3d, and all seals are Viton gaskets which limits the conductance between the chambers to only the installed aperture.
2) A large volume is now available in the main chamber, as seen in Figure 3-3e, 3-3f, and 3-3g that is coupled to the detection chamber and remains at much lower pressures. Mounting holes are provided on the aluminum plate seen in Figure 3-3d for a fast ion gauge detector. This location is only 5" from the rotor while in shooting position making it $1/2$ to $1/3$ the previous distance.
3) The 4" inner diameter allows for much higher pumping speeds throughout the detection chamber as compared to the original setup in Figure 3-3a.
4) Removable plates seen in Figures 3-3f and 3-3g allow for future modifications.

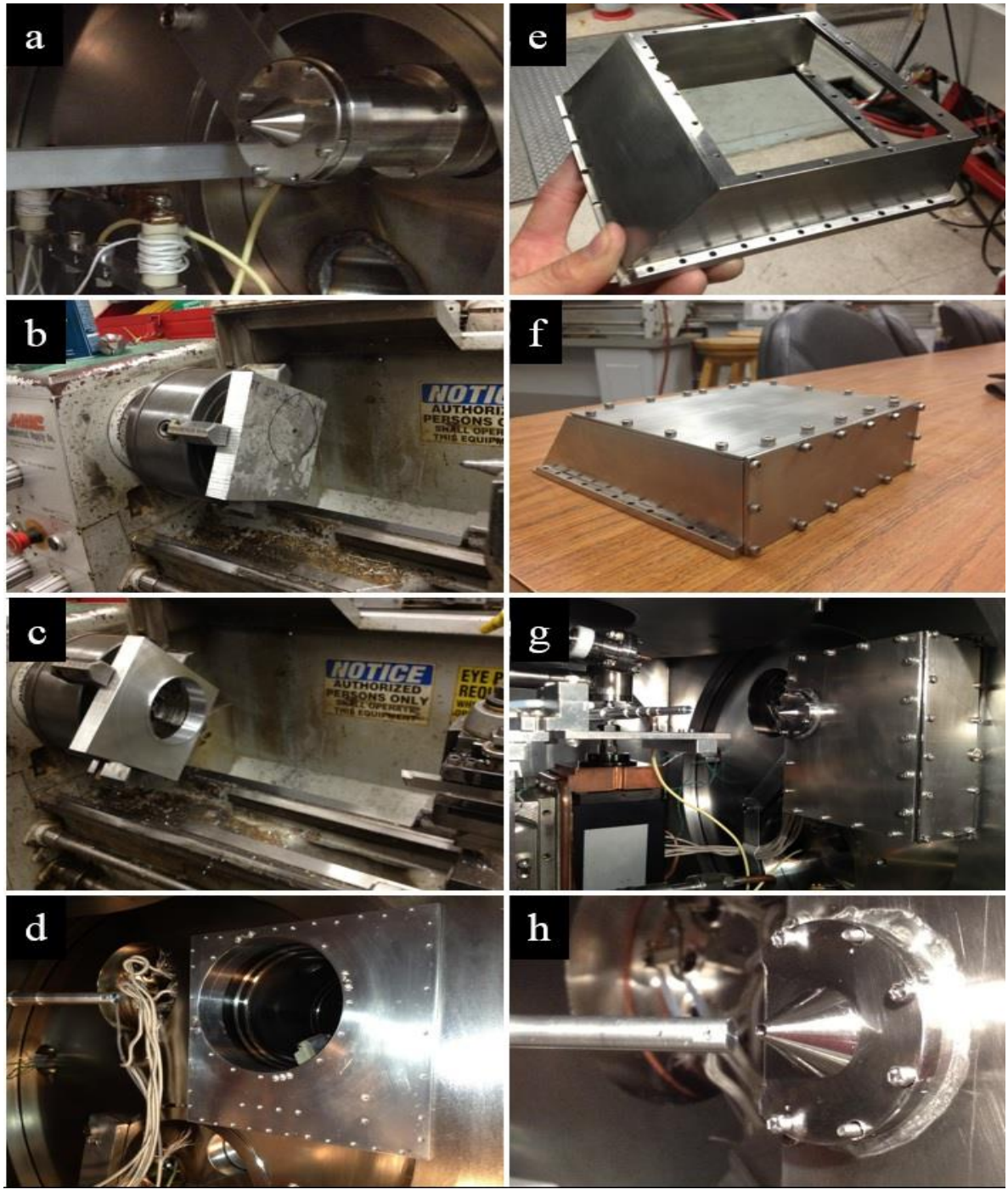

Figure 3 - 3: Beam-Out Flange Upgrade

5) Clearance between rotor and skimmer, as seen in Figure 3-3h, reduced to 1/4" which places the skimmer as close as possible to the rotors shooting position.

Many other flanges, besides the beam out flange, were built and installed throughout the past 5 years to accommodate special electric, water, and manipulation feedthroughs. These flanges were all designed with standard vacuum principles[46] in mind. Primarily, the thickness of each flange was chosen so that the distortion, during high vacuum operation, was kept to a minimum. When the chamber is pumped down every surface has an atmosphere of pressure across it. This pressure deflects the center of the flange by a known amount, and each flange is designed to keep this deflection under three-thousandths of the radius of the flange. To accomplish this we keep the thickness of all stainless steel flanges above $1/20^{th}$ of the radius, and the thickness of all aluminum flanges above $1/15^{th}$ the radius of the flange.

To seal the vacuum system we use Viton O-rings for all custom made flanges, quick connect (QC) couplings, ISO flanges, and Klein Flanges (KF). Viton is chosen primarily because of its low degassing rate up to the limiting temperature of around150℃. A thin layer of vacuum grease is administered to all Viton O-rings prior to installation to fill any microscopic leaks not visible to the naked eye. The only other flange type used is Conflat which utilize a stainless steel knife edge to "bite" into a copper gasket from both sides, filling in any microscopic defects in the metal, and creating the only metal-to-metal seals in our experiment. The knife edge is recessed into a groove in the flange which helps protect it during handling, aligns the metal gasket during installation, and prevents expansion of the gasket during heating. Conflat flanges currently achieve the best seal available, besides welding, and provide the additional benefit of being bakeable up to temperatures of 450℃.

A large mechanical pump (Edwards E2M40) is used for the initial evacuation of the chambers and can pump down to less than 100 millitorr in under 10 minutes. The same mechanical pump is used to back the diffusion pumps in both chambers and during initial pump down this valve, called the fore line valve, is open.

During the startup procedure the diffusion pump isolation valves, installed between both chambers and both diffusion pumps, are closed. After verifying the labs chill water system is operating, the two diffusion pumps are switched on and allowed to warm up for at least an hour. When the mechanical pump has lowered chamber pressure below 10 millitorr, and the diffusion pumps are hot, the roughing valve can be closed and the isolation valves opened. Typically, within four hours, the main chamber reaches a pressure less than 2×10^{-6} Torr, and the detection chamber to less than 2×10^{-7} Torr. With continuous pumping the chambers can reach pressures around half that achieved within the first four hours of operation.

The liquid nitrogen (LN2) traps installed in both chambers are multipurpose. They serve as a boundary to prevent the oil vapor in the diffusion pumps from contamination the vacuum systems that they evacuate. In addition to this, the LN2 acts as a pump itself by freezing any condensable gases on its surface and effectively removing them from the chamber. This pumping reduces the chamber pressures by around one order of magnitude and increases the pumping speed (for condensable gases only) quite drastically.

To insure that proper conditions exist for the operation of the diffusion pumps, a pressure interlock is used that prevents power from being supplied to them if the pressure indicated in the fore line system is above 200 millitorr. Prior to activating the diffusion pump heaters the regions on both sides of the diffusion pump are at similar pressures i.e.

there is no barrier to the flow of gasses. It is important to remember that if the region being pumped is not in the molecular flow regime then the diffusion pump would not operate at all and engaging the heaters will ultimately contaminate the entire system.

In addition to the pressure interlock, a flow detector is installed in the cooling system to prevent operation of the pumps without adequate cooling. This is to protect against mechanical failure of the chill water system and power outages that occur while the pumping systems are operating but no personnel are present i.e. the weekends and holidays. The chill water system utilized in the lab does not auto start in the event of a power outage, meaning the pumping systems would not have cooling if they did restart afterwards.

The pumping speed of diffusion pumps depend directly on the gas being pumped, and since our molecular beam experiments involve many different gasses it is worthwhile to understand why. A diffusion pump operates by vaporizing a special silicon based oil, in our pumps we use Santavac 5, which travels through the center of a set of cones as shown in Figure 3-4. The vapor is then forced outwards through the gaps between the cones and finally collides with the outer walls where it condenses and flows back to the oil reservoir at the bottom. If there are gas molecules present in the pump throat they collide with this stream of oil vapor and the imparted momentum carries the gas towards the exit of the pump. Once at the exit the mechanical pump will then remove the gas from the system completely. Since this mechanism relies on momentum transfer from the oil to the gas molecules, lighter molecules will be pumped more effectively than heavier ones. Edwards and NHS list the speed of their diffusion pumps for nitrogen as well as hydrogen. To extrapolate for other masses, a linear relationship must be assumed which goes as the square root of the mass. With this assumption in hand, the mass dependent pumping speeds, S in L/s, for the

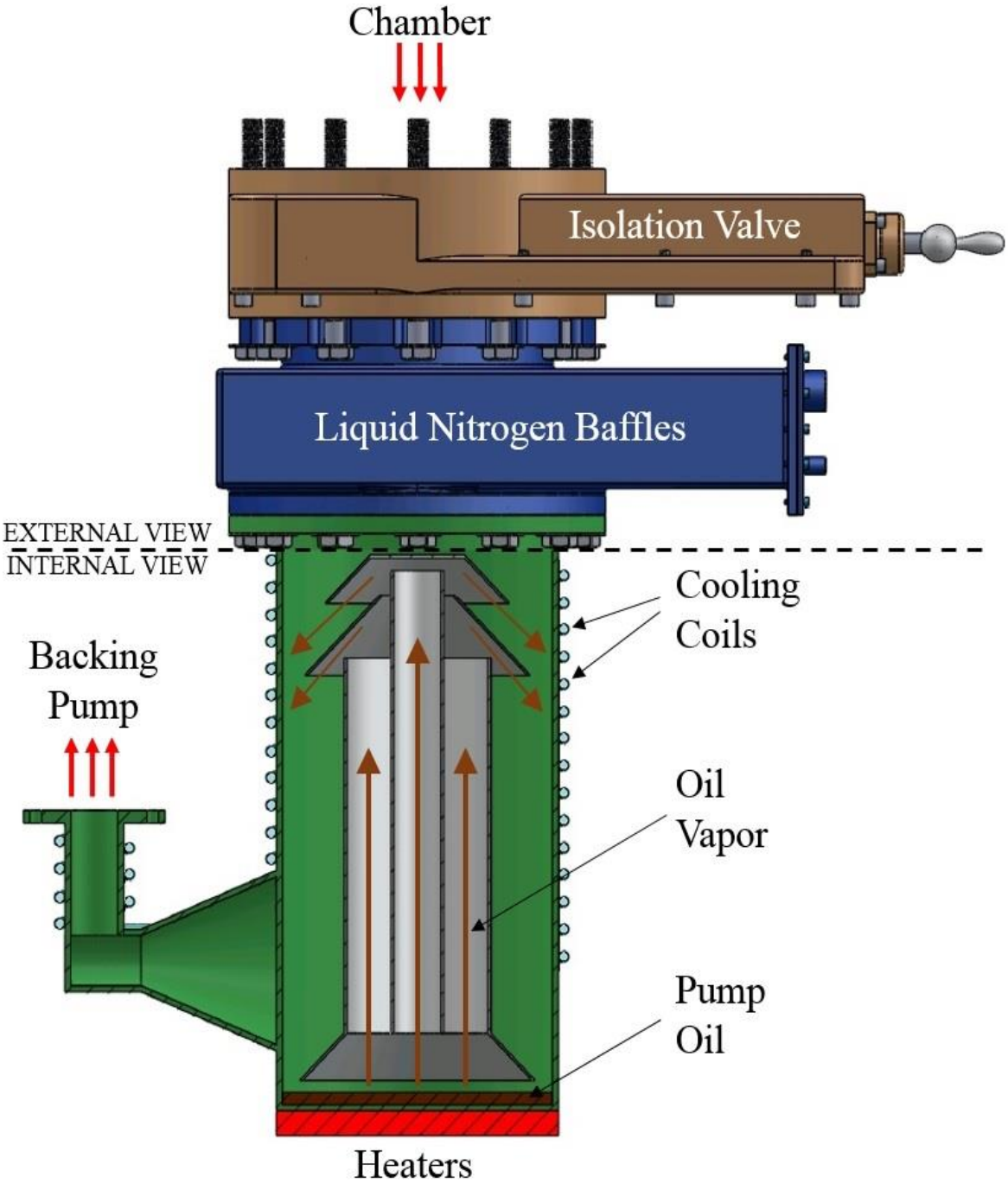

Figure 3 - 4: Diffusion Pump

Edwards E04 and NHS Diffusion pump are given by:

$$S_{E04} = S(He) - \left(\frac{S(He)-S(Air)}{\sqrt{28}}\right)\sqrt{M} \tag{3.1}$$

Where M is the mass of the gas in atomic mass units. The water cooled baffle mounted directly above the diffusion pump limits the pumping speed to $\sim 50\%$ of its estimated value.

In order to introduce gas to the solenoid valves used in a typical molecular beam experiment, a gas inlet system was constructed as seen Figure 3-5. The system contains three or four gas manifolds depending on the experiment being conducted. Most connections are made of ¼" Swagelok fittings to achieve a leak tight seal. Manifold 1 is primarily for corrosive gasses and is constructed completely of stainless steel. The gas supplied directly to this manifold does not have a regulator so pressure is read out on the Bourdon gauge mounted directly on the manifold. All other gasses supplied to the system run through a regulator and into one of the separable manifolds that each have independent gas pressure measurement capabilities. Gas pressures are measured with an assortment of gauge types including: Bourdon gauges, Convectron gauges, and piezoelectric gauges.

Several different orientations of the gas manifold system are shown in the bottom section of Figure 3-5. The system configuration can be changed easily since it utilizes Swagelok fittings and reusable Teflon ferules. Prior to filling with gas the system is pumped down with a small mechanical pump (Edwards Model E2M2) to less than 250 millitorr. The manifold pressures used vary widely, from around 10 torr in a standard effusive beam through the microwave cavity, to over one atmosphere for use with the high speed pulsed solenoid valves. If a low pressure and low contaminant beam is desired then the system is first pumped down over night, then filled, pumped, and refilled with gas several times to

reduce the concentration of any unwanted residual gas in the lines. Between runs the system is kept pumped down below 1 torr to continuously monitor leakage.

In the special case where a seeded beam is desired, but the gasses cannot be combined prior to the expansion, the setup as seen in the top of Figure 3-5 is used. This is perhaps the most elaborate system used in our chamber. The carrier gas is contained in manifold two, and the atomic seed gas is generated in the tubing directly before solenoid valve C. The tubing that is installed in the microwave cavity, which generates the atomic gas from a molecular precursor, has to be quartz tubing and must be replaced every 5-10 hours of operation due to ablation from high energy atoms in the excitation region. The pressure in the microwave cavity is maintained by the Convectron gauge installed in manifold three. This gauge is insensitive to gas type, thus no convolution of the displayed pressure is required when hydrogen is used as the molecular precursor. The atomic gas generated in the excitation region is prevented from flowing back towards the manifold by a Teflon constrictor placed in the quartz tubing. This must be far enough away from the excitation region to prevent damaging the Teflon and contaminating the manifold.

3.2 Background Gas

A precision metering valve (Swagelok, SS-4BMG), as seen in Figure 3-6, is used to control the absolute pressure in the chamber for calibration of the detectors used in time-of-flight measurements. This characterization method does not depend on pulsing a solenoid valve to produce a supersonic beam, and thus does not generate a large pressure fluctuation in the chamber. With the gas manifold providing a backing pressure of $10\ Torr$ the metering valve can control the chamber pressure by increments of $\sim 1 \times 10^{-8}\ Torr$. With an ultimate

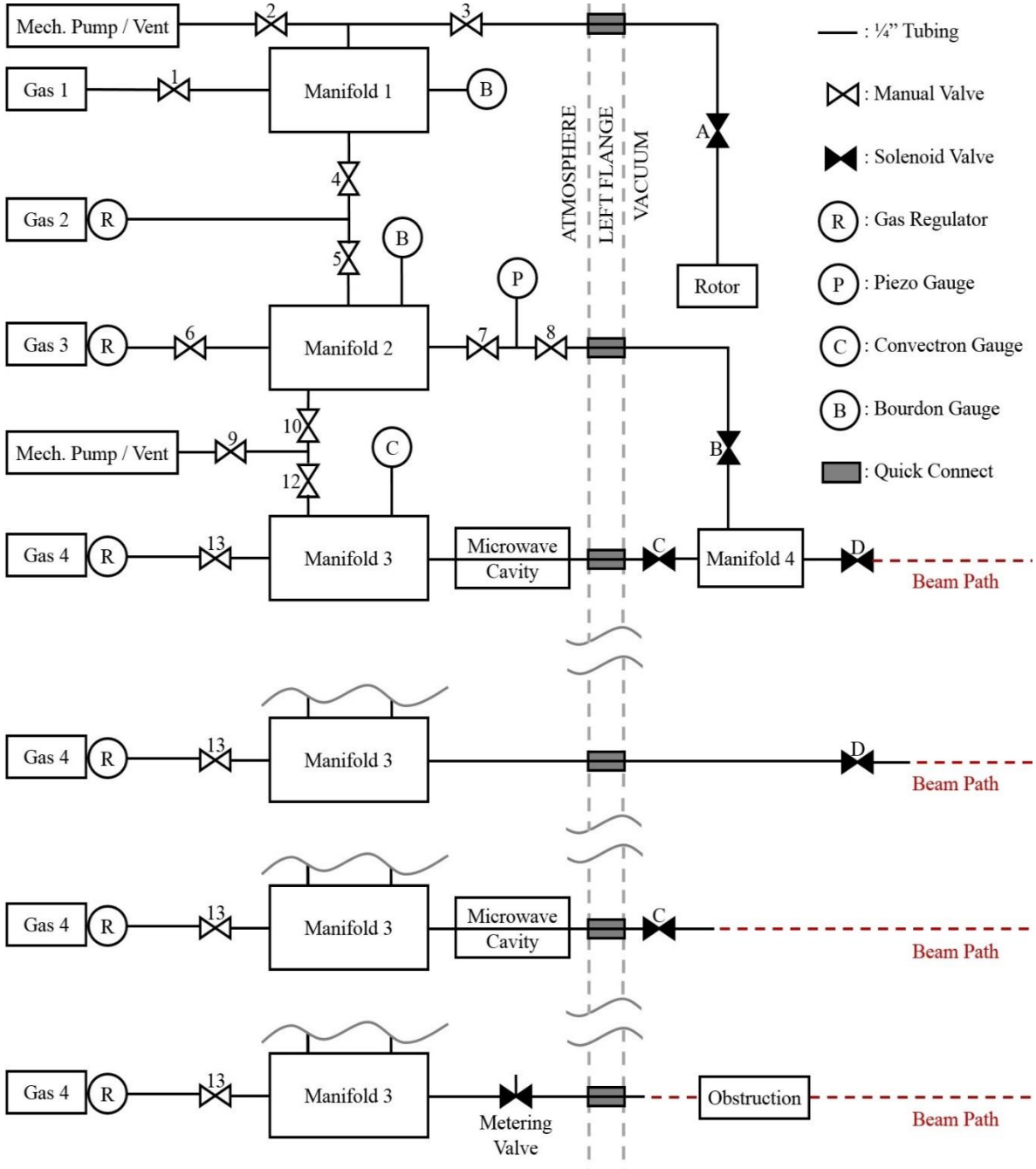

Figure 3 - 5: Gas Manifold

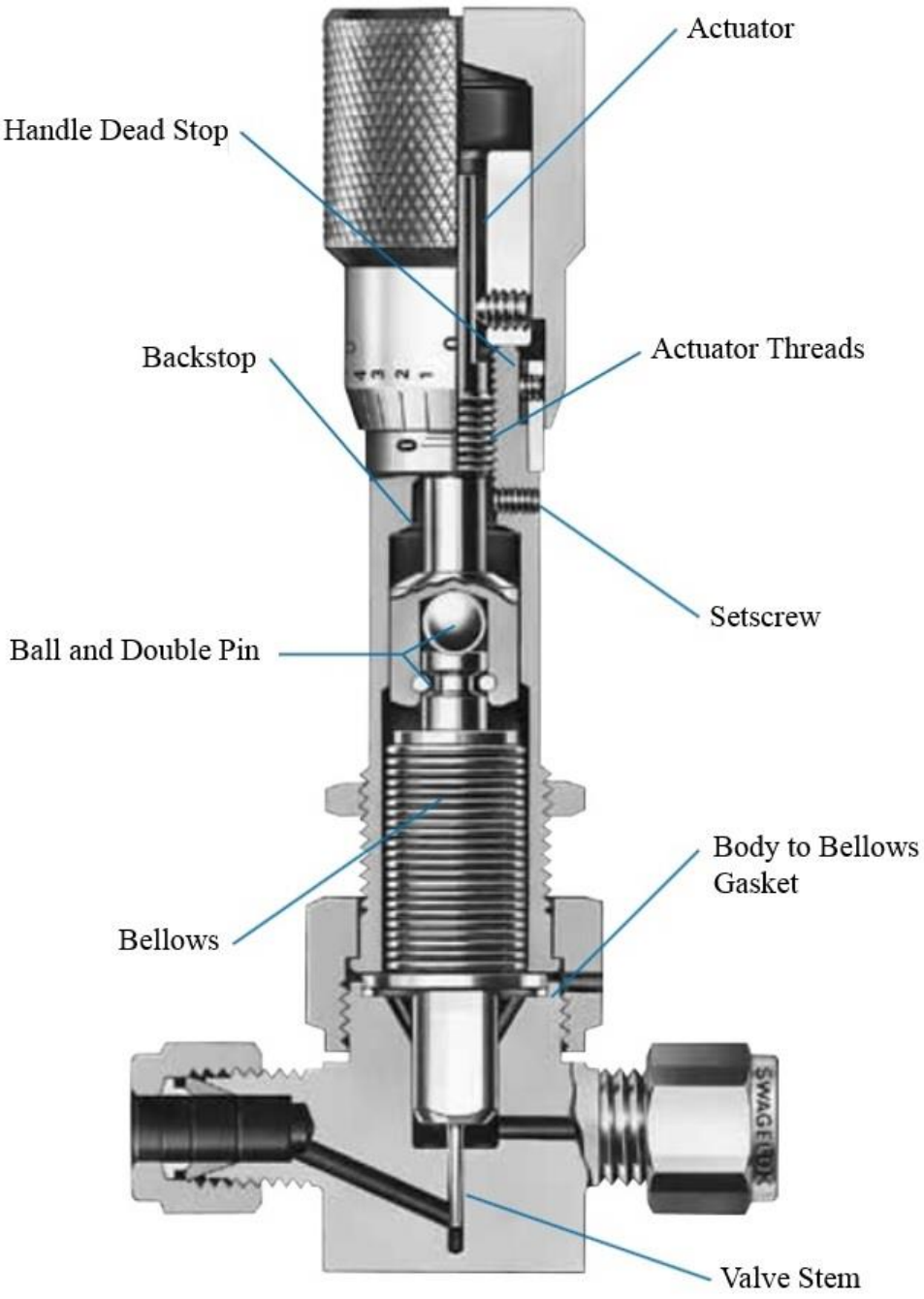

Figure 3 - 6: Swagelok Metering Valve

pressure of $1 \times 10^{-7}\ Torr$ the valve offers control down to the smallest increment of pressure deviation measured on our ion gauge. This precision is provided by the long thin stainless steel stem, as seen in Figure 3-6, with a 3° taper that is positioned by a micrometer handle. The handle allows for positioning of the stem in increments of $0.001"$. The valve has a very small internal volume of $0.07\ in^3$ (or $1.1\ cm^3$). The flow rate through the valve can be calculated using a flow coefficient (c_v) of 0.09.

The metering valve utilizes the quick connect port that is installed in the beam path, but a solenoid valve is left in place that prevents a collimated beam from flowing directly from the metering valve to the beam path. This simplifies the analysis because flow characteristics of the beam do not have to be considered, and the background gas can be considered isotropic and consist of a simple Maxwellian velocity distribution.

Although the valve is not intended to provide shutoff service it has been tested in the fully shut position and no discernable leakage occurs. The handle dead stop prevents damage to the threads and stem in the case of over tightening. If, in the future, leaks do become a concern then the manifold that supplies it with gas can be maintained below $1\ Torr$ and thus no leakage should occur. Since the valve is made completely of 316 stainless steel it is bakeable and the owners' manual indicates that it can operate at temperatures up to500 ℃.

3.3 Supersonic Beam

The two Parker General valves used in this thesis are the Series 99 and Series 1. These valves are very lightweight and have a small footprint making them easy to position and install inside the chamber. In fact, the Series 99 valve is the smallest in its class and provides the highest performance. The first priority in choosing equipment is vacuum compatibility

and this has not been an issue due to the stainless steel and PTFE constructions. The Series 1 model was chosen primarily to deal with corrosive gasses such as NO_2 as well as other valve properties:

1) Diaphragm Isolation
2) Wetted parts are PTFE allowing for the use of corrosive gases
3) Low internal volume
4) 100% tested leak tight with backing pressures up to 1250 PSI
5) Direct acting
6) <10ms cycle time (rated)
7) <1ms cycle time (actual)

These valves, when installed and aligned directly in the beam path, are called the stationary source, as opposed to the rotor which is referred to as the rotating source. The purpose of the stationary source is threefold. First, it provides a means to test out all equipment associated with the rotating source without having to use the rotor itself. This is very important during the initial tests when a wide variety of problems can be encountered. This troubleshooting includes noise in the detector, misalignment of the rotor, and clogging of the feed system. Second, it shows how well the solenoid valves work which is vital when troubleshooting a low density in the produced beams. Finally, the stationary source can be used in a scattering experiment as described in Appendix A.

Beams are produced by cycling the solenoid valve a single time with a reservoir gas, shown in blue in Figure 3-7, held at a pressure much higher than the chamber pressure. When the poppet lifts the gas achieves a stable flow within a few microseconds and this stable flow lasts until the poppet closes and seals the reservoir from the chamber. The

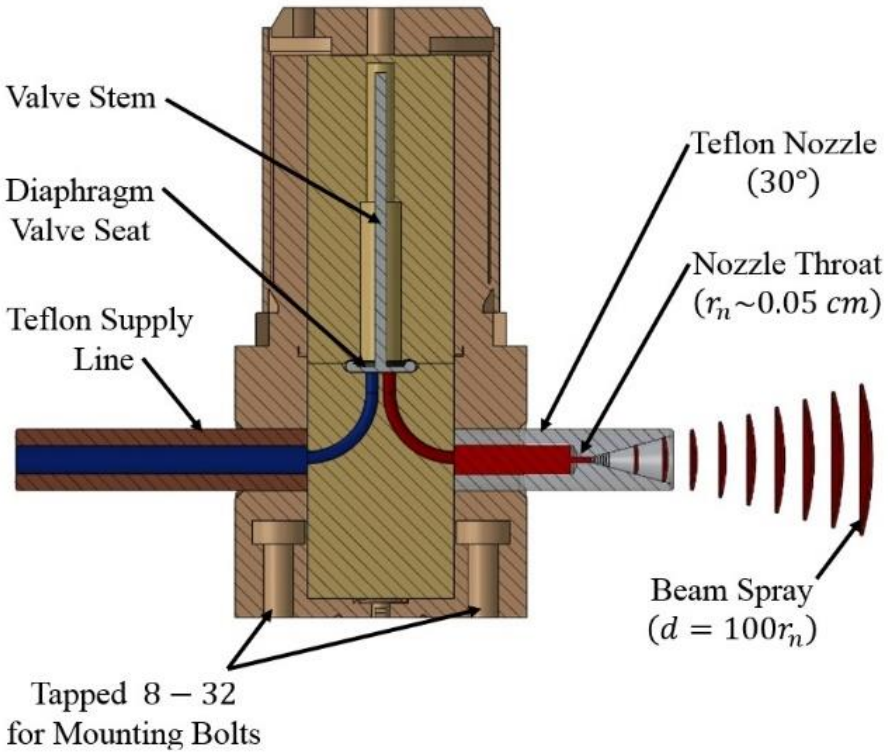

Figure 3 - 7: Parker Valve - Series 1

reservoir pressures are controlled by the gas manifold system shown in Figure 3-5. The fittings used to seal the main chamber from the gas supply line have to withstand large differential pressures as the supply line pressures can reach 2 or 3 atm. The typical conditions for testing both solenoid valves are given in Table 3-1.

Parameter	**Typical Values**
Reservoir Pressure	$10\ Torr \leq P_o \leq 1000\ Torr$
Reservoir Temperature	T_o~300 Kelvin
Nozzle Throat Diameter	$d_{throat} = .05cm$
Valve cycle time	$5\ msec \leq \Delta t \leq 1\ msec$
Distance to the FIG	$\ell = 12cm$
Distance to the skimmer	$\ell_{skimmer} = 6cm$
Nozzle angle	$\theta_{noz} = 15°$

Table 3 - 1: Typical Stationary Source Parameters

Initially, an Iota One Driver was purchased to control the high speed pulsed valves, but this rack mounted unit proved unable to produce the short sub-millisecond pulses that

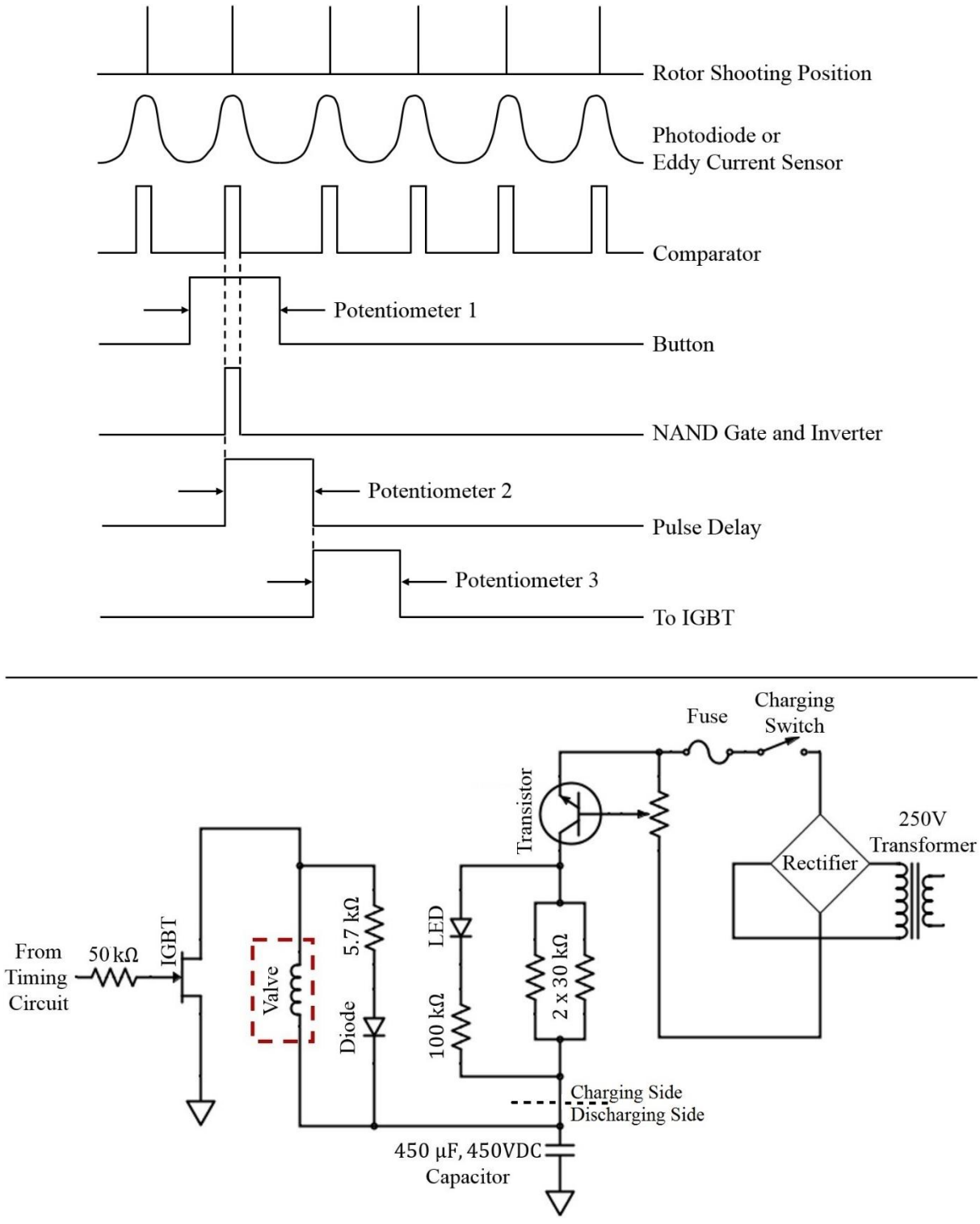

Figure 3 - 8: Custom Valve Driver - Timing Scheme and Circuit

were desired for the rotating source. In order to achieve the desired cycling times a custom valve driver was designed, as shown in Figures 3-8, and this continues to be used in place of the Iota One Driver due to its excellent performance, control, and customization properties. The custom valve driver consists of two parts. The first is a timing circuit which relies on several monostable multivibrators, comparators, and an external trigger. The second is the charging circuit that controls the voltage applied to a large capacitor in series with the solenoid. The pulse from the timing circuit feeds into an insulated-gate bipolar transistor (IGBT) which grounds the charged side of the capacitor through the solenoid, and actuates the valve. The timing circuit will be discussed first and then the charging circuit will be explained. Both of these are contained in the Solenoid Control Box shown in Figure 3-9.

The timing circuit is designed to produce identical pulses from the rotor every time the button is pressed on the valve driver. This requires the valve timing be synchronized with the position of the rotor so it can cycle open and closed with the rotor in essentially the same positions. In order to accomplish this it takes as an input the photodiode or eddy current sensor used to mark the position of the rotor. This signal is fed straight into a comparator which produces an output,

$$V_o = \begin{cases} 1, & if \quad V_+ > V_- \\ 0, & if \quad V_+ < V_- \end{cases} \tag{3.2}$$

consisting of just two states. One state is near zero voltage, and the other is the supply voltage. Now by pressing the button the first square wave signal is generated. This is accomplished by using a multivibrator integrated circuit (IC) which is designed to produce a variety of simple two-state outputs. In this case a monostable multivibrator (MMV) is used

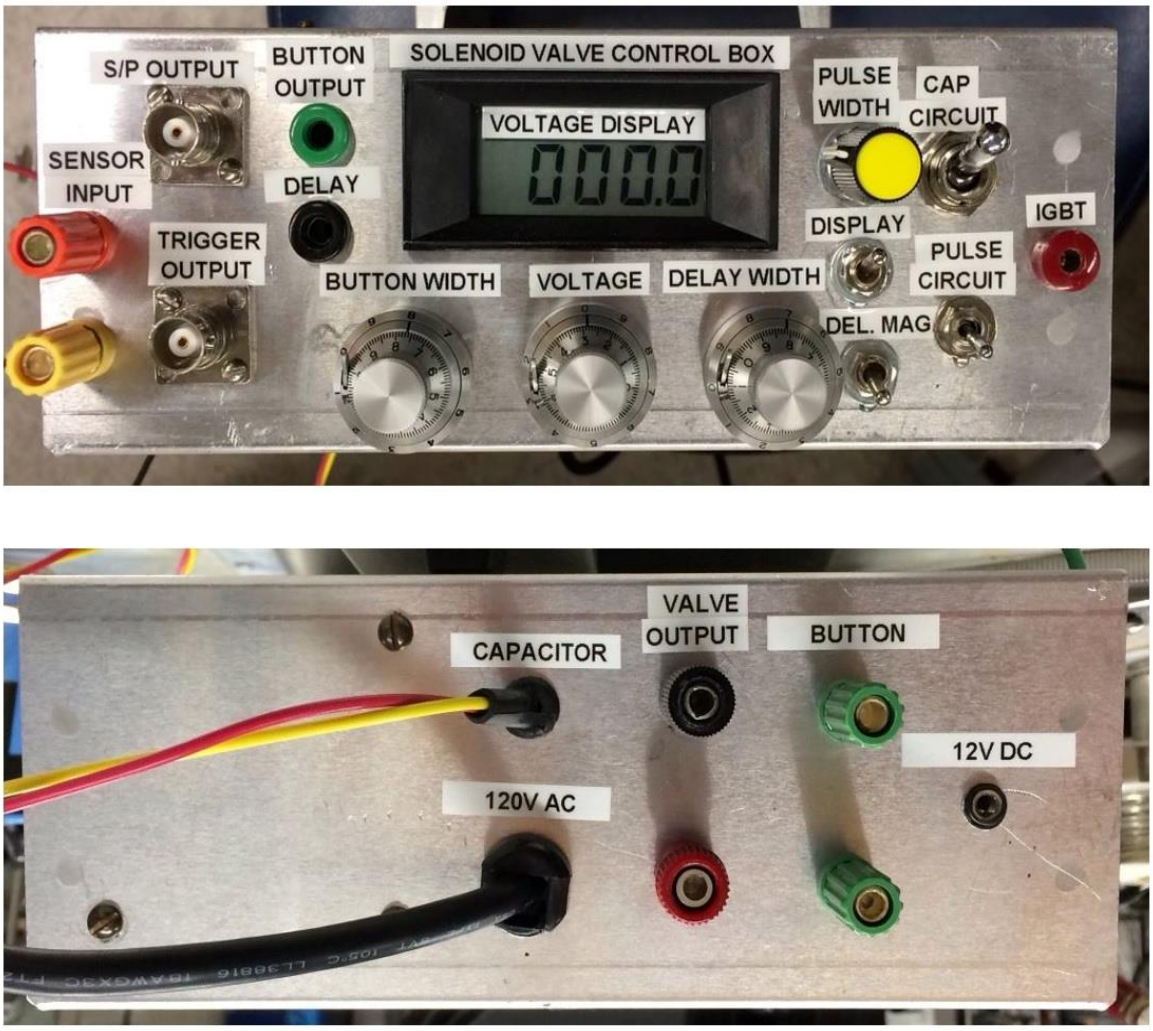

Figure 3 - 9: Custom Valve Driver - Front and Back Panels

which has a single stable state and one transient state. The stable state occurs when the button is not depressed and coincides with a zero voltage output. When the button is pressed a 5V square wave output is produced that has a width determined by the position of a potentiometer. This width, Δt_{button}, is important because if it is longer than the period of the rotor, τ, the possibility exists to actuate the valve multiple times. When Δt_{button} is too small the probability of the signal from the comparator and button overlapping is greatly reduced. For these reasons, Eqn 3-4 is used as a guide for the determining the correct value of Δt_{button}

$$\frac{\tau}{4} < \Delta t_{button} < \tau \tag{3.3}$$

These two signals feed into a NAND logic gate which produces an output that is false only when both of the input signals are true. In this case false means a negative voltage output, and true means a positive voltage. So, as shown in Figure 3-8, the NAND gate, combined with an inverter, produce a positive square wave pulse that is as wide as the comparator. This output connects to a BNC cable mounted on the front of the control box that is used as, and labeled as, a trigger for the data acquisition system. The second MMV triggers off the rising edge of the inverter output and produces its own square wave with adjustable width, Δt_{delay}. The delay time allows the data acquisition system to record data from the beam detectors before any signal is received from the rotor. This is very important for troubleshooting noise in the signal and has been kept at about 5 ms for most of the data presented in this thesis. The third and final monostable multivibrator triggers off the falling edge of the delay pulse and represents the wave form that will be used as an input to the IGBT. Since the IGBT controls the current flow through the valve the width of the square wave produced by this MMV is denoted as Δt_{vlv}. This value can be anywhere from 500

microseconds to several milliseconds depending on the experiment being conducted. In the cases where a large source pressure is used Δt_{vlv} must be small to prevent effectively venting the chamber while the gas detectors are on. All of the MMV waveforms can be monitored independently via the front panel as seen in Figure 3-9.

The charging circuit uses a 250V transformer to supply the current needed to actuate the valve. They are both rated for 24V DC and are good for several million cycles. By using a much larger voltage to actuate the valve the life is greatly reduced but over several months of regular use the solenoid valves have been cycled at most a few hundred times. The voltage is adjusted by using the transistor (MJE 13009) shown in Figure 3-8. The two 30 kΩ resistors in parallel control the rate at which the capacitor is charged, and the LED in parallel with this current path is used to indicate that the charging circuit is operating properly.

The discharging circuit, simplified in Figure 3-10, contains the high performance capacitor (CGS451T450V3C), the valve, and the IGBT in it. Between pulses the system stays

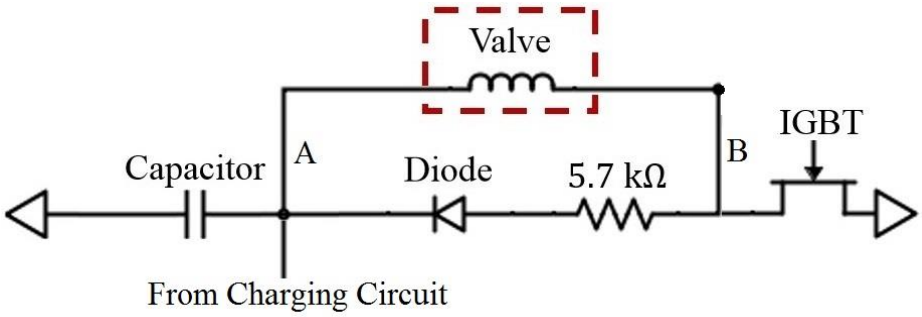

Figure 3 - 10: Custom Valve Driver – Discharge Circuit

charged which means the top and the bottom current paths are at the same voltage determined by the transistor in the charging circuit. When the IGBT receives a signal from the timing circuit, shown in Figure 3-8, it closes the loop to ground and discharges the capacitor. The general equation which dictates the rate at which a capacitor will discharge depends primarily on the voltage across the capacitor which is

$$V = \frac{V_o}{C} \int I dt \tag{3.4}$$

In the case where the current can be considered a constant, this equation returns

$$V = V_o \left(1 + \frac{It}{C}\right) \tag{3.5}$$

In the more general case where the current is a function of time the voltage obeys

$$V = V_o e^{-t/RC} \tag{3.6}$$

The time that it takes the capacitor to discharge from V_o to V is

$$t = -RCln\left(\frac{V}{V_o}\right) \tag{3.7}$$

For the valves used in this experiment $R_{vlv} = 50\Omega$ and the capacitor has $C = 450\mu F$. Thus, the time required to discharge the capacitor from 25V to 1V is 73ms which is much longer than any waveform sent to the IGBT by the timing circuit. The maximum length of time that the valve driver is capable of is 10ms but the typical time is less than 1ms. For the situation where the capacitor is charged to 100V and is discharged for <1ms the voltage drop is below 4 volts. For this reason the voltage across the valve can be thought of as constant during the time period that the valve is cycled.

Once the IGBT waveform returns to a null value the IGBT opens and the capacitor stops draining through the solenoid. At this instant the voltage across the entire circuit attempts to equilibrate. The diode and resistor in the bottom leg of Figure 3-10 prevent a large current from flowing back through the valve. The diode is oriented in a way that allows current to flow only in the direction which equalizes this voltage. Otherwise it would reduce the current that is flowing though the solenoid when the IGBT is closed.

It is clear from the discussion thus far that there are two primary factors, IGBT waveform and capacitor voltage, that dictate the performance of the stationary valve. In addition to these two parameters, the reservoir pressure, P_{res}, impacts the pulses produced by the valve due to the force that this pressure applies on various components of the poppet mechanism. To characterize its' behavior as these parameters are changed, the valve is mounted directly onto the skimmer, as is shown in Figure 3-11. The area between the valve and skimmer allows most of the gas emitted from the stationary source to be removed by the main chamber pumps. This prevents overloading the detector and similar pressures can be used in this configuration and the rotating source configuration.

The pulse shapes from the stationary source, as configured in Figure 3-11, have been analyzed for a wide range of the parameters: V_o, Δt_{IGBT}, and P_{res}. The two data sets shown in Figure 3-12 contain variations of Δt_{IGBT}, on the top data plot, and beaneath that is the variation of P_{res}. Each pulse contains a leading edge with a sharp peak, an amplitude dependent on P_{res}, and a width proportional to Δt_{IGBT}. The sharp peak can be due to recoil of the valve poppet after it impacts the backseat of the valve. This recoil is amplified by the presence of a spring whose purpose is to close the valve after it is cycled open. The overall amplitude of the pulse reflects both the beam density from the valve and the contribution to

Figure 3 - 11: Stationary Valve - Testing

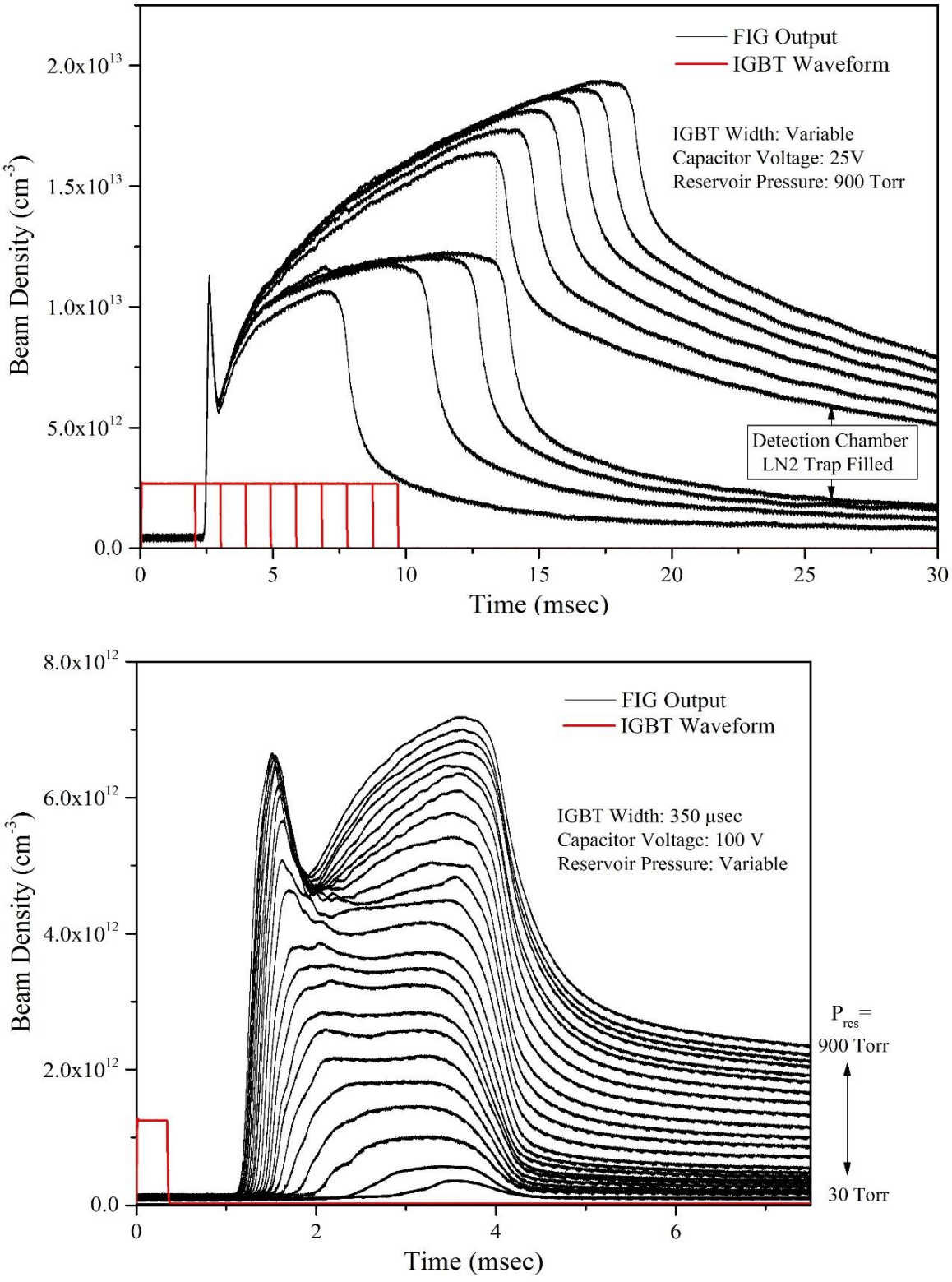

Figure 3 - 12: Stationary Valve Performance

this density from the background gas in the chamber. For this reason, a LN2 trap in the detection chamber was filled during the measurement of the gate widths. The data set before and after filling the LN2 trap has the same parameters, V_o, Δt_{IGBT}, and P_{res}, but show a significant change in amplitude due to the higher pumping speeds in the detection chamber. The width of the pulse follows Δt_{IGBT} although there is an offset in time due to the delayed response of the valve to the current.

The pulses from the stationary valve are not characterized with respect to flow velocity or beam temperature. This is because the purpose of the stationary valve is only to fill the internal volume of the rotor with gas. If the beam produced by the stationary source was going to be used in a crossed beam experiment, as described in Appendix 9-1, then efforts would be made to fully characterize it.

3.4 Rotor Mounted Supersonic Beam

Here I describe the experimental development of the device discussed in section 2.4. The

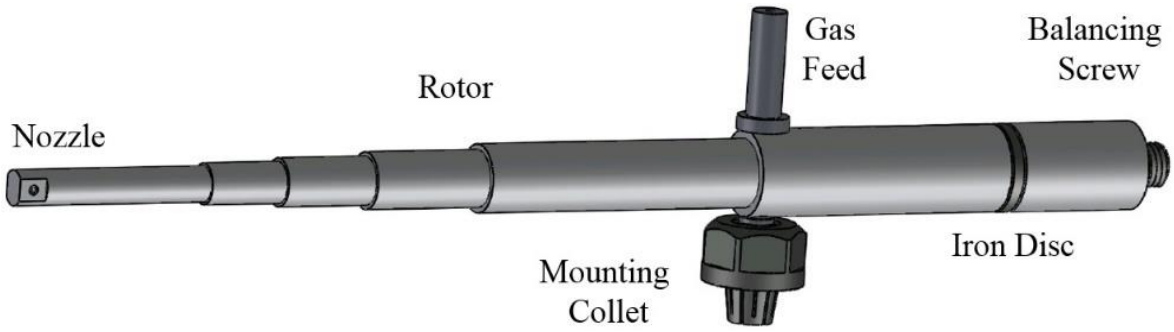

Figure 3 - 13: Rotor 2 Assembled

rotor shape itself, as seen in Figure 3-13, is a staggered set of cylinders chosen for its ease of construction while still maintaining its ability to attain very high peripheral velocities. The rotor was made asymmetric to ease the construction as well, i.e. it is difficult to drill a very long and verystraight hole. The overall shape is carried over from the previous device (Gupta, 1999) and has proved very effective in producing both slowed and accelerated molecular beams. All steps of the construction were performed in-house and did not require elaborate techniques to complete. A comprehensive description of the rotor construction is included in Appendix 9-2. The primary considerations for rotor design are:

- Rotor Breakage: Optimize the shape and chose the correct material to prevent the rotor from being torn apart.
- Endcap Adhesion: Devise a method by which to seal the aperture to the rotor tip
- Heat Conduction: Minimize the heat transferred to the rotor from the gas feed system and the motor.

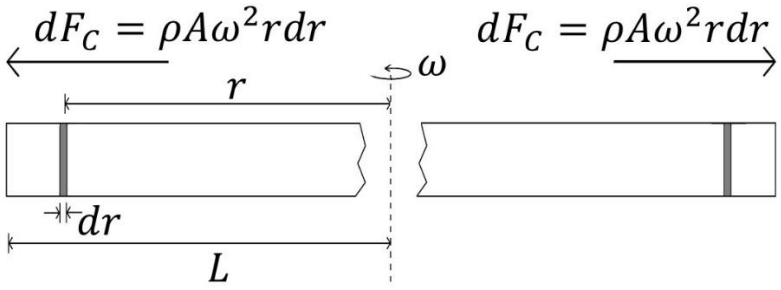

Figure 3 - 14: Centrifugal Force

- Balance: Incorporate a system which minimizes any vibrations via precision balancing.

For a 6" high speed rotor spinning at $500\ Hz$ the tip of the rotor feels a centrifugal force that is 1.6 million times greater than that of gravity. If the rotor cannot withstand these forces due to an improper design or wrong material selection it will rip itself apart. This was seen throughout the design process by Gupta and Herschbach and it resulted in the destruction of several prototype devices! Fortunately we have had no rotors destroyed by the mere act of spinning them. Several impact events have occurred due to the tendency of motor vibration to cause bolts to loosen and the requirement of mounting apparatus above the plane of the rotor. The foil shield is also susceptible to these vibrations as well and thus aluminum foil is chosen as the construction material for the shield.

For a rod of length L rotating around its central point at a frequency ω the centrifugal force, F_c, acts in an outward direction, pulling the material from the central point towards the ends. To understand the magnitude of this force, we first calculate the force exerted on the center of the rod by an infinitesimal mass, dm, positioned a fixed distance, r, from the center:

$$dF_c = \omega^2 r dm \tag{3.8}$$

Since the rotor is not in the shape of a disc, but is long and thin, we can exclude all other dimensions except for the radial component. In this case, dm becomes the circular cross-section of the rotor, and it becomes easy to calculate:

$$dm = A\rho dr \tag{3.9}$$

Now integrate over the length of the rotor to find the total force exerted on the central point:

$$F_c = 2\int_0^L A\rho\omega^2 r dr \tag{3.10}$$

$$F_c = A\rho\omega^2 L^2 \tag{3.11}$$

The factor of 2 comes from the fact that the central point extends in two directions. If the rotor were spun from one end this would not occur, but the balancing would then be impossible and large vibrations would occur.

To find the maximum allowable angular speed of the rotor it is necessary to equate the centrifugal force, which acts to tear the rotor apart, to the strength of the material, which acts to hold the rotor together. The force that holds a solid rod together, S, is calculated using the tensile strength (T), and the cross sectional area (A):

$$S = AT \tag{3.12}$$

Equating the two:

$$A\rho\omega^2 L^2 = AT \tag{3.13}$$

The maximum peripheral velocity $\left(v_p = \omega L\right)$ can now be expressed in terms of the tensile strength and density of the material

$$v_p = \sqrt{\frac{T}{\rho}} \tag{3.14}$$

This equation describes how the material properties of a perfectly straight rod dictate the maximum peripheral velocity it can attain. The stronger and lighter that a material is the higher speed it will be able to attain, and this makes sense from a practical standpoint. Table 3.1 shows some common materials and what velocities they can attain. After considering the large velocities that molecular beams attain, and remembering the primary function of the

rotor is to counteract these velocities, it becomes obvious that some of the maximum velocities displayed in Table 3-2 are not sufficient.

By more ideally shaping the rotor it can be made to withstand much higher velocities. In the preceding calculations this augmentation will occur by expressing the cross sectional area as a function of distance from the center:

$$A \rightarrow A(r) \tag{3.15}$$

Then the integration performed in 3.4 will have a different solution and the resulting velocity

Material	$\boldsymbol{T\ (psi)}$	$\boldsymbol{\rho\ (lb/in^3)}$	$\boldsymbol{v_p(m/s)}$
Delrin	12000	0.052	240
SS-316	60000	0.286	229
Brass	14000	0.306	107
Al – 2024	47000	0.098	346
Al – 7075	73000	0.101	424
Al – 7068	99000	0.101	494
Titanium	145000	0.16	475

Table 3 - 2: Relevant Properties for Rotor Materials

calculations will be different as well. In any rotor that has a changing shape the velocity will not be limited by the force at the central point, but by the force at the weakest point. To find the weakest point on the rotor we find the point of maximum stress and then solve the force equation for that point. Stress is expressed as force divided by area:

$$Y = \frac{F_c(r)}{A(r)} \tag{3.16}$$

The point of maximum stress is where the derivative of the stress with respect to radial position is equal to zero:

$$\frac{\partial Y}{\partial r} = 0 \tag{3.17}$$

If there is a finite solution for this equation then this point along the rotor length where we solve the force equation, as above, and determine the limiting velocity. Now, if the stress is constant throughout the rotor then there will be no point of maximum stress. This constraint takes the form:

$$Y = \frac{F_c(r)}{A(r)} = \frac{2\int_0^L A(r')\rho\omega^2 r' dr'}{A(r)} = \text{Constant} \tag{3.18}$$

Which is solved exactly by a Gaussian shaped rotor with cross sectional area:

$$A(r) = A_o e^{-r^2/\sigma^2} \tag{3.19}$$

This states simply, that an infinitely long rotor with a perfectly Gaussian shape will have an infinite peripheral velocity, but in fact our rotor has a finite length and therefore is classified as a truncated Gaussian. For a rotor truncated at a specified length (L) the spread of the gaussian shape (σ) should be much smaller than this length, i.e.

$$\sigma \sim nL \quad \text{and} \quad n \ll 1 \tag{3.20}$$

Where n represents the ratio of the gaussian spread to the length at which the rotor is truncated. By either truncating the rotor at a longer distance from the center, or reducing the spread of the Gaussian shape, the peripheral velocity can be increased. In other words:

$$\omega \to \frac{1}{nL}\sqrt{\frac{T}{\rho}} \quad \text{and} \quad v_p \to \frac{1}{n}\sqrt{\frac{T}{\rho}} \tag{3.21}$$

To obtain the final dimensions of the rotor a length must first be specified. For this most recent generation of rotor design we have chosen to increase the length from 9.9 cm to 14.9 cm. Then the number of steps in the rotor shaft must be considered. The ancestral device had 4 steps and in our case we chose 6 steps to better conform to the Gaussian shape and more efficiently minimize the larger stresses involved with a longer rotor length. We also chose to increase the maximum diameter of the rotor from $1/2"$ to $5/8"$. With these new parameters in hand we follow the framework established by Gupta and Herschbach and write a set of coupled algebraic equations relating the centrifugal force to the tensile strength.

$$2\rho\omega_6^2 \int_{R_5}^{L} A_6 r dr = TA_6 \tag{3.22}$$

$$2\rho\omega_5^2 \left[\int_{R_5}^{L} A_6 r dr + \int_{R_4}^{R_5} A_5 r dr\right] = TA_5 \tag{3.23}$$

$$2\rho\omega_4^2 \left[\int_{R_5}^{L} A_6 r dr + \int_{R_4}^{R_5} A_5 r dr + \int_{R_3}^{R_4} A_4 r dr\right] = TA_4 \tag{3.24}$$

$$2\rho\omega_3^2 \left[\int_{R_5}^{L} A_6 r dr + \int_{R_4}^{R_5} A_5 r dr + \int_{R_3}^{R_4} A_4 r dr + \int_{R_2}^{R_3} A_3 r dr\right] = TA_3 \tag{3.25}$$

$$2\rho\omega_1^2\left[\int_{R_5}^{L} A_6 r dr + \int_{R_4}^{R_5} A_5 r dr + \cdots + \int_{R_1}^{R_2} A_2 r dr + \int_{R_0}^{R_1} A_1 r dr\right] = TA_1 \quad (3.26)$$

$$2\rho\omega_0^2\left[\int_{R_5}^{L} A_6 r dr + \int_{R_4}^{R_5} A_5 r dr + \cdots + \int_{R_0}^{R_1} A_1 r dr + \int_{0}^{R_0} A_0(r) r dr\right] = TA_0(0) \quad (3.27)$$

When solved, each of these equations will provide a limiting frequency (ω_n) given by

$$\omega_6 = \sqrt{\frac{T}{\rho}(L^2 - R_5^2)^{-1}} \quad (3.28)$$

$$\omega_5 = \sqrt{\frac{T}{\rho}(L^2 - R_5^2)^{-1} + (R_5^2 - R_4^2)^{-1}} \quad (3.29)$$

and so on for each segment of the rotor. The last cross sectional area, R_0 , must include the drilled out section where gas will flow. Therefore, it is the only section that has a radius dependent cross sectional area, as seen in Figure 3-15. Note that the rotor will be drilled the entire length (with a radius of ϕ_o) except for a small volume at the end which will contains the nozzle.

The set of coupled differential equations generated by Eqn 3.28, Eqn 3.29, and the five other equations not listed must be solved by maximizing the minimum frequency. This is accomplished by a "brute-force" method written in FORTRAN by Gupta and Herschbach during the initial development of the rotor design. The program is given a set of constraints, it quickly considers all possible values of the variable parameters, and then outputs the optimized parameters. The parameters for the current rotor are shown in Table 3-3. One of the key constraints we reconsidered, from the original design, was the size of the hollow section inside the rotor. The size of this hole should be kept to a minimum, but the difficulty with drilling a straight hole for the entire length of the rotor increases dramatically with

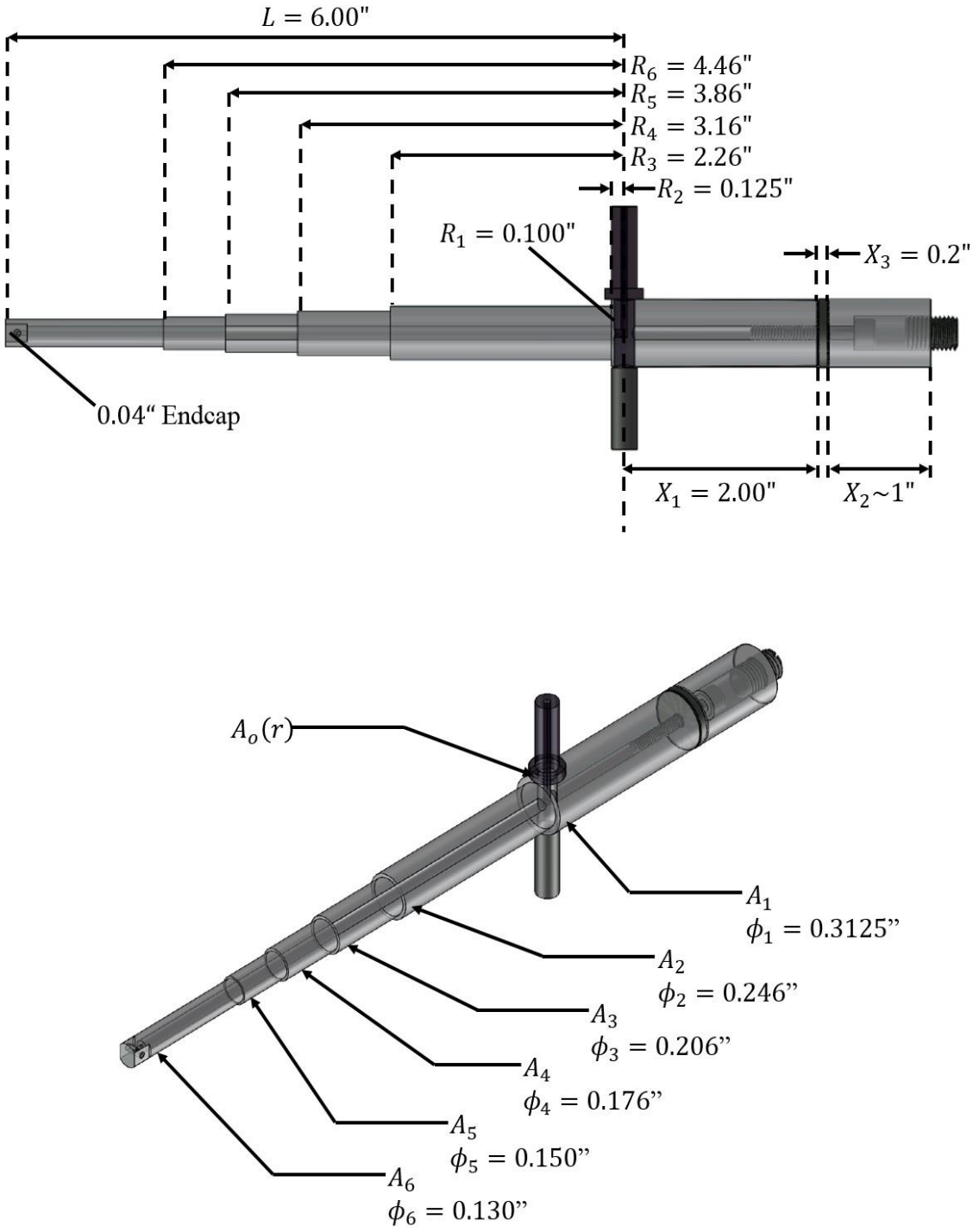

Figure 3 - 15: Final Rotor 2 Dimensions

Parameter	Range	Optimum Value
ϕ_o	$\phi_o = 0.0625"$	$\phi_o = 0.0625"$
ϕ_1	$\phi_1 = 0.3125"$	$\phi_1 = 0.3125"$
ϕ_2	$\phi_3 < \phi_2 < \phi_1$	$\phi_2 = 0.246"$
ϕ_3	$\phi_4 < \phi_3 < \phi_2$	$\phi_3 = 0.206"$
ϕ_4	$\phi_5 < \phi_4 < \phi_3$	$\phi_4 = 0.176"$
ϕ_5	$\phi_6 < \phi_5 < \phi_4$	$\phi_5 = 0.150"$
ϕ_6	$\phi_6 = 0.130"$	$\phi_6 = 0.130"$
R_1	$R_1 = 0.100"$	$R_1 = 0.100"$
R_2	$R_2 = 0.125"$	$R_2 = 0.125"$
R_3	$R_2 < R_3 < R_4$	$R_3 = 2.26"$
R_4	$R_3 < R_4 < R_5$	$R_4 = 3.16"$
R_5	$R_4 < R_5 < R_6$	$R_5 = 3.86"$
R_6	$R_4 < R_5 < L$	$R_6 = 4.46"$
L	$L = 6.00"$	$L = 6.00"$

Table 3 - 3: Rotor 2 - Parameter Ranges and Optimal Values

decreasing drill bit size. The original diameter of $2\phi_o = 0.125$" was therefore kept for the newest iterations of the rotor design. With areas calculated at the center as in Figure 3-16.

The side of the rotor opposite the nozzle holds both the iron disc and the balancing setscrew. The length is determined simply by balancing the centrifugal force acting on both sides of the rotor. This takes the form:

$$\rho\omega^2\left[\begin{matrix}\int_{R_5}^{L} A_6 r dr + \int_{R_4}^{R_5} A_5 r dr + \int_{R_3}^{R_4} A_4 r dr + \int_{R_2}^{R_3} A_3 r dr \\ + \int_{R_2}^{R_3} A_3 r dr + \int_{R_1}^{R_2} A_2 r dr + \int_{R_0}^{R_1} A_1 r dr\end{matrix}\right] = \rho\omega^2 \int_{R_o}^{x} A_1 r dr \quad (3.30)$$

where x is the length of the straight side. This equation does not take into consideration the mass of the extra components on the straight side i.e. the iron disc, disc mounting screw, and balancing screw. Instead this value, determined as $x = 3$" returns a limiting value to prevent the rotor from being cut too short during the initial manufacturing. As an extra precaution, this side is made a bit longer, then slices are incrementally removed during the final balancing procedures.

The rotor is made from Aluminum 7068, which at the time of construction was the highest strength aluminum manufactured, and contains 7.8% zinc, 2.6% magnesium, and 2% copper. The mechanical attributes of this alloy are given in Table 3-3 and are compared to Al-7075 which was the original material choice. Using these attributes, the maximum peripheral velocity the rotor can withstand is calculated as $633\ m/s$ which occurs at an angular velocity of $661\ rps$. This velocity is comparable to most molecular beam speeds, but is not capable of slowing light weight gas species such as helium or hydrogen. One of the key benefits to the current rotor design is that the endcap is built into the body of the rotor. The 1/8” hole, drilled along the length of the rotor for the gas to travel, does not pass

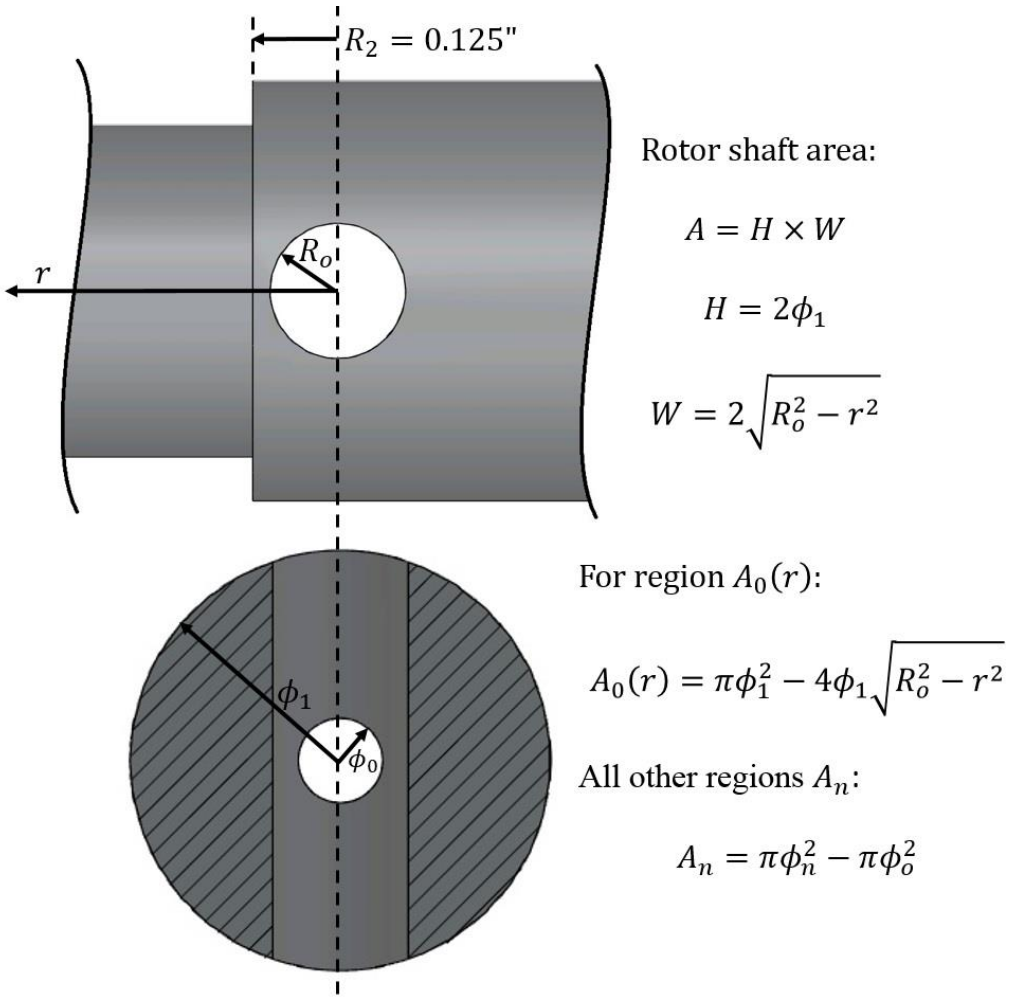

Figure 3 - 16: Rotor2: Cross Sectional Areas

all the way through. Instead, as seen in Figure 3-17, there is ~0.2" of aluminum left to serve as an endcap. The force on the endcap is not merely the centrifugal force, but also a function of the gas pressure inside the rotor. To calculate a limiting value of the force on the end we consider a uniform plug, with a radius of 0.13", a length 0.2", and is positioned at the very end of the rotor. If the rotors velocity is approximately $600\ m/s$, which is very near to the maximum velocity, then the force is given in Newtons as:

$$F = m \cdot a = (V \cdot \rho)\left(\frac{v^2}{R}\right) = (4.865 \times 10^{-4}\ kg)\left(2.362 \times 10^{6}\ \frac{m}{s^2}\right) \qquad (3.31)$$

Which returns a value of $1149\ N$. A limiting force due to the gas pressure inside the rotor can be calculated by considering 6 atmospheres of pressure acting on the end of the 1/8" hole drilled in the center of the rotor. This creates a force:

$$F = P \cdot A = \left(6.08 \times 10^{5}\ \frac{kg}{m \cdot s^2}\right)(7.92 \times 10^{-6}\ m^2) \qquad (3.32)$$

Which returns a value of $4.85\ N$ which is miniscule compared to the centrifugal force. The total force pulling the endcap from the rotor ($1155\ N$) must be smaller than the force holding the endcap on the rotor, which as explained before, is simply the surface area of the contact multiplied times the tensile strength of the aluminim. Utilizing the tensile strength listed in Table 3.1 we obtain a force

$$F = T \cdot A = (99000\ psi)(\pi\phi_6^2 - \pi\phi_o^2) \qquad (3.33)$$

Using the conversion $1\ psi = 6895\ pascals$ we obtain $17{,}977\ N$ which is much larger than the force attempting to rip it off.

The current supersonic nozzle is a large departure from the original design which utilized a 0.0005" thick stainless steel disc and expanded the supersonic beam through a 100

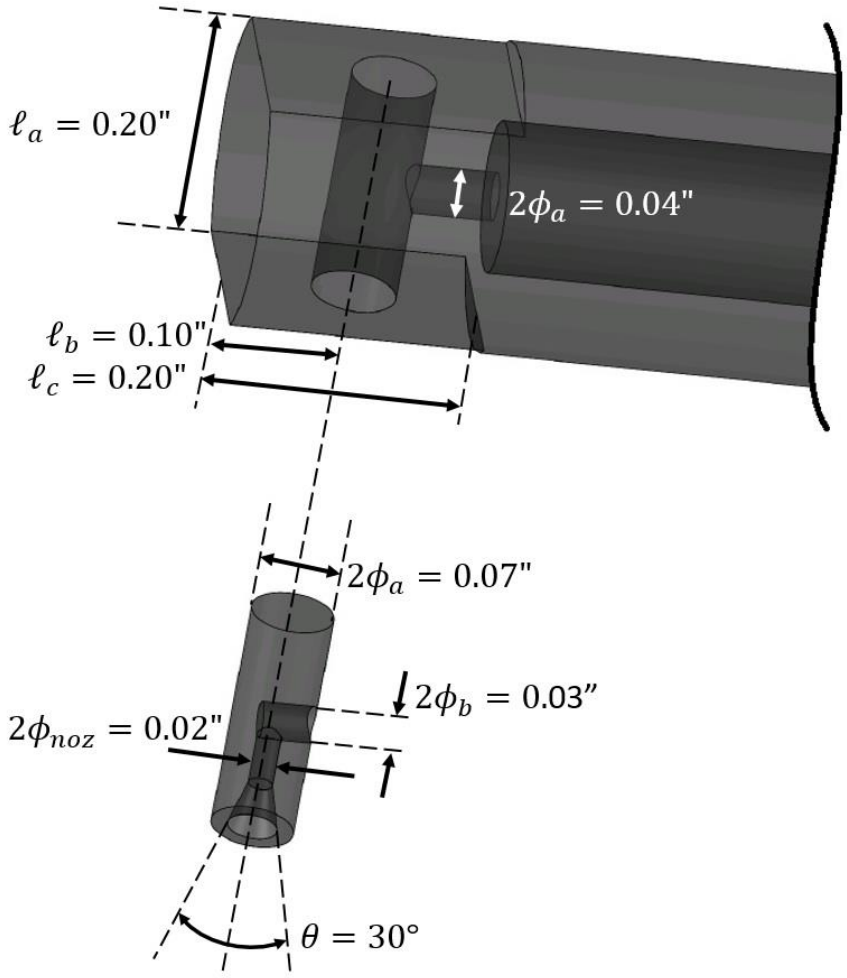

Figure 3 - 17: Rotor 2: Tip Dimensions

micron hole drilled through the center of this disc. The stainless steel disc was epoxied onto a $0.060''$ hole drilled perpendicularly through flats machined onto the end of the rotor, and felt very little centrifugal force because of its exceedingly small mass. The transition was made to the convergent-divergent nozzle due to the repetitive separation of the thin stainless nozzles from the rotor tip. The current design, as seen in Figure 3-17, features a cylinder made from the same aluminum alloy as the rotor and is press fit into a $0.070''$ hole drilled perpendicularly through flats machined at the end of the rotor. The cylinder is cross drilled to the center point from both directions creating a path for gas to escape from the hollow rotor and contains a divergent nozzle near the end of the cylinder as well. The nozzle is machined with a $30°$ single lip cutter (Celeritous Technical Services) to limit the beam angles of the emitted gas. Forces acting on the nozzle cylinder act in a direction that is perpendicular to the direction it is pressed into the rotor and thus will not result in it being dislodged as was the case with the thin stainless apertures.

The other end of Rotor 2, as seen in Figure 3-18, is tapped for a $8-32$ screw at least an inch deep. These threads are meant to hold an iron disc in place for positioning of the rotor. This positioning is accomplished while the chamber is under vacuum by a magnet attached to a rotatable and translatable positioning arm. The $8-32$ screw also holds the last section of the rotor in place that contains the setscrew. The setscrew is manufactured out of a $3/16-24$ bolt that has been heavily modified to meet the weight requirements of balancing. Threads on the balancing screw are wrapped with Telfon Tape to create a tight fit and prevent the screw from becoming dislodged due to high forces and vibrations. Sealing of the gas inside the rotor is accomplished by the $8-32$ screw holding the iron disc in place. It is important to compare the centrifugal forces on the threads to those forces required to break

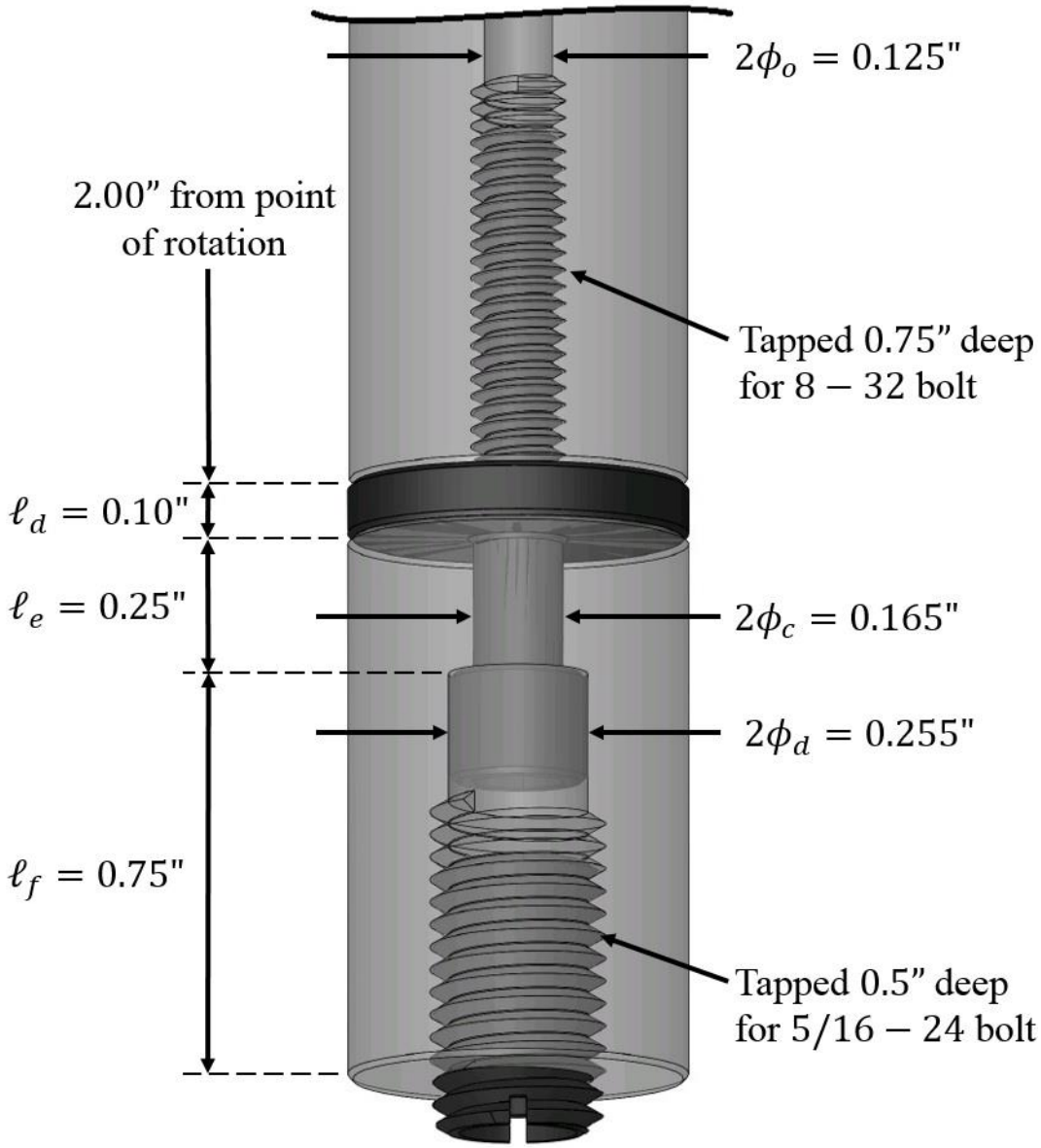

Figure 3 - 18: Rotor 2: Back Dimensions

the threads. Centrifugal forces are calculated as in Eqn 3.21 but the mass of the components must be added up. Masses are determined as:

1. 8-32 screw: density of stainless steel ($0.127\ kg/in^3$), mass of $2.2 \times 10^{-3} kg$
2. Iron disc: density of iron ($0.129\ kg/in^3$), mass of $3.6 \times 10^{-3} kg$
3. Iron disc: density of aluminum alloy $\left(0.046 \frac{kg}{in^3}\right)$, mass of $1.2 \times 10^{-2} kg$
4. 5/16-24 setscrew: density of stainless steel ($0.129\ kg/in^3$), mass of $1 \times 10^{-3} kg$

Which returns a total mass of $1.8 \times 10^{-2} kg$ for all the components mounted on the rotor. The center of mass for these components, determined by the built in feature of Solidworks, lies in the iron disc, or 2" from the center of rotation. With a rotational frequency of 350 Hz this point experiences $245{,}674\ m/s^2$ of acceleration and this produces 4,422 N of centrifugal force. This force is felt on the screw threads of the 8-32 bolt and must be smaller than the strength of the threads or the entire assembly will rip itself apart as it rotates at high frequencies creating a very dangerous situation for the users. The force required to break the threads is

$$P = T \cdot A_t \tag{3.34}$$

Where T is the tensile strength of the stainless steel screw, and A_t is the tensile stress area of the threads. The tensile stress area is

$$A_t = 0.7854 \cdot \left(D_{maj} - \frac{0.98743}{n}\right)^2 \tag{3.35}$$

Where D_{maj} is the major diameter of the threads, given as 0.164in for an 8-32 screw, and n is the number of threads per inch (32). For the bolt used here, $A_t = 0.0140\ in^2$, returning a force of $4919\ N$ holding the screw to the rotor. This value is very close to the centrifugal

force calculated for spinning the rotor at 350 Hz. Therefore, 300 Hz becomes the limiting frequency with which we can safely spin the rotor without risking catastrophic failure of the entire system.

For Rotor 1 only an 8-32 setscrew was installed in the end opposing the nozzle. This design incurs drastically lower forces due to the smaller mass that is loading the threads of the screw. The length of the back end of the rotor is calculated by balancing the weight on both side of the rotation point. For a 6" rotor this length is 3". A setscrew with mass $9 \times 10^{-4} kg$ held a distance of 3" from the point of rotation experiences an acceleration of $1.1 \times 10^{6}\, m/s^2$, and a centrifugal force of $972\ N$. This force does not limit the ultimate speed of rotation because it is 4 times smaller than what the threads can handle.

The rotor is mounted to the motor, as seen in Figure 3-19, by a 0.200" diameter stainless steel rod and a 0.025" thick aluminum sleeve. The rotor is machined to make this rod press fit into the rotor body, and the aluminum sleeve is machined to make the rod press fit into it as well. This sleeve is needed to fit the rod into the 1/4" mounting collet of the motor. Prior to press fitting the rod and shaft into place the rotor is filled with 1mm diameter glass beads to minimize the internal volume of the rotor. Once the rotor has been filled up to the shaft hole with beads then the rod can be press fit into place. The cross drilled holes in the rod are aligned with the through-hole drilled into the rotor body to allow for gas to flow. Different materials have been considered for the sheath in order to minimize heat conduction but ultimately aluminum was chosen for its high strength. The heat transfer from the motor was instead minimized by a large copper cooling block mounted directly to the upper bearing of the motor. The inner diameter of the stainless rod is drilled to a diameter of 0.100" to ensure very small clearance with the PEEK (Poly-Ether Eher Ketone) tube that is used by the

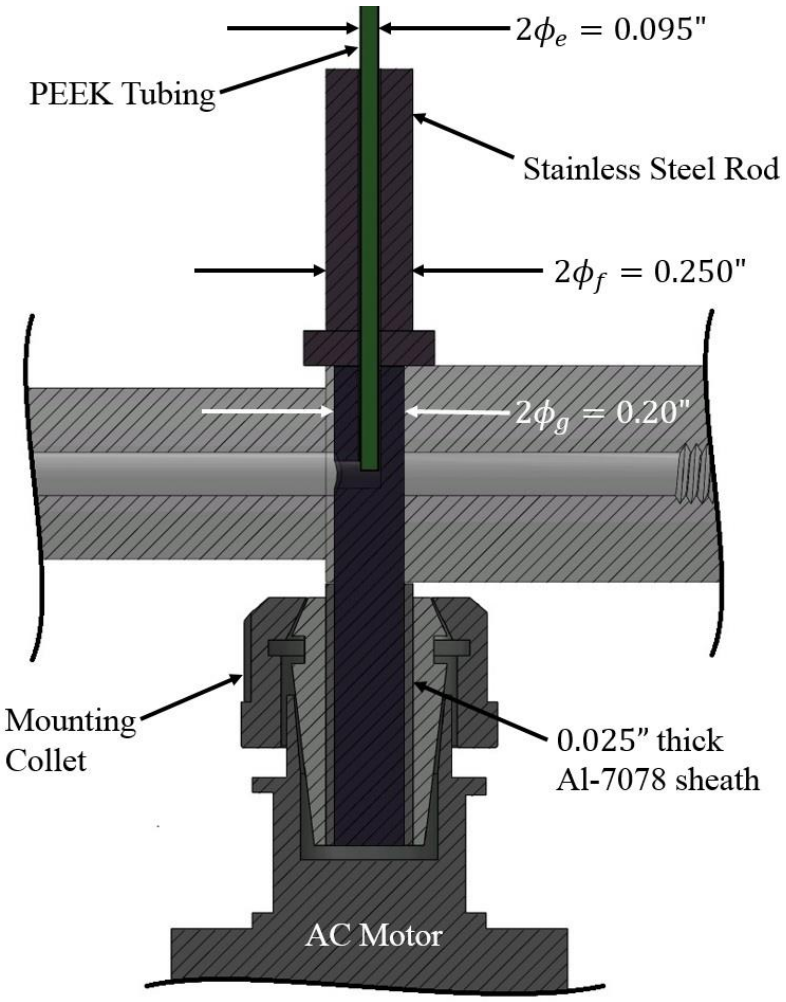

Figure 3 - 19: Rotor 2: Mounting Close-up

gas feed system. This prevents excessive gas from traveling back from inside the rotor to leak into the chamber. Any gas that did so would contribute to the background gas in the chamber and potentially scatter gas from the beam produced by the supersonic nozzle.

The upper diameter of the stainless rod is the same as the outer diameter of the aluminum sleeve. This allows for precision balancing across a set of pre-leveled razor blades. Balancing takes place by adjusting the setscrew until the rotor maintains its horizontal position when undisturbed, and actually regains this horizontal position when briefly pushed in either the upwards or downwards directions. This balancing procedure is repeated every time the rotor is removed to ensure that it is never spun at high velocities unbalanced. This unbalancing can also occur if the setscrew unthreads itself during rotation. Even a 1/8 turn of the setscrew results in an unbalanced outcome.

This current design of the rotor has been very successful at producing many beams of gas over the past 4 years. The first signal from our apparatus occurred on a simple 4" rotor in 2009, the new nozzle system was developed in 2010, the upgrade to the 6" rotor occurred in 2011, the rotor was filled with beads in 2012, the iron disc for magnetic positioning was included in 2013, and the rotor was completely rebuilt without the need of a setscrew in 2014. All the rotors that were constructed operated as expected and most were spun up to frequencies of 400 Hz.

Future rotor designs can increase the number of steps in the Gaussian profile to maximize the limiting peripheral velocity. The shape of the nozzle can be altered to increase the peaking factor which could lead to a larger pulse intensity. The sleeve which separates

the rotor mounting shaft from the motor collet can be constructed with an insulating material to minimize heat transfer from the upper motor bearing.

3.4.1 Motor Selection and Mounting

The motor used for this work is a G. Colombo, RA 90, Electric Spindle and this motor is driven by a Delta AC Motor Drive (VFD-VE Series). The primary considerations for motor selection are the frequency range, vibration during operation, high vacuum compatibility, and heat generation at the upper bearing.

The required frequency range of the motor is dependent on the length of the rotor, the gas being used, and the lab frame velocity being pursued. For example, a 6" rotor length requires between 300 Hz and 2000 Hz for the nozzle to reach molecular velocities of Xe and H_2 respectively. The current motor operates at frequencies up to 600 Hz and thus restricts the study of very slow lab frame gas beams to Xe.

Vibration produced by the motor should not propagate through the surrounding equipment to interfere with sensitive measurements. The motor is mounted, as seen in Figure 3-20, to a breadboard which is mechanically coupled to the gas detectors and the vacuum apparatus. Several Teflon spacers are used to mount the breadboard to the vacuum chamber. These spacers are intended to prevent the transfer of vibrational frequencies from being transmitted to the surrounding equipment.

Excessive outgassing of the motor would limit the ultimate vacuum achievable and thus the smallest signal measurable. This outgassing can come from incompatible materials or from high temperatures. The materials used to manufacture the motor are vacuum compatible but the temperature control is problematic in a high vacuum environment.

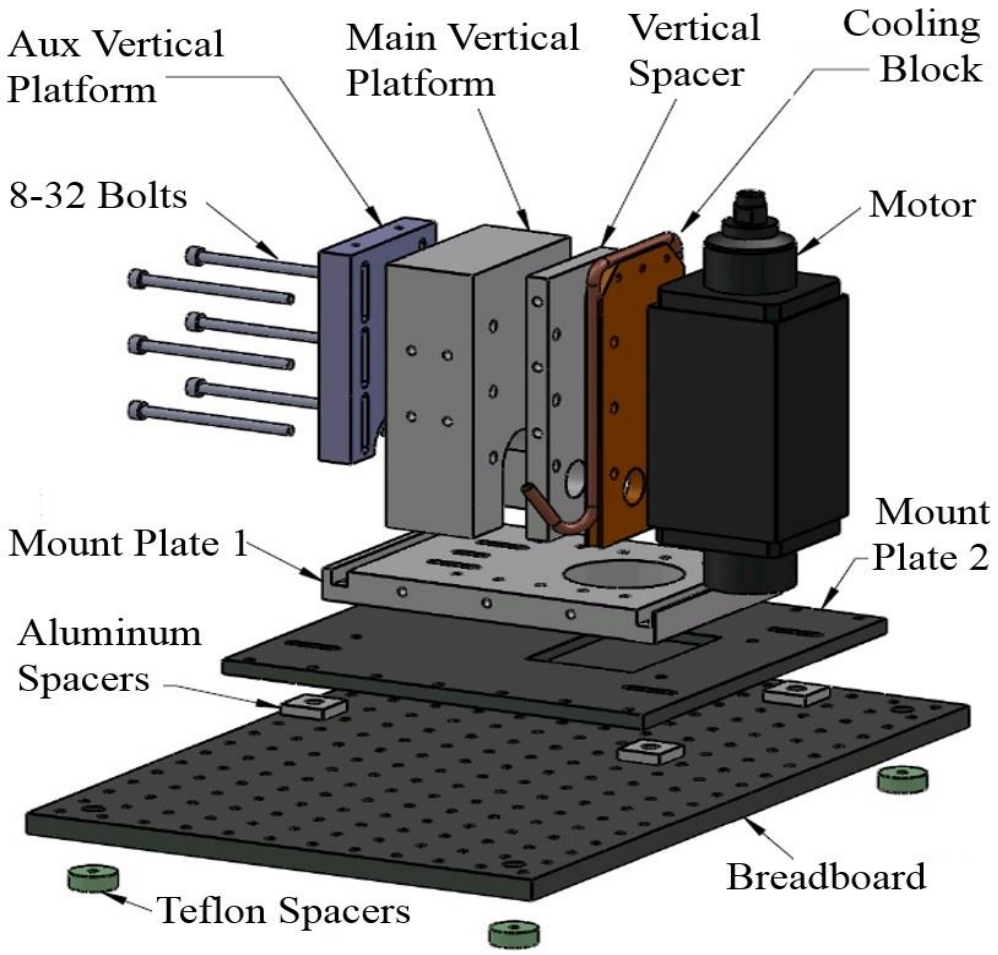

Figure 3 - 20: Motor Mounting Assembly

Towards this end the motor is water cooled, as seen in Figure 3-21, and a high quality vacuum grease has been used to replace the original factory grease in the motor bearings. This grease has a low outgassing rate even at the temperatures the bearings reach during high frequency operation. These efforts have reduced the outgassing of the motor significantly and the pressure in the main chamber does not exceed 2×10^{-7} Torr during high frequency motor operation.

Heat generation in the upper motor bearing is transmitted to the rotor though the collet and mounting shaft. The gas emitted from a warm or hot nozzle has a larger speed and thus requires higher motor frequencies. If the rotor is heated too quickly then slow lab frame velocities will be unachievable even for species with a large mass. To minimize this heat propagation the motor is fitted with two forms of water cooling. The first, a water cooled copper plate, is inserted into the mounting assembly directly between the motor and the rest of the assembly components. The second, a water cooled bearing cover, is placed around the upper motor bearing to minimize the heat transferred to the rotor directly. Both are shown in Figure 3-21.

3.4.2 Gas Feed System

Having completed the rotor development and chosen an AC motor to spin it at high frequencies, there is still the challenge of feeding gas into the rotor. A perfect feed system would withstand the high speeds of rotation while generating very little heat and maintaining a perfect gas seal. The seal also needs to be durable enough to withstand slight vibrations of the rotor that occur during high speed rotation. Gas Feed System 1 (GFS 1) was designed specifically to address these challenges. However, several recent attempts have been made to address the inadequacies of GFS 1. This section will begin by describing GFS 1 and then

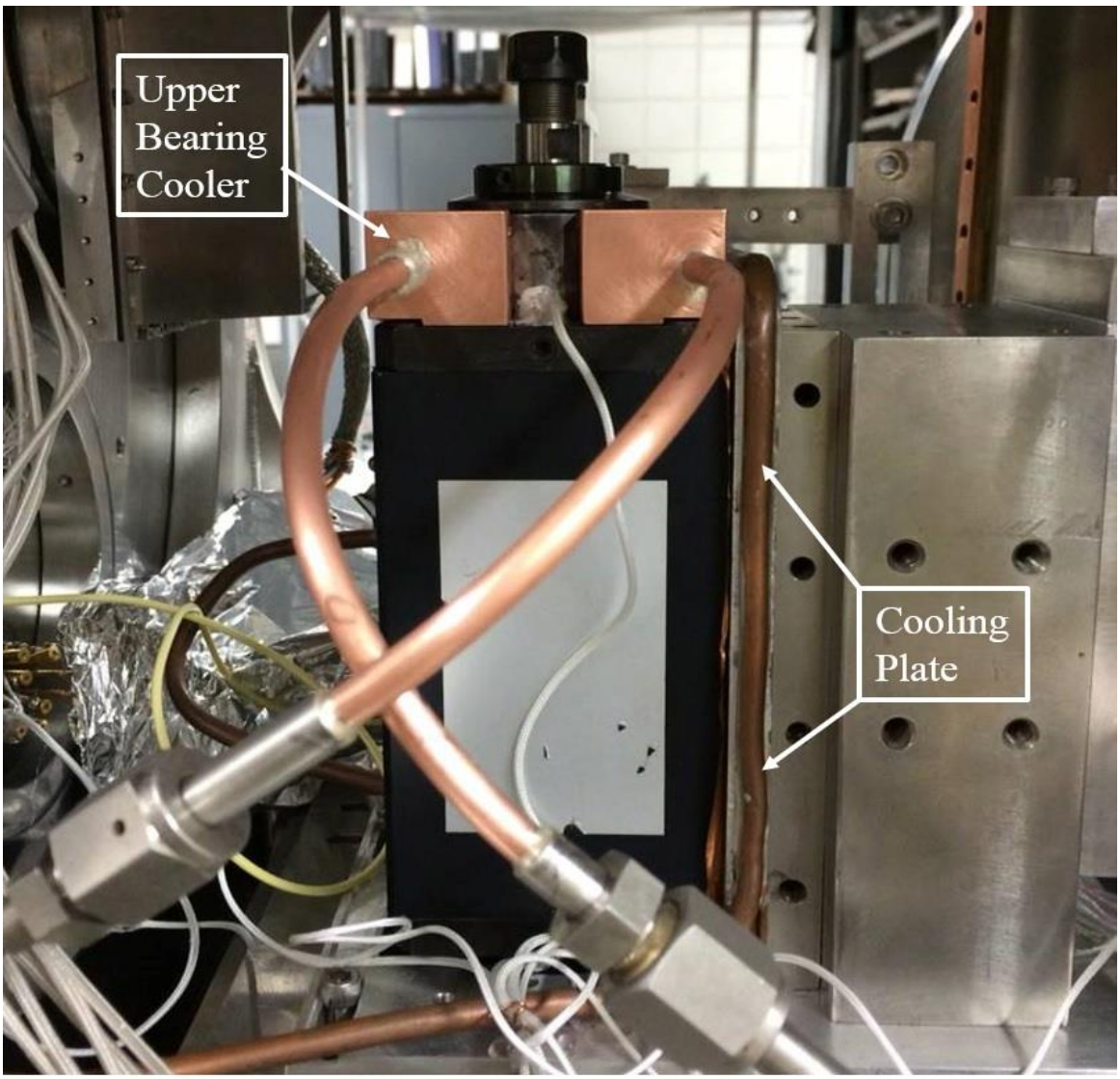

Figure 3 - 21: Motor Cooling Assembly

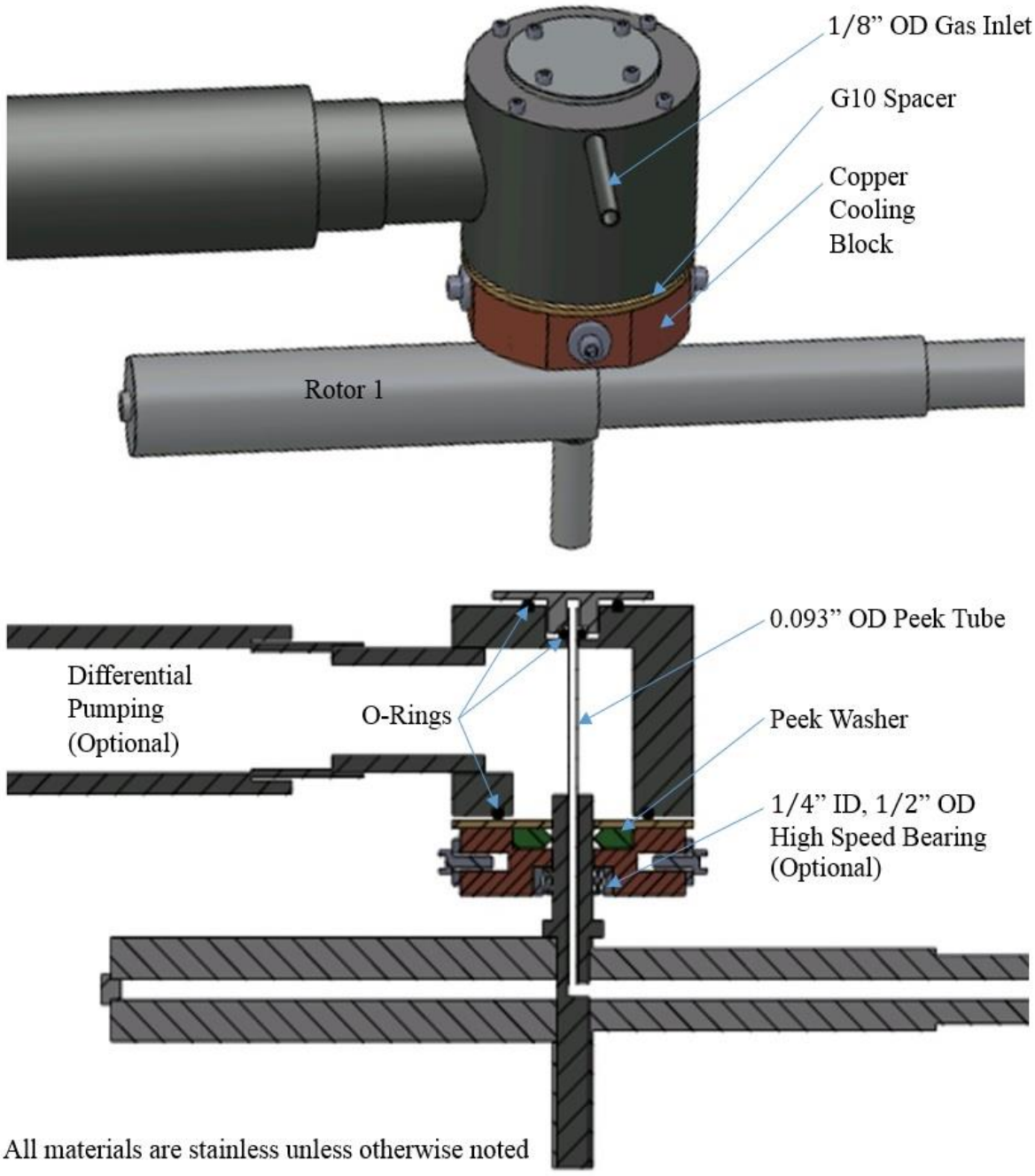

Figure 3 - 22: Gas Feed System 1

progress through each subsequent design. Rotor 1 and Rotor 2 used GFS 1, Rotor 3 used GFS 2 through 6a, and Rotor 4 used GFS 6b which is the most modern iteration of the feed system. This large number of designs for an auxiliary system signifies its importance in the overall success of the experiment.

While the feed system cannot prevent background gas from building up in the main chamber, due to the rotor emitting gas in all 360 degrees of rotation, it can lower the backing pressure behind the nozzle significantly which prevents the detection of very low density beams. Since this is the primary goal of this research, all efforts have been made to design a system that attains a large backing pressure behind the nozzle. Lowering of the backing pressure can occur due to excessive gas leakage between the rotor stem at high frequencies and the nonrotating components of the feed system. A small tolerance, usually 0.002" to 0.005", between nonrotating and rotating components is included to prevent rubbing. If contact occurs the friction at high frequencies will easily cause the temperature to rise above the melting temperature of PEEK, or 350° C. This is important because many components of the various feed systems utilized PEEK.

Gas Feed System 1, seen in Figure 3-22, was designed in 2007 and considered to be a major improvement over the original velocity augmentation experiment. The system works by utilizing a pulsed solenoid valve as described in Section 3.3. This valve actuates sending gas into the upper region of the stainless steel feed enclosure. This upper region is sealed by Viton O-rings and directs the gas into a thin PEEK stinger. Once in the rotor the pressure builds behind the nozzle until the valve closes which is between 1 and 10 msec. As pressure builds the gas enters the viscous regime and conductance parameters can be used to characterize the behavior of the system. As can be seen by Table 3-4 the conductance

Component Name	**Length**	**Radius**	**Conductance**
Thin Wall Orifice (R1)	0.001”	50 μm	6.4E-5
Nozzle Throat (R2 and up)	3mm	0.2 mm	5.41914E-4
Rotor Shaft	6 in	.0625”	4.13798E-5
Rotor Stem (R1 and R2)	1.2 in	0.05”	1.04167E-4
Rotor Stem (R3 and up)	1.2 in	.0625”	2.03451E-4
PEEK Tube	2.5 in	.06” ID	8.64E-5
Rotor Stem and PEEK Washer 1	0.25 in	0.250” ID 0.255” OD	0.00191
Rotor Stem and PEEK Washer 2	0.25 in	0.250” ID 0.260” OD	0.0039
Rotor Stem and PEEK Washer 3	0.25 in	0.250” ID 0.265” OD	0.00597

Table 3 - 4: Conductance Estimates for Feed Components

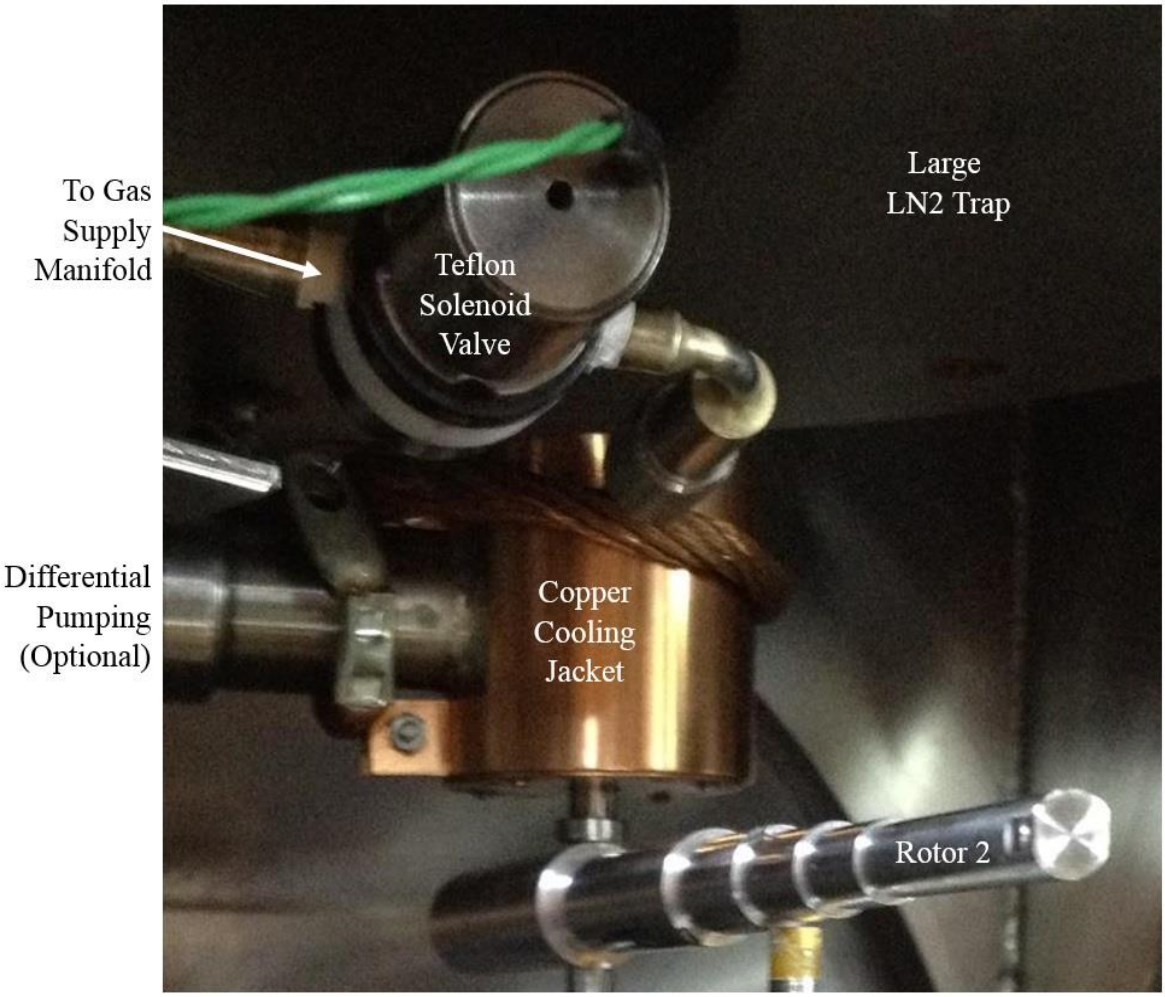

Figure 3 - 23: Rotor 2: with Gas Feed System 1

through the PEEK stinger is small compared to most other values due to its very small radius and long length. This conductance limits the performance of the rotor and the PEEK stinger is removed in subsequent versions of the feed system.

The primary advances from the original design are the addition of a pulsed valve to supply gas to the rotor and the ability to differentially pump the internal volume of the gas feed enclosure. Other optional features tested over the years focused on removing heat generated by friction and aligning the feed enclosure with the rotor. These features include:

- Including a ¼" ID high speed bearing in enclosure base to prevent misalignment
    - Only attempted once and resulted in excessive noise and vibration
- Remanufacturing enclosure base out of copper to remove heat
    - As seen in Figure 3-23
- Direct LN2 cooling of enclosure base
    - Only attempted once
- Direct LN2 cooling using cooling jacket
    - As seen in Figure 3-23
- Including G10 spacer to minimize thermal transport
    - As seen in Figure 3-24
- Utilizing Stainless Steel Valve
    - As seen in Figure 3-25
- Utilizing Teflon Solenoid valve for corrosive gasses
    - As seen in Figure 3-23, and 24
- Precision alignment of feed enclosure

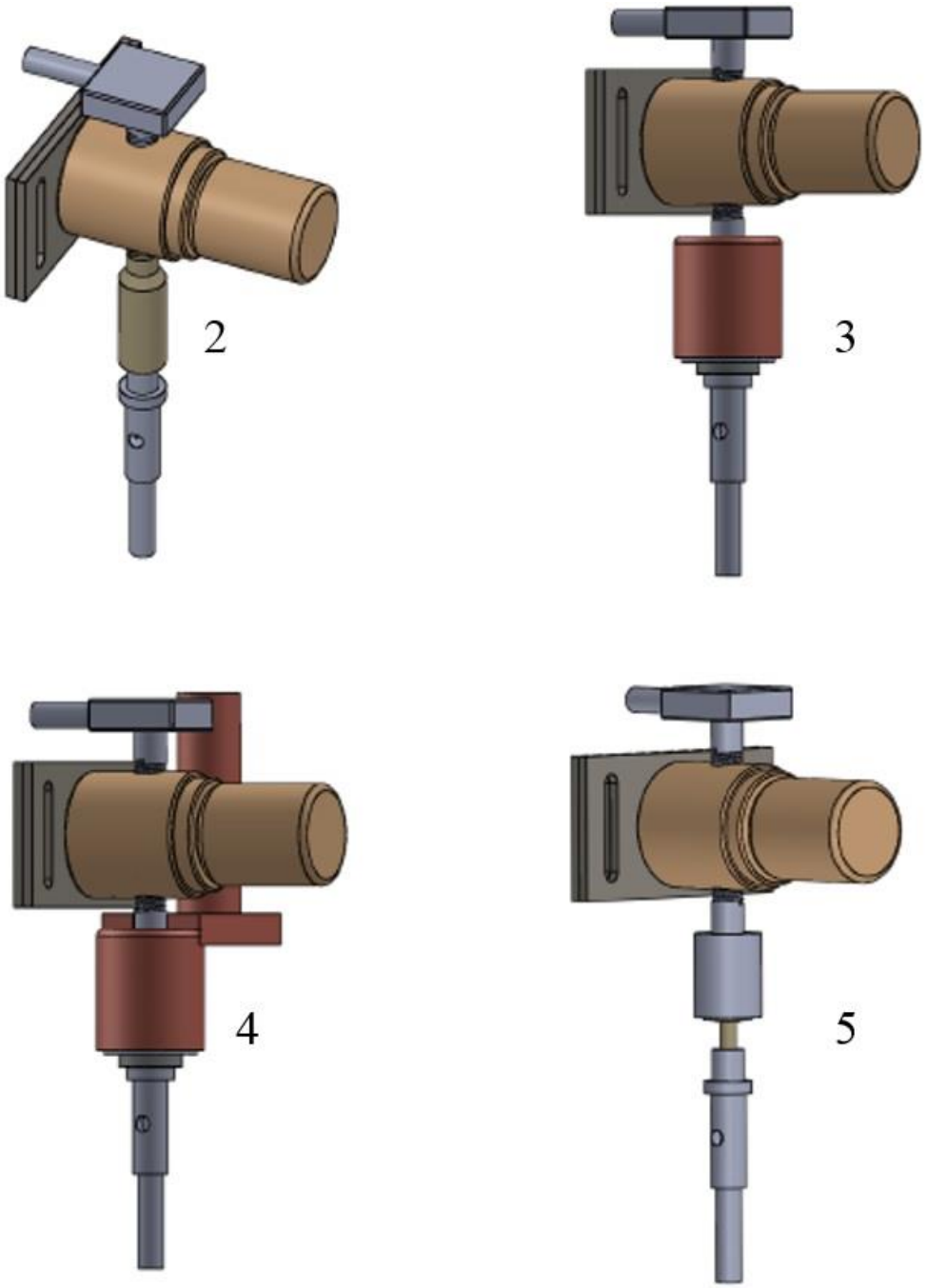

Figure 3 - 24: Gas Feed Systems 2-5

The initial testing of the differential pumping system showed that the background did not rise before the pulse train from the rotor began. This pre-emptive rise in background pressure would indicate that gas leaked around the feed system, into the main chamber, and into the detection chamber before it appeared from the nozzle as a gas beam. Ultimately, the differential pumping only effected the background pressure at much later times than the pulses under analysis, and the differential pumping idea was abandoned after a few weeks of testing.

Gas Feed Systems 2-5 are shown in Figure 3-24 and all attempted to simplify the entire system considerably. Initially by reducing the entire assembly down to one single piece of PEEK connecting the Teflon solenoid valve directly to the rotor stem. By moving the valve much closer to the rotor stem a large volume is removed and the effective pressure behind the nozzle should increase. In order to maximize the conductance to the nozzle the rotor stem was bored out to 1/8" diameter.

Gas Feed System 2 consisted of an inner PEEK stinger and an outer PEEK sheath. Tolerances between the rotor stem and the PEEK stinger/sheath was within 0.001" and this turned out to be its downfall. During high speed operation the temperatures reached in the rotor stem melted the PEEK and effectively plugged the feed line. Thus, only one partial data set was taken with GFS 2. There was enough data to indicate a drastic improvement over GFS 1 and during this time a foil shield system was being implemented to reduce scattering. Combining the effects of both improvements resulted in a very low background signal with a narrow time distribution and no double peaks at any frequency.

Gas Feed System 3 and 4 contain an aluminum enclosure with two high speed bearings that were intended to align the feed system with the rotor stem. The only difference

between the two is that GFS 4 was attached to the LN2 trap during the run so it could be actively cooled by filling the trap. Each of the designs only lasted at high frequencies for a very short amount of time and then the bearings failed.

Gas Feed System 5 attempted to solve the problem of coupling gas into the rotor by using two very small high speed bearings that seal onto a PEEK stinger. The PEEK stinger is then glued directly onto the rotor stem preventing any gas leakage. The bearings have 1/8"ID and 1/4" OD and are contained in a PEEK Enclosure that screws directly into the Teflon solenoid valve.

Initially these failures were thought to be due to a misalignment when mounting the feed system. Later the problem that destroyed GFS 3, 4, and 5 became apparent: a rotor stem that does not run true. This means that the rotor stem itself is bent and carves out a large path during one complete rotation. It is no surprise then that the bearings failed at high frequencies with such a problem. This has been a recurring trend which may be attributable to a misbalanced rotor, large vibrations in the motor, or any type of impact with the rotor while spinning. As can be seen

Gas Feed System 6, seen in Figure 3-25, was a complete redesign of every component of the feed system. The slotted plates visible in Figure 3-24 are replaced with a water cooled copper block containing several tapped 6-32 bolt holes. A T-shaped copper mounting stage is bolted onto this block and serves as the basis for future feed systems. To complete the assembly an aluminum clamping ring is installed using 4-40 bolt holes tapped into the mounting stage. This structure is much more rigid than the slotted plates utilized in GFS 2 through 5.

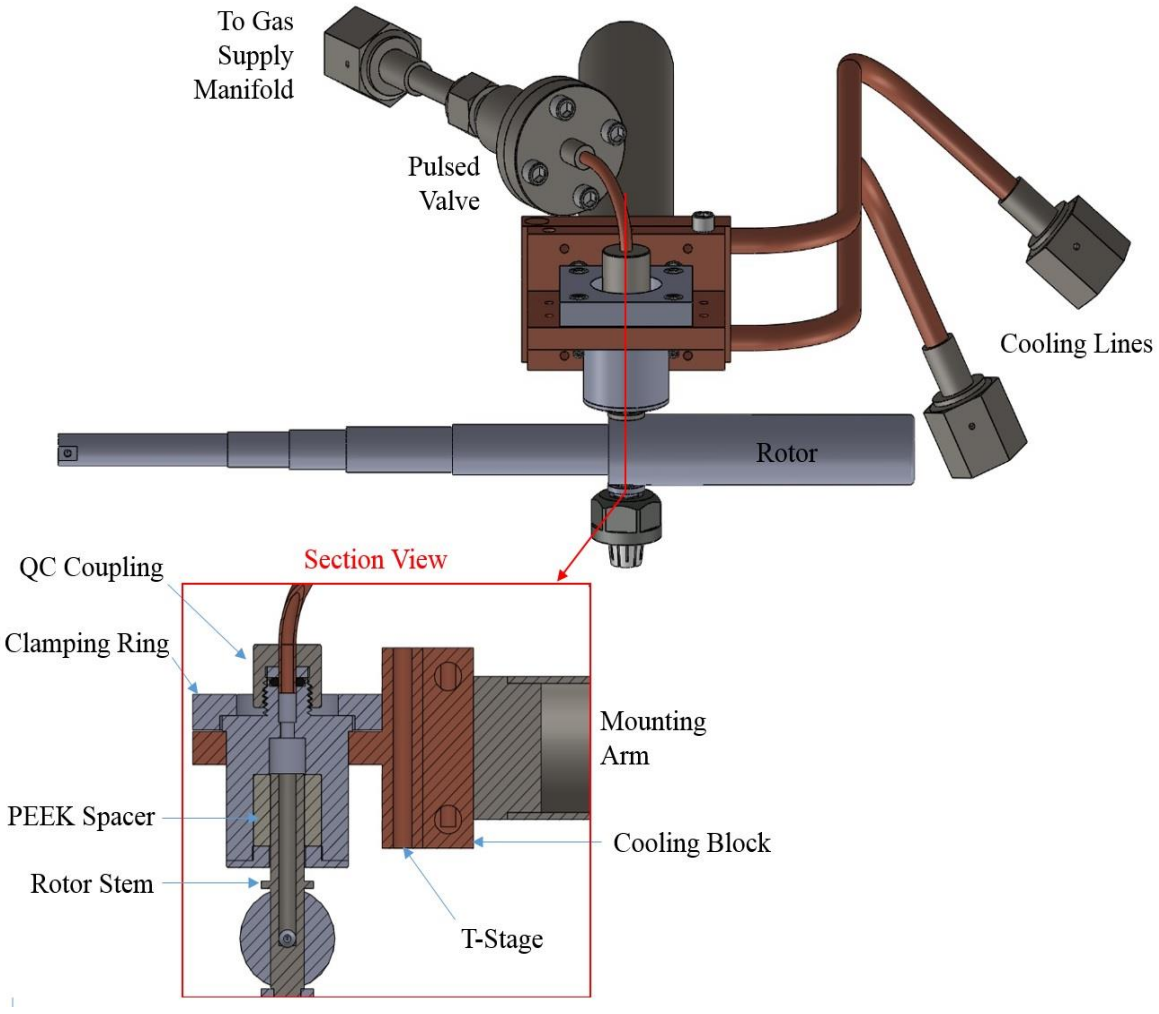

Figure 3 - 25: Gas Feed System 6 - Schematic

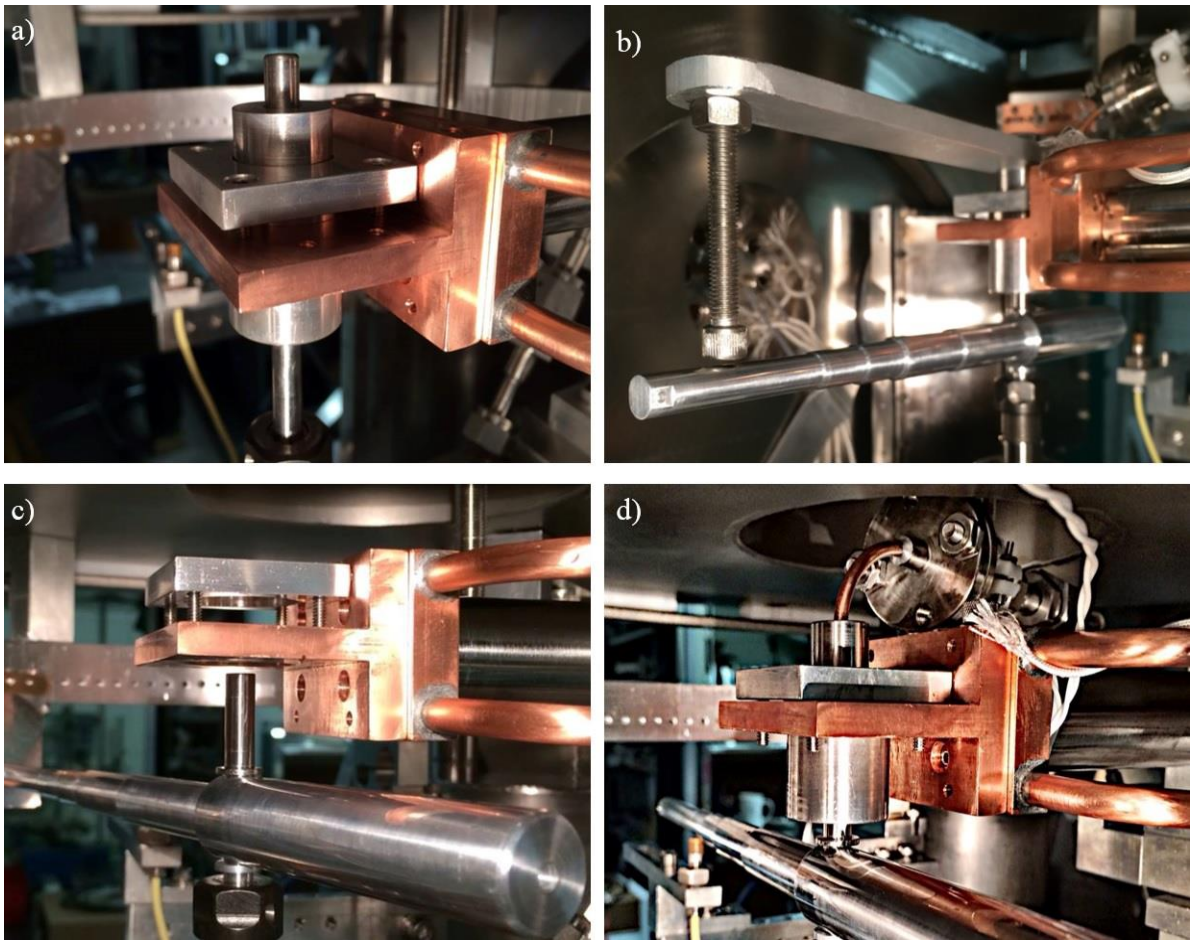

Figure 3 - 26: Gas Feed System 6 - Alignment

Considering the trouble encountered with the previous feed systems it makes sense to proceed with caution and verify all components are as precisely aligned as possible. Towards this end, angular adjustments were added to the feed system mounting tube using setscrews and stainless steel shims. This along with the X and Y translation stages allow the T-shaped copper mounting stage to be aligned utilizing the techniques seen in Figure 3-26a and Figure 3-26b. In these photos the mounting stage is centered over the motor collet using a ¼" stainless steel rod, and the tilt of the mounting stage is measured and adjusted by rotating the rotor and measuring bolt around 180°. As seen in Figure 3-26b, if the gap between the measuring bolt and rotor changes then the setscrews can be adjusted and the tilt angle improved. This process is repeated several times before the stage is considered completely aligned. In addition, alignment verifications are performed anytime the system is disassembled.

Once the rotor and the mounting stage are both aligned the final component of the feed system is installed: the feed enclosure. It is seen in Figure 3-26d with Rotor 3. This enclosure contains a PEEK washer to seal on the outside of the rotor and a 1/8" quick connect coupling that adapts to the gas supply line from the solenoid valve. This enclosure slides directly into the mounting stage and is bolted down by the aluminum clamping ring.

The tolerance between the feed enclosure and mounting stage is very small, typically less than 0.001". This is such a critical parameter because anything mounted directly onto the stage will be effected by this positioning error. By reducing the error as much as possible the distance can be minimized between the rotor stem and the PEEK washer. To be clear, the only path for gas to escape the feed system is between the rotor stem and PEEK washer. By

minimizing this leakage the backing pressure behind the nozzle can be increased without increasing the pressure in the supply line.

The primary advantage of GFS 6 is its easy accessibility and the simplicity of disassembly and reassembly. The clamping ring holds the feed enclosure in place and with its removal the entire system quickly slides apart. Previous designs required complete realignment after disassembly and offered no real means to verify the alignment was correct other than attempting a complete data run.

Future gas feed designs should attempt to improve one of the three main objectives of the system: reducing heat generation, preventing gas leakage, and minimizing internal volume. While current designs have considered these objectives throughout the construction process, there has been considerable focus on ease of use and ease of replacement as well. I will proceed through these objectives and consider how future designs can improve upon each.

The internal volume can be minimized by using a compact solenoid valve and mounting it very close to the rotor stem itself. Reducing the length of the rotor stem will also satisfy this aim. The absolute minimum volume possible in the feed system is if the valve was placed directly at the entrance to the rotor shaft. This defines the absolute minimum internal volume of the feed system which is $0.0736\ \text{in}^3$. Current designs did not focus on this objective entirely because limited space above the rotor preempted the installation of the solenoid valve in the appropriate position.

The minimization of heat generation seeks to remove any contact which may exist between the rotor and stationary components while the minimization of gas leakage attempts

to reduce the gap as much as possible. To satisfy both requirements the outer surface of the rotor stem must be precision machined and very smooth and the inside of the PEEK washer should be precision machined as well with a very smooth inner surface. If both dimensions are correct and the feed system is well aligned then there will be very little heat generation or gas leakage. Future designs should seek methods which allow higher precision in the feed system alignment as well as better precision when machining the critical components. This includes the possibility of electroplating of the stainless components to reduce the surface roughness or incorporating a more elaborate approach to aligning the copper mounting block and feed enclosure itself.

3.4.3 Position Detection

In order to measure the time of flight (ToF) of gas emitted along the beam path the rotor position must be marked once per rotation. The signal should preferably coincide with the actual line-of-sight between source and detector. However, due to the inherent difficulty of exact positioning of the marking device, a frequency dependent correction term is added to this value during data processing. Its time resolution of the position detection system must be at least sub-microsecond due to the high speed of rotation and large need for accuracy. The location signal is recorded simultaneous to the gas detector output on a second channel available in the high speed data acquisition card utilized for data collection. Two methods have been utilized to accomplish this goal of marking the position of the rotor.

The original system utilized a 5mW green laser pointer and a photodiode to mark the location of the rotor. The laser itself is mounted outside the vacuum chamber and shines through an optical feedthrough and into the chamber where it is incident on Mirror 1, as seen in Figure 3-27. The laser light then travels through the plane of the rotor, reflects off Mirror

2, and finally out of the chamber through another optical feedthrough to where the photodiode is mounted. The rotor will only block the laser for a short time but during that time the photodiode output voltage is reduced to zero. This signal from the photodiode is inverted and offset in a small circuit to produce a zero signal that rises to a positive value instead of a constant signal that drops to zero.

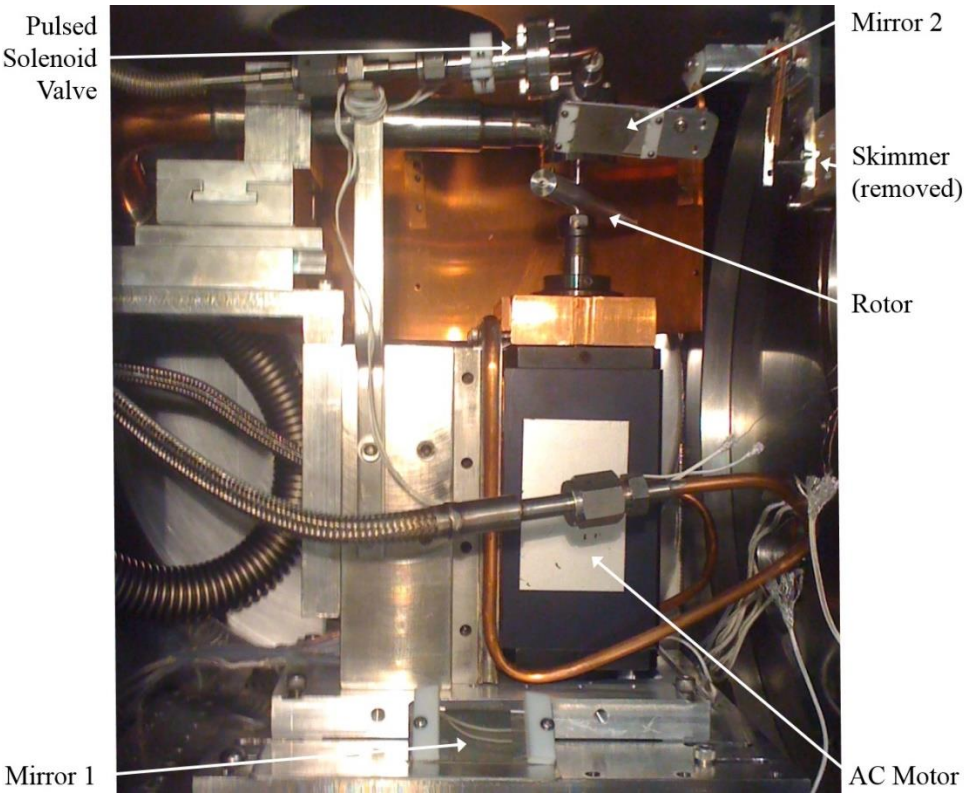

Figure 3 - 27: Rotor Detection with Photodiode

The original system was replaced due to difficulties experienced during high frequency operation of the AC motor. The difficulties were due to the fact that the laser,

photodiode, and mirror 2 are all mounted on adjustable arms that are each susceptible to vibrations at different frequencies. These vibrations shift the position of the outgoing beam and since the photodiode has a relatively small sensitive area, when the laser light shifts, the signal fades to nothing very quickly.

The method currently in use is an eddy current sensor (Proximitor, Bentley Nevada) which generates an output voltage proportional to the distance between the sensor and the nearest conductive surface. This technology has been extensively developed for its primary use which is vibration monitoring in turbo machinery applications. The probe, seen in Figure 3-28, is placed within 1 mm of the plane of the rotor to maximize the signal produced by the rotors motion. Unlike the original method, the Proximitor is insensitive to the vibrations from the motor. The output is described by a scale factor which for this model is 200 mV/mil. The output of the device is shown in Figure 3-29 and the signal shows very little noise due to vibration or electrical interference. Even at high frequencies the positive identification of the rotor position is possible with this data.

To make rotor marking easier for frequencies beyond 400 Hz the position of the sensor should be moved closer to the motor. Due to the rotors staggered cylindrical shape it has a larger diameter closer to the motor and will create a larger profile in the Proximitor output. Also, the sampling speed of the data acquisition can be increased to better sample the device.

3.5 Movable Shield

The next component in the experimental setup is the movable foil shield. The purpose of this system is twofold. On one hand, particles that travel from the rotor in the radial direction can

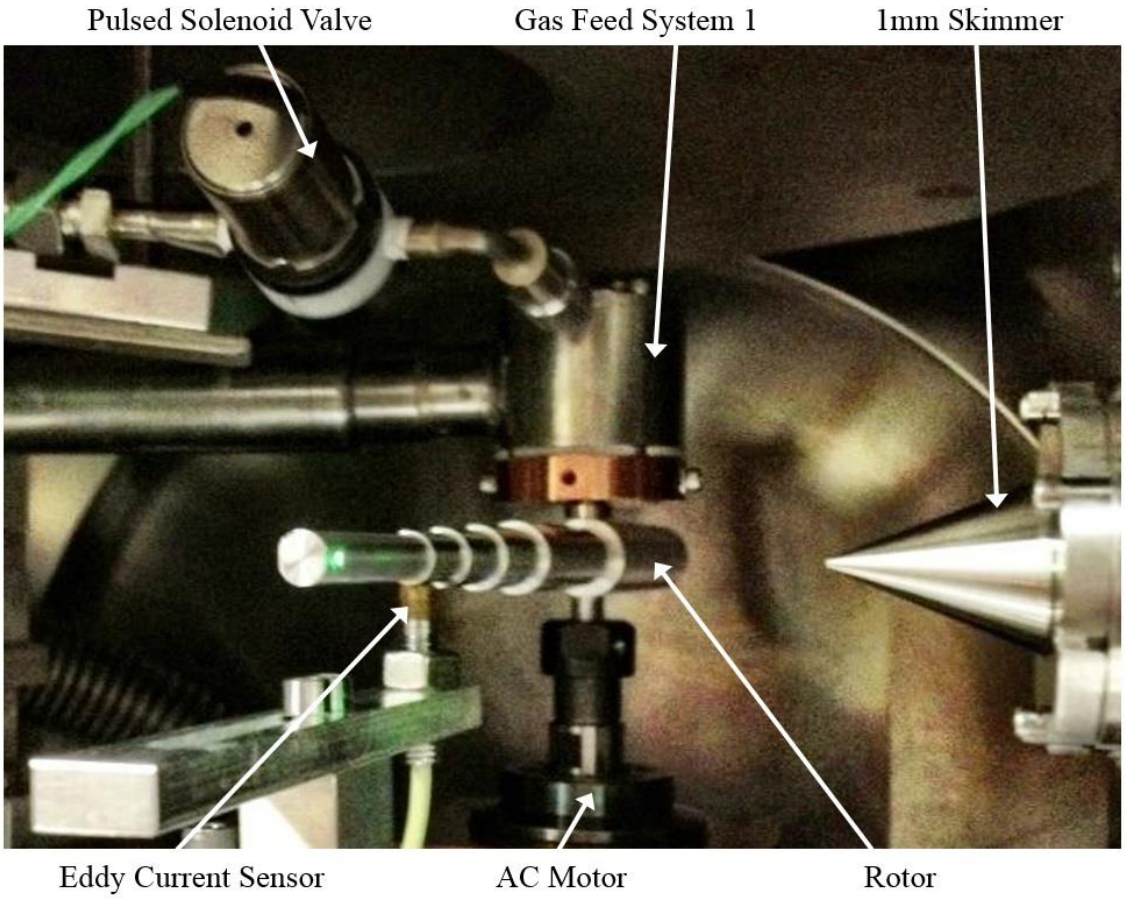

Figure 3 - 28: Rotor Detection with Eddy Current Sensor

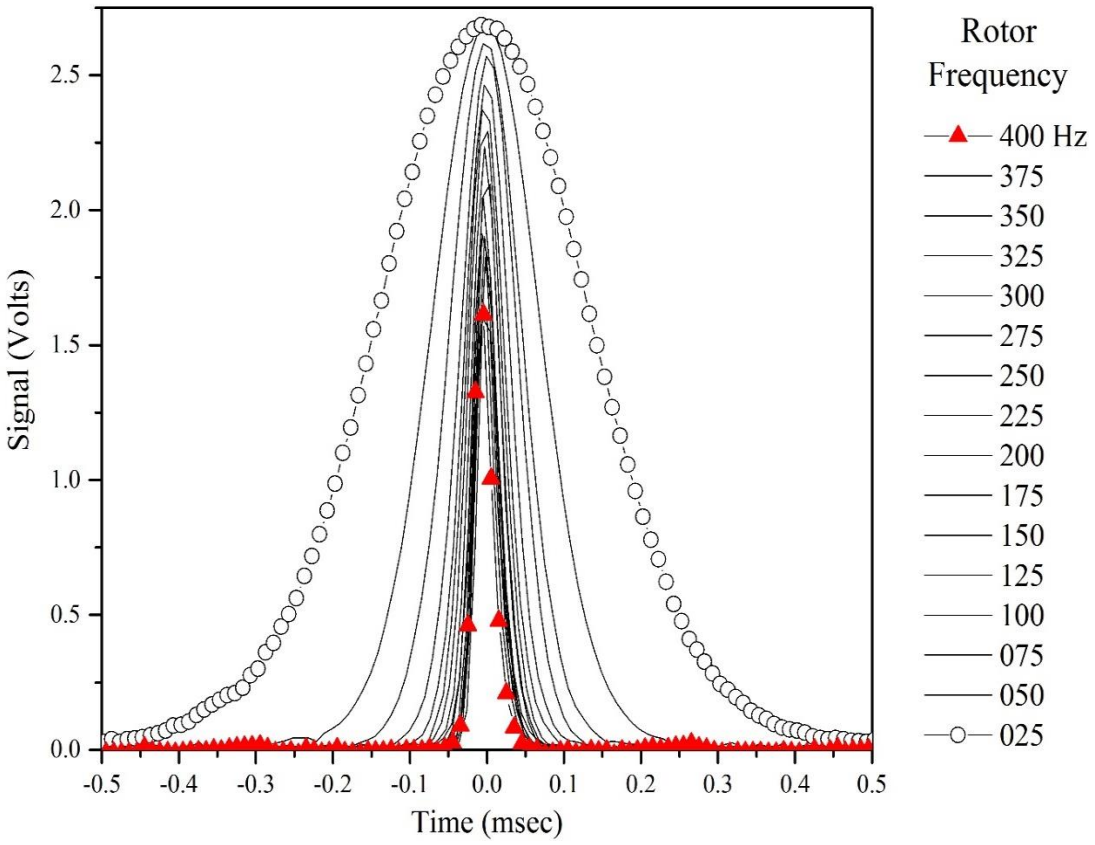

Figure 3 - 29: Proximitor Signal vs Rotor Frequency

scatter directly off the outside edge of the skimmer and be directed into the detection region. This results in the 'shoulder' occurring either before or after the main peak depending on the direction of rotation. This radial beam can occur due to gas leaking through the feed system, traveling down the length of the rotor, and being scattered by the rotor itself. Now when the gas has a very long time of flight, and the rotor has a very short period, the rotor can come back around a subsequent time and scatter the original pulse before it reaches the skimmer. This scattering will occur more prominently when attempting to slow species that have a smaller mass, i.e. larger flow velocity. These species require much higher rotational velocities to approach $50\ m/s$ final lab frame velocity. The higher rotational frequency means the rotor period is going to be much smaller and the slowest attainable beam will be faster than those achieved with a larger mass, i.e. smaller supersonic flow velocity.

The movable shield has seen three generations in a matter of a few weeks. The first

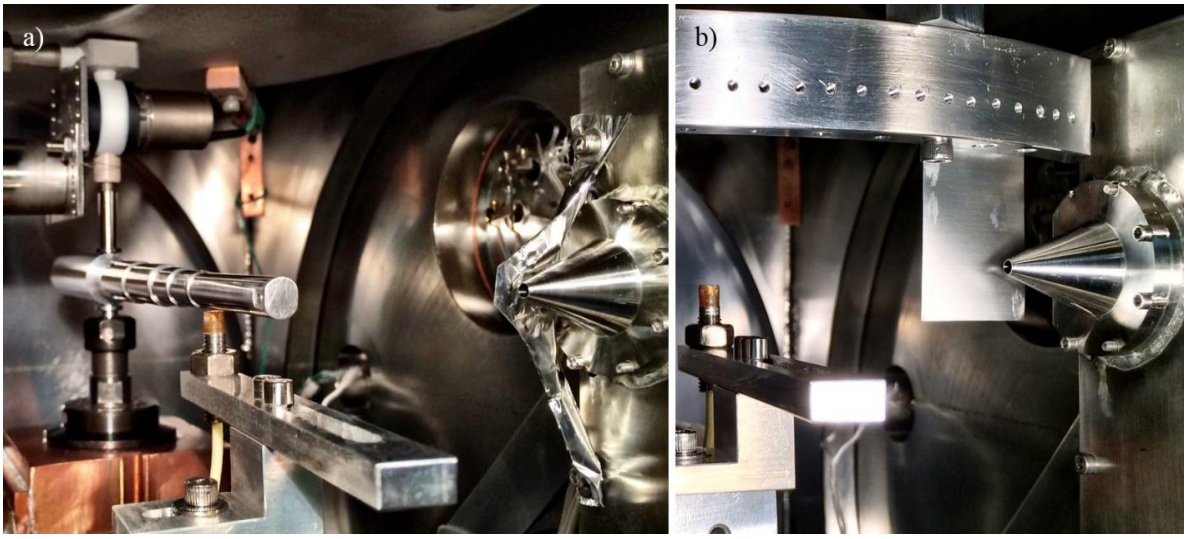

Figure 3 - 30: Foil Shield 1 and 2

version was made of a piece of aluminum, trimmed down with scissors, and finally installed on the skimmer mounting bolts. This shield, as seen in Figure 3-30a, did not completely prevent the shoulders from appearing on the main peaks but it did change the produced beam dramatically. Unfortunately the feed system was destroyed and rebuilding it took two weeks. In this time a second version of the shield system was planned and built. This second version, seen in Figure 3-30b, involved mounting a rail with an inner radius matching the length of the rotor. To this rail a piece of aluminum foil is attached which protects both the outer edge of the skimmer and the beam path from gas which may scatter the beam or scatter into the detection region. This second version completely transformed the beam produced by the rotor. It changed the geometric conditions defining the beam and the final product which can be systematically analyzed.

The problem encountered with the second version of the foil shield is that there was no way to tell where the ideal position of the shield was. Every adjustment of the shield position corresponded to a unique set of geometric conditions which produced a unique set of beam characteristics. Once this was realized a movable mechanism was proposed that would allow for the shield positions to be scanned while the system was under vacuum. This movable system would allow for the optimum position of the shield to be determined over a sequence of measurements prior to scanning a complete set of frequencies.

The moving shield configuration, seen in Figure 3-31, uses the same shield geometry as the previous version but instead mounts it on an aluminum block that slides along the upper rail. Since the block and the rail are both aluminum a stainless steel shim is inserted between them to prevent binding and allow smooth operation. The block is limited to about 2” of travel along

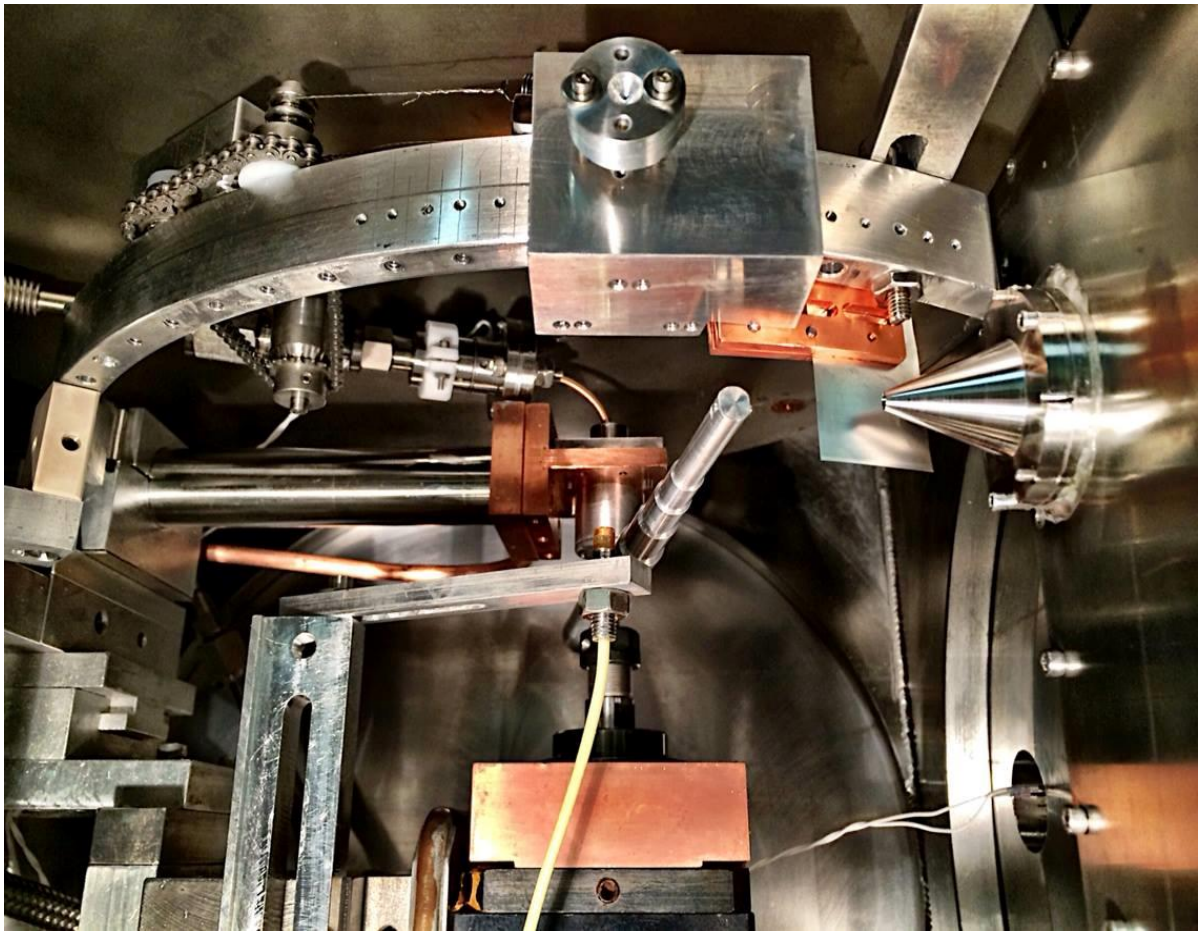

Figure 3 - 31: Movable Shield Configuration

the upper rail. When the shield is in the far right position the rotor beam is completely blocked and the skimmer is exposed. This will allow the 'double' peak to be produced without any main peak. When the shield is in the far right position it has no bearing on the geometric conditions determining the beam characteristics and in fact the purpose of the shield can be verified when further modifications to the rotor system bring its usefulness into question.

The mounting block is held tight on the rail by two rollers on the back side and a spring loaded ball bearing on the front. The horizontal line engraved on the upper rail, as seen in Figure 3-31, is where the ball bearing comes into contact with the upper rail. The spring can be adjusted by tightening the bolts visible on the front of the mounting block. It must be tightened enough to prevent any backlash in the shield position from ever occurring. It must be assumed during final construction stages that the rotor will be in very close proximity to the shield and it will be spinning at a very high rate. Several shields were destroyed right in the middle of an experiment due to this backlash. These events are frustrating due to the 2 hour process required to fill LN2 traps, degas filaments, warmup motor oil, and finally begin data collection!

A rotatable feedthrough is mounted on the top of the chamber and is aligned with the center of the large donut shaped LN2 trap occupying the top of the chamber. It is customized with an extra O-ring to allow for the up and down movement of the sealing surface as well as precise rotational movement. At the end of the shaft protruding through this feedthrough is the gear seen in Figure 3-31. This gear is 1" in diameter and contains 16 teeth. Three identical gears make up this gear assembly. The farthest gear to the left is used to apply tension to the chain. It is mounted on a swing arm and once released allows for the easy

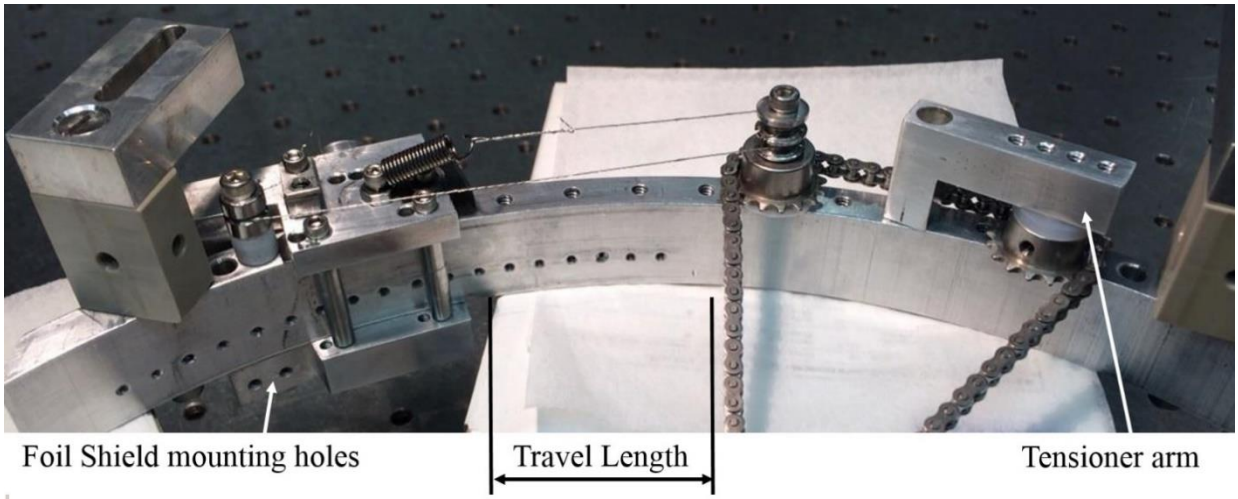

Figure 3 - 32: Upper Rail Assembly

removal of the entire assembly. Double checking the tension on the chain is required prior to using the rotor.

The final gear in the assembly has a Teflon spacer between it and the aluminum upper rail to allow for easy rotation. It transfers the force to a double pulley system which controls the positioning of the mounting block. From the perspective of Figure 3-32, the braided stainless steel wire is first clamped to the left side of the mounting block and then wound around the leftmost pulley. Then it crosses the length of the assembly and is wound around the right pulley which contains a locking crevice. Finally the wire is hooked onto the spring attached to the right side of the mounting block. The spring keeps the wire taught at all times and the locking crevice in the double pulley forces the wire to rotate with the gearing assembly.

Future versions of this system might include a lower rail assembly which will hold the foil shield from both sides. This double clamping will prevent any oscillations from

resonating through the shield which may cause enough displacement to contact the rotor. The closer the tolerance that is needed with the rotor the more of a problem these vibrations will become.

3.6 Beam Detection

To complete the experimental setup a method by which to measure the beam is needed. An ideal detection scheme is easy to implement, sensitive to all molecular species, and provides accurate density information. The detector components should be compatible with a high vacuum environment and the devices should be easy to install and relatively compact. To satisfy these requirements time of flight ionization spectroscopy seemed well suited. It is also one of the cheapest forms of gas detection currently available.

The ionization gauge (Beam Dynamics, FIG-1) used in this experiment, as seen in Figure 3-33, was chosen because it is very durable and sensitive to all atomic and molecular species. The gain of the device is fully controllable over 4 orders of magnitude allowing a broad range of beams to be produced and measured from high pressure supersonic beams to low pressure effusive beams.

Since Beam Dynamics no longer manufactures ion gauges a complete reconstruction of the device was required. Two devices were ultimately manufactured, as seen in Figure 3-33, to allow for precision velocity measurements which require multiple beam detectors. Having two functioning devices aids tremendously in troubleshooting a malfunctioning device. The primary difference between the two devices is the direction of the wiring connector. FIG-1 is the unit with the connector in line with the body of device, on the right side of Figure 3-33, and FIG-2 has a connector at a 90 degree angle to the body of the device,

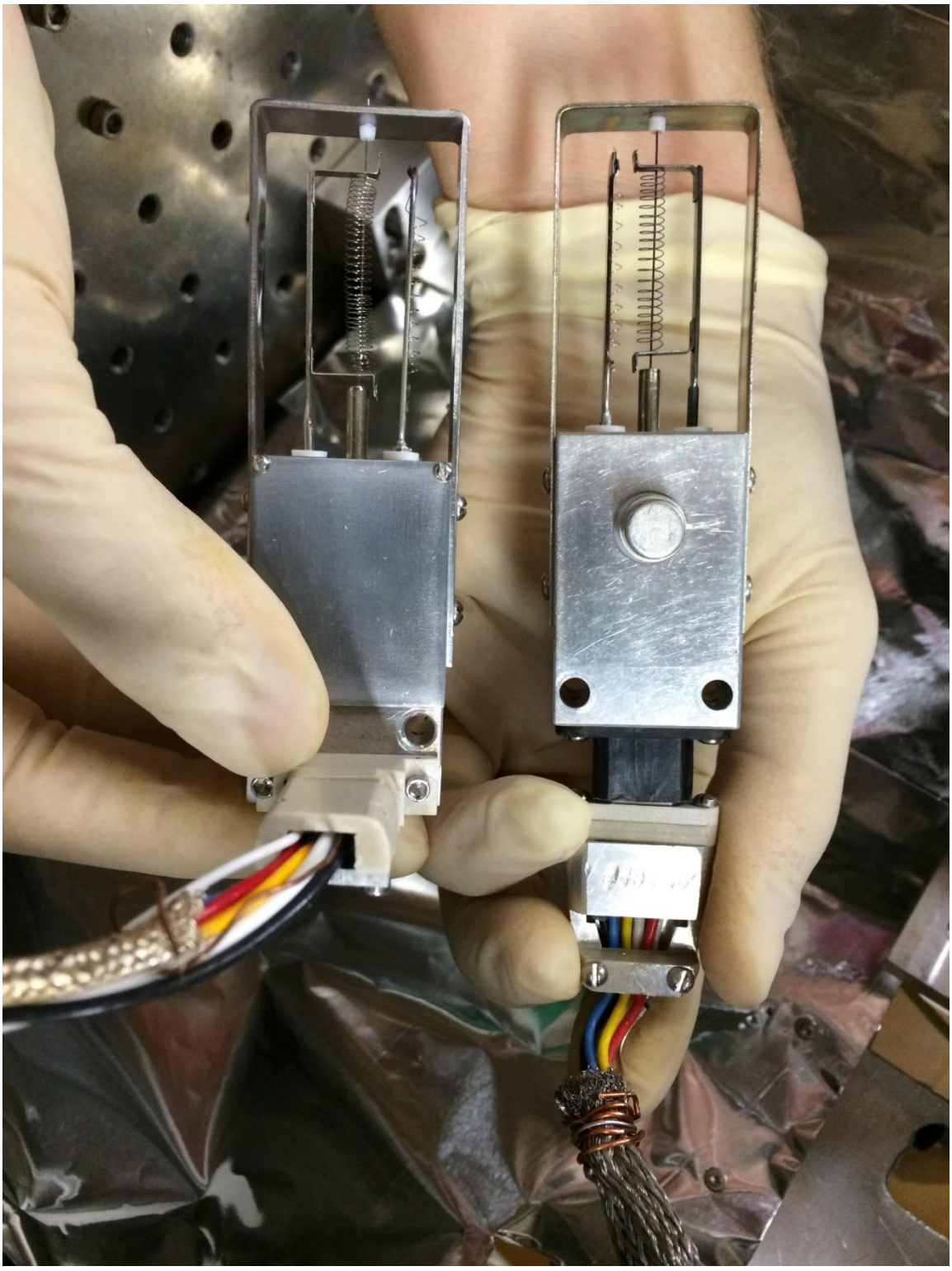

Figure 3 - 33: Fast Ion Gauge Comparison

and is seen on the left side of Figure 3-33.

The body of both devices are machined out of aluminum and contain all the wiring for the FIG components. The only part of the electronics which is prone to failure is the operational amplifier so it is mounted externally on a wall mounted Teflon cylinder with 8 gold pins. In Figure 3-33 the op amp side is shown for FIG-1 and the front plate side is shown for FIG-2. The front plate protects the internal components from the potential corrosive gases in the environment while allowing for easy access in case the internal electronics require troubleshooting.

Species	Enhancement Factor
He	0.133
Ne	0.202
Ar	1.0
Kr	1.56
Xe	2.29
O2	1.0
SF6	2.29

Table 3 - 5: Signal Enhancement due to Ion Gauge Sensitivity

The sensitivity of the fast ion gauge to different gasses is shown in Table 3-5. This reflects the ionization potential of different gasses and means only one calibration curve is required to estimate the density of many different beams.

The detector operates by running almost 2 amps of current through the tungsten filament which is held at a 2V potential. This current causes electrons to be ejected from the filament and accelerated towards the grid which is held at +160 volts. By the time these electrons reach the collector region they have sufficient energy to ionize molecules and atoms in the space. The collection volume is defined as anything inside the grid region. Once an ionization event does occur, the positive ion is attracted to the collector wire which is held at 0 volts. Any ionization events that occur outside the collector region are not collected. The current generated on the collector wire reflects the number of molecules within the grid. The specifications used for this detector are shown in Table 3-6 and are similar to many other Bayard-Alpert gauges.

The volume of the grid space is 317 mm^3 and the fraction of molecules that are ionized is 1 in 10000 so the majority of the gas passes through without detection. The time it takes an ion to travel to the collector wire is approximately 3 microseconds and this determines the response time of the device. The current in the collector wire runs directly into an op-amp which amplifies it by a factor of 50. It is this special feature which makes the fast ion gauge 'fast'. Normal ionization gauges contain their amplifiers in the control unit which is at the end of a long cable. The fast ionization gauges we use have an amplifier that is only 2 cm from the collection region generating the current. There are amplifiers in the controller for the FIG as well, but the presence of the op amp on the device itself provides a large and immediate response to changes in background gas density.

Response Rise time	<5 microseconds
Useful DC Pressure Range	10^{-8} to 10^{-2} Torr
Sensitivity	$1x10^{5}$ Volt $torr^{-1}$ mA^{-1}
R.M.S. Noise	20 mV, with filament on
D.C. Voltage Out	4mV to -10V
Emission Current	5 μA to 3mA, 7 ranges
Filament Current	2 A
Filament Voltage	Up to 5 V
Filament Potential	2V
Grid Potential	160 V
Collector Potential	0 V
Power Requirement	40 Watts, 115 V / 60 Hz
Maximum Temperature	70° C

Table 3 - 6: Fast Ion Gauge Specifications

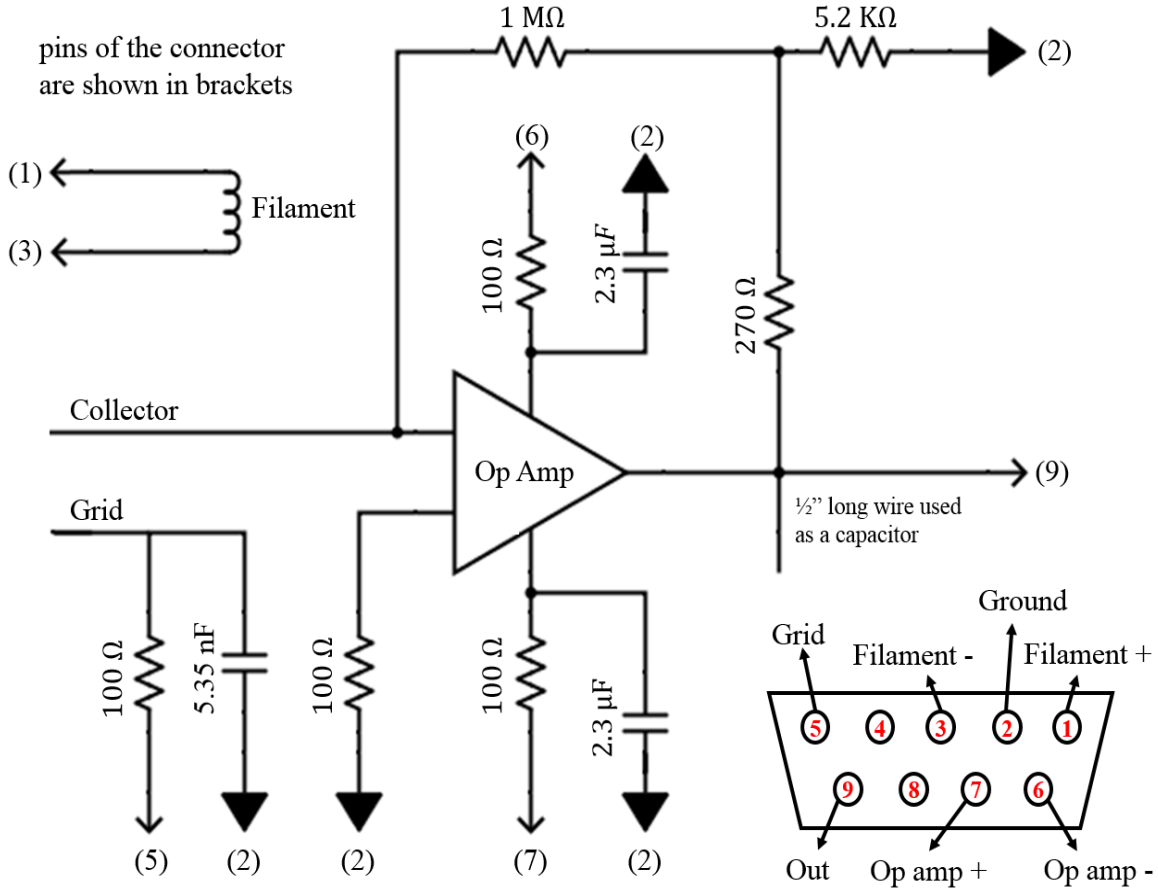

Figure 3 - 34: Fast Ion Gauge Circuit and Connector

To control the gain of the device a simple turn knob and multi position switch is mounted on the front panel of the controller. The output of the device circuit, shown in Figure 3-34, is available on the front panel as well as in the form of a BNC plug. This output is connected to both a multimeter which displays the voltage output and the PCI data acquisition card that will be described in the next section. One limiting factor of the FIG-1 controller is the lack of an output for the emission current. This is overcome in the FIG-2 controller which contains an output on the front panel that can be sampled and recorded automatically.

The response of the detector is estimated to be 10^5 Volt $\text{torr}^{-1}\text{ma}^{-1}$ and an rms noise of around 20 mV. Active calibration runs comparing the FIG output with a separate detector was performed with xenon gas and a Granville Phillips 355 Micro-Ion Gauge (GP-355). The output of the GP-355 is sampled and recorded by the same GPIB card using two Kennith Multimeters. These results are shown in Figure 3-35 where the GP-355 is plotted on the Y-axis in order to attain usable fitting parameters. The data was fit with a quadratic line and the components of this fit are shown in Figure 3-36. The nonlinearity of the response can be attributed to space charge effects that occur at high pressures. For high gains the fast ion gauge output overloaded before the chamber pressure even doubled its original value of 1×10^{-7} Torr. While at very low gains, below 0.01 mA, the FIG dynamic range is broader than the detector it is being compared to.

The calibration is performed with a completely exposed detector which means the entire detection volume contributes to the signal. The constant term is generally around 90 mV whereas the noise in the signal is around 20 mV rms. The linear 10^5 Volt $\text{torr}^{-1}\text{ma}^{-1}$

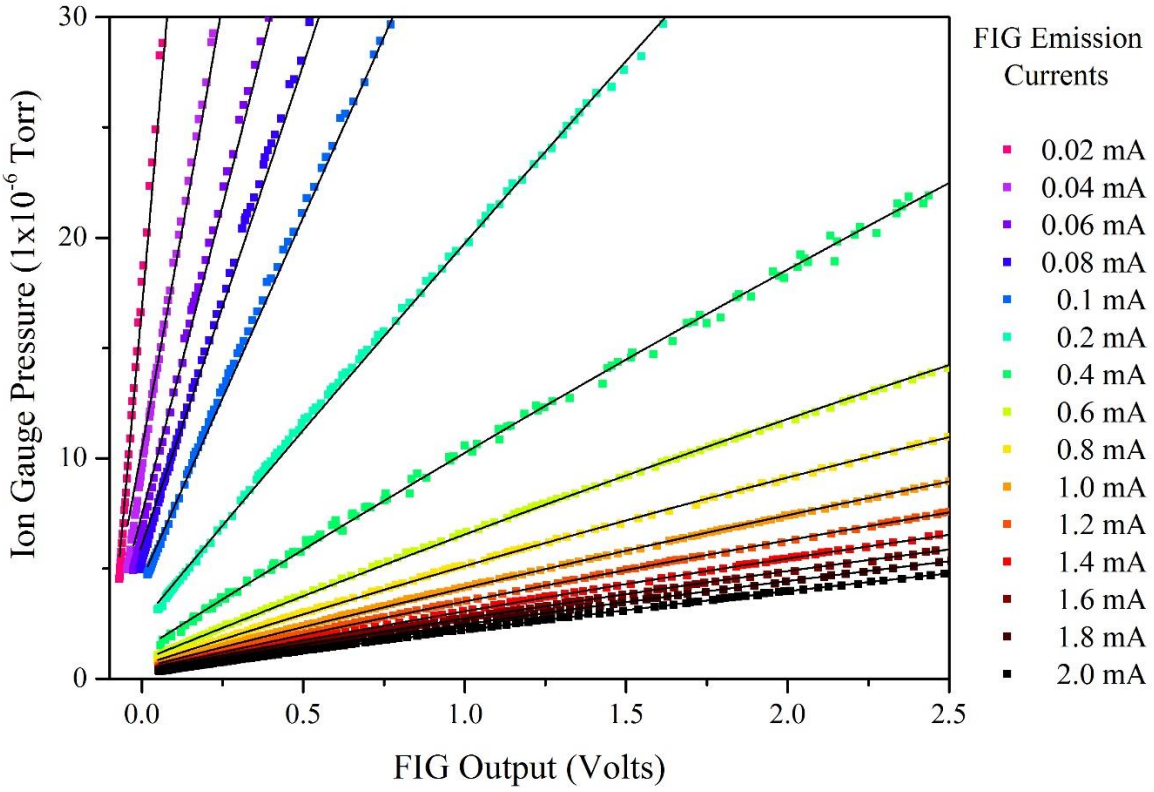

Figure 3 - 35: Fast Ion Gauge Calibration

response listed by the manufacturer of the original unit is 2.5×10^5 Volt $\text{torr}^{-1}\text{ma}^{-1}$ in the unit constructed for this experiment. This variation most likely occurs either due to the geometry of the grid wire or because a different, faster, op amp is used in our build.

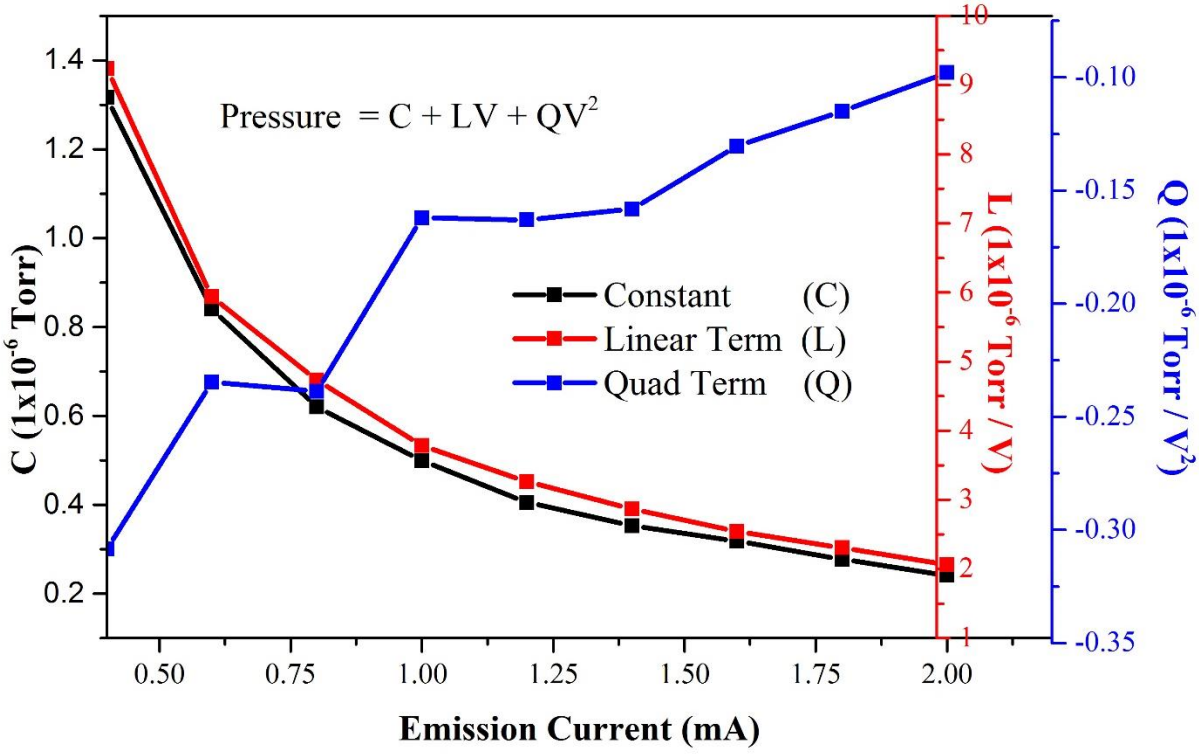

Figure 3 - 36: Fitting Parameters from FIG Calibration

During a typical beam experiment any one of 3 different sized skimmers are used to separate the main chamber from the detection chamber. This separation serves to protect the FIG from the high pressures attained in the main chamber during a pulse sequence. The beam density can be determined by using the appropriate fitting term from the calibration run

and then multiplying by the volume ratio between the skimmed region and the entire detection region.

The low pressure sensitivity of the device is limited to 10^{-10} Torr by the photoelectric effect. Electrons emitted from the filament collide with the grid and produce x-rays. These photons interact with the collector wire to produce a photoelectric noise. This noise is less than 20 mV in the current device and very high frequency digital sampling of the signal at high gains shows the noise very clearly.

3.7 Data Collection

Before the signal from the FIG can be analyzed it must be recorded. This is accomplished by either an oscilloscope or a high speed data acquisition card. The first succesful pulse by our team occured in late 2009, about 6 months after I began working in the lab. It was collected on a 4-channel Tektronix oscilloscope, Model TDS 2014B, and is shown in Figure 3-37. Soon after these initial data sets were recorded an "ultra high-speed" data acquisition card made by Measurement Computing Corporation was purchased. It's installed in a PCI slot on

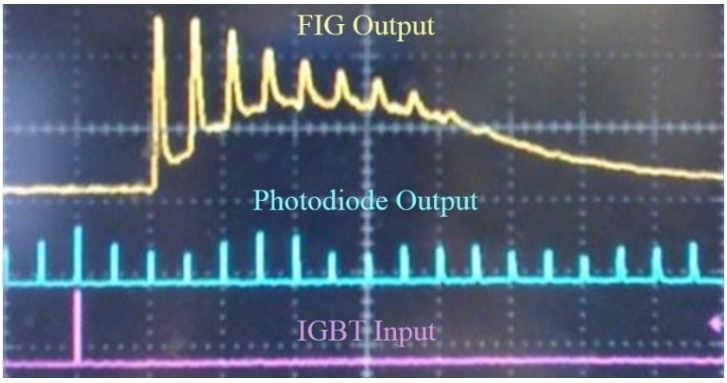

Figure 3 - 37: Oscilloscope Data Capture

Sample Rate	20 MS/s
Buffer Size	32,000 data points, total
Resolution	12-bits
Number of Channels	4 independent BNC
Programmable Ranges	$\pm 1V$, $\pm 5V$
Maximum Input Voltage	$\pm 15V$
Input Impedance	1.5 $M\Omega$, or 50 Ω, selectable
Bandwidth	17 MHz typical
Coupling	DC

Table 3 - 7: Data Acquisition Card Specifications

a Dell Inspiron computer. This card was chosen for several key reasons, each listed in Table 3-7.

To protect the computer and DAQ card an isolation amplifier was built and installed according to Figure 3-38. It is externally powered and contains seven input and output channels. All of the channels are intended for use with the DAQ Card, 4 input channels, 1 trigger channel, and 2 digital output channels. Each of the input channels contains its own isolation amplifier circuit. This is important because it prevents crosstalk between the channels which would contaminate the data with noise. The purpose of the circuit is to provide a 1 to 1 gain ratio between the input and output channels for signals beneath $\pm 5V$ and to overload at $\pm 5V$ preventing any higher voltages from being transmitted across the channel. This prevents any large currents generated in the custom valve driver from accidentally shorting through the data collection system.

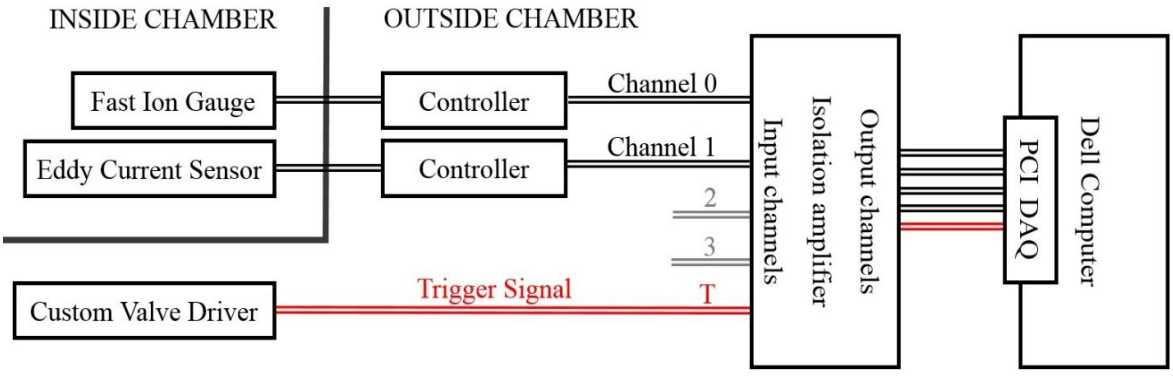

Figure 3 - 38: Data Acquisition System

Unlike the design utilized by Gupta and Herschbach [7-9], the beams collected in this thesis are pulsed. The beam shapes and the type of data collected by the two experiments are similar, but there are important differences. Instead of a relatively small signal with high background, large signals are created at the beginning of the pulse train very soon after the valve is cycled. These large signals combined with the very low initial background in the chamber means that only one pulse train is needed to characterize a particular rotor frequency. This signal size also precludes the need for an amplifier or data averaging.

In order to maximize data quality the collection frequency of the DAQ has to be set correctly. If the collection frequency is too high then only one or two pulses will be collected, and if it is too low the number of data points per pulse is insufficient. For this

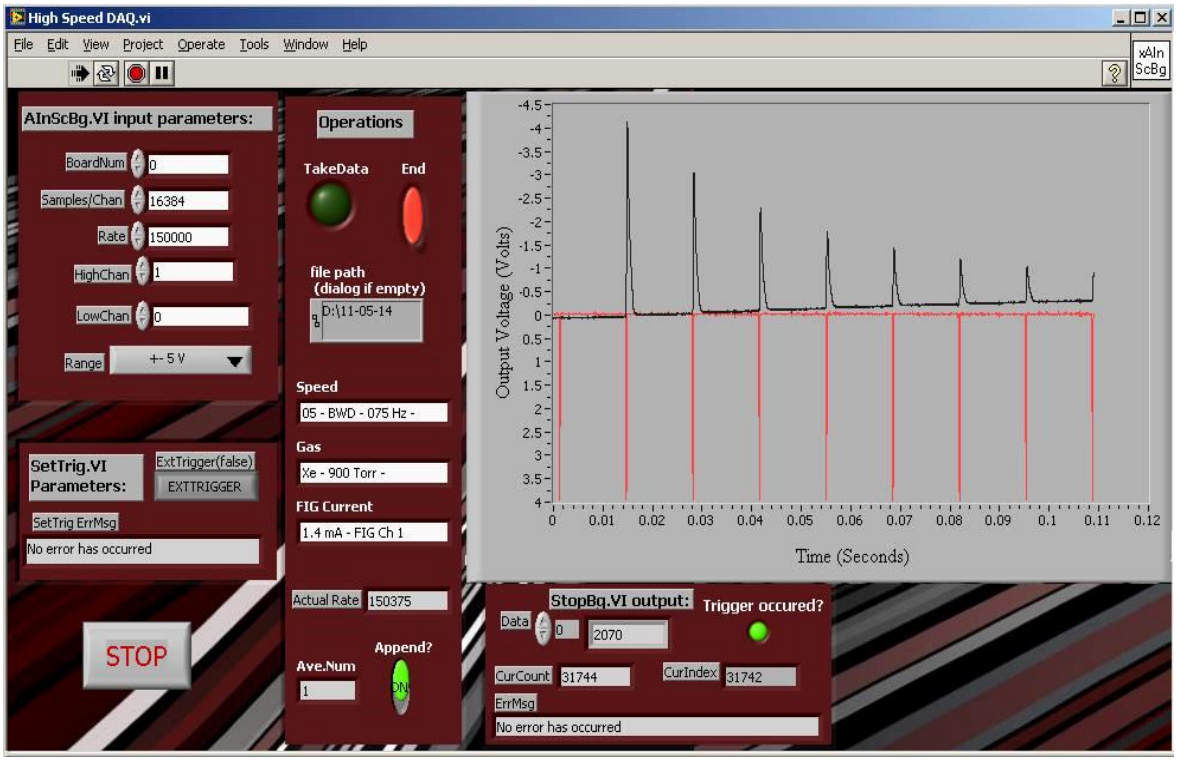

Figure 3 - 39: Data Acquisition Program - Front Panel

reason an optimum sampling rate is one that collects just enough peaks for satisfactory analysis and no more than that. This requires careful consideration of the time required for the pulses to appear from the trigger pulse. Since the DAQ card is triggered from the same circuit that actuates the pulsed valve there must be 'dead' time in the collected data where no rotor signal is recorded. This time is seen in the first few milliseconds of Figure 3-39, and represents the delay in the timing circuit, the reaction time of the valve, the filling of the rotor, and the time it takes for the rotor to complete a revolution and produce a detectable beam. This section of data is important because it provides two pieces of vital information that are relevant to every signal: the background pressure in the detection chamber and the noise level of the data collection system. For these reasons a delayed trigger system was never developed for the DAQ card.

A simple labview program was developed to control all of the DAQ card parameters as well as name and save the data files appropriately. The graphic user interface shown in Figure 3-39 is the most recent iteration of this program. As can be seen in the figure all collected data is shown on the screen for each data capture. Each file name describes all the relevant data to allow for future analysis.

To obtain the appropriate frequency for the data collection system first consider the ratio of buffer size and sampling rate. For a sampling frequency, F_{DAQ} the buffer is full in

$$t_{DAQ} = \frac{Buffer\ Size}{Channels} F_{DAQ}^{-1} \tag{3.36}$$

Most experiments require only two channels: FIG detector and eddy current sensor. Therefore the number of data points collected per channel is 16,000 and at 100kHz sampling rate the entire collection takes 160 ms.

To sufficiently characterize a particular configuration about 5 pulses should be collected by the DAQ card. This means for a rotor frequency, F, the elapsed time should be

$$t = 20\ msec + 5/F \tag{3.37}$$

Which means the sampling rate of the data acquisition card can be set by:

$$F_{DAQ} = \frac{Buffer\ Size}{Channels}(20\ msec + 5/F)^{-1} \tag{3.38}$$

This is shown in Figure 3-39 for three different channel configurations. Most of the data collected in this thesis, unless otherwise noted, is collected in 2-Channel mode.

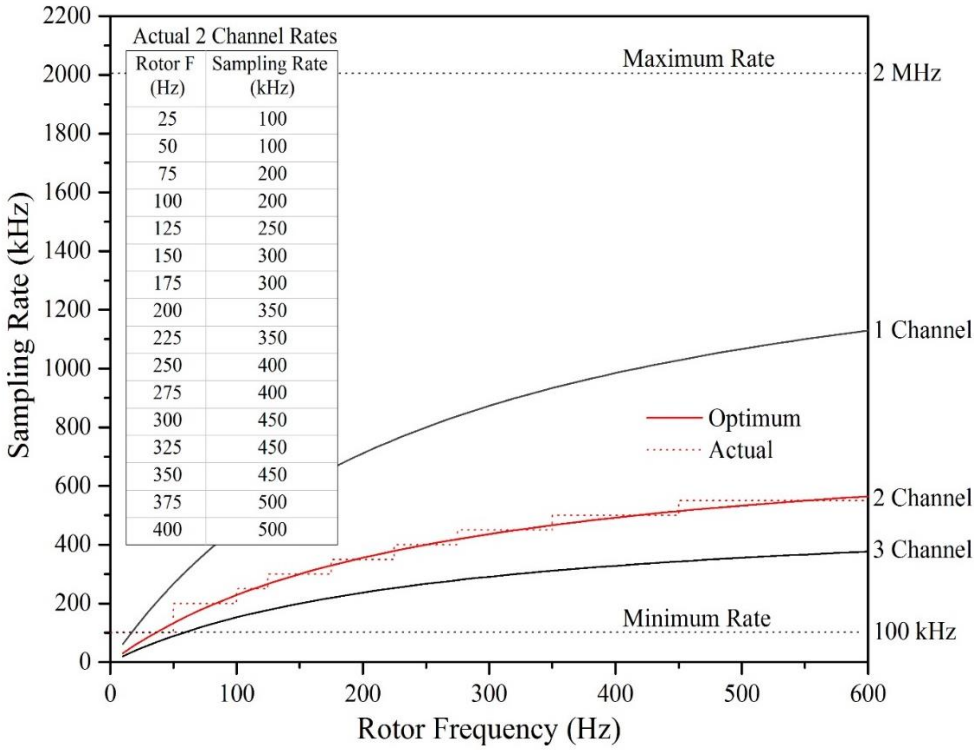

Figure 3 - 40: High Speed DAQ: Sampling Rate

4. DATA AND CONCLUSION

In this section, the theory developed in Section 2 is applied to the experimental results that are collected using the setup described in Section 3. The first section characterizes the beams produced with high backing pressure and clear supersonic nature. The second section analyzes beams produced with progressively smaller backing pressures. The third section compares and contrasts the slowest beams produced by the rotating source with other slowing schemes used in physics and chemistry research.

4.1 Rotating Supersonic Beam

The FIG-1 detector, as described in Section 3, utilizes electron impact to ionize species in the detection chamber, the measured signal is proportional to the number of these species as a function of time. The time dependent density, $D(t)$, from a rotating source with a linear velocity, V_{rot}, is described by

$$\mathrm{D(t)} = \frac{\mathrm{C}}{\mathrm{t}} \left(\frac{\mathrm{L}}{\mathrm{t}}\right)^2 \left(\frac{\mathrm{L}}{\mathrm{t}} - \mathrm{V_{rot}}\right) \mathrm{e}^{-\frac{\left(\frac{\mathrm{L}}{\mathrm{t}} - \mathrm{u'}\right)^2}{\Delta \mathrm{v}^2}} \tag{4.1}$$

where C is a constant and L is the distance to the detector. The value of the lab frame velocity, u', is determined by both the velocity of the rotor tip and the flow velocity of the beam produced at the nozzle. The velocity spread, Δv, is a property of the beam itself and is not augmented by the rotor velocity. The parameter C is evaluated in Section 2 during the intensity calculation for supersonic expansions.

In this section I will focus on the characteristics of supersonic beams. To classify a beam as supersonic two requirements must be satisfied. First, it requires $\mathrm{P_0 d} > 1$ where $\mathrm{P_0}$ is the pressure behind the nozzle, in units Torr, and d is the diameter of the nozzle throat, in

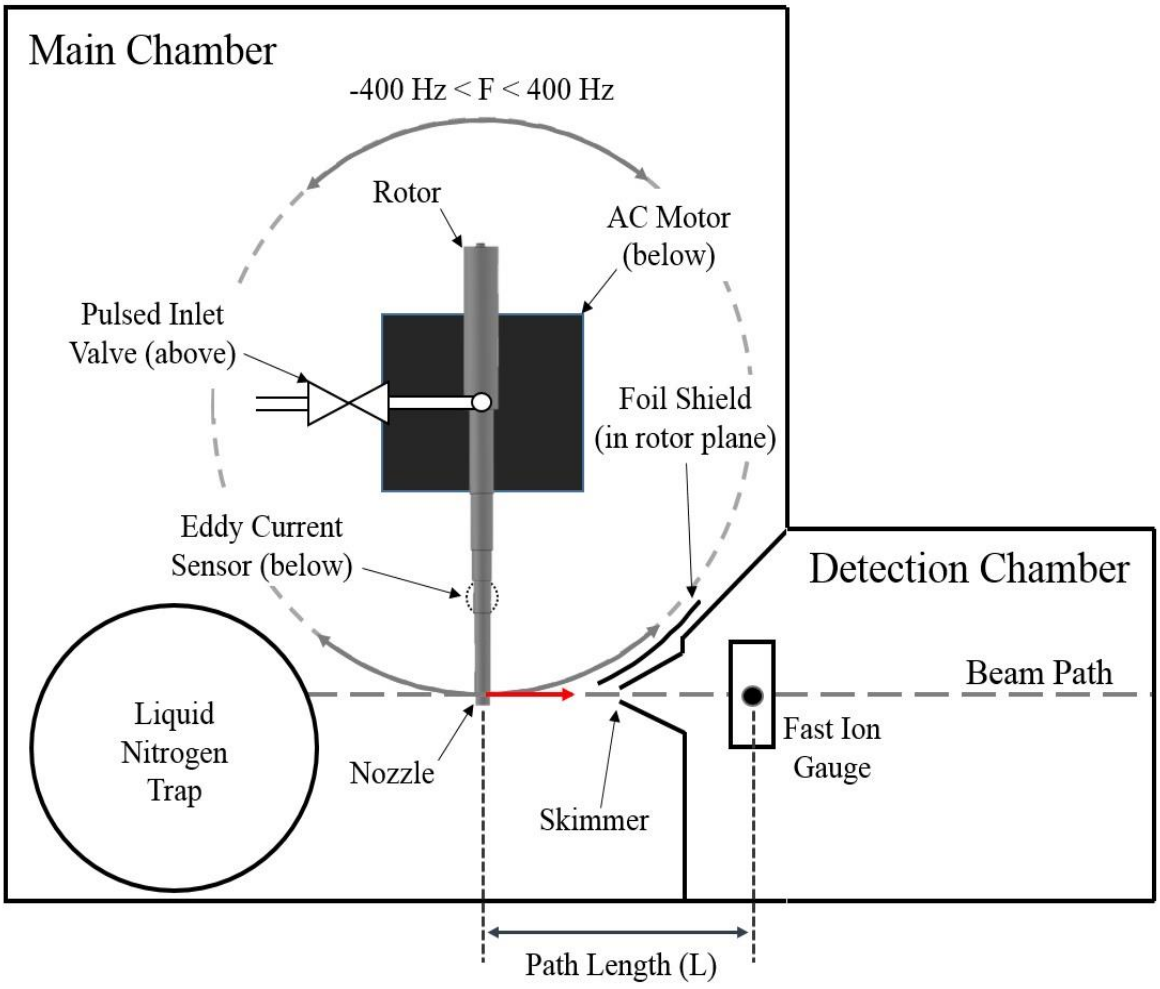

Figure 4 - 1: Slowing and Speeding - Experimental Configuration

units cm. The nozzles used in Rotor 2, 3, and 4 all have $\mathrm{d} = 0.0254$ cm. Second, it requires the mean free path to be smaller than the diameter of the nozzle. If these conditions are satisfied the flow velocity and beam temperature can be described by:

$$u' = \mathrm{V}_{rot} + u \tag{4.2}$$

$$u = \sqrt{\frac{\gamma}{\gamma-1}}\sqrt{\frac{2kT_o}{m}} \tag{4.3}$$

$$\Delta v = \sqrt{\frac{2kT_{\parallel}}{m}} \tag{4.4}$$

$$T_{\parallel} = \left(\frac{T_o}{40.8}\right)(\mathrm{P_O d})^{-12/11} \tag{4.5}$$

where γ is the Poisson Coefficient, and the Thermal Conduction Model has been used to generate the working formula for the beams parallel temperature.

A typical signal recorded during one pulse train is shown in Figure 4-2. Each pulse is seperated from adjacent pulses by the rotor period, as is expected. The signal is offset from 0V due to internal components of the FIG electronics. This is a constant voltage for each value of the detector gain and is thus compensated for during the detector calibration. The time-zero of each gas pulse is determined by the output of the eddy current sensor, also seen in Figure 4-1. It is clear that the signal should be modelled by a set of values each assigned to a pulse number which designates its position in the pulse train. Here $S(t)$ represents the time dependent signal from the FIG that is collected by the high speed data acquisition card

$$S(t) = D_{-1}(t) + D_0(t) + D_{+1}(t) + B(t) \tag{4.6}$$

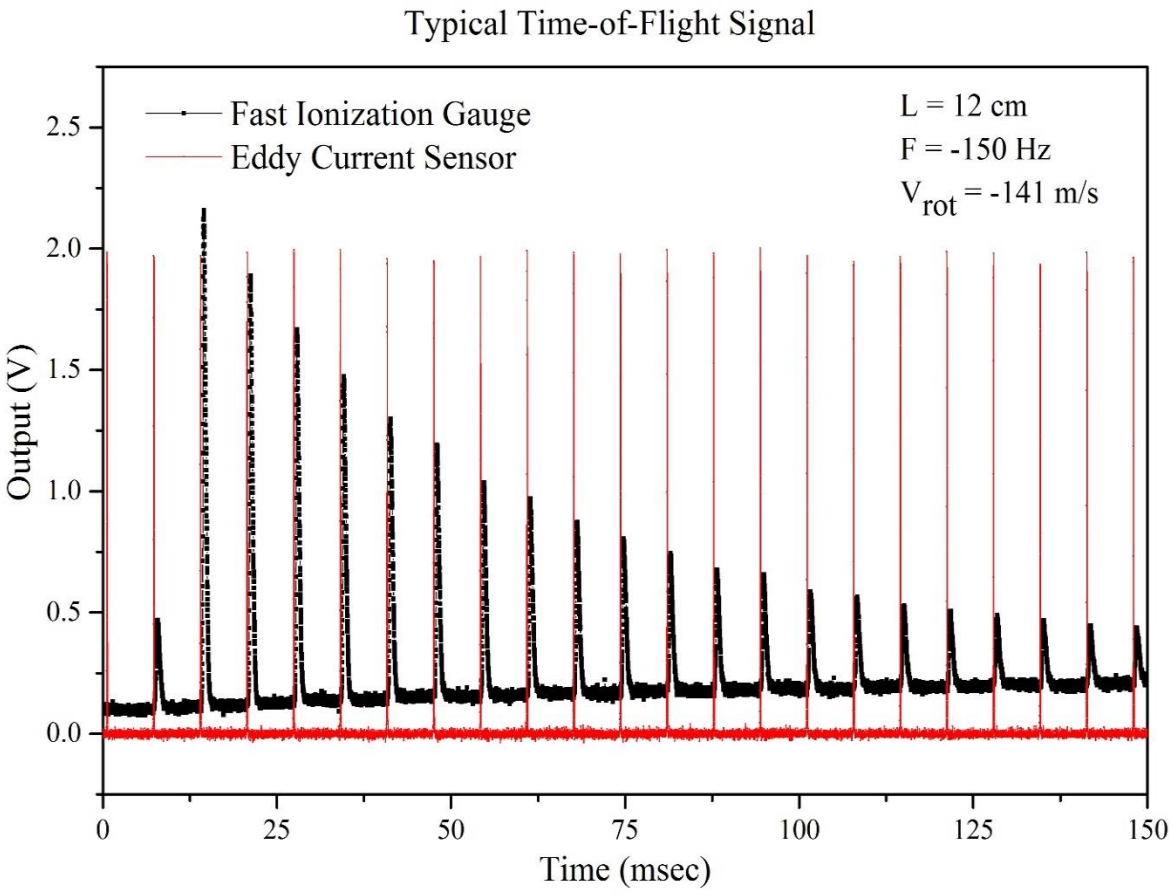

Figure 4 - 2: Typical Time-of-Flight Signal

The values recorded for each peak are then correlated to beam density, velocity, and width. These values evolve as the pressure behind the source decreases and the pressure in the main chamber and detection chamber increase. The following sections will describe the required steps for fully characterizing the velocity augmented supersonic beam over the entire range of frequencies under study. This range is dictated by the length of the rotor and the flow velocity of the gas under study. For example, xenon at ambient temperature has a flow velocity well below 350 m/s. To generate a nozzle velocity comparable to that a motor frequency of 350 Hz is needed ($1\text{Hz} \approx 0.94\,\text{m/s}$).

4.1.1 Background Removal

Processing of the data begins by utilizing the FIG calibration data shown in Table 4-1. This is used to convert the signal from voltage vs time to torr vs time. This effective pressure, P^*, can then be converted directly to number density since $1\text{ torr} = 3.216\text{E}13\text{ molecules/cm}^3$.

$$P^* = \text{C} + \text{LV} + \text{QV}^2 \tag{4.7}$$

$$D = \text{A} * |\text{P}^*(\text{torr})| * 3.216\text{E}13 \tag{4.8}$$

The constant, A, represents the ratio of volumes between the full collection region, and the region defined by projecting the skimmer onto the collection region. This corrects for the fact that during calibration the entire detection region of the FIG is exposed to the background gas, and during normal operating conditions the FIG is completely enclosed in the detection chamber and only gas that travels through the skimmer contributes to the pulse signal. There are three skimmers constructed for use in this experiment. Their diameters are 1mm, 3mm, and 5mm. The volume ratios are 105.7, 12.2, and 5.6 respectively.

Emission Current	Constant Term (C)	Linear Term (L)	Quadratic Term (Q)
0.02	16.8402	166.221	35.6538
0.06	7.45274	55.1135	3.51113
0.1	4.50616	32.887	-0.107843
0.2	2.57869	17.5922	-0.340008
0.6	0.838769	6.03662	-0.279097
0.8	0.620096	4.61383	-0.248641
1	0.496608	3.81781	-0.218185
1.6	0.309255	2.55048	-0.126818
1.8	0.274069	2.28649	-0.00963618
2	0.246643	2.0693	-0.0065906
2.2	0.225203	1.88999	-0.00354502
2.4	0.208425	1.74176	-0.00049944
2.6	0.195289	1.61915	0.00254614
2.8	0.185002	1.51772	0.00559172
3	0.176947	1.4338	0.0086373

Table 4 - 1: FIG Calibration Parameters

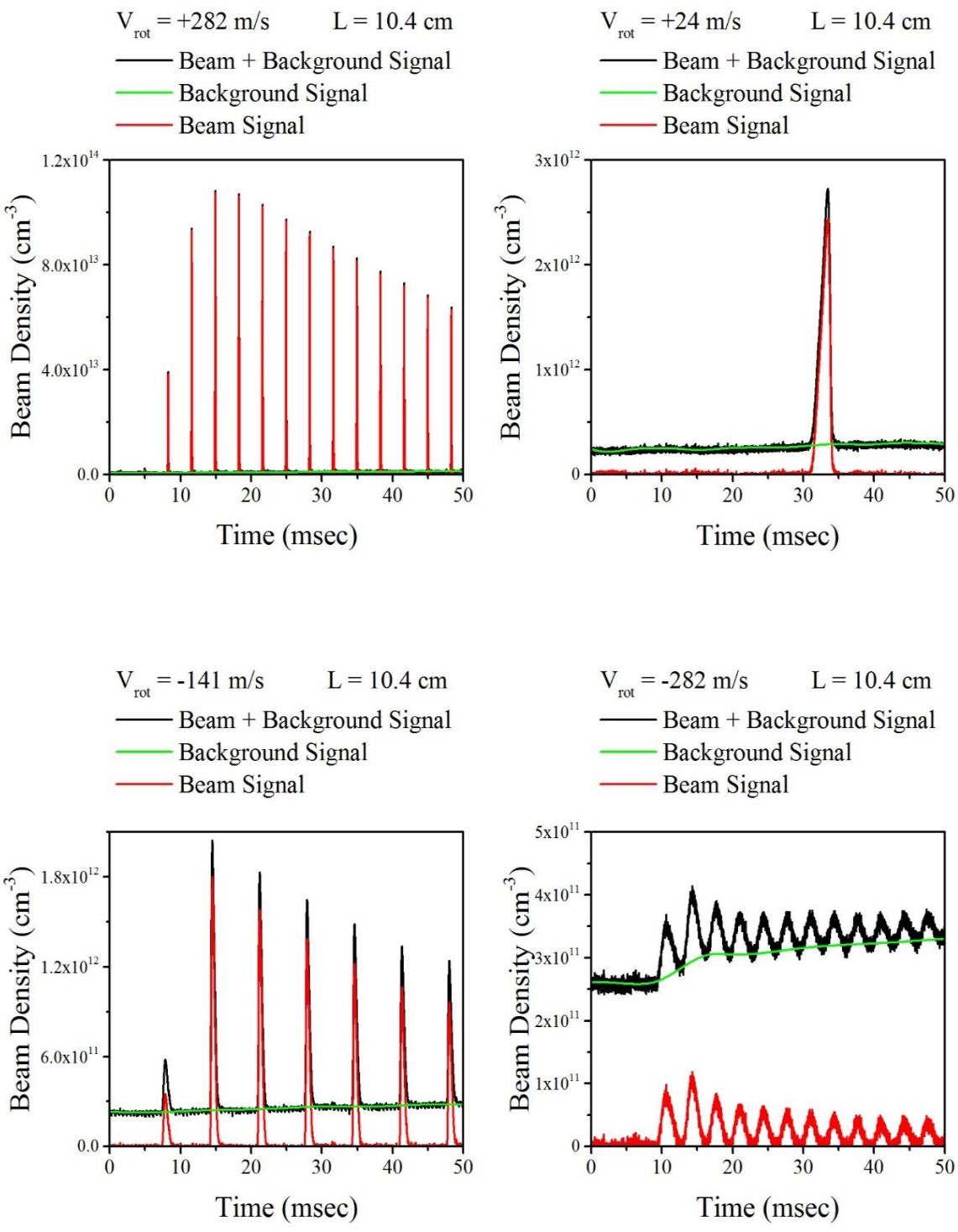

Figure 4 - 3: Background Removal

It is clear from Section 3.6 that the signal from the fast ion gauge is the cumulative sum of three different sources. The first source is the rotor which has been the focus of discussion thus far. The second source is the effusive beam created by the large differential pressure between the main chamber and detection chamber. When a pulse train is initiated the main chamber pressure grows very quickly up to 10^{-4} Torr and causes the detection chamber pressure to rise as well. The conductance between the two chambers is dependent on the size of the skimmer installed. Since the source of interest is the rotor augmented beam the signal originating from the effusive beam should be removed from the data set. The third source is due to residual gas in the detection chamber, and combined with the effusive source is broadly categorized as the background signal. In Eqn 4.6 the background signal is shown as $\mathrm{B(t)}$.

Removing the background signal from the pulse train prevents it from obscuring the estimated density of the molecular beam produced by the rotor. Since the pulse densities being measured span 3 or 4 orders of magnitude this background removal will be very important for the lower densities and unnecessary for the highest density beams measured. For the pulses that have very low density the removal of the background signal can reduce the estimated density by up to a factor of 10. Therefore, a failure to remove this signal would result in a drastic over-estimation of the beam density.

The form of the background signal is generated in OriginPro 9.1 which allows the user to manually select points which are then fit to a splined line. The generated line is then subtracted from the data set and the processed data is considered to reflect the true density of the velocity augmented molecular beam. The background removal process is verified by

analyzing the three data sets together, as is done in Figure 4-3, and checking the beam density goes to zero between each pulse in the pulse train.

The removed signal can be broken into two components, as previously mentioned. The first section of data is recorded prior to the initiation of a pulse train and thus gives an accurate indication of the preexisting vacuum conditions. This is usually the first 10 milliseconds of data and serves to indicate any aberrant conditions in the detector or data acquisition system. If there is any interference or noise it will be clearly visible in this section of data and shouldn't be mistaken for originating from the rotor itself.

The second section of the removed signal is the effusive beam produced by the nontrivial conduction of gas through the skimmer. This gas is emitted from the nozzle at rotor angles which do not correspond to the shooting position. Once it has been scattered by the chamber walls the gas no longer has any supersonic properties. It can either be pumped out of the main chamber, or travel through the skimmer to be pumped out of the detection chamber. If its trajectory passes through the skimmer the gas will most likely travel through the collection region of the FIG and contribute to the collected signal.

If adequate pumping time between the pulse trains is not given, the pressure in both the main chamber and detection chamber will increase throughout the entire data run. For this reason the backwards direction of rotation is always collected first since the beams it produces are much lower in density. However, this single step does not completely negate the problem of a rising background pressure. Only by monitoring the continuous DC output of the FIG prior to the initiation of a pulse train can the user be sure that the detection chamber pressure is similar from one pulse train to the next. If extra time is required to allow

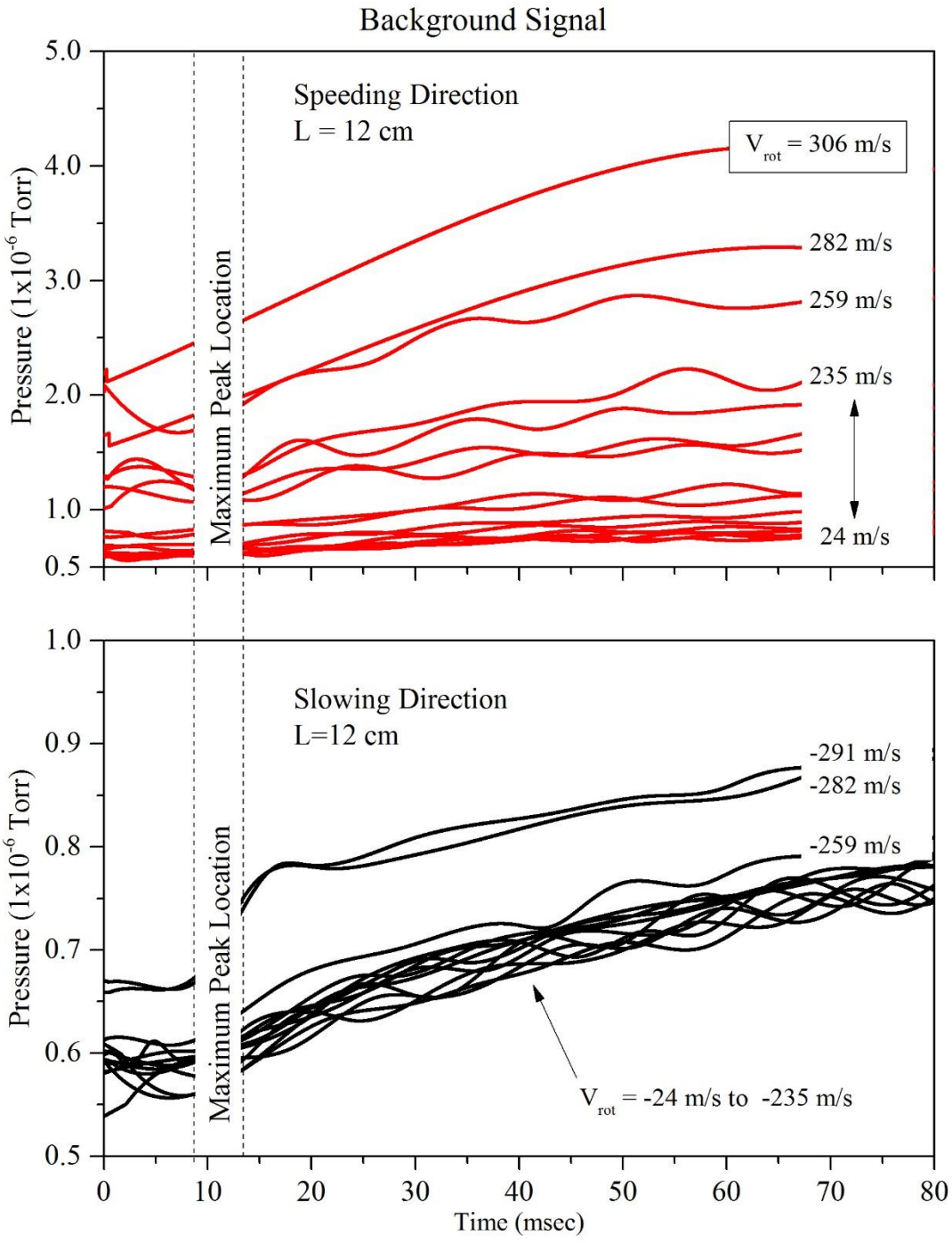

Figure 4 - 4: Background Comparison

pressure stabilization then the performance of the pulsed valve and pumping systems must be verified and careful analysis of the produced beams is required.

As can be seen in Figure 4-4, the background signal, $B(t)$, for the majority of the produced beams is the same. The exception to this occurs at very high rotational velocities in both the forward and backward directions. An increase in background in the forward direction is likely due to the fact that the augmented supersonic beam is much more dense and during each pulse more gas makes it into the detection chamber. An increase in background in the reverse direction can be attributed to pulse overlap. The differences in time of flight between a stationary rotor and a slowed beam can be around an order of magnitude. This increase in time of flight allows the constant, and finite velocity dispersion to cause neighboring pulses to both contribute to the signal at the midpoint between them. This means that the background signals shown in Figure 4-4 for $V_{rot} < -235\ m/s$ are wrong and must be shifted downwards to account for this pulse overlap. A similar shift is not needed for the forward direction because the magnitude of this correction is two or more orders of magnitude smaller than the amplitude of the rotor signal.

4.1.2 Beam Density

Once the background signal has been removed, the location and amplitude of each peak in the pulse train can be recorded as a set of (x, y) coordinates. In the set $(t, D(t))$ where t is time (in seconds) and $D(t)$ is the time dependent number density in cm^{-3}. The beam densities produced by the rotor at a given frequency will be analyzed in this section, and each subsequent property of the beam will be reviewed in the sections following.

To execute the Peak Finding subroutine use the Analysis dropdown menu and select the Peaks and Baseline subtab, select the Peak Analyzer subtab, and finally select the Open Dialog option. The dialog box which opens will allow the user to define several parameters related to the Peak Finding subroutine. These parameters include the required size of the peaks, the number of points that each peak must contain, and whether any smoothing is to be applied to the data within the subroutine. The subroutine makes defining each parameter very easy by plotting the data side by side with the dialog box. On this data the peak fitting results are displayed and automattically refreshed when any parameters are altered. This feature prevents the saving of any peak locations that have not been visually verified by the user. In addition, the zoom feature is available for the graph accompanying the dialog box.

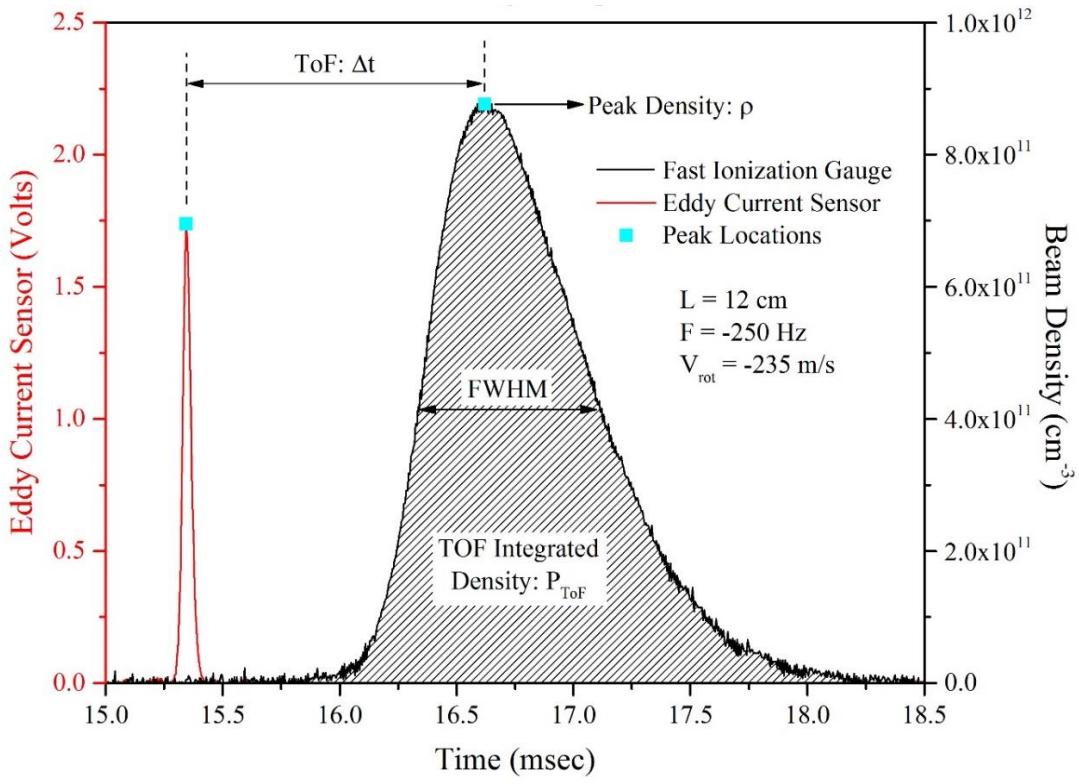

Figure 4 - 5: Time-of-Flight Properties

Thus allowing the user to inspect the peak locations in much more detail. Typical results of the Peak Finding subroutine are shown as black dots in Figure 4-6.

Direct comparison of one density profile to another requires both similar starting conditions in the chamber and a highly repeatable output from the pulsed solenoid valve. For this reason the valve control parameters, described in Section 3.3, are not changed after optimization procedures have been performed. And yet, regardless of the pulsed valve performance, there is still a lack of synchronization in the time domain that must be dealt with. This random nature of the pulse train starting point prevents the direct comparison of individual peak amplitudes. Instead, each data set is fit to an exponential decay function, as seen in Figure 4-6 and 4-7. This function represents the pressure behind the nozzle as a function of time. If too few points are available in a single data set, for instance at very low motor frequencies, multiple sets are collected and used for the exponential decay fit. These repeated measurements are shown as white squares in Figures 4-6 and 4-7. The value of the exponential decay function is then collected for a given point in time and plotted as a function of rotor velocity, as is seen in Figure 4-8. This technique prevents the lack of pulse synchronization from interfering with the estimated maximum density.

Once the maximum density has been estimated for the entire range of frequencies then its dependence on rotor velocity can be explored. The expected behavior, as described in Section 2, should include both the centrifugal enhancement of the input pressure as well as the geometric V^2 term. The geometric consideration shows how drastically the final lab frame velocity effects the amount of gas entering the detection chamber. This attenuation of the beam is due to a constant and finite transverse velocity in the rotor frame. It is not offset by the centrifugal enhancement term

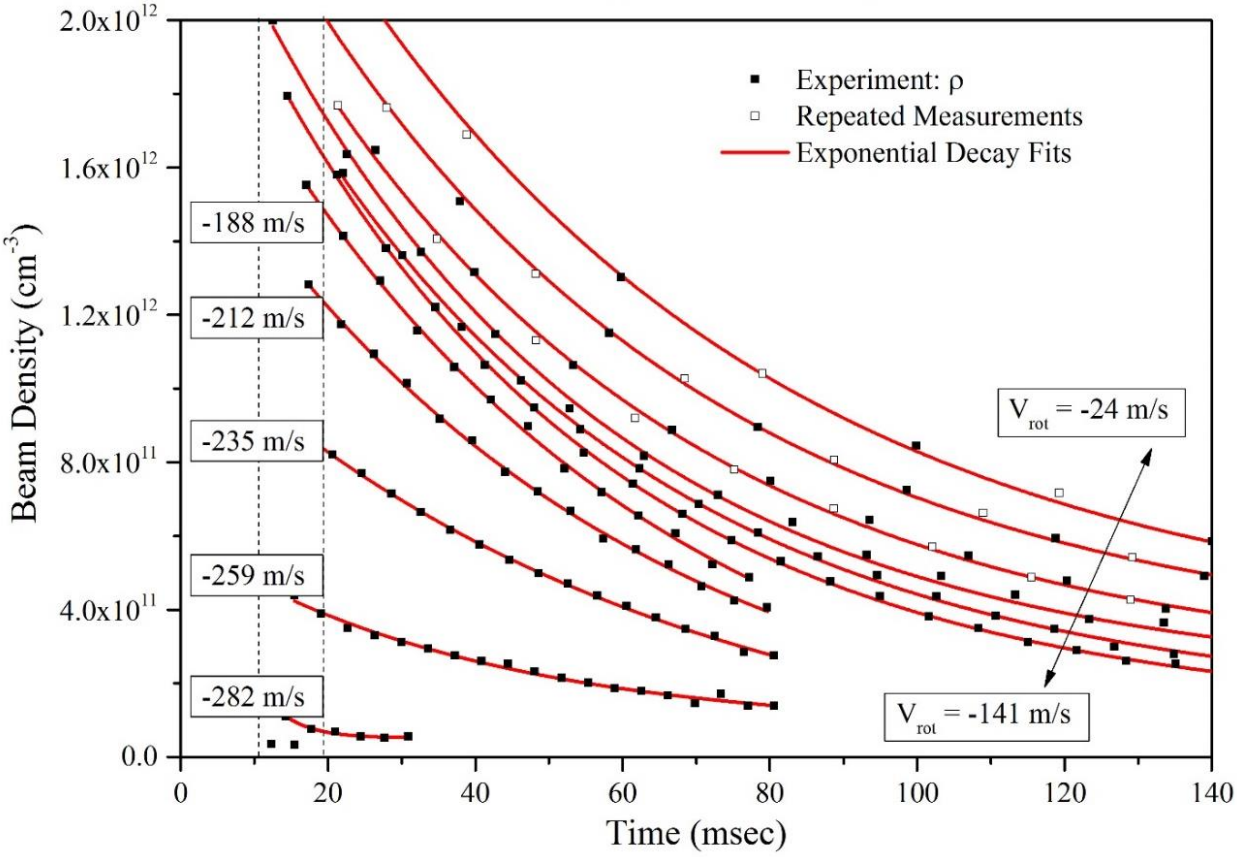

Figure 4 - 6: Peak Amplitudes - Slowing

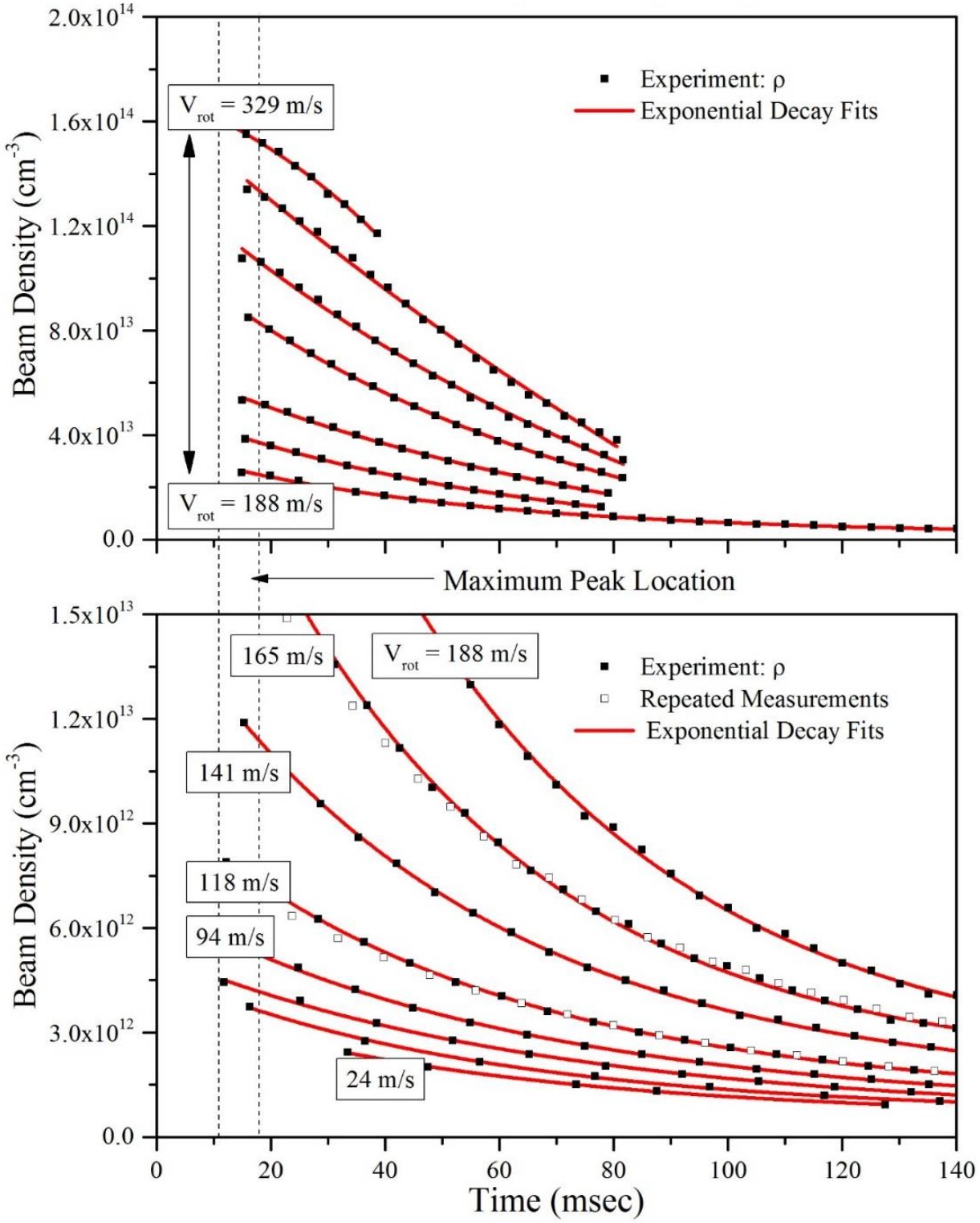

Figure 4 - 7: Peak Amplitudes - Speeding

$$P_{eff} = P_o e^{\frac{mV_{rot}^2}{2kt}} \tag{4.9}$$

in the limit of very low lab frame velocities.

The two fitting functions in Figure 4 - 8 both contain the geometric term but only function 1 contains the centrifugal enhancement of the nozzle pressure. Where X is the supersonic flow velocity of the gas, in this case xenon with $X = 320\ m/s$ and the final augmented velocity is $V = X + V_{rot}$. Figure 4 - 8 clearly demonstrates that the number density, $D(t)$, of the velocity augmented beam behaves as theoretically predicted in Section 2. This occurs over 4 orders of magnitude with very little deviation. It also predicts the beam density at the FIG, n_{FIG}, for a stationary rotor is around $3 \times 10^{12}\ cm^{-3}$. This density can be used to calculate the nozzle density, n_o, by using

$$n_{FIG}(r, \theta) = a^2 n_o \left(\frac{R_n}{r}\right)^2 \cos^b\left(\frac{\pi}{2}\frac{\theta}{\theta_o}\right) \tag{4.10}$$

where a and b are constants based on the Poisson coefficient of the gas used. For a monatomic gas such as xenon they are 0.8 and 3 respectively. The nozzle radius, R_n, for Rotor 3 is 0.2 mm and θ_o is the angle that defines where the angular distribution tends to zero. Rotor 3 utilizes a conical nozzle whch fixes θ_o at 15°. In Section 4.2 the peak is shown to occur near $\theta \approx 6$. This returns a nozzle pressure of 66 Torr which in turn gives a value of $P_o d \approx 2.8$. This value is well inside the range of a supersonic expansion which in Section 2 was shown to prevail at $P_o d > 1$.

The deviation in beam density that occurs at high rotor velocities, and therefore high lab frame velocities, can be attributed to either skimmer interference or to dimerization of the beam. Skimmers are known to interfere with the quality of a beam that travels through it.

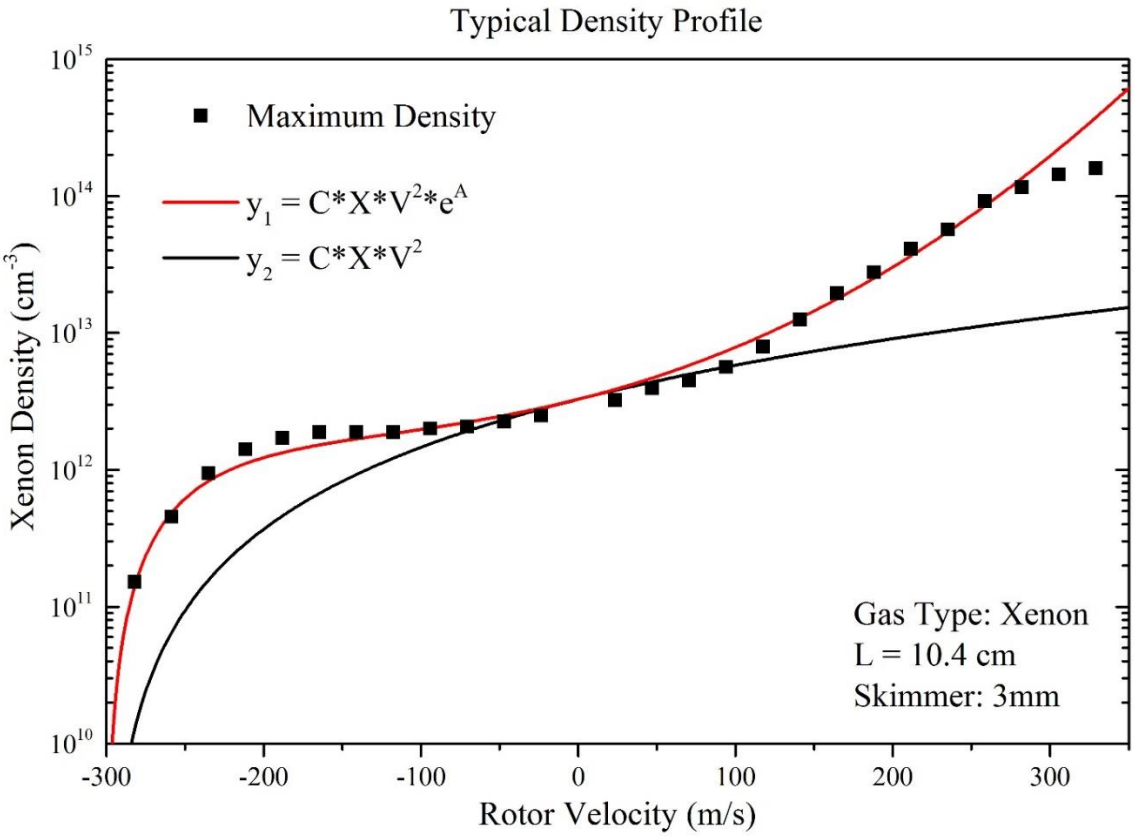

Figure 4 - 8: Peak Density

This results in a drop in density as well as heating of the beam itself. The amount of interference that occurs in a skimmer is a function of the edge thickness. All of the data in this thesis, unless otherwise noted, was collected with the 3mm diameter skimmer. This is the top middle skimmer shown in Figure 4-9.

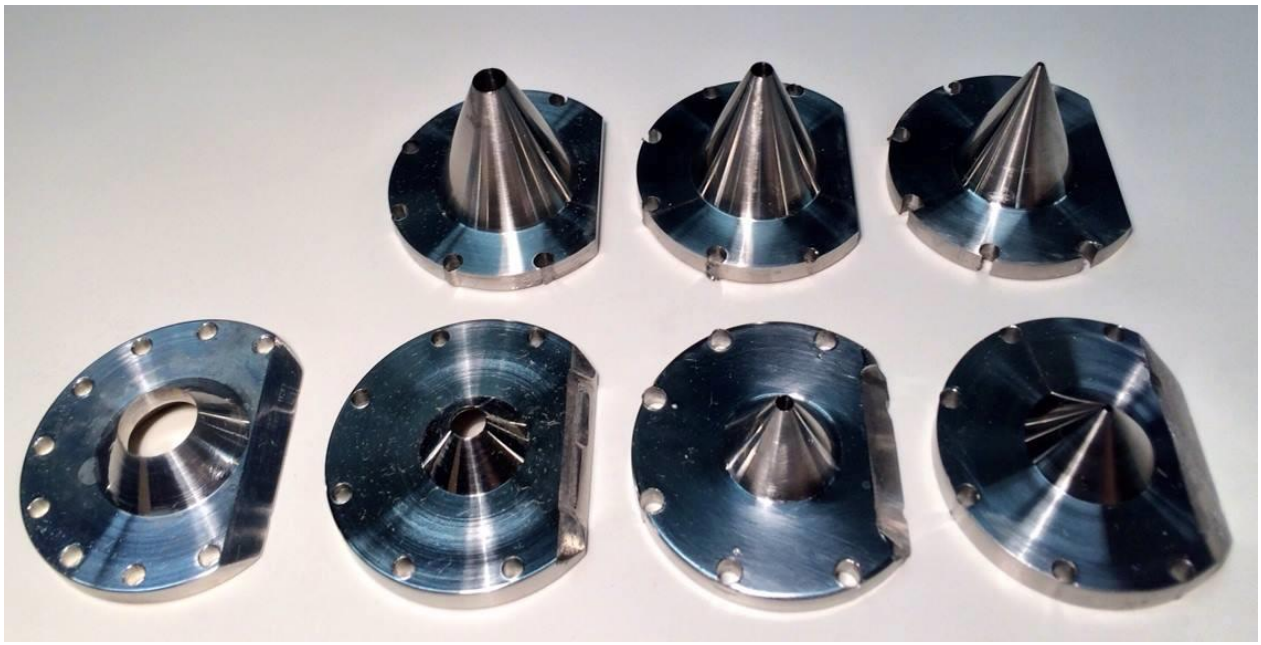

Figure 4 - 9: Skimmer Variations

Dimerization, on the other hand, is an effect which occurs due to the pressure and temperature conditions present in the nozzle throat. Since the pressure has been shown to be a function of rotor velocity, the concept that a dimerization region can be entered at very high rotational frequencies is not unexpected. It occurs when three body collissions begin stabilizing the formation of Xe - Xe dimers in the supersonic expansion. To limit the

formation of dimers to less than 1% of the beam the parameter D^* must be kept below 0.1[47]

$$D^* = \mathrm{P_o}\left(\frac{\sigma^3}{\varepsilon}\right)\left(\frac{2\mathrm{R_n}}{\sigma}\right)^{0.4}\left(\frac{\mathrm{kT_o}}{\varepsilon}\right)^{-2.4} \tag{4.11}$$

where σ and ε are typical Lennard-Jones parameters. For a pressure of 330 Torr this returns a dimerization rate between 1% and 2% which should not be enough to significantly alter the measured beam density. However, once the rotor velocity has reached the point where dimers begin to form in the beam, it will be impossible to remove these dimers. Unless they become the object of study their formation will heat the beam as well as reduce the measured beam density at the detector.

4.1.3 Time of Flight

Velocity augmentation of the molecular beam produced by the nozzle is the primary purpose of the rotating source. This means that all possible effects considered in Section 2 that may impact the flow velocity of the beam must be considered. This includes the temperature of the rotor, the centrifugal enhancement of the backing pressure, and possible cluster formation in the beam itself. A clear understanding of the velocity augmentation effect offered by the rotor will require all of these effects be accounted for.

The distance from the collection region of the FIG to the eddy current sensor is typically 12 cm. This single dimension along with the time of flight spectrum can be used to analyze the mean velocity of the produced beam over the entire range of rotor velocities. It is important to note that only the peak location is used for this TOF analysis. A more detailed discussion of the pulse shape is reserved for Section 4 - 3.

The time of flight is calculated for every single peak in the pulse train and including those frequencies that are repeated. The stability of the beam is important, and as seen in Figure 4 - 6, the repeated frequencies produce results very similar to the first data set. The measured time of flight, Δt_m, is calculated by

$$\Delta t_m = t_{rotor} - t_{prox} \tag{4.12}$$

where t_{rotor} is the location of the peak in the FIG signal and t_{prox} is the location of the peak in the eddy current signal. Both time values are calculated using the OriginPro 9.1 peak finding subroutine described in Section 4.1. This is done for all peaks that occur in the collected signal and the results are shown in Figure 4-10 and 4-11. These are fit to a straight line, the values are collected at $t = 10\ ms$, and the results are plotted vs rotor velocity in Figure 4-12.

The eddy current sensor marks a single point in the rotation of the rotor that will be called $\phi = 0$. At this point the rotor angle is 90° from the beam path and the nozzle has direct line of sight with the FIG. The measured time of flight, Δt_m, must be corrected due to the fact that the peak produced in the FIG signal does not originate from $\phi = 0$ but in fact comes from some other angle: ϕ_o. The negative time of flight values for a slowly moving rotor in the backward direction can only be explained by this phenomenon. By simply adding a frequency dependent term

$$\Delta t_a(F) = \left(\frac{\phi_o}{360}\right) F^{-1} \tag{4.13}$$

to the entire time of flight spectrum all the measurements match very closely to the estimated time of flight spectrum.

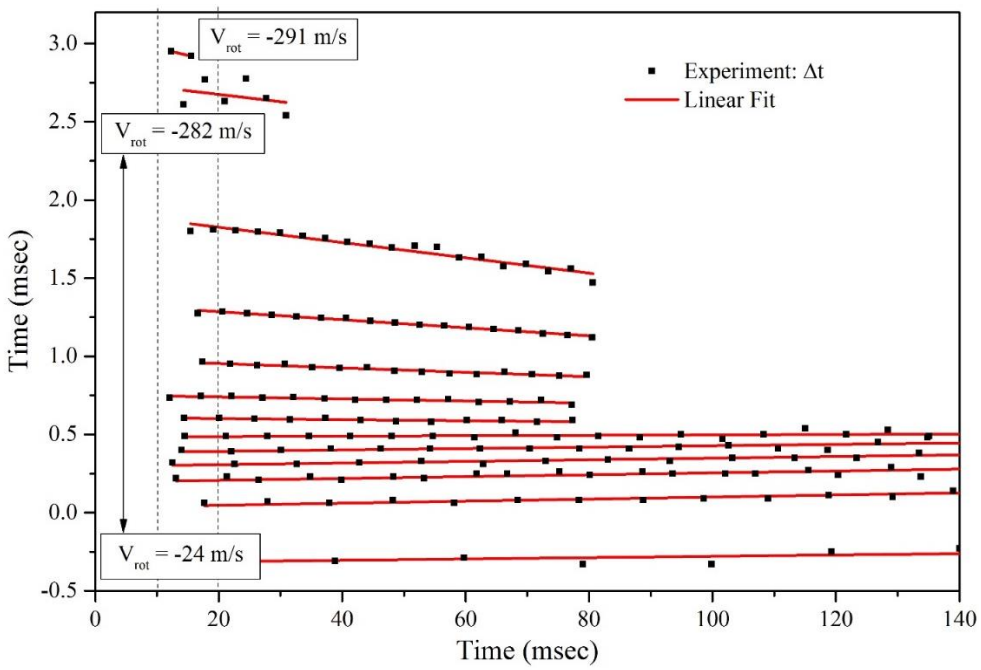

Figure 4 - 10: Time of Flight - Slowing

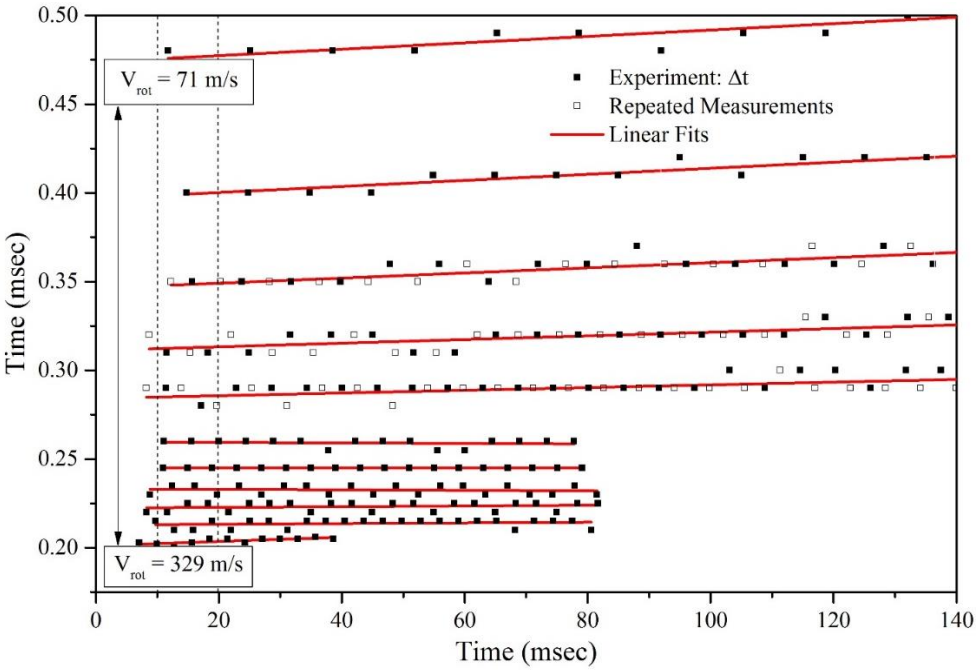

Figure 4 - 11: Time of Flight - Speeding

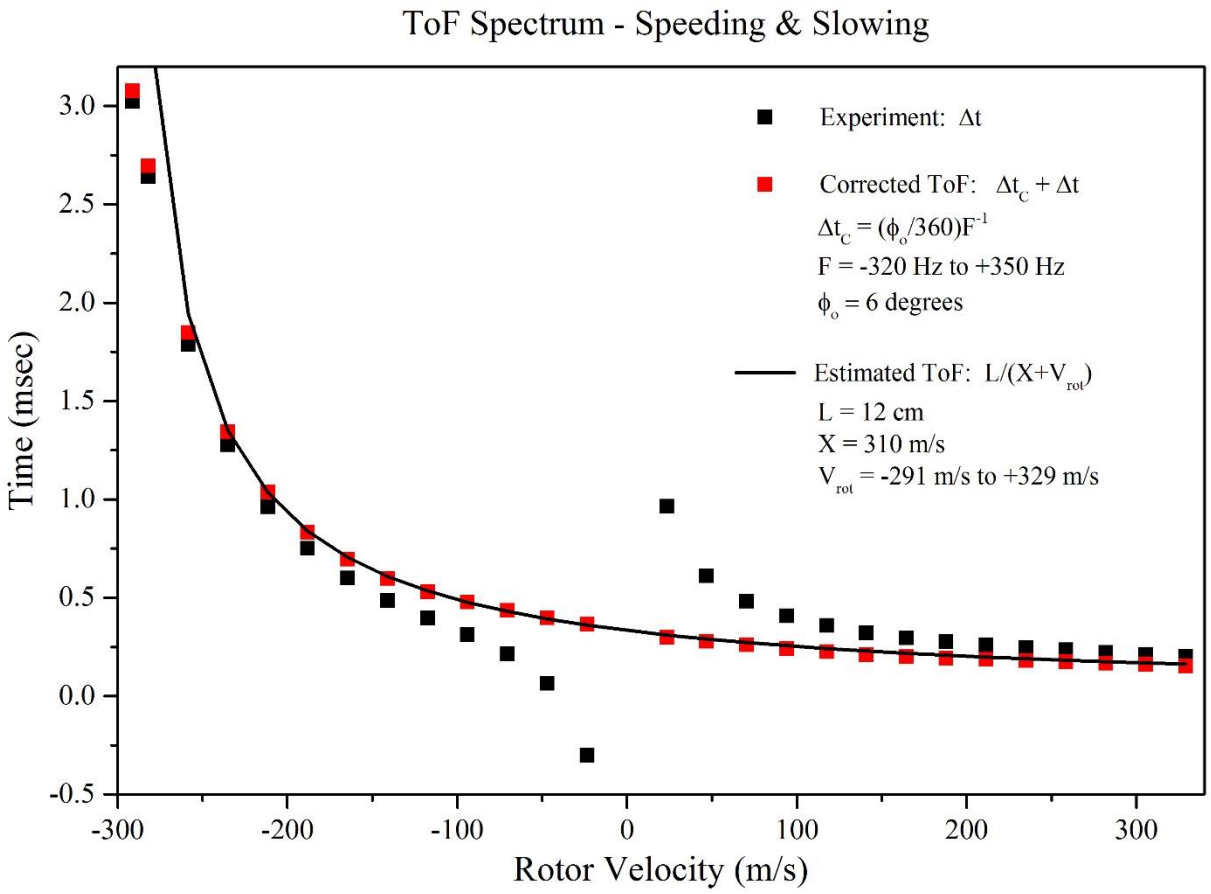

Figure 4 - 12: Peak Time of Flight

Where F is the frequency of rotation and ϕ_o is the true angle that generates the peaks found in the FIG signal. This correction term corresponds to amount of time it takes the rotor to travel from angle ϕ_o to the eddy current sensor. This value is equal in magnitude and opposite in sign for equivalent slowing and speeding frequencies. The largest value of this correction term is for 25 Hz where it is $666\ \mu s$. Since this is larger than the actual time of flight, the peak maximum is able to travel to the detector before the rotor passes into the region that activates the eddy current sensor.

In order to calculate the lab frame velocity of the beam, shown in Figure 4-13, the distance from the nozzle to the FIG collection region must be calculated. It must take into consideration the correction angle ϕ_o. For this arrangement $\phi_o = 6°$ which corresponds to a path length correction of 1.6 cm, and returns an overall beam length, L, of 10.4 cm. A further 0.4 cm is removed due to the thickness of the collection grid region and the protruding nature of the nozzle itself. The lab frame velocity of the beam including these corrections is

$$V_{lab}(F) = \frac{[0.12\ \text{m} - R*\sin(\phi_o) - 0.04m]}{\Delta t_a(F)} = \frac{0.1\ \text{m}}{\Delta t_a(F)} \tag{4.14}$$

which is shown in Figure 4-9. The deviation from the estimated beam velocity can occur due to:

- Heating of the rotor: This occurs due to friction in the motor bearings and potential contact that occurs in the feed system.
- Centrifugal enhancement of backing pressure: A direct consequence of the rotational motion of the rotor and thermal equilibrium of the gas inside.
- Centrifugal force acting on the expanding beam.

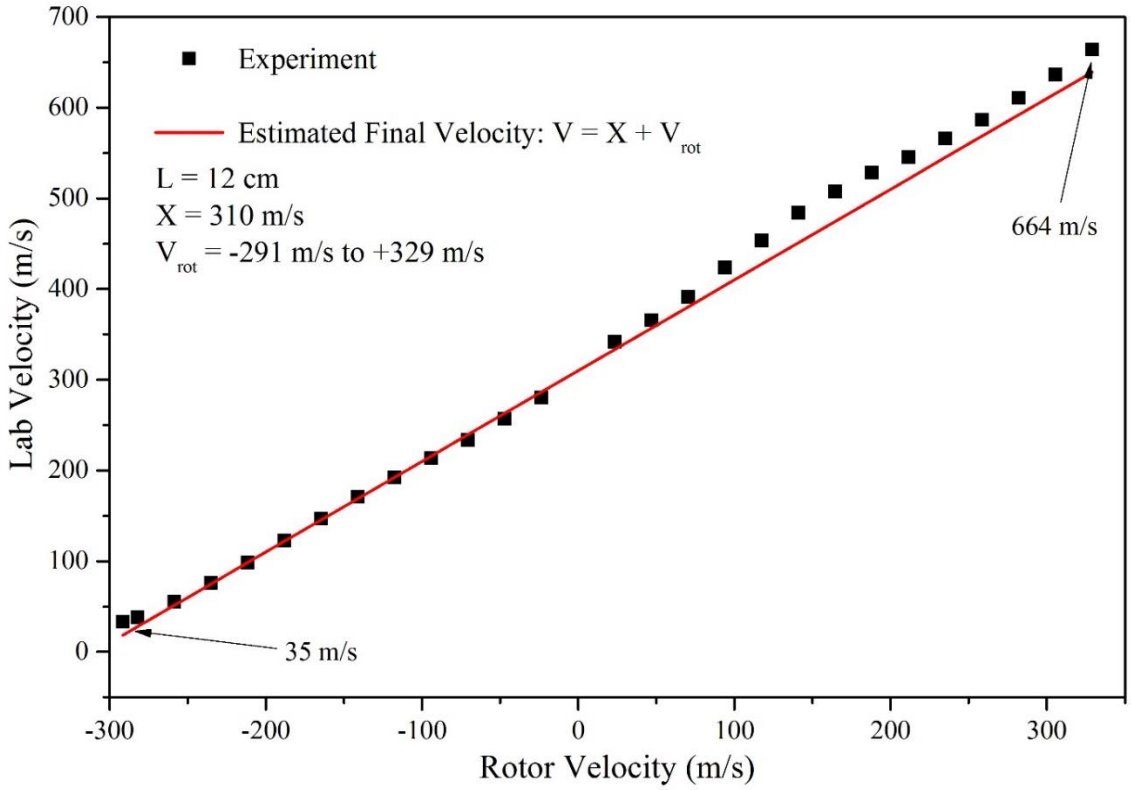

Figure 4 - 13: Slowing & Speeding - Xenon Gas

- Cluster formation within the beam. At extremely high pressures 3-body collisions stabilize the formation of dimers, trimers, and higher order clusters.
- Interference by the skimmer: This is due to backward scattering of gas at the edge of the skimmer and the interaction of this scattered gas with the rest of the beam.

Of these effects the most probable two are heating of rotor due to high temperatures in the gas feed system and the skimmer interference. The gas feed system was designed to minimize the conduction between the stationary components and the stem of the rotor. This design, as described in Section 3.4.2, requires very precise alignment of the mounting stage on which the feed system is mounted. Due to the very close tolerance the possibility exists that contact occurs between these components and the heat generated by this contact propagates through the rotor due to the high thermal conductivity of aluminum.

The skimmer interference is likely to detract from the overall quality of the beam due to its very blunt edge. Unlike the rotor heating dilemma, skimmer interference is well known in beam experiments[48]. As the ensemble propagates into the skimmer region a shock wave is produced at the tip of the skimmer that heats and compresses the beam as it passes through. In some extreme cases this shock wave can completely block the beam[49]. Even for large skimmers, the size used here is 3mm, the transmission can be lower than 60%. The interference is a function of beam density at the skimmer opening as this defines the density of the shock wave. For this reason, the easiest improvement in beam quality for future experiments stems from a simple replacement of the entire skimmer or at least the edge. This has not been done previously due to constraints placed on the shape of the skimmer as can be seen in Figure 4-9. All of the effects mentioned above are included in Table 4-2 which also considers the degradation of the beam density and temperature as well.

Effect	**Beam Temperature**	**Beam Density**	**Beam Velocity**
Rotor Heating	Increase	Slow Frequencies: Decrease	Increase
Enhanced Backing Pressure	Decrease	Increase	Decrease
Centrifugal Force	N/A	N/A	Increase
Cluster Formation	Increase	Decrease	Increase
Skimmer Interference	Increase	Decrease	Increase

Table 4 - 2: Potential Velocity Augmentation Mechanisms

What limits the lowest measured velocities achievable in this velocity augmented beam? One of the goals of this research project is to produce intense beams of cold and slow molecular beams and establish what limits the measurement of even slower beams. In an attempt to measure beams slower than 35 m/s dozens of frequency scans were produced both before, and after, the data shown in this section. From these frequency scans the 4 primary reasons a lower velocity is not attainable are:

- The scattering cross section is velocity dependent and at extremely low beam velocities a large portion of the ensemble will be scattered by the background gas.
- The transverse velocity of the beam is not removed by the velocity of the rotor tip and at very low beam velocities becomes the dominant factor in determining the beam trajectories.
- The very large time of flight, and small rotor period, mean that the pulses overlap and become indistinguishable from one another.
- The number of particles per pulse is a function of the amount of time the rotor spends in the shooting position. As the rotor frequency increases the number of particles per pulse lowers, regardless of the lab frame velocity.

These effects primarily detract from the measured density of the beam and have very little to do with the velocity. However, the peak location is the primary method for determining the velocity and therefore if the density is drastically attenuated by a combination of these 4 effects the velocity becomes impossible to measure. It is possible for the rotor to be used as a continuous source instead of isolating individual peaks. In fact, the RSI paper contained in Appendix 5.1 contains a description of a mechanical chopping device which can be used to 'pulse' a continuous beam from the rotor. Methods to counteract these effects are contained

Effect	Corrective Measure
Scattering cross section	Better vacuum along the beam path
Transverse velocity	Cooling the rotor Hexapole guides for polar molecules
Pulse Overlap	Longer rotor Cooling the rotor
Number of particles per pulse	Longer rotor Chopping a continuous beam

Table 4 - 3: Limitation of Beam Velocity Measurements

in Table 4-3. It should be noted that this reduction in beam intensity prevents a slow velocity from being measured, but that does not imply that the lower velocities are not produced. As is shown in Table 4-3, the improvements for the rotor system that will likely yield slower velocities include a longer rotor and a method for cooling the rotor. The fastest and slowest pulses described in this thesis are shown in Figure 4-14. The current iteration of the experimental setup does not allow for a longer rotor due to space constraints. The construction of a new chamber for the longer rotor is planned for next year.

Cooling the rotor requires it to be in a stationary position and cooling is applied either from the stem area close to the motor or the nozzle area near the tip. A copper block attached to a rotatable feedthrough can be used to contact the rotor once it is in the appropriate position. The block is cooled via liquid nitrogen using thermally isolated feedthroughs in the vacuum chamber. Unfortunately, due to the high thermal conductivity of aluminum, the cooling that is applied to the rotor also cools the motor bearings. At liquid nitrogen temperatures it is likely that the grease used in the motor bearings will solidify and the motor will not turn at all. Attempting to spin the motor at even low frequencies can damage the motor windings. This problem ultimately prevented successful cooling of the rotor in the past. One method to circumvent this problem is using a lower sheath of the rotor stem that has very low thermal conductivity. One possibility is ceramic, though it is unclear whether it would survive the vibration and stress that occurs at very high motor frequencies.

4.1.4 Pulse Width

In a fashion similar to the beam density and the beam velocity, the pulse width of each peak in the pulse train is measured independently. This width is then plotted versus the temporal

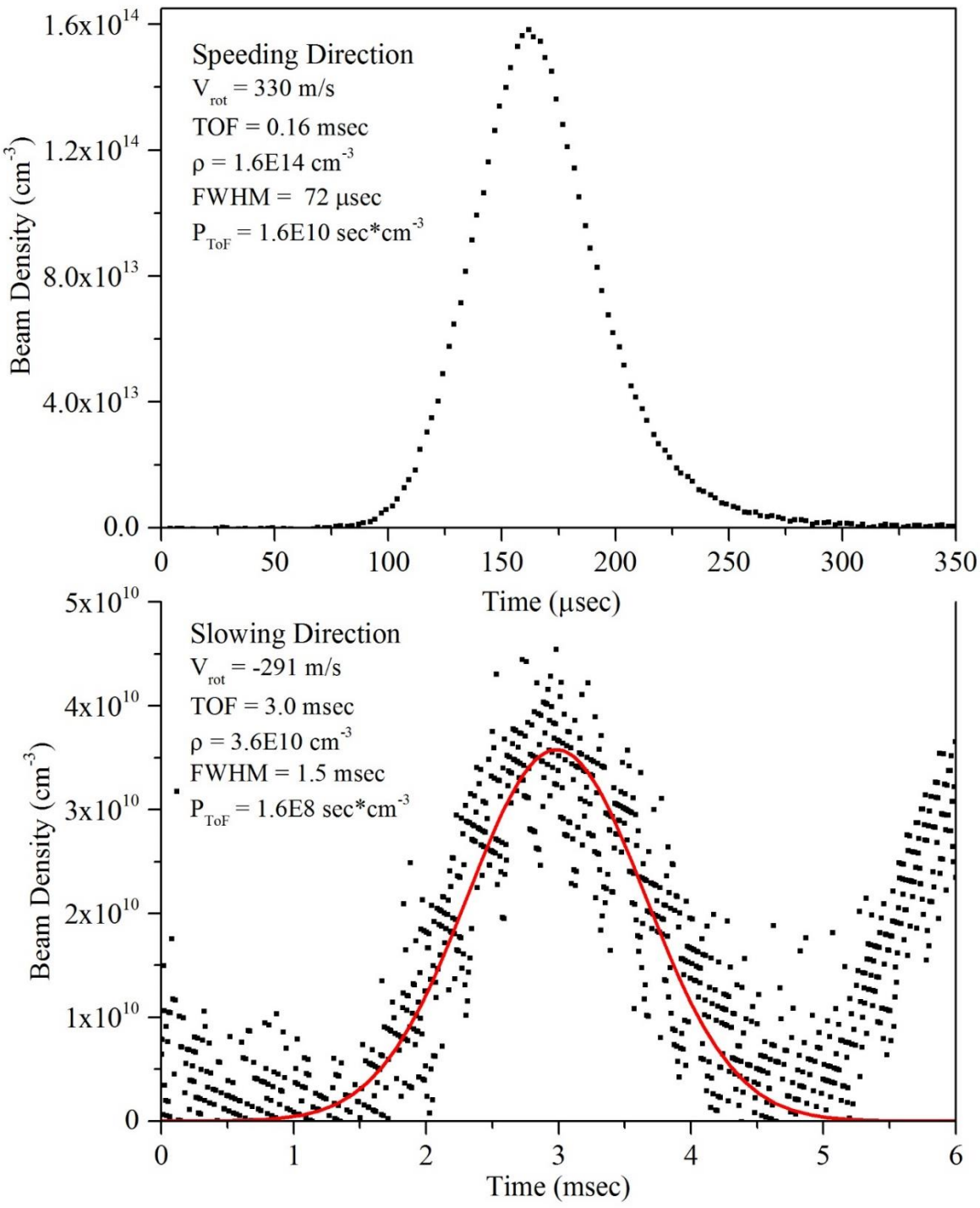

Figure 4 - 14: Fastest and Slowest Xenon Beams Produced

location of the peak itself and a straight line is fit to the resulting data points. The straight line is evaluated for a time which corresponds to the maximum density of the produced pulse train. This means, even if a peak does not occur at the maximum of the beam density its properties can be estimated based on the performance of all other peaks in the pulse train. Unfortunately, the peak finding algorithm utilized in pervious sections only produces a single (x,y) coordinate corresponding to the temporal position and amplitude of the peak itself. It does not entail any information about the shape, or width, of the pulse.

To gain insight into the pulse width OriginPro 9.1 is used again and a peak fitting algorithm is used with a Gaussian fitting function. To execute the Peak Fitting subroutine use the Analysis dropdown menu and select the Peaks and Baseline subtab, select the Peak Analyzer subtab, and finally select the Open Dialog option. The dialog box which opens will allow the user to define several parameters related to the Peak Fitting subroutine. These parameters include the fitting function to be used, the removal of a baseline signal, the number of points that each peak must contain, and whether any smoothing is to be applied to the data within the subroutine. The subroutine makes defining each parameter very easy by plotting the raw data side by side with the dialog box. On this raw data the peak fitting results are displayed and automattically refreshed when any parameters are altered. Once the user is satisfied with the peak fits the data is saved alongside the original data.

For most frequencies the peaks produced by the rotor are assymetric. This can be seen in Figure 4-5 which has a very modest rotational frequency of 250 Hz. The peaks which have the most symmetry correspond to very high rotational frequencies because the shape of the pulse is dictated by the velocity spread. Both accelerated and decelerated pulses become

more symmetric as the rotor frequency is increased, this can be seen in Figure 4-14 which shows the fastest and slowest beams produced in this particular data set.

To begin the analysis of peak width consider the "shutter" function of the rotor generated by the angles explained in Section 2.3.3. These angles are defined by the detector line of sight for the relevant skimmer sizes:

$$\Delta\phi = (\phi_{2*} - \phi_{3*})F^{-1} \tag{4.15}$$

Where ϕ_{2*} and ϕ_{3*} are defined as the region in which the detector is fully illuminated. ϕ_1 and ϕ_4 are defined as the rotor positions in which the detector begins to see any signal from the nozzle, and the position where the detector loses sight of the nozzle. From those two definitions a first order approximation of the FWHM becomes

$$FWHM = \left[\frac{(\phi_1 - \phi_{2*})}{2} - \frac{(\phi_{4*} - \phi_{3*})}{2}\right] F^{-1} \tag{4.16}$$

Which for a 3mm skimmer returns:

$$FWHM = \left[\frac{14}{360}\right] F^{-1} \tag{4.17}$$

This is plotted in Figure 4-16 in dark red. A correction to this value is included that considers beam narrowing for the pulse width in a speeded beam. This effect is described visually in Figure 4-15 and shows how the rotor velocity adds to the supersonic flow velocity in the longitudinal direction only and does not contibute to the transverse velocity of the beam.

The second contribution to the FWHM of the pulse is due to longitudinal spreading caused by the velocity spread of the beam. This depends on the amount of time given for

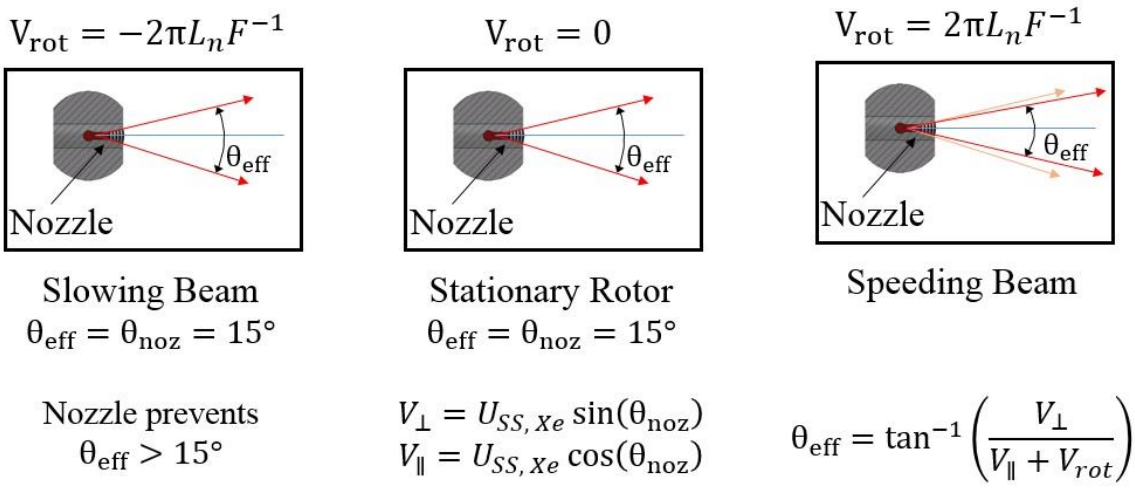

Figure 4 - 15: Beam Narrowing Effect

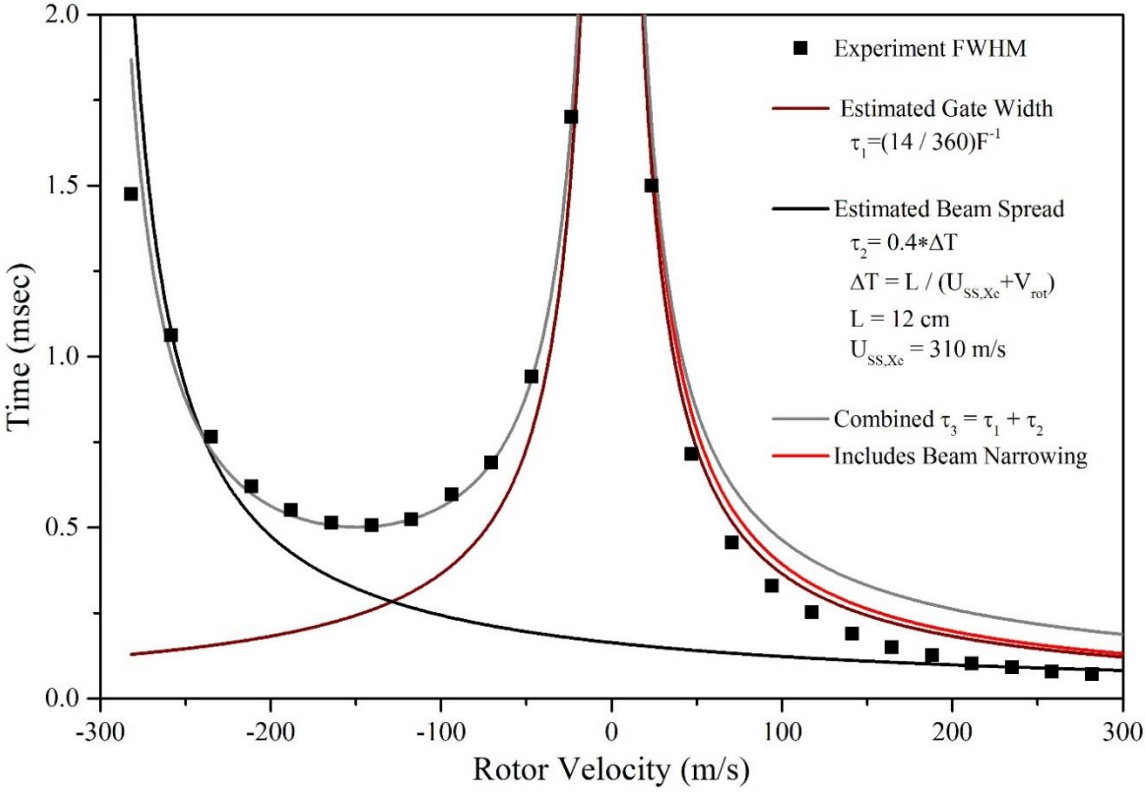

Figure 4 - 16: Peak Width

this expansion to occur, which is exactly the time of flight of the pulse. The TOF is shown in Figure 4-16 and is multiplied by a constant whose magnitude is determined by the ratio of the supersonic velocity spread vs the final flow velocity of the beam. This parameter is chosen to best fit the data produced by the rotor in slowing direction since the time-of-flight is much large in magnitude.

The deviation of the data from the estimated FWHM of the pulse is due either to a deviation in τ_1 due to skimmer interference, or to a deviation in τ_2 due to the narrowing of the velocity spread. The densities produced by the beam, shown in Figure 4-8, span over 3 orders of magnitude. Since the skimmer interference is a function of beam density in the edge region it follows naturally that it would deflect a portion of the beam and reduce the acceptance angles defined by the beam line of sight. Likewise if the beam is cooled from the increasing backing pressure caused by the centrifugal enhancement of the input pressure. The deviation of τ_1 should occur only in the forward direction where the highest density pulses occur near the skimmer and τ_2 should occur in both rotating directions since it depends on the pressure behind the nozzle which is ultimately dependent on V_{rot}^2.

This section only considered the FWHM of the pulse qualitatively. Other characteristics of the pulse will be discussed later in Section 4.1.5. This is because the shape of the pulse for different skimmers is easier to understand when considering data generated by a stationary rotor that is moved incrementally through the shooting position.

4.1.5 TOF-Integrated Density

The fitted pulses generated by OriginPro 9.1 also contain the area of the pulse, which is useful as long as the background contribution has been removed from the signal. Figure 4-17

shows the TOF integrated density of every fitted peak in the pulse train as well as an exponential decay fit to these values. This allows a qualitative understanding of how much gas makes it into the detector region for a pulse occuring at $t = 15ms$. It is interesting to note that even though the beam density increases by 3 or 4 orders of magnitude the integrated density only changes about two orders of magnitude. This is due to the F^{-1} reduction in pulse width that influences high frequencies pulses. As can be seen in Figure 4-8, the beams generated at high rotor velocities in the forward directions can have pulse widths on the order of $100\ \mu sec$. For rotor frequencies larger than those measured, a lower bound of around $50\ \mu sec$ can most likely be achieved.

An estimate of the integrated intensity, whose experimental values are shown in Figure 4-17 and 4-18, is generated by multiplying the pulse width estimate generated in the Section 4.1.3 with the beam density estimate from Section 4.1.2. Unfortunately, the estimates in both of these sections were larger than the values obtained by experiment. Thus the deviations carry over to this estimate as well and, especially in the forward direction, the estimated TOF integrated density is much larger than the data obtained from the OriginPro fitting subroutine. This overestimation is obvious in Figure 4-19.

Even though the pulse shapes generated by the rotor are not symmetric, and thus not exactly representative of a shifted gaussian fitting function, the values are very similar to what would be achieved with an assymetric fitting function composed of a series of gaussian fitting functions as has been done previously[50].

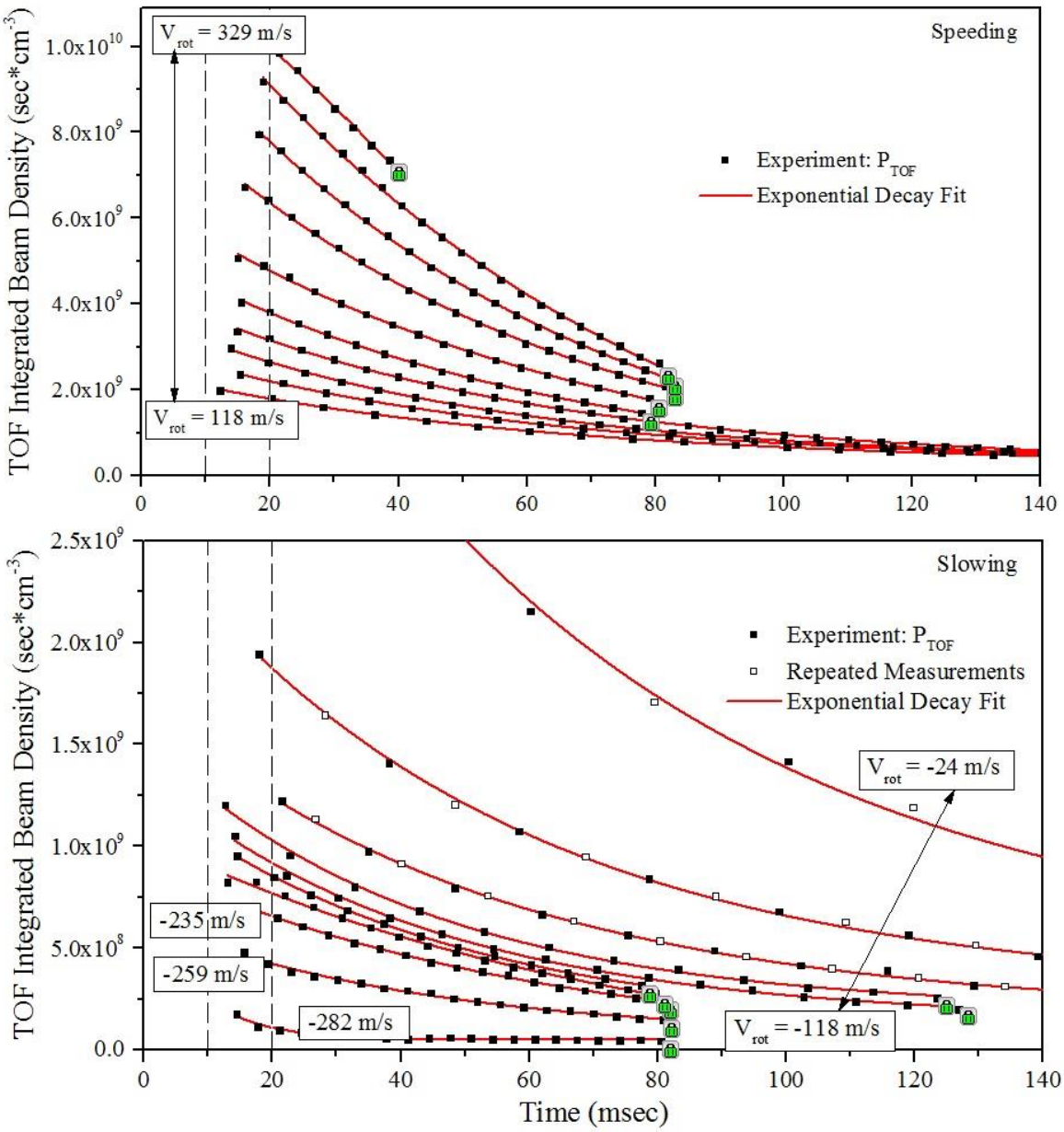

Figure 4 - 17: TOF Integrated Density - Slowing & Speeding

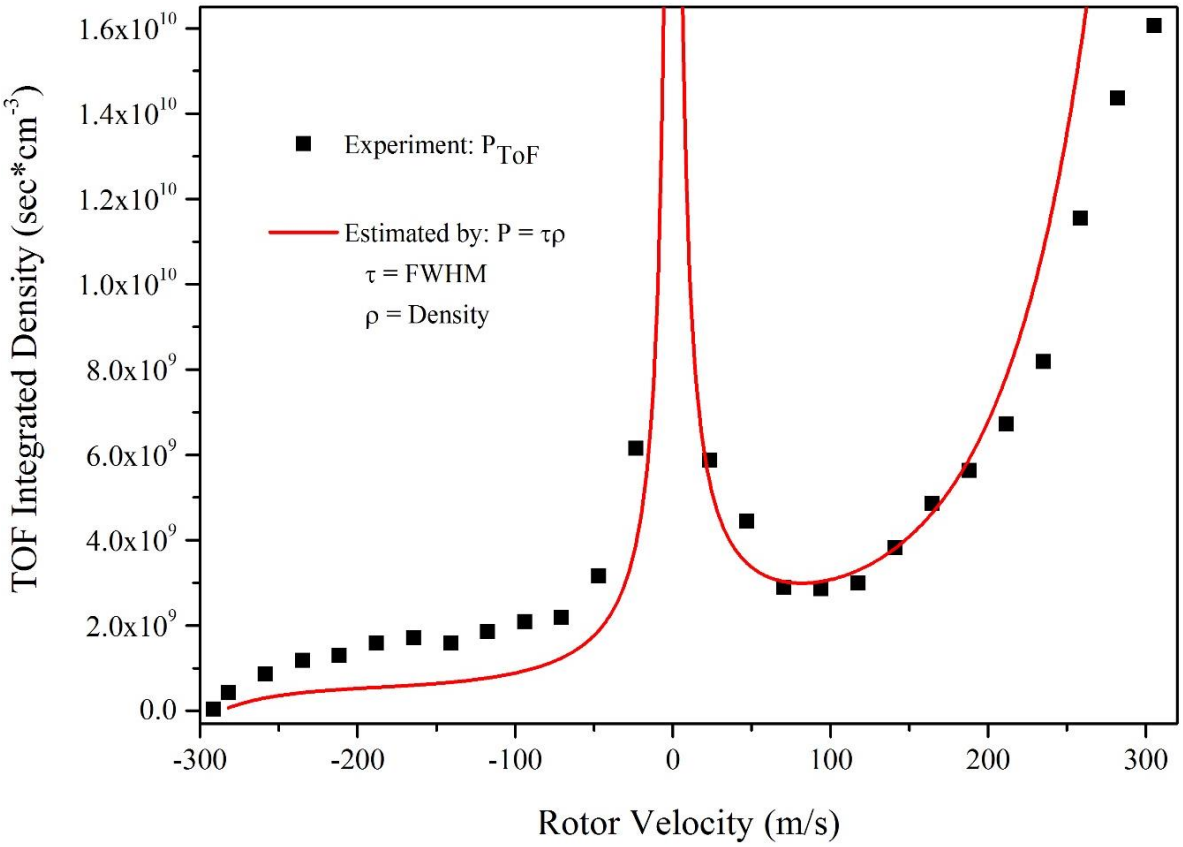

Figure 4 - 18: Peak TOF Integrated Density

4.1.6 Pulse Shape

To understand the peak shapes produced by the rotor throughout the entire range of frequencies the signal, S_{FIG}, must be considered as a product of two functions

$$S_{FIG} \propto V_{FIG}(\phi) * n(\phi) \tag{4.18}$$

Where V_{FIG} is the volume of the detection region in which the beam is being measured, and n is the density of the pulse considered at a distance r from the nozzle. Both of these are expressed as a function of the rotor angle and are shown in Figures 4-19 and 4-20.

Figure 4-19 shows how the radial distribution of the number density causes the peak to be shifted from $\phi = 0$, where it would be expected, to an angle which positions the nozzle closer to the detector. The constants in the number density equation are normalized in Figure 4-19 as they are not dependent on the rotor angle. This is the first theoretical indication that the peaks produced by the rotor do not correspond to the shooting position: $\phi = 0$.

The differential volume element of the detection region creates a "shutter" function or "gate" function as well which is dependent on the angles described in Section 2.3.3. This gate function, two of which are shown in Figure 4-20, convolutes the signal produced by the detector. The result of this convolution is a shifted peak location and faster rise times on each of the sides. The peak location is once again shifted away from the true "shooting" position but the magnitude of this shift is smaller than expected. While these product functions give an adequate estimate of the peak shapes as seen in Figure 4-21 they do not generate a peak location near $\phi = 6°$. This can be due to an inadequate estimate of the gate function representing the differential volume element.

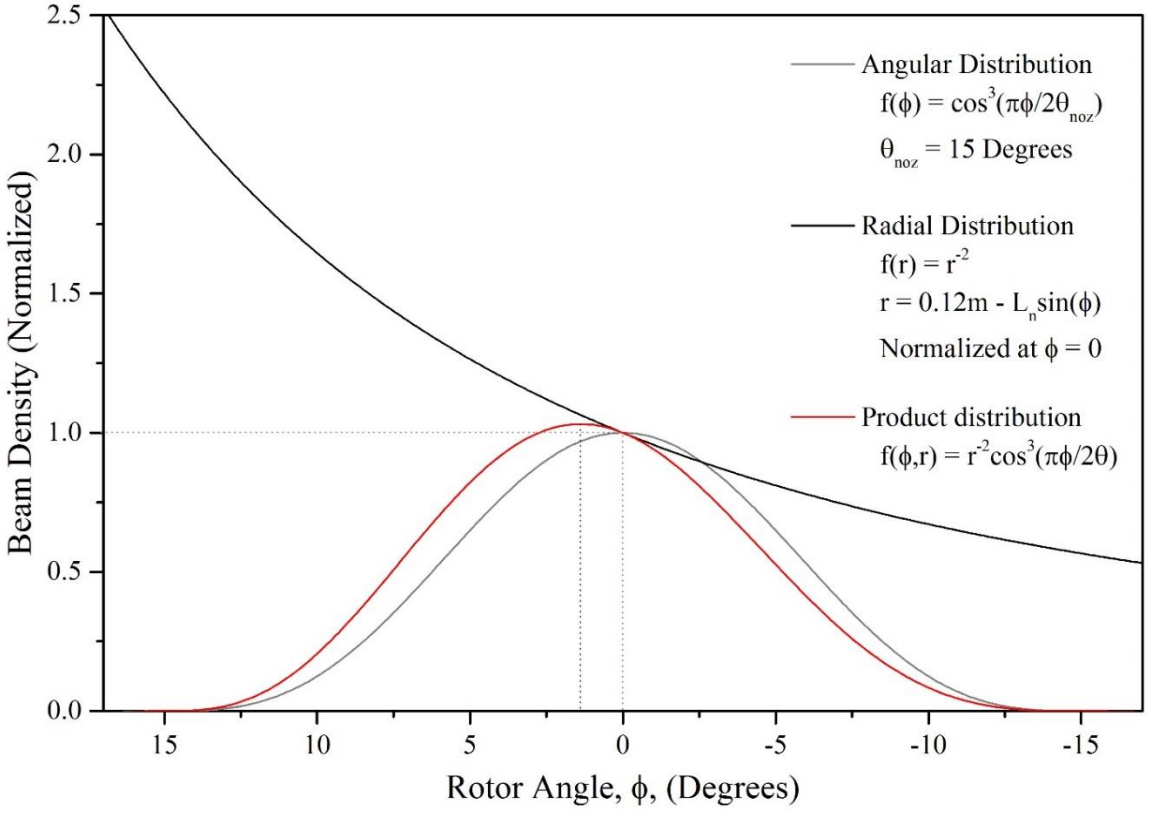

Figure 4 - 19: Supersonic Beam Density Distributions

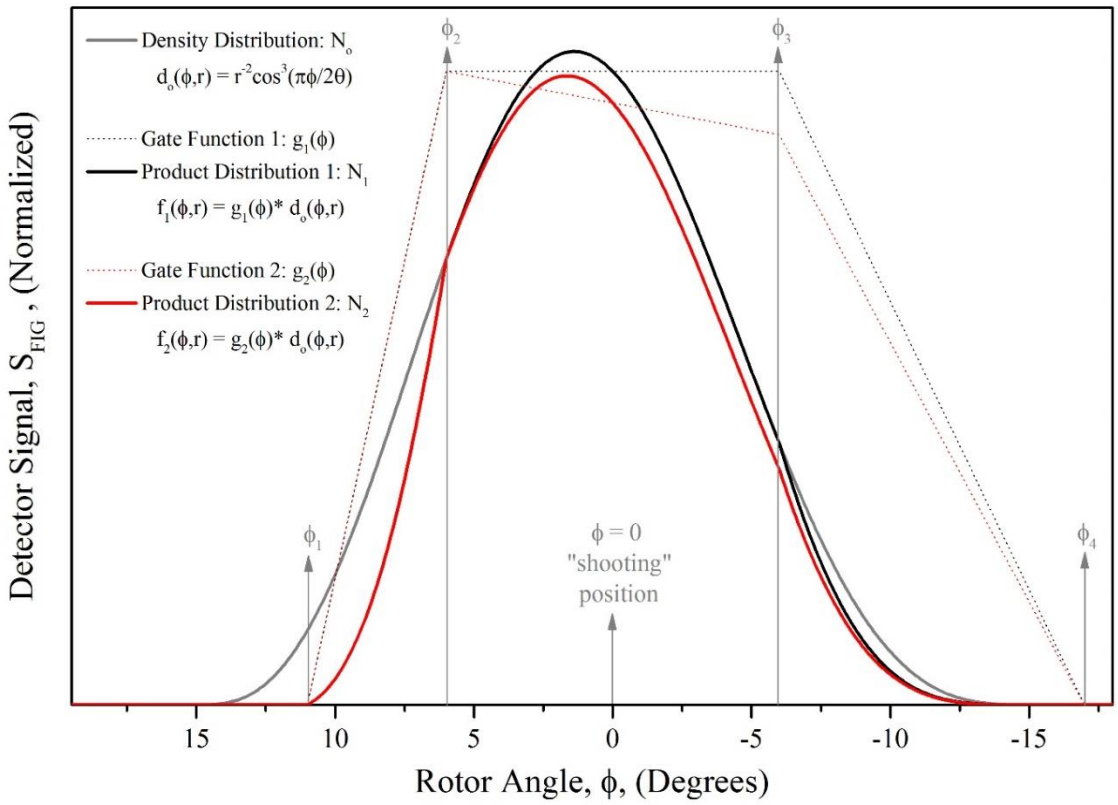

Figure 4 - 20: Estimated Peak Shape

In Figure 4-21 the portion of the FIG signal attributed to background gasses in the detection chamber have already been removed. In addition, the time positioning of every peak has been corrected by the time constant developed in the previous section

$$\Delta T_C = \left(\frac{\Phi_o}{360}\right) \mathrm{F}^{-1} \tag{4.19}$$

Where ϕ_o represents the angle between the eddy current sensor at $\phi_o = 0$ and the rotor position which generates the maximum in S_{FIG}. Finally, the peak amplitudes have been normalized to allow an easy comparison of all peak shapes generated in the entire spectrum of frequencies.

It is easy to see that the peaks generated at the lowest rotor frequencies have a similar shape. Their shape is determined not by the velocity distribution of the beam, but instead by the gate function described in Figure 4-20. This is because the rotor velocity is small compared to the flow velocity of the gas, and thus the particles are detected prior to the rotor angle changing a significant amount. For higher rotational frequencies the rotor moves through the angles defining the gate function before any gas arrives at the detector. As the gas travels along the beam path it has a chance to spread and effect the peak shape. This is directly dependent on the final time of flight of the beam as was seen when analyzing the FWHM of the signal. However, very high frequencies in the speeding direction produce symmetric profiles and have a very short time of flight. This may be due to the beam narrowing effect reducing the angular width of the gate function which moves ϕ_3 and ϕ_4 to smaller vallues.

To improve this gate function estimation an integration over the detection region would provide a realistic $g(\phi)$. It is the intersecting volume of a cone and a cylinder. Where

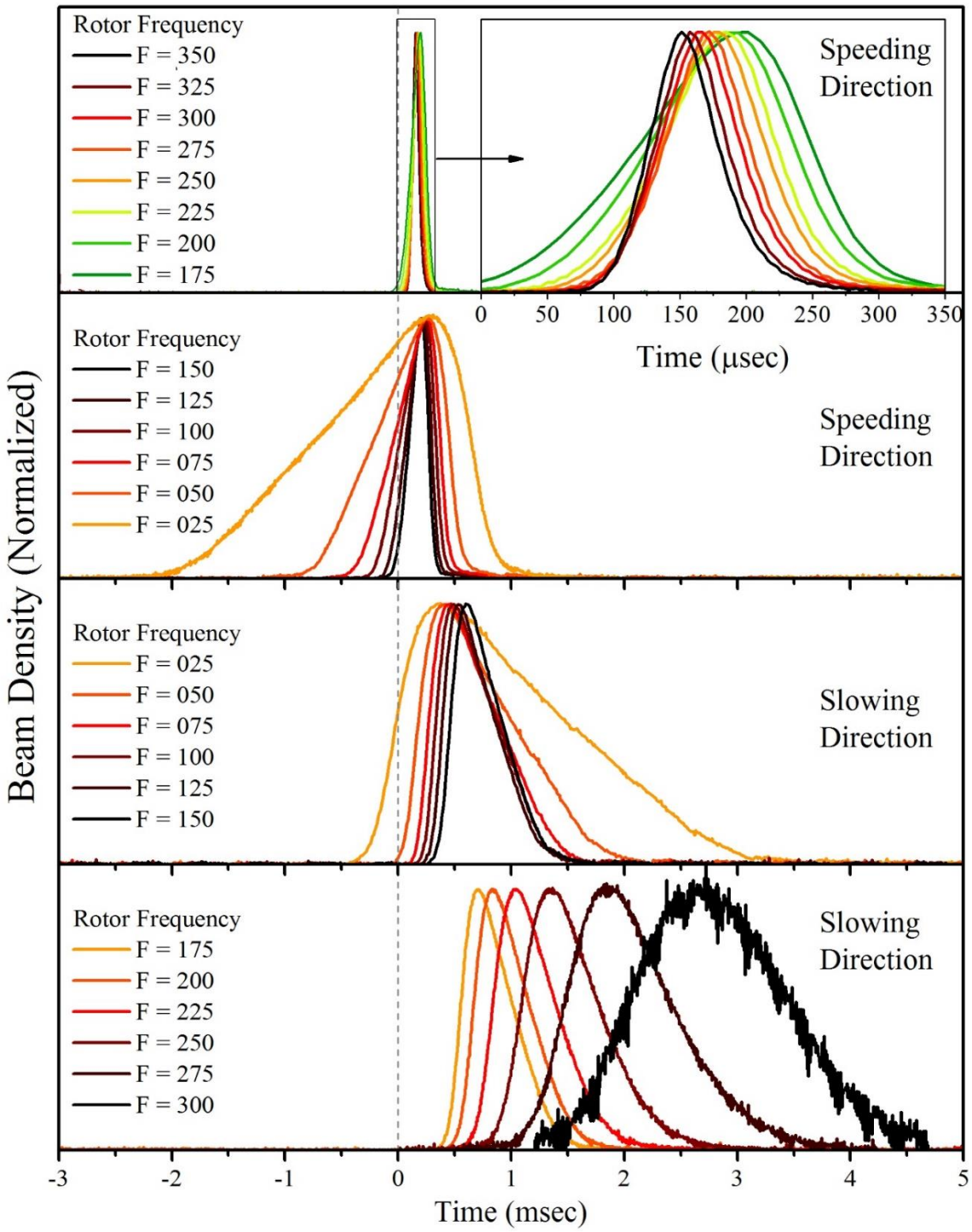

Figure 4 - 21: Peak Shape - Slowing & Speeding

the cone represents the beam whose point, shape, and direction are determined by the nozzle positions and skimmer location. The detector is represented by the cylinder.

4.2 Experimental Parameters

Now that all the properties of a complete frequency scan have been established the experimental parameters that effect the beam quality can be discussed in detail. These are all established by the user prior to initializing the data acquisition program and are recorded as the title of the file in which the data set is recorded. In this way no initial processing of the data is needed by the user during a data scan. The file name: 01 – BWD – 025 Hz – Xe – 900 Torr – FS 2.6 – 1.0 mA is describing the first set of data in this particular scan, and the rotor is spinning in the slowing direction at 25 Hz, and xenon gas is being used at a reservoir pressure of 900 Torr, and the foil shield is at position 2.6, and the detector gain is 1.0 mA. The rest of Section 4.2 is used to discuss the variation of these parameters. Where additional data is needed, it is provided, but Section 4.1, and particularly the high quality data shown in Figure 4-21, provide a basis for much of the discussion.

4.2.1 Rotor Frequency and Direction

At very low rotational frequencies both directions produce a similar peak profile with the only difference being the time reversal. This is due to the fact that the gate function is dictating the beam profile and not the flow velocity of the gas. In this region from 10 to 20 Hz the rotor takes around 3 ms for the rotor to move through 10 degrees of rotation. While the time of flight in this regime is an order of magnitude smaller for the heaviest, and slowest, of gasses. This huge difference is what allows the gate function to dictate the profile shape.

For higher rotational frequencies the gasses must be discussed in light of their atomic weight. For heavier gasses such as xenon or SF6 the centrifugal enhancement of the input pressure becomes quite dramatic. This allows very large peaks to be seen at very low emission current values of around 0.05 mA. At least in the forward direction. In the backward direction the transverse spreading of the beam and the very close pacing of the peaks eventually create a continuous source with no discerable peaks. Lighter gasses did not experience the dramatic centrifugal enhancement but due to the larger flow velocity of these lighter gasses the signal remained quite strong even across a velocity range of 700 m/s.

4.2.2 Reservoir Pressure

For the slowest beams described in this thesis a source gas of xenon was used because it had the slowest lab frame velocity. In addition it has the advantage of being an atomic gas meaning it is very efficiently cooled during a supersonic expansion. It is also a condesible gas and therefore pumps very efficiently from the system thereby reducing pumpdown time between pulses. It is because of these advantages that the supply pressure was tested with xenon exclusively and other gases were simply tested to verify the velocity augmentation properties of the produced beam.

For the supply pressure test the gas manifold described in Section 3.4.2 was initially pumped down overnight by an attached diffusion pump. The pressure in the morning read less than 10 microns meaning there were no significant leaks into the system from atmosphere. Once the rest of the experiment has been prepped the gas manifold is filled with xenon and pumped down to 100 microns at least two times to verify purity of the gas. Then the manifold is pressurized to 900 Torr for the first set of scans. At this point the rotor is cycled through a set of frequencies and data is collected for each. The pressure is then

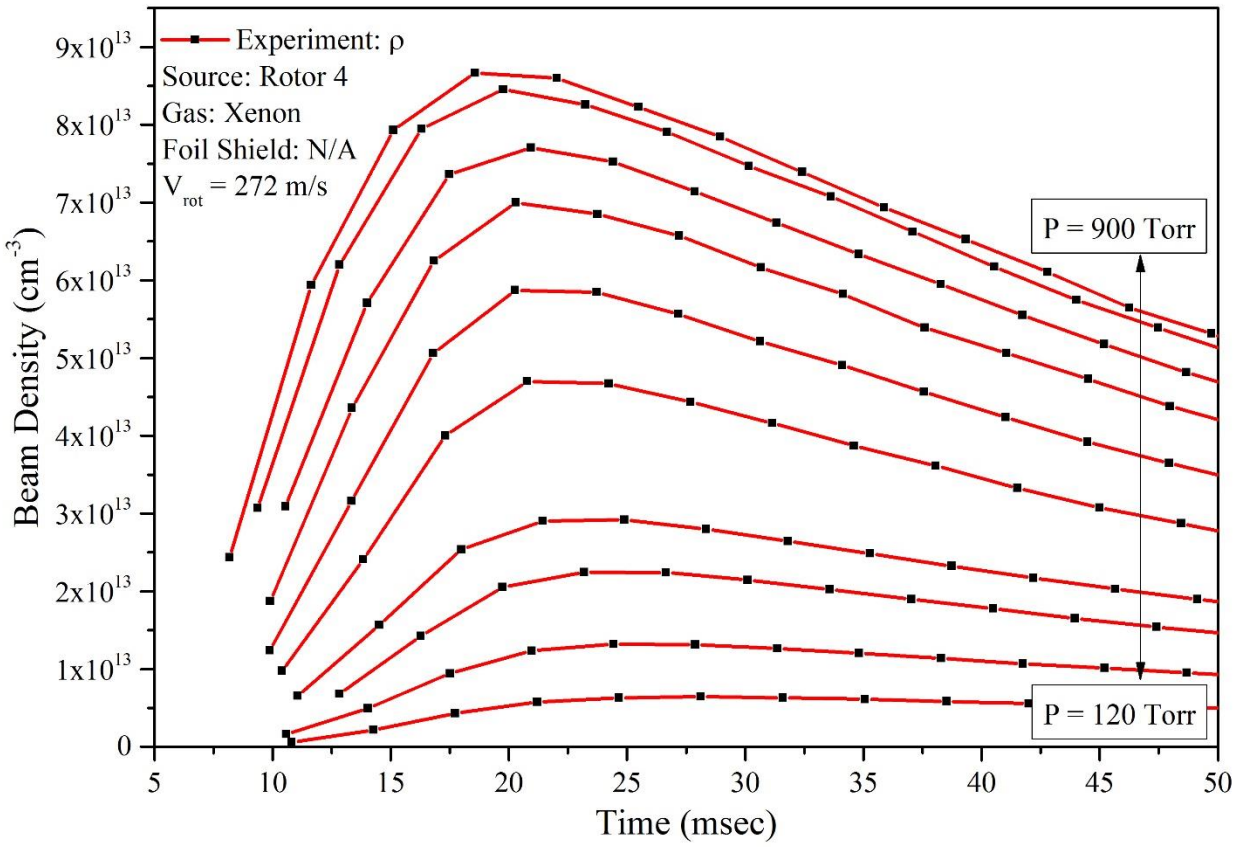

Figure 4 - 22: Density Profile - Pressure Variation

reduced with a throttling valve and an Edwards rotary vane mechanical pump. This process is repeated, producing the peak profiles shown in Figure 4-22, until the manifold is brought down to several Torr and the signal produced by the rotor is barely visible even at the highest allowed gain settings of the detector.

This data is processed using the same technique as Section 4.1.2, namely the peak finding subroutine in OriginPro allows the peak amplitudes to be plotted as a function of time. Where time t=0 corresponds to the IGBT signal which cycles the solenoid valve and begins to fill the rotor. The gas is not seen immediately from the nozzle because the solenoid requires time to respond to the actuating current and the gas requires time to travel through the feed system, down the rotor, out the nozzle, and through the vacuum chamber.

As can be seen in Figure 4-22, once the density profile of the peak has been collected, the entire pressure range can be plotted for individual frequencies. These frequencies were chosen because they correspond to integer values of the centrifugal enhancement term described in Section 2.3.1. Meaning that the chosen frequencies will produce effective pressures behind the nozzle in integer unit of the initial pressure.

Upon closer inspection of Figure 4-22, it becomes apparent that the locations of the peak in the density profile change with pressure as well. This effect has been noted before[39] and in order to get a better grasp on the peak location the profiles are normalized. This normalized profile is shown in Figure 4-23, and it becomes very obvious how the maximum of the density produced by the rotor, and sampled by the skimmer, evolves with time. This feature is not unique to the frequency chosen in Figure 4-22 and 4-23. In fact, Figure 4-24 combines the time locations of these density maximums for all the frequencies

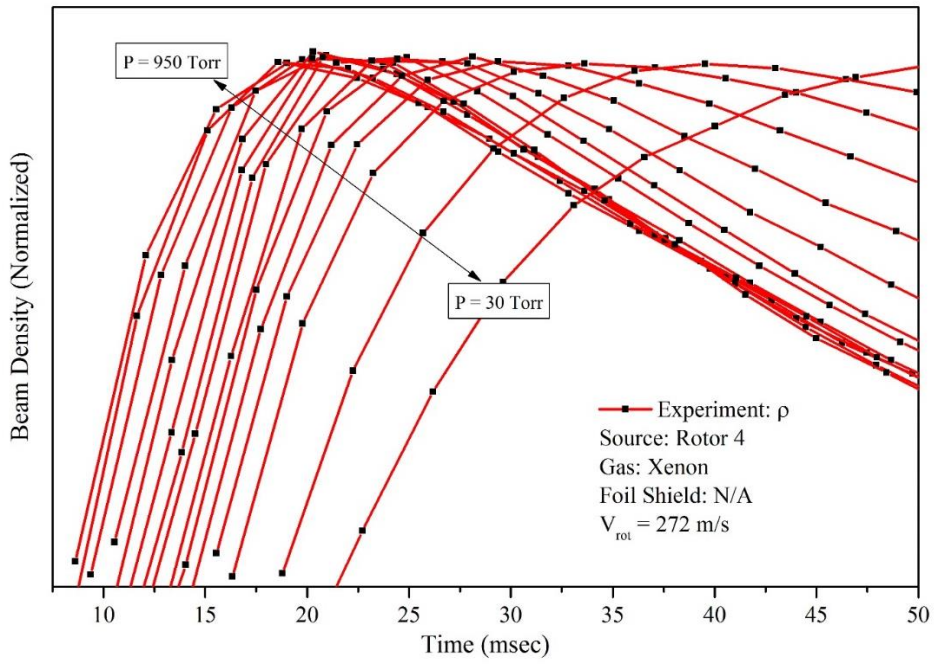

Figure 4 - 23: Normalized Density Profile - Pressure Variation

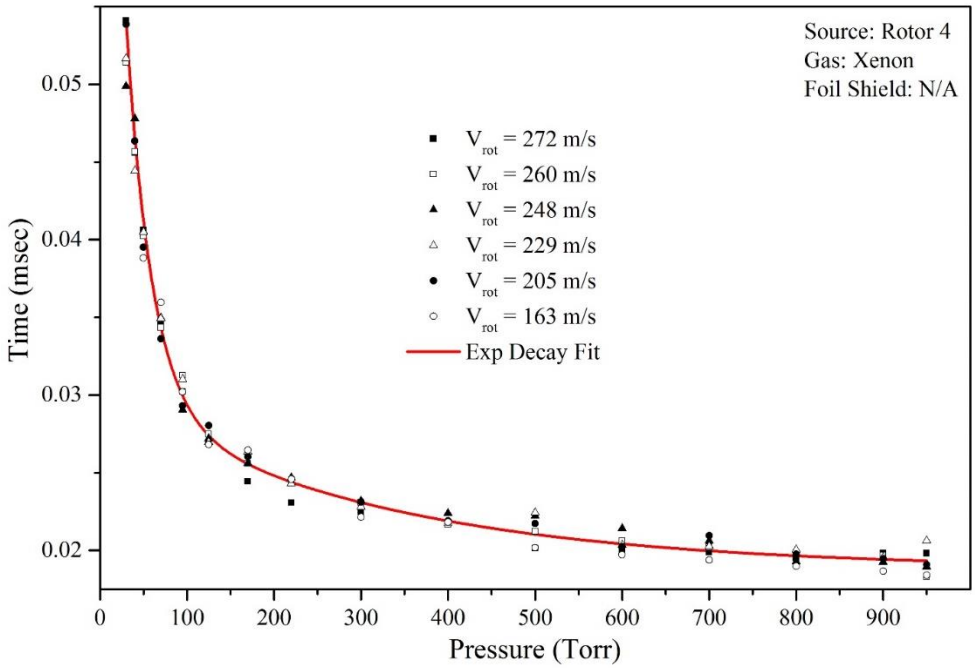

Figure 4 - 24: Density Maximum – Temporal Location

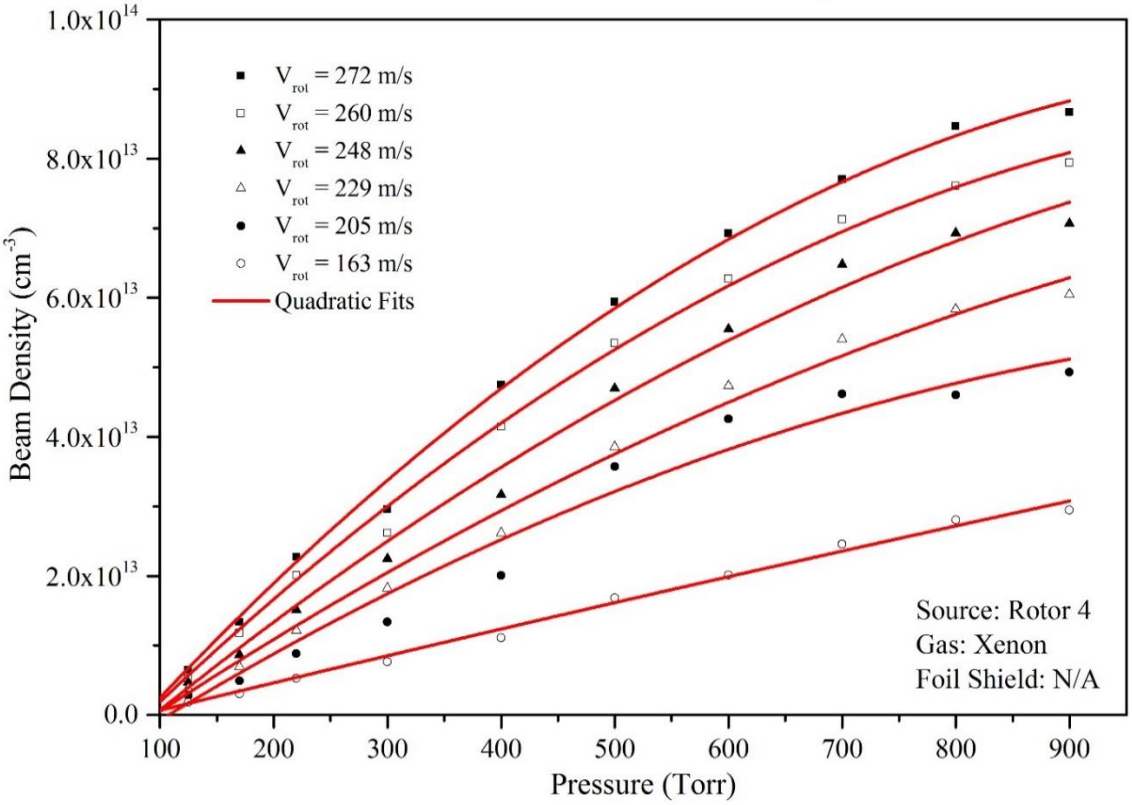

Figure 4 - 25: Density Maximum - Amplitude

in this study. The data is fitted to an exponential decay fit which shows that an increase in reservoir pressure does not reduce the response time of the valve or make the gas travel faster down the rotor path. If either of these occured then the time variation would have been altered.

It is in Figure 4-25 where the centrifugal enhancement of the input pressure becomes obvious. For a given pressure the highest forward frequency collected in the scan will always produce the highest beam density. This is due to not only the centrifugal enhancement but also to the final lab frame velocity of the beam as is seen in Figure 4-8. A simple linear fit is expected but the skimmer interference is proportional to the beam density in the skimmer edge region and thus some attenuation occurs.

Lighter gasses are not expected to experience such an extreme centrifugal enhancement because of their smaller mass. In addition to their lighter mass they also have a much faster flow velocity which means that the density variation due to the lab frame velocity will be smaller for a given rotor frequency.

4.2.3 Skimmer Size and Shield Installation

The shape and location of the skimmers determine many factors of the produced beam. This is obvious because it is the only thing which the beam must travel through before it arrives at the detector. The 7 skimmers manufactured throughout the years are all shown in Figure 4-9. The longer skimmers have been put to use more recently and have a sharper edge than the older, shorter skimmers. The inside edge of the skimmer determines the detector line of sight, and thus is a vital parameter to determining the density profile of the beam. Larger skimmers, for instance the 3 mm and 5 mm skimmers produce a similar peak shape because

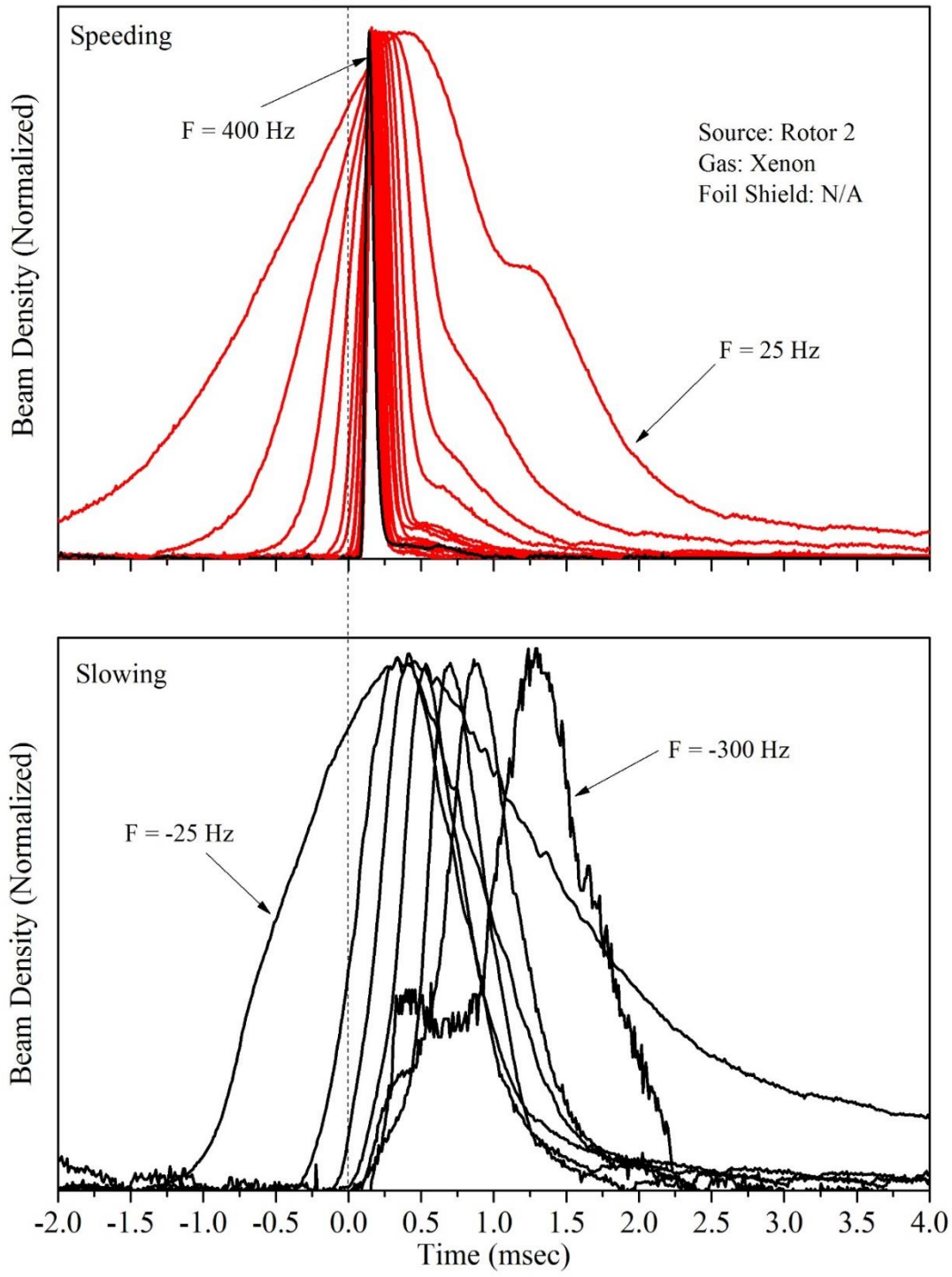

Figure 4 - 26: Peak Shape Progression - 1 mm Skimmer

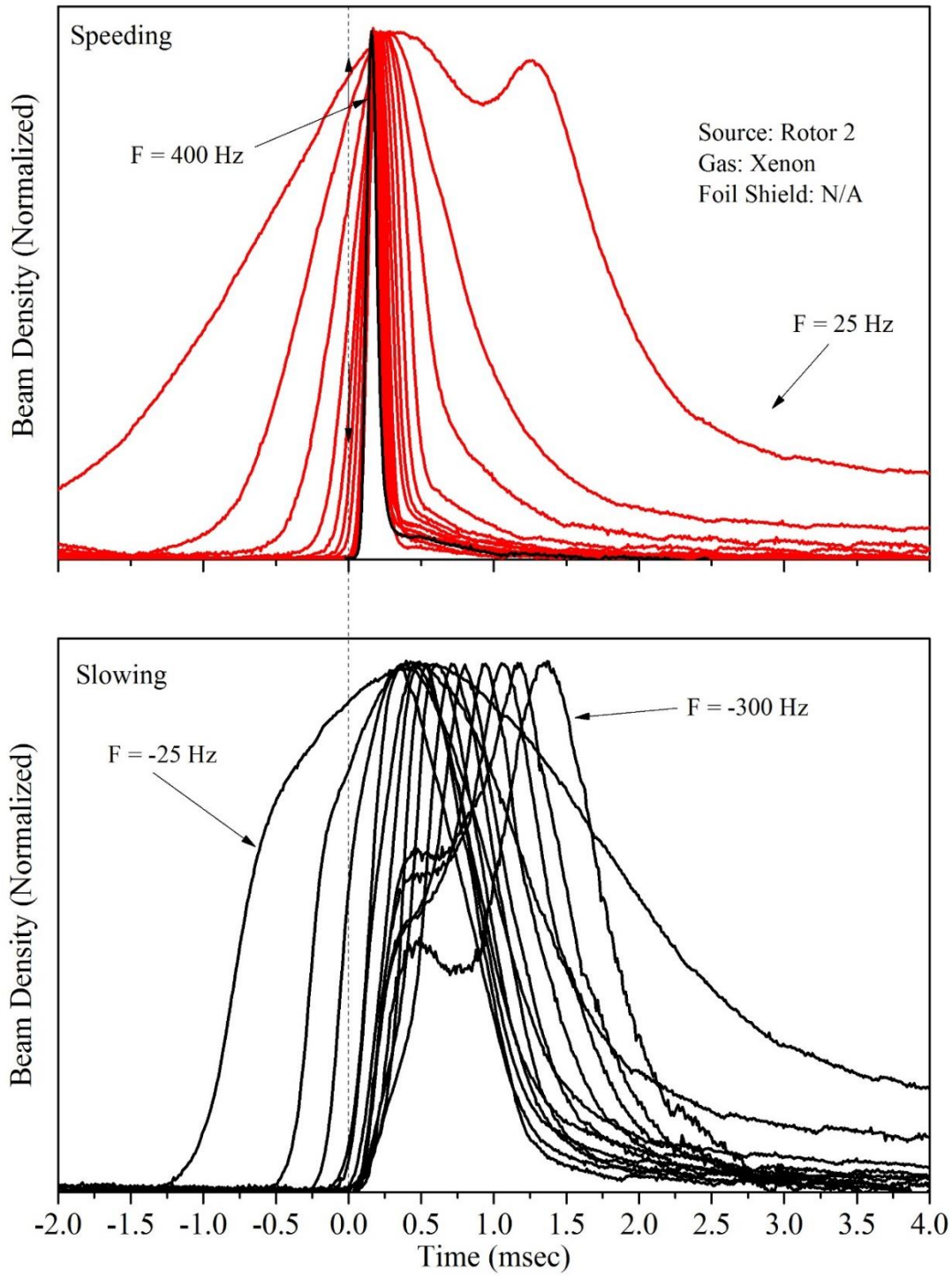

Figure 4 - 27: Peak Shape Progression - 3 mm Skimmer

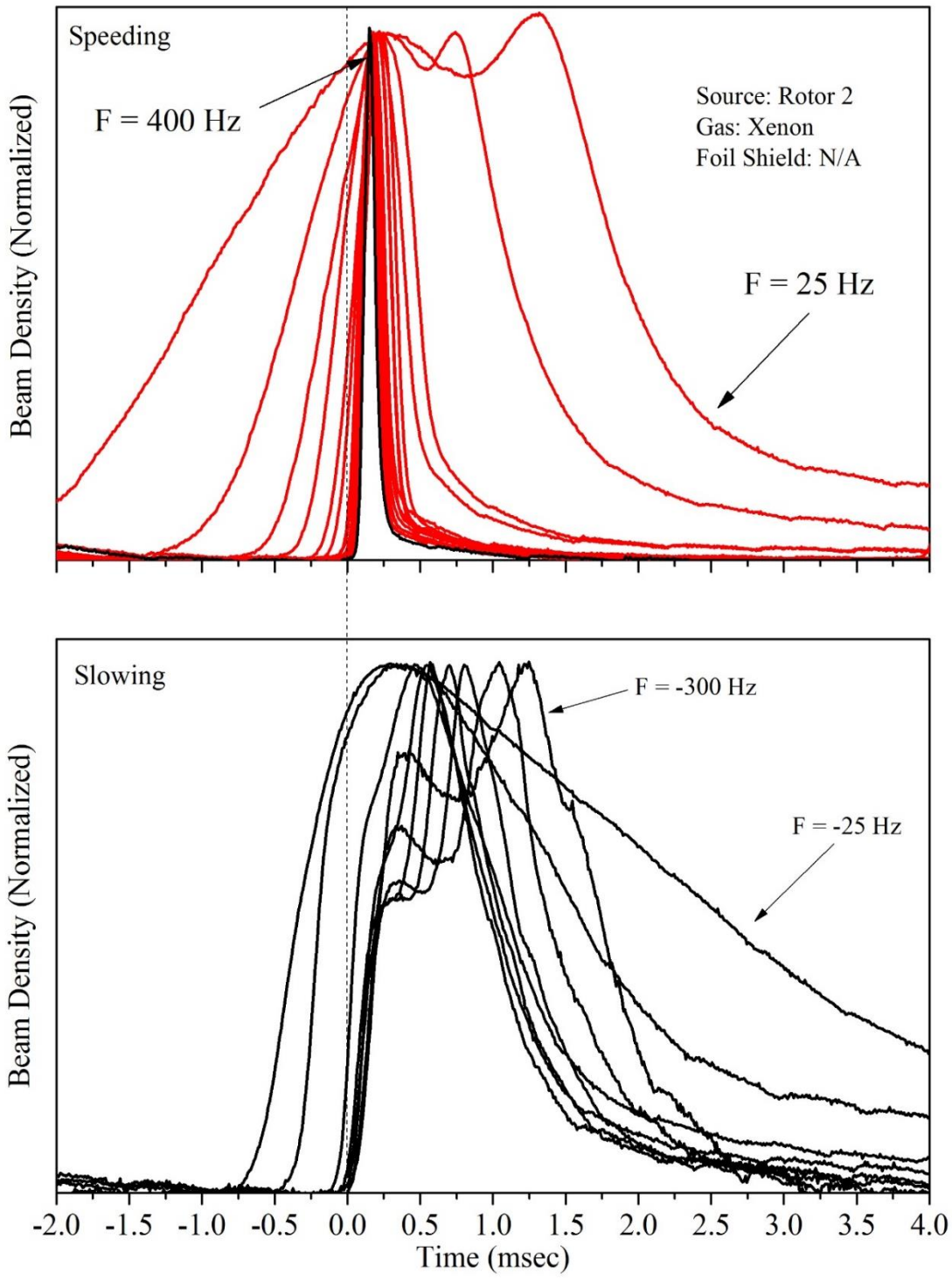

Figure 4 - 28: Peak Shape Progression - 5 mm Skimmer

the nozzle limits the angles used in the gate function esimation as well as the detector line of sight. One important factor to consider is the overall conductance of the skimmer between the two chambers. This becomes important when he slowest beams are desired and the background rise in the detection chamber for large skimmers prevents using the FIG at large emission currents.

Figures 4-26, 4-27, and 4-28 were all collected with the same operating conditions throughout the entire experiment except for the skimmer size. The signals have been corrected for the presence of a background signal using the baseline removal algorithm described in Section 4.1.1. The tallest peak in the spectrum is identified and its amplitude normalized to allow direct comparison across all frequencies. The time component of the data set is shifted to give the eddy current sensor for the tallest peak a value of $t = 0$. Once this is done the time of flight for the tallest peak is collected and plotted vs the estimated time of flight, as is shown in Figure 4-12. Each of these frequency scans showed the same deviation as in Figure 4-12 and required a simple F^{-1} correction term to coincide with the esimated time of flight values. This term is recorded for each of the collected frequencies and then used to shift each corresponding time component by the required amount. Thus the final processed figures correspond to the correct time of flight for each pulse and the peak shape progression can studied in detail.

The overall properties of these three frequency scans are very similar to those described in previous sections. The primary difference is the lack of a foil shield to protect the skimmer from reflected beams. The lack of a shield allows gas to scatter off the outside edge of the skimmer and into the detection region. This is what creates the large shoulders and double peaks in each of the frequency scans. The shoulder that occurs in the forward

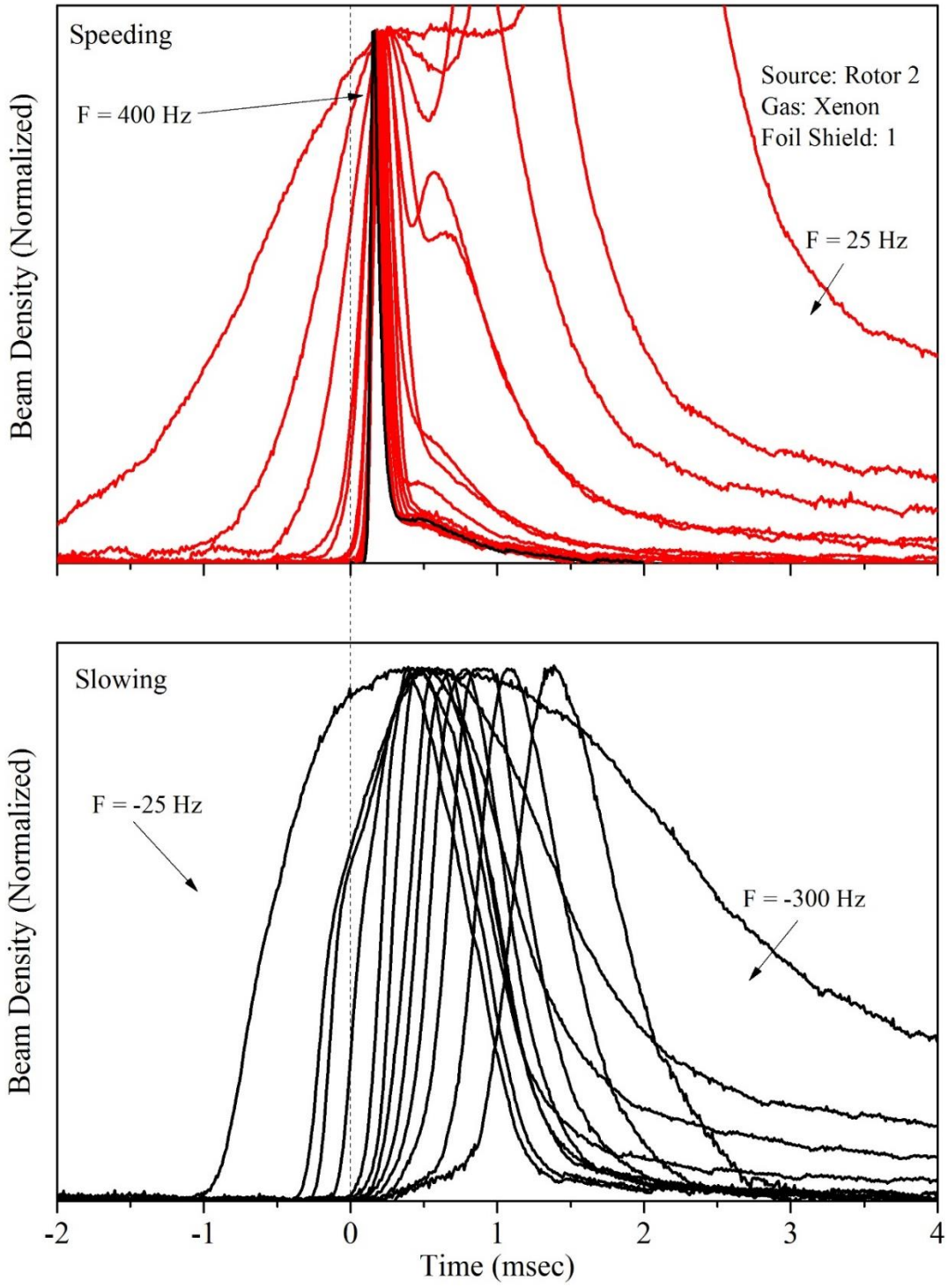

Figure 4 - 29: Peak Shape Progression - 3 mm Skimmer and Foil Shield 1

direction doesn't necessarily dissappear as it seems to in this picture, what does occur however is a dramatic growth of the primary beam component which dwarfs the shoulder. In the backwards direction however the effect is opposite. The beam density reduces to such a point that the scattered component of the beam becomes comparable to the mean beam. This shoulder occurs before the primary part of the beam and thus the scattered beam originates from a rotor angle larger than the shooting position. To test this hypothesis a small foil shield was installed on the bolts holding the skimmer in place. A photograph of this installation is shown on the left hand side of Figure 3-30, and the results of the measurement are shown in Figure 4-29. What is immediately noticeable in this figure is the complete lack of a double peak in backwards direction. This is much more appealing then the previous frequency scan with the same size skimmer. Unfortunately there is a much larger double peak in the forward direction. The double peak turns into a shoulder and is visible even in the very high frequency scans. If the purpose of the rotor is to produce slow beams this would have been considered a success, but I wanted to produce a clean beam with no double peaks in any directions and this occured immediately after I installed the next foil shield system.

The second generation of the foil shield was immensely better than the first. It was mounted on a curved rail whose radius exactly matched the length of the rotor tip. The foil shield, as is seen in Figure 3-30b, is clean with a sharp edge and no creases whatsoever. The shield was positioned so that it would not change the detector line of sight established by the skimmer. Its purpose was simply to limit any gas from reaching the skimmer from outside the "shooting" positions. Several of the foil shields were destroyed by the rotor due to being mounted too close to the rotor. Certain motor frequencies cause excessive vibration of the

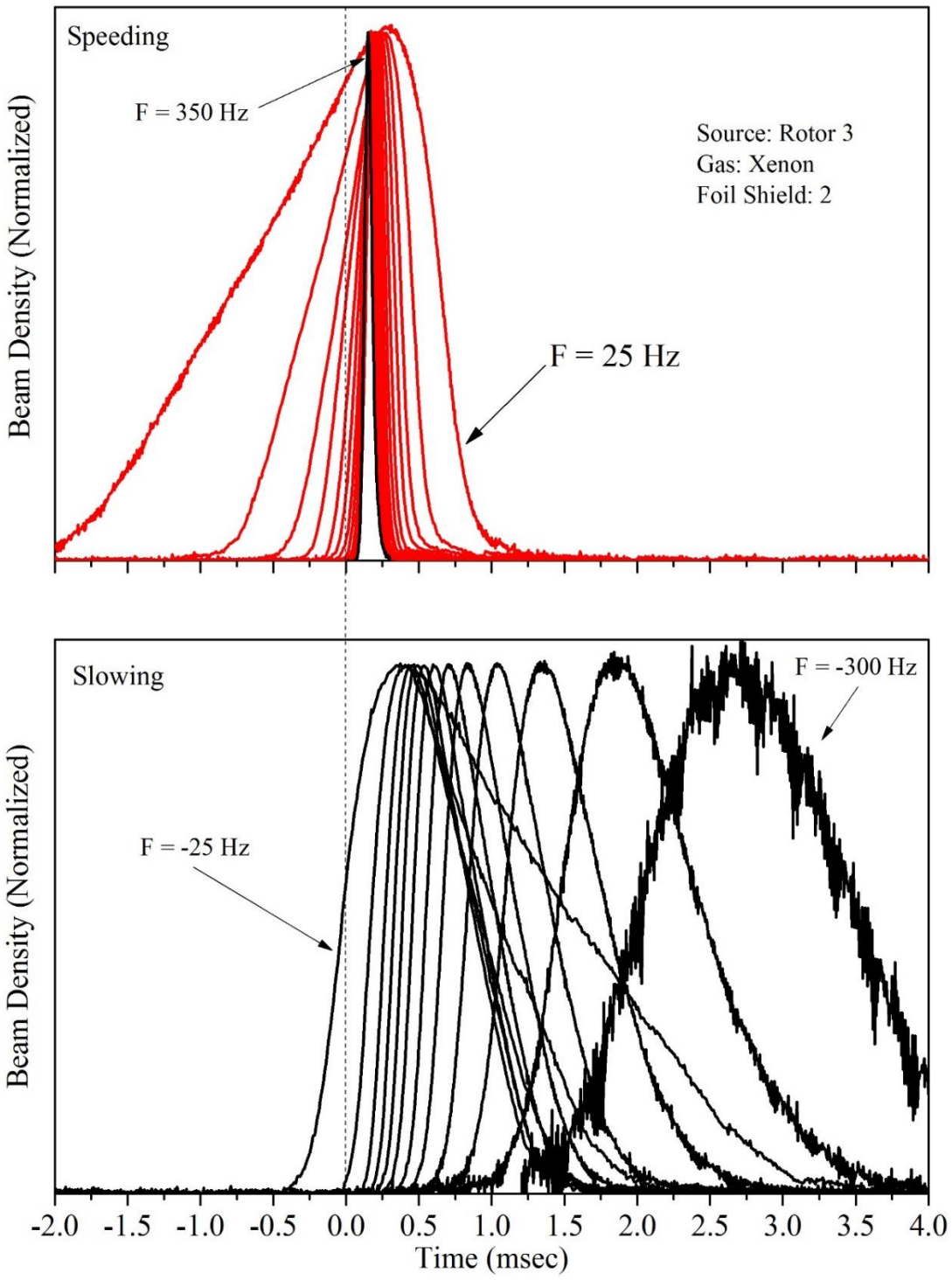

Figure 4 - 30: Peak Shape Progression - 3 mm Skimmer and Foil Shield 2

foil shield and result in contact between the rotor tip and the shield. In these cases it is beneficial to use 3 mil aluminum foil which does not damage the hardened aluminum alloy of the rotor tip.

After several attempts at a correct position the data scan shown in Figure 4-30 was collected which achieves all of the goals of the foil shield system. The double peaks were removed in both directions and the gate function corresponds to rotor peaks that originate from the "shooting" positions only.

4.2.4 Foil Shield Position

Once it was realized that the foil shield could impact the shape and quality of the produced beam a method was devised which could change the position of the foil shield while the chamber was still under vacuum. This prevented the user from having to vent the system and manually change the position. The system is described in Section 3.5 and consists of an aluminum foil shield mounted on a movable stage which is controlled via rotatable feedthrough installed on the top flange of the vacuum chamber.

Throughout the collection of this data set all liquid nitrogen traps were filled to facilitate a shorter pumpdown time between pulses. In addition, xenon was used as a test gas since it has a high pumping speed on cryogenic pumps at liquid nitrogen temperatures. The foil shield was initially placed far out of the way and moved incrementally forward throughout the experiment. This allowed a baseline to be established for all rotor frequencies which did not include the foil shield effects. In Figure 4-31 the completely unblocked region is on the far right at $\phi_{FS} = 12°$. In Section 3.2.2 the 3 mm skimmer shows $\phi_1 = 6°$ so it is expected that as the foil shield travels from $\phi_{FS} = 12°$ to $\phi_{FS} = 7°$ the beam amplitude and

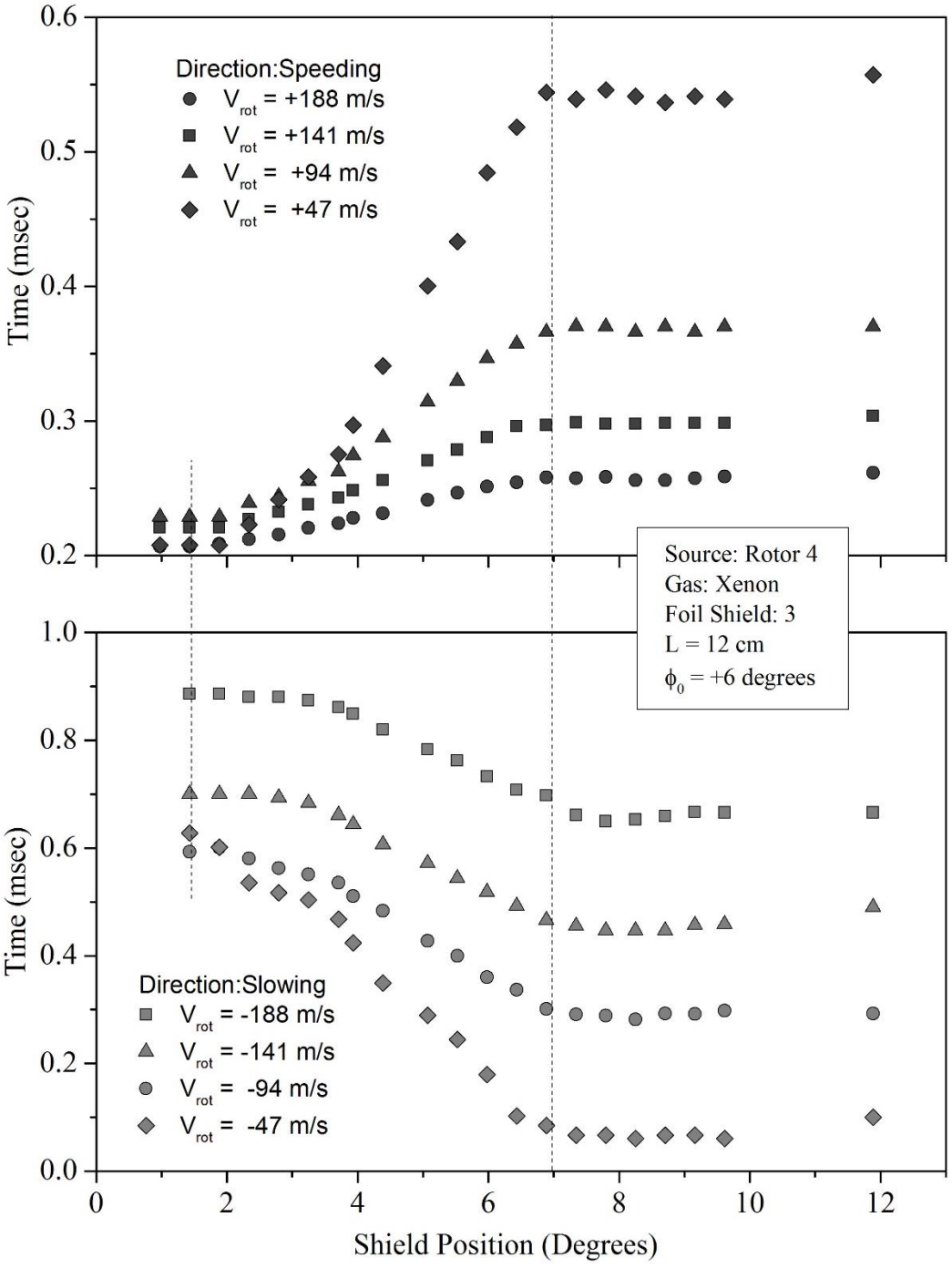

Figure 4 - 31: Time of Flight - Variable Shield Position

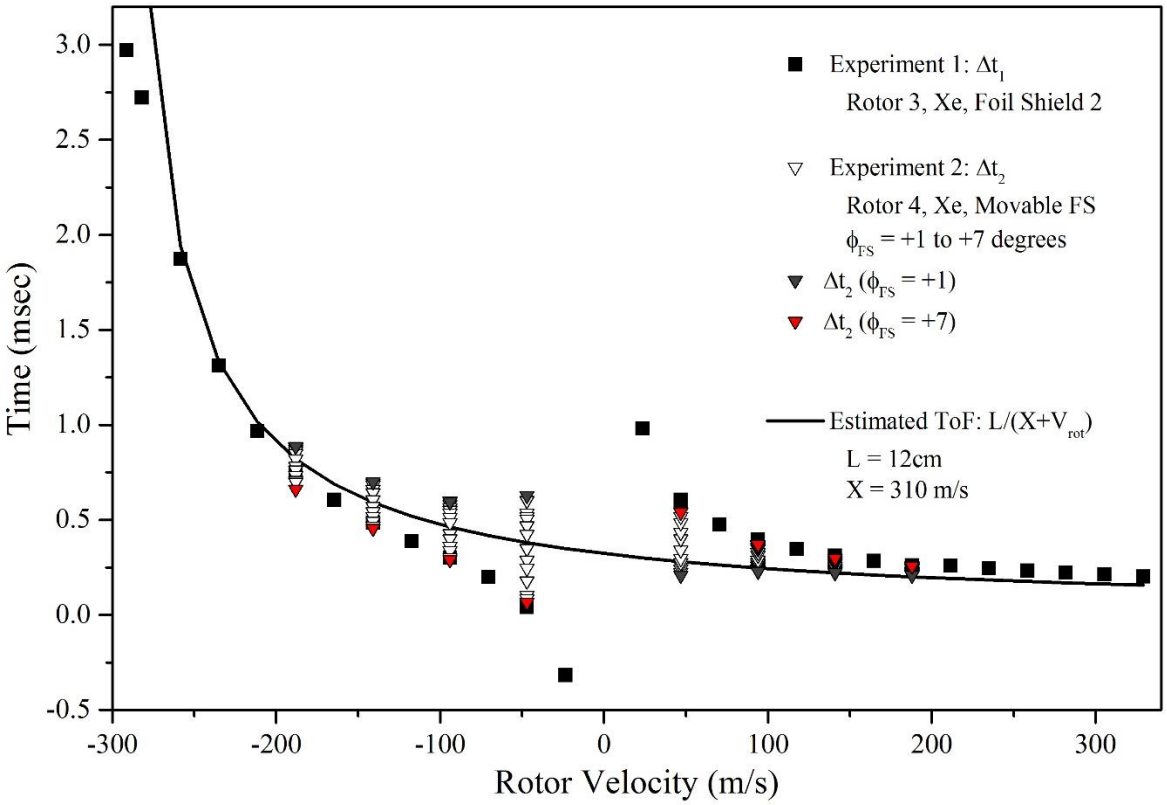

Figure 4 - 32: ToF Spectrum - Variable Shield Position

time of flight remain unchanged. As the shield begins cutting into the shooting positions the time of flight and the beam amplitudes change dramatically. In Figure 4-31 the shield blocks more of the beam as the angle approaches zero. In Figure 4-32 the points that are farthest from the estimated ToF line correspond to peaks without any foil shield interference. As the shield is brought across the beam path to block direct line of sight the ToF decrease for the speeding direction and increases for the slowing direction. This is due to the gate function augmentation imposed by the shield on the relevant angles calculated in Section 2.3.3. As can be seen in Figure 4-32, the ToF values correspond more closely with estimations which assume the beam originates from $\phi_n = 0°$ and travels directly to the detector. However many collected values fall on the other side of the estimated time of flight curve. These signals are very small compared to the original values and can easily correspond to gas scattered from the foil shield itself. It must be noted that these changes in time of flight do not correspond to changes in the beam velocity. The shield simply redefines the gate function angles and the slow frequencies whose shapes are dictated by the gate function are effected the most.

Future shields designs do not need to be mobile but should be optimized for different skimmer and detector arrangements. It is beneficial to keep the material thin and lightweight in case of accidental impacts with the rotor. If at all possible the shield should be mounted to a LN2 trap so that it can be brought to low temperatures. Finally, the front edge of the shield should be considered in the same class of object as the leading edge of the skimmer. If the edge is dull it will act as a scattering surface and heat the chopped beam. For this reason a considerable amount of thought should go into material selection and handling procedures.

4.2.5 Reservoir Gas Type

To justify the choice of xenon as the primary source gas used throughout this experiment several other gas types were tested. These include oxygen, SF6, argon, and krypton. They were compared with the best results obtained with xenon. This side by side comparison was not done throughout the development process because the broad shoulders and double peaks made data interpretation very difficult.

The scans were all performed in an identical fashion and the chamber had at least 20 hours to refresh the cryopump surfaces. The gas manifold was evacuated by a diffusion pump overnight between each set of scans. This along with several charge and discharge cycles with the target gas ensured a high level of purity. The pressure of the manifold was read by a piezoelectric gauge which is insensitive to gas type.

The processing steps performed on this data are identical to those described in Section 4.1. However the output density must be scaled by the ionization efficiency of the gas type. Which are shown in Table 4-4. Many of the data sets were repeated below 200 Hz and this allowed multiple data sets to be collected for the same frequency. Since these scans were only performed once this repeatability test is very impotant.

In the top panel of Figure 4-33 the time of flights measured by the ionization gauge are converted directly to a beam velocity. For this calculation it is imperitive to know the correct angle from which to attribute the peak in the ToF signal. These calculations use 10.4 cm as the distance from the rotor to the detector. There is at least a 5% error due to the thickness of the detection volume and uncertainty in the angle corresponding to the peak in the ToF signal.

Gas Type	Ionization Efficiency
He	0.133
Ne	0.202
Ar	1.0
Kr	1.56
Xe	2.29
O2	1.0
SF6	2.29

Table 4 - 4: Ion Gauge Sensitivity vs Gas Type

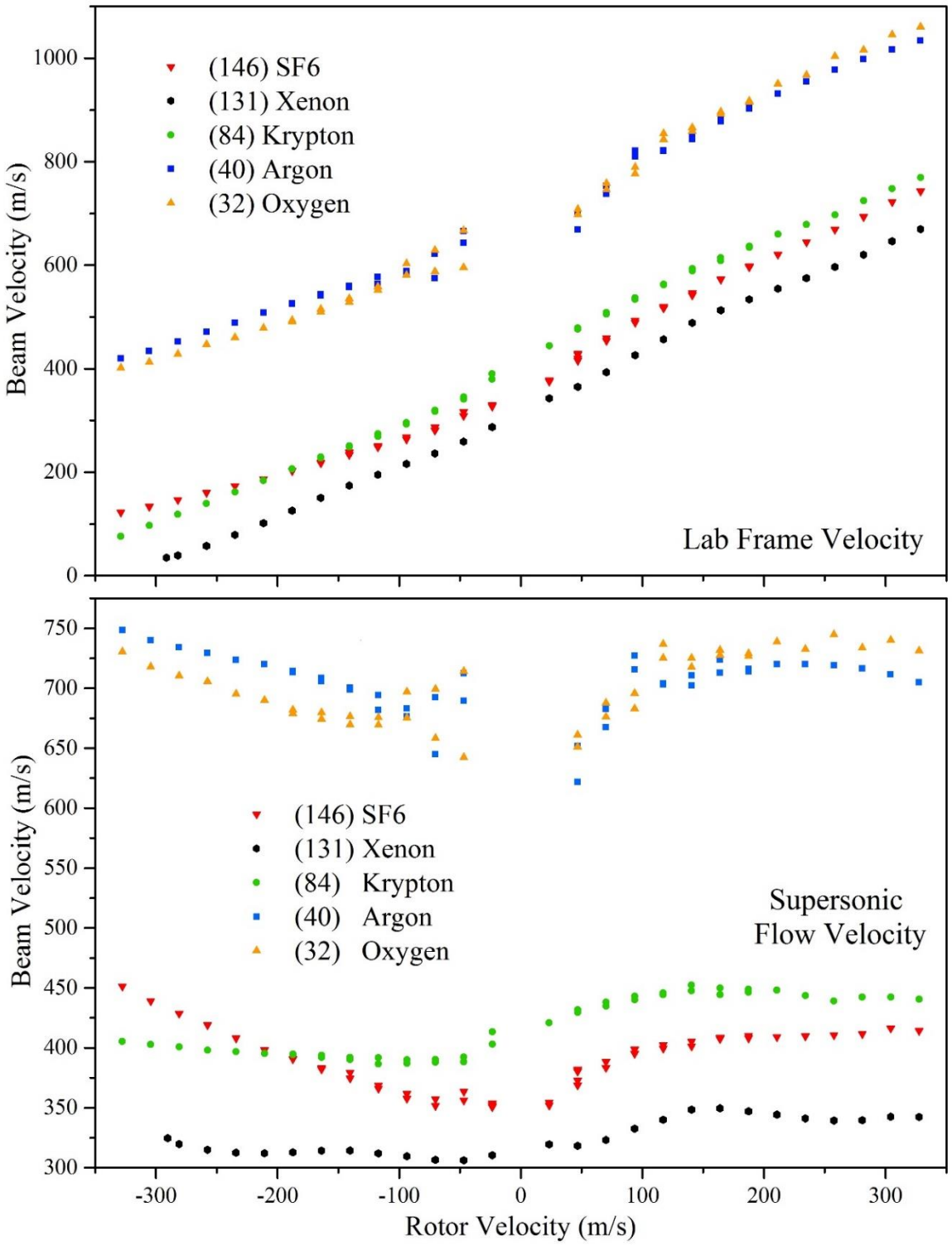

Figure 4 - 33: Beam Velocity - Different Gas Types

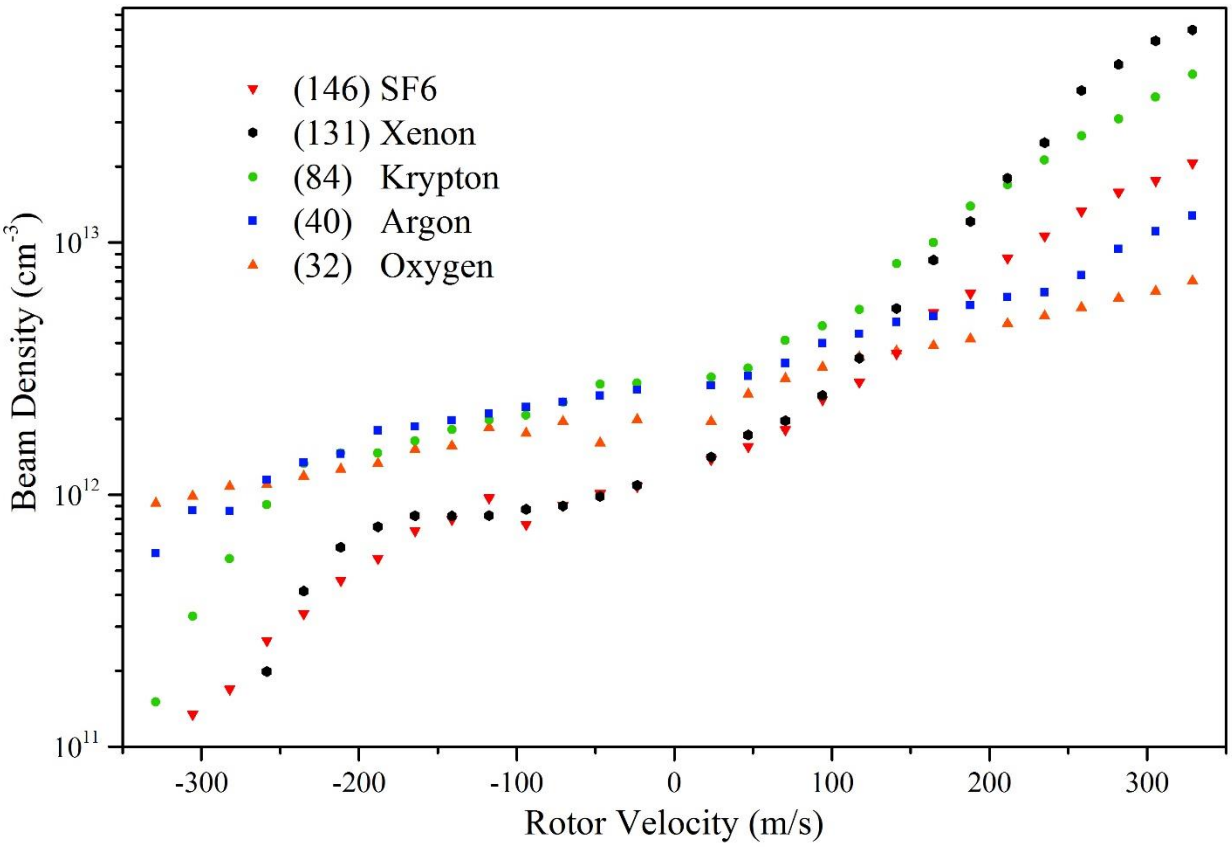

Figure 4 - 34: Maximum Beam Density - Different Gas Types

The supersonic flow velocity for different gas types is shown in the bottom panel of Figure 4-33. It is estimated by subtracting the rotor velocity from the final lab frame velocity. This shows that most gases exhibit the same heating trends witnessed in the xenon beam. In fact this heating is much more noticeable in the SF6 beam and can be attributed to the polyatomic nature of the molecule and the inefficiency in the supersonic expansion.

The beam density is shown for the different gas types in Figure 4-34. For all the gas types tested the stationary rotor produced a beam that was within a factor of 10 of all other beams. This is important because the backing pressures for each gas type was 900 Torr. This presure was verified several times throughout each experiment. If they produced a drastically different intensity of beam the valve or valve driver would have been inspected for failure.

The lightest gas type tested, oxygen, has the smallest change in density over the entire range of frequencies tested. This follows from the fact that the centrifugal enhancement is mass dependent and therefore effects oxygen the least. In addition, its large supersonic velocity means the velocity augmentation is not as significant

The heaviest gas type tested, SF6, exhibits a clear centrifugal enhancement similar to that shown in the xenon beam. However at large frequencies in the forward direction the density does not reach the level of the xenon beam. This is attributed again to the lack of efficiency in the supersonic expansion of a polyatomic gas.

The three atomic gases tested showed very similar behavior and will function very well as carrier gases in the future. Krypton has a mass high enough to exhibit centrifugal enhancement of the input pressure but only for very large rotor frequencies.

4.3 Comparison with Other Slowing Methods

To understand the advantages of the rotating source other methods of slow beam production must be discussed. These methods can be broadly categorized as direct and indirect cooling. Indirect cooling is the photoassociation of already cooled atomic gasses. The techniques applied to atomic gasses and their implications will be discussed in Section 4.5.1.

In this section the focus will remain upon direct cooling. It starts with an ensemble of molecules in thermodynamic equilibrium, often at room temperature, and applies methods to cool it. For many techniques a fast acting solenoid valve is used to expand a supersonic beam through collimating apertures and into an interaction region. This technique has several advantages! The cooling that occurs in supersonic expansions will produce rotational and vibrationaly cold ensembles. The expansion produces a very directed beam that is easy to characterize. The valve itself can be cooled down to cryogenic temperatures if needed[51]. The load on the pumping equipment is reduced for short duration pulses and the valves have a highly repeatable performance. For extremely high pressure sources a differential pumping chamber can be used which is connected to a third vacuum pump. This reduces the background in the interaction region and results in a much higher collimation of the beam.

The type of interaction used to slow the beam can be classified as either electromagnetic, kinetic, or mechanical in nature. It should be clear that methods utilizing a supersonic beam do not cool the ensemble any further but only try and reduce the lab frame beam velocity. These different methods and their associated references are contained in Table 4-5. The following sections describe the operating mechanism behind several of the

Method	**Molecule**	**T(μK)**	**N**
Laser Cooling	SrF[52], YO[53], CaF[54]	0.3	
Buffer Gas[55]	CaH[56], VO[57], CaF[58], PbO[59, 60], O2[61], NH[62], ND, CrH, MnH[63], ND3, H2CO[64], YbF[65],	400,000	10^{12}
Stark Electrode[66]	CO[67], NH3, ND3 [68, 69], OH [70, 71], OD[72], H2CO[73], NH[74], SO2 [75], C7H5N[76], YbF[77], LiH[78], CaF[79]	10,000	1,000,000
Stark Optical	C6H6[80], NO[81]		
Zeeman	O2[82], He2[51]		
Beam Collision	NO[83], KBr[84], ND3[85]	400,000	
Beam Dissociation	NO[86]	1,600,000	
Rotating Nozzle	O2, SF6, CH3F[8, 9], Xe[39], CHF3[50]	1,000,000	
Velocity Filtering	H2CO[73], ND3[87], D2O[88], CH3F[89] CF3H[90], CH3CN[91], H2O, D2O, HDO [92], NH3, CH3I, C6H5CN, C6H5Cl[93]	1,000,000	10^{9}

Table 4 - 5: Methods for Slowing Molecules

most popular methods as well as compare and contrast these methods with the rotating source.

4.3.1 Stark Deceleration

Stark deceleration utilizes the interaction of a polar molecule with an electric field. The magnitude of the force applied to the molecule depends on its dipole moment and the gradient of the electric field through which it travels. A molecules response to an inhomogenous electric field is known as the Stark effect and individual quantum states of a molecule may have either positive or negative Stark shifts. If a molecular state has a negative Stark shift it will lose potential energy with increasing field and are thus attracted to electric field maximums. These states are labeled high field seeking (HFS) states. All ground state molecules are HFS. Consequently, low field seeking (LFS) states have a positive Stark shift and will be attracted to electric field minimums where they have the lowest potential energy.

Many variations on the electrode array exist but typically the electrode paris are oriented parallel to one another and straddle the beam path. They are typically 3 mm in diameter, the gap between them is 2 mm, and the distance between stages is 2.5 mm. As a LFS molecule enters the first stage its interaction with the electric field increases its potential energy. At the point along the beam axis directly between the electrodes the highest fields are experienced by the molecules. To conserve energy the molecules must slow down in this high field area and if allowed to continue along the beam path it would accelerate back to its original velocity. However, the stark decelerator switches off the field before the molecule has a chance to leave the high field region. This results in the molecule entering the next

stage with a lower velocity than the first. By repeating this process over tens, or hundreds, of stages any desired velocity can be achieved.

The Stark decelerator is state selective. If a state selective decelerator is desired for the collision experiment then it becomes an attractive feature. However this means it only effects a fraction of the molecules that pass through the collimating aperture and into the interaction region. If a seeded beam is used to establish specific flow conditions in the supersonic expansion the intensity of the target molecule is reduced even further. Towards this end the rotating source can provide an appealing alternative to a seeded supersonic expansion. By operating in slowing mode the rotor can generate quite intense beams of pure molecular precursers at low lab frame velocities. The disadvantage is the cooling which occurs in a heavy atomic supersonic expansion will not occur in a light molecular expansion with the addition of internal degrees of freedom.

4.3.2 Zeeman Deceleration

Zeeman deceleration utilizes the interaction of a polar molecule with a magnetic field. The magnitude of the force applied to the molecule depends on its magnetic dipole moment and the gradient of the field through which it traverses. A molecules response to an inhomogeneous magnetic field is known as the Zeeman effect. Individual states of a molecule may have either a positive or a negative Zeeman effect. For a molecule with a negative Zeeman effect it will lose potential energy with increasing field and are thus attracted to high field regions. These states, in a similar labeling to Stark states, are called high field seeking (HFS) states. Consequently, low field seeking (LFS) states are attracted to low magnetic field regions where they have the lowest potential energy.

Instead of the electrode array utilized in a Stark decelerator the Zeeman decelerator has a series of coils. Although many variations on the coil design exist they typcally have an inner bore of 3-10 mm and are around 5-10 mm thick. The inner bore of the coil stages is where the beam travels. The stages are separated by insulating discs and each deceleration solenoid has its own pulse control electronics. Large capacitors are discharged through the coils to generate magnetic field up to several Tesla in strength.

As a LFS molecule enters the first coil its interaction with the magnetic field increases its potential energy. At the point along the beam axis directly inside the coil the largest magnetic fields are experienced by the molecule. To conserve energy the molecule must slow down and if allowed to exit the stage it would regain all of its original velocity. However, in a similar vein as the Stark decelerator, the coils are switched off using high speed transistors. This means the field has a chance to drop to near zero before the molecules can regain their kinetic energy. This results in a molecule entering the next stage with a lower initial velocity. By repeating the process in each stage of the decelerator any desired velocity can be achieved. The efficiency of the decelerator drops significantly when very low lab frame velocities are produced using this technique. This efficiency drop is due to transverse spreading that becomes much more significant of a loss mechanism at low velocities.

The Zeeman decelerator can be used on molecules that do not have a significant Stark shift. Thus its development is a welcome addition to the available deceleration techniques. It does not cool the ensemble but attempts to transfer a precooled ensemble into the lab frame. Once this deceleration has occured trapping and further manipulation become possible.

4.3.3 Electrostatic Filtering

Electrostatic filtering utilizes a constant field arrangement to deflect incoming molecules. The magnitude of the force applied to the molecule depends on its dipole moment and the gradient of the electric field through which it travels. The interaction was discussed in a previous section and is known as the Stark effect. The Stark effect can be either positive or negative and each state of a molecule can have either a positive or negative Stark effect.

The guide itself consists of four or six metal rods positioned around a central beam region. This produces a quadropole or hexapole field through which the molecules travel. The rods are typically bent 90 or 180 degrees around a central point with a radius of 5-10 cm. This makes a beam path of around 15-20 cm with only LFS molecules obtaining a stable trajectory throughout the guide system. Any molecule that enters the guide in a HFS state will continue flying into a pumping region and be removed from further consideration. As a LFS molecule enters the guide its interaction with the electric field decreases its potential energy in a direction tangential to its propagation. To conserve energy in the high field region the kinetic energy must change as the field strength reaches its maximum. This alters the trajectory of a molecule within the guide regions. Since the field is static throughout the course of the beam propagation the energy of the molecules is conserved and they exit the guide at the same velocity that they entered it. If a molecule enters the guide with excessive energy it will not transition into a stable trajectory. Only the molecules beneath a threshold energy will completely traverse the guide and make it through the exit aperture. Thus the guide acts as a state selective low pass energy filter for beams.

Electrostatic deflection techniques do not cool or decelerate the molecular beam. Instead they act as a powerful tool to select a polar molecule from an ensemble and guide it

to an interaction region. If a seeded supersonic expansion or a buffer gas beam is used to generate the initial beam this deflection becomes a convenient way to seperate the target polar molecule from the atomic seed or buffer gas. In the case of a rotating source, the deflection provides a convenient method to seperate the effusive source created by the high pressure in the main chamber from the pulse train created by the rotor. This seperation occurs due to the effusive source velocity distribution being effusive centered around room temperature and the pulse train from the rotor having a much slower velocity distribution.

4.3.4 Buffer Gas Cooling

One method that does not depend on the cooling mechanism offered by supersonic expansion is the buffer gas cooling method. This technique utilizes a cryogenic cell cooled to below 20 K and a buffer gas that is in thermodynamic equilibrium with the cell. Hot gas, anywhere from 300 K to 10,000 K is introduced to the cell and is cooled by repeated collisions with the buffer gas. The density of the buffer gas is kept at a specific value which ensures the hot gas thermalizes to the temperature of the cell wall before it actually reaches the wall. This thermalization prevents the wall from acting as a cryopump and removing the target molecules. An opening, typically on the order of a few mm, directs the gas mixture into a high vacuum area where the beam can be characterized and utilized.

The formation of clusters via 3-body collisions involving the buffer gas places an upper limit on cell pressure. The density required to thermalize the target gas before a wall collision places a lower bound on the cell pressure. These intermediate pressures prevent the formation of effusive or supersonic beams as is discussed in Section 2. This is due to the intermediate Reynolds number of the expansion and lacks the cooling that is characteristic of supersonic beams. However, such cooling is not required to bring a buffer gas beam into the

Kelvin range. This occurs as a byproduct of the low operating temperature of the cell and several hydrodynamic features that occur due to the mass ratio of the buffer gas and hot target molecule.

The introduction of hot species can take many forms in the buffer gas method. For molecular species that are gaseous at room temperature a simple pulsed valve supply or even a continuous supply of the hot species is used. If a species has insufficient vapor pressure at room temperature either an oven can be connected to the buffer cell through several thermal isolation stages, or a sample can be mounted inside the cell and ablated by a laser. This ability to generate high densities in the buffer cell at temperatures where the hot species has no appreciable vapor pressure is unique to the buffer cell approach[55].

Since the cooling mechanism for a buffer gas cell relies on elastic collisions with an inert atomic species, usually helium or neon. This means there is no state selectivity and all stable molecular precursors can be cooled. However the formation of dimers in the beam prohibits using very large pressures and the highest densities achieved are therefore comparable to state selective methods which begin with a much larger ensemble size. The presence of cryogenic surfaces and the aforementioned upper limit on cell pressure means that high vacuum can be maintained without the use of vacuum pumps.

4.3.5 Ultracold Atomic Physics

The focus on cooling molecules stems directly from the amazing properties displayed by ensembles of gaseous atoms as temperatures drop to around one hundred nanokelvin. At this temperature the ensemble condenses into a single quantum state[94] and every atom occupies the ground state energy level of its container. This effect, and in fact the idea of a

discrete ground state, was predicted by Bose and Einstein some 70 years before[95] and stems from the laws of quantum mechanics. Such a theoretical prediction made little impact at the time due to other paradigm shifts being brought on by quantum mechanics. But the experimental discovery of an entirely new phase of matter, appropriately named Bose Einstein Condensates (BEC) has been a great boon to the scientific community. It was the realization of a macroscopic quantum system, or an object easy to observe whose behavior is completely governed by quantum laws. This ensemble of gas particles is revolutionary in that it is not a microscopic quantum effect on a measurement of an otherwise classical system. These quantum laws are well known to modern physicists but the scale of the interactions usually restricts any observable phenomenon to truly microscopic systems, on the scale of an atom. It has renewed interest in the effort to extend these techniques directly or find analogous routes to cool molecules.

For many years it was thought that hydrogen was the best candidate for the formation of BECs but ultimately the alkali metals were the only suitable candidates for the task. To attain temperatures in the nanokelvin range requires the application of a diverse range of experimental techniques. Each stage of cooling was developed chronologically as the knowledge and experience of the science community grew. While there are many methods for creating BECs I will focus on the dilute atomic gas method used by Eric Cornell and Carl Wieman. Their experiment contained three stages: precooling, gas trapping, and evaporative cooling. I will review each stage so its applicability to molecules can be addressed in the next section.

Precooling is defined as anything done to prepare the ensemble for trapping so depositing the cooled atoms in the center of the vacuum chamber is a necessary function in

all precooling setups. This can be accomplished by either the use of a slowed atom beam preferentially aligned to deposit atoms in the center of the chamber, redirecting the 'tail' of a thermal vapor, or the cryogenic cooling of a cloud already in the trap location. Since such a wide variety of techniques are available, the critical factor determining which to use can be either the price of equipment, ease of use, or overall availability.

- Atomic beam slowing: This method often uses a precooled gas sample that undergoes supersonic expansion into a loading chamber whilst being subjected to further cooling (Zeeman, Stark deceleration) before it is directed towards the center of the trap.
- Thermal vapor: This simple method requires a finely tuned shutter system to function. At one instant in time a thermal vapor begins its expansion into a loading chamber, and the cycling of the high speed shutter allows only atoms to pass that have a very specific velocity. This allows precise velocity selection from an initial distribution.
- Cryogenic cooling: This buffer gas cooling method uses collisions with He3 atoms to lower the seed gas temperature. With sympathetic cooling between hyperfine states the applicability of this method to other atom types is drastically extended. After the seed gas meets velocity requirements the He3 is cryogenically pumped to reduce its partial pressure to negligible levels.

The last stage of precooling is optical cooling. This procedure takes place after the atomic vapor has been placed in the magneto-optical trap (MOT) and is a common element in all successful BEC setups. It was one of the last hurtles to be overcome in the production of a condensate and wasn't successfully demonstrated until the groups of Wineland and Dehmelt in 1978 [96]. This research cooled an ensemble of atoms to below 40 K by irradiating it with a laser. The laser is detuned from the exact energy needed for an electronic excited state.

This detuning means that there is a small gap in energy between the absorbed and emitted photons. With enough absorption/emission events the ensemble will cool considerably and be confined to the center of the MOT.

Once a precooled ensemble of atoms has been formed in the center of the chamber a trapping potential can be built around it. Its purpose is to contain the ensemble during subsequent cooling stages as well as compress and hold it for imaging. Every aspect of the field has a purpose including the shape, biasing, frequency of rotation, and strength. This is due to the simple fact that every dynamic variable of the cloud is dependent to some extent on the shapes and strengths the field exhibits, as well as the interparticle forces. The alkali metals are chosen for their large dipole moment produced by the unpaired electron in its outermost shell.

The technique of evaporative cooling requires a trapped and precooled condensate. It transforms the trapping potential to allow the highest energy particles to exit the trap. Between each cycle the cloud rethermalizes and collisions reoccupy the higher energy states. For each collision that produces an excited atom there exists another atom that enters the ground state of the trap. Starting with a large enough cloud the temperature can be dropped below the transition temperature by repeated evaporative cooling cycles. This is how in Cornell and Wieman cooled 2000 rubidium atoms down to 20 nK in 1995. This along with a sodium condensate produced by Ketterle in a separate effort resulted in all three scientists being awarded the Physics Nobel Prize in 2001.

4.4 Future Rotor Experiments

The original prototyping of the rotating sources described in this thesis was accomplished by Manish Gupta and Dudley Herschbach in 1999-2000 time frame[8, 9]. The work performed on this advanced version took into consideration all of the work performed by these two pioneers. In fact, the source designated as Rotor 1 was manufactured at Texas A&M and was identical to the final version developed by Gupta & Herschbach. From this initial design many improvements were developed as the performance of the rotor was evaluated. This work occurred over the course of five years from 2009 to 2015 and is included in Section 3.4. It is useful, however, to consider the individual aspects of the experiment and point out what can be easily improved. These improvements will be considered in three key areas. The first is the design of the core experiment which includes the motor, the rotor, and the gas feed system. The second is the geometry of the experiment which includes the type and location of vacuum pumps and apertures. The last point that will be discussed is an improvement in detection method which will consider other methods and compare them to the fast ion gauge used in this work.

The three basic components of the rotating source experiment include the motor, the rotor, and the gas feed system. The motor mounting and cooling systems described in Section 3.4.1 were completely adequate for high speed operation of the motor, in high vacuum, for extended periods of time. This is no small feat considering the motor was operating in a vacuum less than 10^{-7} Torr and if the oil degassed due to high temperatures in the motor bearings the beam would not be measurable. Therefore only three improvements are recommended for a new motor system. First is an increase in the maximum RPM from 600Hz to 1000Hz which allows the slowing of lighter noble gasses such as argon and neon.

Second is temperature sensors with outputs that can be measured with data acquisition systems. Third is a noise reduction system installed between the motor and the controller. These features are all offered on current models and would not be hard to include in a new purchase. Combined they create a motor system that can operate at higher frequencies while indicating whether excessive heat is generated in the spindle. These higher frequencies require further optimization of the rotor.

The rotor itself will benefit from advanced aluminum and titanium alloys being produced for automotive and aerospace applications. In fact, the material chosen for the current version of the rotor is Al 7078 which has a tensil strength 30% higher than the alloy used in the original version. Future rotor designs should take advantage of new alloy development because this correlates directly with the maximum frequency of rotation. Another improvement to consider would be dynamic balancing of the rotor which can be performed by balancing specialists in the aerospace, engineering, or automotive industry. It balances the rotor in the two directions orthogonal to the rotor stem by removing small amounts of the aluminum alloy. This should remove any resonant vibrations that occur at different motor frequencies and thus allow the entire experiment to perform better over its lifetime. Finally, the rotor length can be increased if there is not a limit on the chamber size. Only consider a longer rotor if a new high speed aluminum alloy is selected and the dynamic balancing is performed after initial construction. The rotor length and frequency limitation of the motor establish the capability of the rotor system.

The rotor stem and feed system should be the focal point of any redesign efforts. It was the last component of the current system to be completely rebuilt and the difference in performance of the rotor was drastic. The design efforts are all contained in Section 3.4.2.

They focused on constructing a rigid stage on which to mount all associated hardware that was water cooled and contained precision alignment features. Additional features that would improve the quality of the beam should focus on reducing the tolerances between the stationary components of the feed system and the moving surfaces of the rotor stem. Any reduction in the gas bypassing the rotor and leaking into the background gas will lead to a higher quality beam. It should be noted however that all-metal feed systems are inadvisable due to the high potential for misalignment of the feed system. If the system is misaligned, contact occurs between the two metallic components, and the motor is engaged the results could be disasterous. It could either overload the motor due to high torque requirement or damage the upper motor bearings from the excessive heat. For these reasons it is advisable for one sealing surface to made of a high performance plastic that is compatible with high vacuum environment and has a very low heat capacity.

The geometry of the vacuum equipment will change based on the intended purpose of the rotating source. For those experiments attempting to measure the highest quality beams the rotor is capable of producing two aspects must be prioritized. One is minimizing the interference of the produced beam and the other is reducing the distance required for the beam to travel before it is detected.

The beam interference can come from background gas, reflected beams, or a dull skimmer edge. Background gas interference is considered in Section 3.2 and becomes more prominent at low lab frame velocities. High capacity diffusion pumps or turbomolecular pumps should be chosen to maintain a high level of vacuum during a typical data collection. To aid in the removal of background gases and to prevent reflected beams large cryopumps should be installed around the outside edge of the rotor. This surface would capture a large

portion of the beam emitted from the rotor. This was not performed in the current system because the tolerance between the rotor tip and chamber wall is less than a 0.25". However it should lead to improved vacuum throughout the data collection process and much faster pumping if the gas used is condensible at the cryopump operating temperature.

The influence a skimmer has on a propagating molecular beam has been studied recently[48] and the required tolerance of the edge is 3 μm. Anything more rounded than this acts as a scattering surface and degrades the transmitted beams characteristics, ie density, temperature, and angular spread. Mass produced skimmers are available from Beam Dynamics and should be utilized in future experiments. This was not done in the current system because the focus was on measuring very slow beams. Since the skimmer influence is determined by the density of the beam at the skimmed region it becomes much more apparent in accelerated beams at high rotational frequencies.

The final improvement anticipated for the future is the addition of a secondary detection method. This would allow complete characterization of the produced beam and complement the data produced by a fast ion gauge. This secondary method can take many forms and the current literature should be reviewed to understand the limitation of the various methods. The references listed in Table 4-4 provide a great place to start as a wide variety of methods are utilized by the different researchers.

BIBLIOGRAPHY

1. G. Scoles and D. Bassi, *Atomic and Molecular Beam Methods*. (Oxford University Press Oxford, 1988).

2. H. Pauly, *Atom, Molecule, and Cluster Beams Ii: Cluster Beams, Fast and Slow Beams, Accessory Equipment and Applications*. (Springer, 2000).

3. P. Redhead, History of Vacuum Devices, CERN European Organization for Nuclear Research, 281-290 (1999).

4. A. Kantrowitz and J. Grey, A High Intensity Source for the Molecular Beam. Part I. Theoretical, Review of Scientific Instruments **22** (5), 328-332 (1951).

5. E. Becker, K. Bier and W. Henkes, Strahlen Aus Kondensierten Atomen Und Molekeln Im Hochvakuum, Zeitschrift für Physik **146** (3), 333-338 (1956).

6. K. Bier and O. Hagena, presented at the Rarefied Gas Dynamics, Volume 1, 1963 (unpublished).

7. M. Gupta, PhD Thesis, A Mechanical Means of Producing Cold, Slow Beams of Molecules, Harvard University, 2000.

8. M. Gupta and D. Herschbach, A Mechanical Means to Produce Intense Beams of Slow Molecules, The Journal of Physical Chemistry A **103** (50), 10670-10673 (1999).

9. M. Gupta and D. Herschbach, Slowing and Speeding Molecular Beams by Means of a Rapidly Rotating Source, The Journal of Physical Chemistry A **105** (9), 1626-1637 (2001).

10. F. Dalfovo, S. Giorgini, L. P. Pitaevskii and S. Stringari, Theory of Bose-Einstein Condensation in Trapped Gases, Reviews of Modern Physics **71** (3), 463-512 (1999).

11. A. B. Henson, S. Gersten, Y. Shagam, J. Narevicius and E. Narevicius, Observation of Resonances in Penning Ionization Reactions at Sub-Kelvin Temperatures in Merged Beams, Science **338** (6104), 234-238 (2012).

12. D. W. Keith, C. R. Ekstrom, Q. A. Turchette and D. E. Pritchard, An Interferometer for Atoms, Physical Review Letters **66** (21), 2693-2696 (1991).

13. J. Pendlebury and K. Smith, Molecular Beams, Contemporary Physics **28** (1), 3-32 (1987).

14. E. H. Kennard and E. H. Kennard, *Kinetic Theory of Gases: With an Introduction to Statistical Mechanics*. (McGraw-Hill New York, 1938).

15. G. Sanna and G. Tomassetti, *Introduction to Molecular Beams Gas Dynamics*. (World Scientific, 2005).

16. H. C. W. Beijerinck and N. F. Verster, Absolute Intensities and Perpendicular Temperatures of Supersonic Beams of Polyatomic Gases, Physica B+C **111** (2–3), 327-352 (1981).

17. A. Dalgarno, Advances in Chemical Physics **12**, 143 (1967).

18. J. O. Hirschfelder, C. F. Curtiss and R. B. Bird, *Molecular Theory of Gases and Liquids*. (Wiley New York, 1954).

19. W. Braker, A. L. Mossman and C. L. Yaws, *Matheson Gas Data Book*. (Matheson East Rutherford, NJ, 1980).

20. W. Christen, K. Rademann and U. Even, Supersonic Beams at High Particle Densities: Model Description Beyond the Ideal Gas Approximation†, The Journal of Physical Chemistry A **114** (42), 11189-11201 (2010).

21. C. Tegeler, R. Span and W. Wagner, A New Equation of State for Argon Covering the Fluid Region for Temperatures from the Melting Line to 700 K at Pressures up to 1000 Mpa, Journal of Physical and Chemical Reference Data **28** (3), 779-850 (1999).

22. V. D. Arp and R. D. Mccarty, 1989.

23. W. Christen and K. Rademann, Probing Free Jet Expansions of Supercritical Fluids, Physica Scripta **80** (4), 048127 (2009).

24. W. Demtröder, *Laser Spectroscopy*. (Springer, 1982).

25. G. M. Mcclelland, K. L. Saenger, J. J. Valentini and D. R. Herschbach, Vibrational and Rotational Relaxation of Iodine in Seeded Supersonic Beams, The Journal of Physical Chemistry **83** (8), 947-959 (1979).

26. C. E. Klots, Rotational Relaxation in Sonic Nozzle Expansions, The Journal of Chemical Physics **72** (1), 192-197 (1980).

27. H. Buchenau, E. Knuth, J. Northby, J. Toennies and C. Winkler, Mass Spectra and Time-of-Flight Distributions of Helium Cluster Beams, The Journal of Chemical Physics **92** (11), 6875-6889 (1990).

28. J. Harms, J. Toennies and E. Knuth, Droplets Formed in Helium Free-Jet Expansions from States near the Critical Point, The Journal of Chemical Physics **106** (8), 3348-3357 (1997).

29. L. Pedemonte, R. Tatarek and G. Bracco, Study of He Clusters by Means of a Compact Time-of-Flight Detector for Atom Scattering, Review of Scientific Instruments **74** (10), 4404-4409 (2003).

30. A. Scheidemann, J. Toennies and J. Northby, Capture of Neon Atoms by He 4 Clusters, Physical Review Letters **64** (16), 1899 (1990).

31. E. L. Knuth, F. Schünemann and J. P. Toennies, Supercooling of H2 Clusters Produced in Free-Jet Expansions from Supercritical States, The Journal of Chemical Physics **102** (15), 6258-6271 (1995).

32. W. Christen, K. Rademann and U. Even, Efficient Cooling in Supersonic Jet Expansions of Supercritical Fluids: Co and Co2, The Journal of Chemical Physics **125** (17), - (2006).

33. S. De Dea, D. R. Miller and R. E. Continetti, Cluster and Solute Velocity Distributions in Free-Jet Expansions of Supercritical Co2, The Journal of Physical Chemistry A **113** (2), 388-398 (2008).

34. W. Christen, T. Krause and K. Rademann, Precise Thermodynamic Control of High Pressure Jet Expansions, Review of Scientific Instruments **78** (7), - (2007).

35. R. Span, W. Wagner, E. Lemmon and R. Jacobsen, Multiparameter Equations of State—Recent Trends and Future Challenges, Fluid Phase Equilibria **183**, 1-20 (2001).

36. R. Katti, R. Jacobsen, R. Stewart and M. Jahangiri, in *Advances in Cryogenic Engineering* (Springer, 1986), pp. 1189-1197.

37. E. W. Lemmon and R. Span, Short Fundamental Equations of State for 20 Industrial Fluids, Journal of Chemical & Engineering Data **51** (3), 785-850 (2006).

38. K. L. Saenger, Pulsed Molecular Beams: A Lower Limit on Pulse Duration for Fully Developed Supersonic Expansions, The Journal of Chemical Physics **75** (5), 2467-2469 (1981).

39. L. Sheffield, M. S. Hickey, V. Krasovitskiy, K. D. D. Rathnayaka, I. F. Lyuksyutov, et al., Pulsed Rotating Supersonic Source for Merged Molecular Beams, Review of Scientific Instruments **83** (6), 064102-064102-064109 (2012).

40. R. Rhoad, G. Milauskas, R. Whipple and L. Mcdougal, *Geometry for Enjoyment and Challenge*. (McDougal, Littell, 1991).

41. P. B. Moon, C. T. Rettner and J. P. Simons, Rotor Accelerated Molecular Beams, Journal of the Chemical Society, Faraday Transactions 2: Molecular and Chemical Physics **74** (0), 630-643 (1978).

42. Q. Wei, I. Lyuksyutov and D. Herschbach, Merged-Beams for Slow Molecular Collision Experiments, The Journal of Chemical Physics **137** (5), - (2012).

43. Y. Shagam and E. Narevicius, Sub-Kelvin Collision Temperatures in Merged Neutral Beams by Correlation in Phase-Space, The Journal of Physical Chemistry C **117** (43), 22454-22461 (2013).

44. A. Roth, *Vacuum Technology*. (Elsevier, 2012).

45. W. Espe, Materials of High Vacuum Technology, (1968).

46. C. C. Davis and M. A. Coplan, *Building Scientific Apparatus*. (Cambridge University Press, 2009).

47. E. L. Knuth, Dimer-Formation Rate Coefficients from Measurements of Terminal Dimer Concentrations in Free-Jet Expansions, The Journal of Chemical Physics **66** (8), 3515-3525 (1977).

48. K. Luria, W. Christen and U. Even, Generation and Propagation of Intense Supersonic Beams, The Journal of Physical Chemistry A **115** (25), 7362-7367 (2011).

49. J. Braun, P. K. Day, J. P. Toennies, G. Witte and E. Neher, Micrometer-Sized Nozzles and Skimmers for the Production of Supersonic He Atom Beams, Review of Scientific Instruments **68** (8), 3001-3009 (1997).

50. M. Strebel, F. Stienkemeier and M. Mudrich, Improved Setup for Producing Slow Beams of Cold Molecules Using a Rotating Nozzle, Physical Review A **81** (3), 033409 (2010).

51. M. Motsch, P. Jansen, J. A. Agner, H. Schmutz and F. Merkt, Slow and Velocity-Tunable Beams of Metastable He2 by Multistage Zeeman Deceleration, Physical Review A **89** (4), 043420 (2014).

52. E. S. Shuman, J. F. Barry and D. Demille, Laser Cooling of a Diatomic Molecule, Nature **467** (7317), 820-823 (2010).

53. M. T. Hummon, M. Yeo, B. K. Stuhl, A. L. Collopy, Y. Xia, et al., 2d Magneto-Optical Trapping of Diatomic Molecules, Physical Review Letters **110** (14), 143001 (2013).

54. V. Zhelyazkova, A. Cournol, T. E. Wall, A. Matsushima, J. J. Hudson, et al., Laser Cooling and Slowing of Caf Molecules, Physical Review A **89** (5), 053416 (2014).

55. N. R. Hutzler, H.-I. Lu and J. M. Doyle, The Buffer Gas Beam: An Intense, Cold, and Slow Source for Atoms and Molecules, Chemical Reviews **112** (9), 4803-4827 (2012).

56. J. D. Weinstein, R. Decarvalho, T. Guillet, B. Friedrich and J. M. Doyle, Magnetic Trapping of Calcium Monohydride Molecules at Millikelvin Temperatures, Nature **395** (6698), 148-150 (1998).

57. J. D. Weinstein, R. Decarvalho, K. Amar, A. Boca, B. C. Odom, et al., Spectroscopy of Buffer-Gas Cooled Vanadium Monoxide in a Magnetic Trapping Field, The Journal of Chemical Physics **109** (7), 2656-2661 (1998).

58. K. Maussang, D. Egorov, J. S. Helton, S. V. Nguyen and J. M. Doyle, Zeeman Relaxation of Caf in Low-Temperature Collisions with Helium, Physical Review Letters **94** (12), 123002 (2005).

59. D. Egorov, J. D. Weinstein, D. Patterson, B. Friedrich and J. M. Doyle, Spectroscopy of Laser-Ablated Buffer-Gas-Cooled Pbo at 4 K and the Prospects for Measuring the Electric Dipole Moment of the Electron, Physical Review A **63** (3), 030501 (2001).

60. S. E. Maxwell, N. Brahms, R. Decarvalho, D. R. Glenn, J. S. Helton, et al., High-Flux Beam Source for Cold, Slow Atoms or Molecules, Physical Review Letters **95** (17), 173201 (2005).

61. D. Patterson and J. M. Doyle, Bright, Guided Molecular Beam with Hydrodynamic Enhancement, The Journal of Chemical Physics **126** (15), - (2007).

62. D. Egorov, W. C. Campbell, B. Friedrich, S. E. Maxwell, E. Tsikata, et al., Buffer-Gas Cooling of Nh Via the Beam Loaded Buffer-Gas Method, The European Physical Journal D **31** (2), 307-311 (2004).

63. M. Stoll, J. M. Bakker, T. C. Steimle, G. Meijer and A. Peters, Cryogenic Buffer-Gas Loading and Magnetic Trapping of Crh and Mnh Molecules, Physical Review A **78** (3), 032707 (2008).

64. L. D. Van Buuren, C. Sommer, M. Motsch, S. Pohle, M. Schenk, et al., Electrostatic Extraction of Cold Molecules from a Cryogenic Reservoir, Physical Review Letters **102** (3), 033001 (2009).

65. S. Skoff, R. Hendricks, C. Sinclair, M. Tarbutt, J. Hudson, et al., Doppler-Free Laser Spectroscopy of Buffer-Gas-Cooled Molecular Radicals, New Journal of Physics **11** (12), 123026 (2009).

66. S. Y. T. Van De Meerakker, H. L. Bethlem and G. Meijer, Taming Molecular Beams, Nature Physics **4** (8), 595-602 (2008).

67. H. L. Bethlem, G. Berden and G. Meijer, Decelerating Neutral Dipolar Molecules, Physical Review Letters **83** (8), 1558-1561 (1999).

68. H. L. Bethlem, G. Berden, F. M. H. Crompvoets, R. T. Jongma, A. J. A. Van Roij, et al., Electrostatic Trapping of Ammonia Molecules, Nature **406** (6795), 491-494 (2000).

69. F. M. H. Crompvoets, H. L. Bethlem, R. T. Jongma and G. Meijer, A Prototype Storage Ring for Neutral Molecules, Nature **411** (6834), 174-176 (2001).

70. J. R. Bochinski, E. R. Hudson, H. J. Lewandowski, G. Meijer and J. Ye, Phase Space Manipulation of Cold Free Radical Oh Molecules, Physical Review Letters **91** (24), 243001 (2003).

71. J. R. Bochinski, E. R. Hudson, H. J. Lewandowski and J. Ye, Cold Free-Radical Molecules in the Laboratory Frame, Physical Review A **70** (4), 043410 (2004).

72. S. Y. T. Van De Meerakker, P. H. M. Smeets, N. Vanhaecke, R. T. Jongma and G. Meijer, Deceleration and Electrostatic Trapping of Oh Radicals, Physical Review Letters **94** (2), 023004 (2005).

73. E. R. Hudson, C. Ticknor, B. C. Sawyer, C. A. Taatjes, H. J. Lewandowski, et al., Production of Cold Formaldehyde Molecules for Study and Control of Chemical Reaction Dynamics with Hydroxyl Radicals, Physical Review A **73** (6), 063404 (2006).

74. Y. T. V. D. M. Sebastiaan, L. Irena, H. Steven, K. Jochen and M. Gerard, Production and Deceleration of a Pulsed Beam of Metastable Nh (a 1 Δ) Radicals, Journal of Physics B: Atomic, Molecular and Optical Physics **39** (19), S1077 (2006).

75. O. Bucicov, M. Nowak, S. Jung, G. Meijer, E. Tiemann, et al., Cold So2 Molecules by Stark Deceleration, The European Physical Journal D **46** (3), 463-469 (2008).

76. K. Wohlfart, F. Grätz, F. Filsinger, H. Haak, G. Meijer, et al., Alternating-Gradient Focusing and Deceleration of Large Molecules, Physical Review A **77** (3), 031404 (2008).

77. M. R. Tarbutt, H. L. Bethlem, J. J. Hudson, V. L. Ryabov, V. A. Ryzhov, et al., Slowing Heavy, Ground-State Molecules Using an Alternating Gradient Decelerator, Physical Review Letters **92** (17), 173002 (2004).

78. S. K. Tokunaga, J. M. Dyne, E. A. Hinds and M. R. Tarbutt, Stark Deceleration of Lithium Hydride Molecules, New Journal of Physics **11** (5), 055038 (2009).

79. T. E. Wall, S. K. Tokunaga, E. A. Hinds and M. R. Tarbutt, Nonadiabatic Transitions in a Stark Decelerator, Physical Review A **81** (3), 033414 (2010).

80. R. Fulton, A. I. Bishop and P. F. Barker, Optical Stark Decelerator for Molecules, Physical Review Letters **93** (24), 243004 (2004).

81. R. Fulton, A. I. Bishop, M. N. Shneider and P. F. Barker, Optical Stark Deceleration of Nitric Oxide and Benzene Molecules Using Optical Lattices, Journal of Physics B: Atomic, Molecular and Optical Physics **39** (19), S1097 (2006).

82. E. Narevicius, A. Libson, C. G. Parthey, I. Chavez, J. Narevicius, et al., Stopping Supersonic Oxygen with a Series of Pulsed Electromagnetic Coils: A Molecular Coilgun, arXiv preprint arXiv:0804.0219 (2008).

83. M. S. Elioff, J. J. Valentini and D. W. Chandler, Subkelvin Cooling No Molecules Via "Billiard-Like" Collisions with Argon, Science **302** (5652), 1940-1943 (2003).

84. N.-N. Liu and H. Loesch, Kinematic Slowing of Molecules Formed by Reactive Collisions, Physical Review Letters **98** (10), 103002 (2007).

85. J. J. Kay, S. Y. T. Van De Meerakker, K. E. Strecker and D. W. Chandler, Production of Cold Nd3 by Kinematic Cooling, Faraday Discussions **142** (0), 143-153 (2009).

86. A. Trottier, D. Carty and E. Wrede, Photostop: Production of Zero-Velocity Molecules by Photodissociation in a Molecular Beam, Molecular Physics **109** (5), 725-733 (2011).

87. S. A. Rangwala, T. Junglen, T. Rieger, P. W. H. Pinkse and G. Rempe, Continuous Source of Translationally Cold Dipolar Molecules, Physical Review A **67** (4), 043406 (2003).

88. T. Rieger, T. Junglen, S. A. Rangwala, G. Rempe, P. W. H. Pinkse, et al., Water Vapor at a Translational Temperature of 1k, Physical Review A **73** (6), 061402 (2006).

89. S. Willitsch, M. T. Bell, A. D. Gingell, S. R. Procter and T. P. Softley, Cold Reactive Collisions between Laser-Cooled Ions and Velocity-Selected Neutral Molecules, Physical Review Letters **100** (4), 043203 (2008).

90. C. Sommer, L. D. Van Buuren, M. Motsch, S. Pohle, J. Bayerl, et al., Continuous Guided Beams of Slow and Internally Cold Polar Molecules, Faraday Discussions **142** (0), 203-220 (2009).

91. Y. Liu, M. Yun, Y. Xia, L. Deng and J. Yin, Experimental Generation of a Cw Cold Ch3cn Molecular Beam by a Low-Pass Energy Filtering, Physical Chemistry Chemical Physics **12** (3), 745-752 (2010).

92. M. Motsch, L. D. Van Buuren, C. Sommer, M. Zeppenfeld, G. Rempe, et al., Cold Guided Beams of Water Isotopologs, Physical Review A **79** (1), 013405 (2009).

93. T. Hidenobu, S. Takao, M. Tetsuya, M. Takamasa and K. Hideto, Stark Velocity Filter for Nonlinear Polar Molecules, Journal of Physics B: Atomic, Molecular and Optical Physics **43** (9), 095202 (2010).

94. M. H. Anderson, J. R. Ensher, M. R. Matthews, C. E. Wieman and E. A. Cornell, Observation of Bose-Einstein Condensation in a Dilute Atomic Vapor, Science **269** (5221), 198-201 (1995).

95. F. Dalfovo, S. Giorgini, L. P. Pitaevskii and S. Stringari, Theory of Bose-Einstein Condensation in Trapped Gases, Reviews of Modern Physics **71** (3), 463 (1999).

96. D. J. Wineland, R. E. Drullinger and F. L. Walls, Radiation-Pressure Cooling of Bound Resonant Absorbers, Physical Review Letters **40** (25), 1639-1642 (1978).

97. D. C. Lincoln, D. David, V. K. Roman and Y. Jun, Cold and Ultracold Molecules: Science, Technology and Applications, New Journal of Physics **11** (5), 055049 (2009).

98. R. Krems, B. Friedrich and W. C. Stwalley, *Cold Molecules: Theory, Experiment, Applications*. (CRC press, 2010).

99. D. C. Lincoln and Y. Jun, Focus on Cold and Ultracold Molecules, New Journal of Physics **11** (5), 055009 (2009).

100. I. W. Smith, *Low Temperatures and Cold Molecules*. (Imperial College Press, 2008).

101. O. Dulieu, R. Krems, M. Weidemuller and S. Willitsch, Physics and Chemistry of Cold Molecules, Physical Chemistry Chemical Physics **13** (42), 18703-18704 (2011).

102. M. H. G. De Miranda, A. Chotia, B. Neyenhuis, D. Wang, G. Quemener, et al., Controlling the Quantum Stereodynamics of Ultracold Bimolecular Reactions, Nature Physics **7** (6), 502-507 (2011).

103. J. Deiglmayr, M. Repp, A. Grochola, K. Mortlbauer, C. Gluck, et al., Formation of Ultracold Dipolar Molecules in the Lowest Vibrational Levels by Photoassociation, Faraday Discussions **142** (0), 335-349 (2009).

104. K. K. Ni, S. Ospelkaus, D. Wang, G. Quemener, B. Neyenhuis, et al., Dipolar Collisions of Polar Molecules in the Quantum Regime, Nature **464** (7293), 1324-1328 (2010).

105. S. Ospelkaus, K. K. Ni, M. H. G. De Miranda, B. Neyenhuis, D. Wang, et al., Ultracold Polar Molecules near Quantum Degeneracy, Faraday Discussions **142** (0), 351-359 (2009).

106. S. Ospelkaus, K.-K. Ni, D. Wang, M. H. G. De Miranda, B. Neyenhuis, et al., Quantum-State Controlled Chemical Reactions of Ultracold Potassium-Rubidium Molecules, Science **327** (5967), 853-857 (2010).

107. N. R. Hutzler, M. F. Parsons, Y. V. Gurevich, P. W. Hess, E. Petrik, et al., A Cryogenic Beam of Refractory, Chemically Reactive Molecules with Expansion Cooling, Physical Chemistry Chemical Physics **13** (42), 18976-18985 (2011).

108. H. L. Bethlem and G. Meijer, Production and Application of Translationally Cold Molecules, International Reviews in Physical Chemistry **22** (1), 73-128 (2003).

109. L. Scharfenberg, S. Y. T. Van De Meerakker and G. Meijer, Crossed Beam Scattering Experiments with Optimized Energy Resolution, Physical Chemistry Chemical Physics **13** (18), 8448-8456 (2011).

110. S. Y. T. Van De Meerakker and G. Meijer, Collision Experiments with Stark-Decelerated Beams, Faraday Discussions **142** (0), 113-126 (2009).

111. S. D. Hogan, M. Motsch and F. Merkt, Deceleration of Supersonic Beams Using Inhomogeneous Electric and Magnetic Fields, Physical Chemistry Chemical Physics **13** (42), 18705-18723 (2011).

112. S. D. Hogan, D. Sprecher, M. Andrist, N. Vanhaecke and F. Merkt, Zeeman Deceleration of H and D, Physical Review A **76** (2), 023412 (2007).

113. E. Narevicius, A. Libson, C. G. Parthey, I. Chavez, J. Narevicius, et al., Stopping Supersonic Beams with a Series of Pulsed Electromagnetic Coils: An Atomic Coilgun, Physical Review Letters **100** (9), 093003 (2008).

114. E. Narevicius, A. Libson, C. G. Parthey, I. Chavez, J. Narevicius, et al., Stopping Supersonic Oxygen with a Series of Pulsed Electromagnetic Coils: A Molecular Coilgun, Physical Review A **77** (5), 051401 (2008).

115. M. G. Raizen, Comprehensive Control of Atomic Motion, Science **324** (5933), 1403-1406 (2009).

116. B. Friedrich, Slowing of Supersonically Cooled Atoms and Molecules by Time-Varying Nonresonant Induced Dipole Forces, Physical Review A **61** (2), 025403 (2000).

117. R. Fulton, A. I. Bishop, M. N. Shneider and P. F. Barker, Controlling the Motion of Cold Molecules with Deep Periodic Optical Potentials, Nature Physics **2** (7), 465-468 (2006).

118. E. Narevicius, A. Libson, M. F. Riedel, C. G. Parthey, I. Chavez, et al., Coherent Slowing of a Supersonic Beam with an Atomic Paddle, Physical Review Letters **98** (10), 103201 (2007).

119. S. D. Hogan, C. Seiler and F. Merkt, Rydberg-State-Enabled Deceleration and Trapping of Cold Molecules, Physical Review Letters **103** (12), 123001 (2009).

120. J. F. Barry, E. S. Shuman, E. B. Norrgard and D. Demille, Laser Radiation Pressure Slowing of a Molecular Beam, Physical Review Letters **108** (10), 103002 (2012).

121. K. E. Strecker and D. W. Chandler, Kinematic Production of Isolated Millikelvin Molecules, Physical Review A **78** (6), 063406 (2008).

122. R. A. Phaneuf, C. C. Havener, G. H. Dunn and A. Müller, Merged-Beams Experiments in Atomic and Molecular Physics, Reports on Progress in Physics **62** (7), 1143 (1999).

123. R. E. Boltnev, V. V. Khmelenko and D. M. Lee, Stabilization of H and D Atoms in Krypton–Helium Nanocondensates, Low Temperature Physics **36** (5), 382-391 (2010).

124. J. W. Beams, High Speed Centrifuging, Reviews of Modern Physics **10** (4), 245-263 (1938).

125. P. Horowitz, W. Hill and T. C. Hayes, *The Art of Electronics*. (Cambridge university press Cambridge, 1989).

126. W. Gentry and G. Scoles, Atomic and Molecular Beam Methods, Atomic and Molecular Beam Methods **1**, 70 (1988).

127. P. B. Moon, C. T. Simms and J. P. Simons, Faraday Discussions **77** (630) (1977).

128. J. H. Brophy, J. A. Silver and J. L. Kinsey, Vibrationally Excited Oh from the Reaction of H with No2 Observed by Laser-Induced Fluorescence, The Journal of Chemical Physics **62** (9), 3820-3822 (1975).

129. A. M. L. Irvine, I. W. M. Smith and R. P. Tuckett, A Laser-Induced Fluorescence Determination of the Internal State Distribution of No Produced in the Reaction: H+No2→Oh+No, The Journal of Chemical Physics **93** (5), 3187-3195 (1990).

130. A. M. L. Irvine, I. W. M. Smith, R. P. Tuckett and X. F. Yang, A Laser-Induced Fluorescence Determination of the Complete Internal State Distribution of Oh Produced in the Reaction: H+No2→Oh+No, The Journal of Chemical Physics **93** (5), 3177-3186 (1990).

131. J. L. Kinsey, Comments on the Preferential Population of Λ-Doublet States of the Oh Product from H + No2, The Journal of Chemical Physics **81** (12), 6410-6412 (1984).

132. R. P. Mariella, B. Lantzsch, V. T. Maxson and A. C. Luntz, Molecular Beam-Laser Induced Fluorescence Studies on the Chemical Reactions H+No2→Oh+No and H+Clo2→Oh+Clo, The Journal of Chemical Physics **69** (12), 5411-5418 (1978).

133. E. J. Murphy, J. H. Brophy, G. S. Arnold, W. L. Dimpfl and J. L. Kinsey, Laser-Induced Fluorescence Measurement of the Internal and Fine Structure States Distributions of Od(X $^2\pi$,V,J,N) from D+No2 The Journal of Chemical Physics **74** (1), 324-330 (1981).

134. D. G. Sauder and P. J. Dagdigian, Determination of the Internal State Distribution of No Produced from the H+No2 Reaction, The Journal of Chemical Physics **92** (4), 2389-2396 (1990).

135. J. A. Silver, W. L. Dimpfl, J. H. Brophy and J. L. Kinsey, Laser-Induced Fluorescence Determination of Internal-State Distribution of Oh Produced by H+No2 in Crossed Molecular Beams, The Journal of Chemical Physics **65** (5), 1811-1822 (1976).

136. M. C. Su, S. S. Kumaran, K. P. Lim, J. V. Michael, A. F. Wagner, et al., Rate Constants, $1100 \leq T \leq 2000$ K, for H + No2 → Oh + No Using Two Shock Tube Techniques: Comparison of Theory to Experiment†, The Journal of Physical Chemistry A **106** (36), 8261-8270 (2002).

137. C. Szewc, J. D. Collier and H. Ulbricht, A Helical Velocity Selector for Continuous Molecular Beams, Review of Scientific Instruments **81** (10), - (2010).

APPENDIX A

Pulsed Rotating Supersonic Source for Merged Molecular Beams

We describe a pulsed rotating supersonic beam source, evolved from an ancestral device [M. Gupta and D. Herschbach, J. Phys. Chem. A **105**, 1626 (2001)]. The beam emerges from a nozzle near the tip of a hollow rotor which can be spun at high-speed to shift the molecular velocity distribution downward or upward over a wide range. Here we consider mostly the slowing mode. Introducing a pulsed gas inlet system, cryocooling, and a shutter gate eliminated the main handicap of the original device in which continuous gas flow imposed high background pressure. The new version provides intense pulses, of duration 0.1–0.6 ms (depending on rotor speed) and containing $\sim 10^{12}$ molecules at lab speeds as low as 35 m/s and $\sim 10^{15}$ molecules at 400 m/s. Beams of any molecule available as a gas can be slowed (or speeded); e.g., we have produced slow and fast beams of rare gases, O_2, Cl_2, NO_2, NH_3, and SF_6. For collision experiments, the ability to scan the beam speed by merely adjusting the rotor is especially advantageous when using two merged beams.

Introduction

The compelling frontier of cold (<1 K) and ultracold (<1 mK) gas-phase molecular physics, bristling with prospective applications and challenges, has been amply surveyed in recent evangelical reviews.[97-101] At present, the most effective experimental approach has been to induce formation of alkali dimer molecules from ultracold trapped alkali atoms by photoassociation or Feshbach resonances.[102-106] Over the past decade, however, much effort has been devoted to widening the chemical scope (“beyond the alkali age”) by developing means to slow and cool preexisting molecules. Chief among these means are

cooling by use of ^{3}He as a buffer gas,[56, 60, 61, 107] which reaches 0.3 K; Stark deceleration of beams of polar molecules, using multiple stages of timed electric fields, which (depending on the molecule) can reduce translational energy well below 100 mK;[108-110] and Zeeman deceleration of magnetic atoms and molecules in analogous fashion.[111-115] Other methods, as yet less well developed or requiring unusual circumstances, include filtering slow polar molecules from an effusive or buffer-gas cooled source;[87, 90] deceleration by optical fields;[116, 117] reflection from a moving surface;[118] Stark slowing a nonpolar molecule, H_2, by exciting it to a Rydberg state;[119] cooling SrF with three lasers to exploit highly diagonal Franck-Condon factors;[120] "milking" collisions with special kinematic constraints;[83-85, 121] or attaching molecules to superfluid helium nanodroplets.[100]

Here we consider a mechanical means to produce intense beams of slow (or fast) molecules, applicable to any substance available as a gas at ambient temperatures.[7, 8, 50] This employs a supersonic nozzle mounted near the tip of a high-speed rotor, which when spun contrary to the exiting beam markedly reduces the net lab velocity. An exploratory prototype device proved able to slow down, e.g., a Kr beam to below 42 m/s.[8] Recently, an improved version has been developed at Freiburg University.[50] It has a carbon fiber rotor, enhanced pumping, gas injection via a rotary feedthrough with ferrofluidic metal seals, and translation stages enabling adjustment of the nozzle position even during operation. Also, for use with polar molecules, the rotor source was augmented by an electrostatic quadrupole focusing field. We have developed another improved version of the rotating source. It does not include any of the Freiburg improvements, so is almost as rudimentary as the original version. The most important new feature is a pulsed gas inlet system, coupled

with a gated shutter preceding the beam skimmer. This eliminated a major handicap of the original device (still present in the Freiburg version), in which continuous gas flow imposed high background pressure in the rotor chamber, both attenuating the yield of slow molecules and creating an interfering effusive flow into the detector chamber.

As well as providing slow beams with the familiar virtues of a supersonic molecular beam (high intensity, narrowed velocity distribution, drastic cooling of vibration and rotation), the rotating source enables scanning the lab beam velocity over a wide range by merely adjusting the rotor speed. For a stationary source shifting the beam velocity can only be done rather coarsely and awkwardly by changing the beam temperature or the ratio of seeded to carrier gas. A rotating source is subject to an intrinsic disability, however, because transverse spreading of the beam, which becomes more pronounced as the beam slows, causes the beam intensity to fall off with the square of the velocity.[7, 8, 50] That is a severe limitation; e.g., compared with a stationary supersonic source, the intensity of a Xe beam from the rotating source drops a hundredfold when the lab velocity is lowered to ~100 m/s.[8] Fortunately, this limitation can be avoided in pursuit of our prime goal, the study of slow collisions. The redeeming strategy makes use of merged beams to obtain very low *relative* collision energies. Then neither beam needs to be particularly slow, provided the beam speeds can be closely matched. Merged beams have been extensively employed for ion-molecule, ion-ion, and electron-molecule collisions, using beams with keV energies to perform experiments at relative energies below 1 eV.[122] In similar fashion, merging a beam with fixed speed from a stationary source with the beam of adjustable speed from the rotor source can provide access to relative collision energies in the millikelvin range.

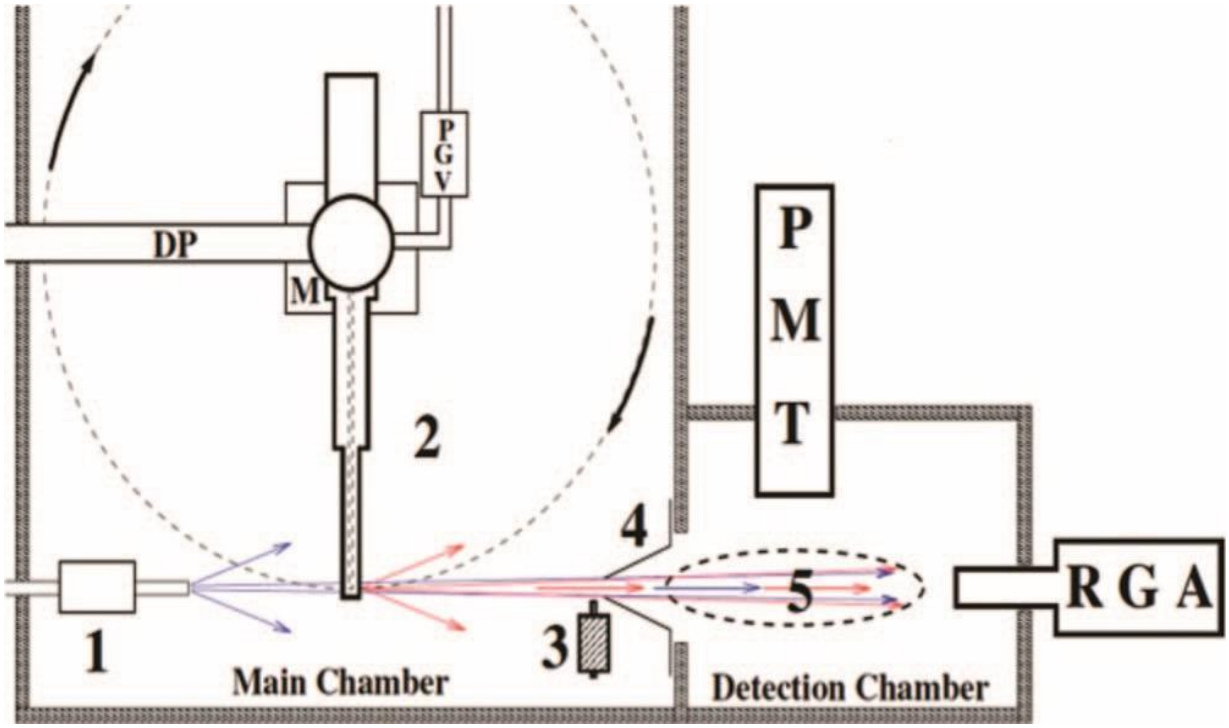

FIG. 5-1. Schematic (top view, not to scale) of basic apparatus, set-up in merged-beam mode, for study of H + NO_2 reaction: (**1**) Stationary pulsed supersonic beam source of H or D atoms, formed in RF discharge (mounted outside main chamber); valving system seeds atoms in Xe or Kr carrier gas before emerging from a pulsed nozzle. (**2**) Rotating supersonic source, driven by motor (M) and with pulsed gas inlet valve (PGV), and differentially pumped (DP) feed-in, used for NO_2 beam; (**3**) solenoid-controlled shutter preceding (**4**) skimmer that gives sole entry to detection chamber; (**5**) observation zone where parent beams are monitored by a RGA and laser-induced fluorescence from OH product is recorded by a photomultiplier (PMT).

In keeping with customary practice in the field of cold (<1 K) and ultracold (<1 mK) molecules, we usually use degrees Kelvin (or milliKelvin) as the energy unit. 1 K = 3.16 millihartrees = 0.0862 meV = 0.695 cm^{-1} = 1.98 cal/mol = 8.28 joule/mol.

Apparatus

Figures 1 and 2 show schematic views of our current apparatus, configured for merged-beam experiments. The stationary source (labeled **1**) supplies a pulsed supersonic beam of H (or D) atoms, produced by dissociation of H_2 (or D_2) in an RF discharge[123] and seeded in Xe or Kr carrier gas. The rotating source (labeled **2**) has the same basic anatomy pictured in Ref. 35; the mounting, balancing procedure, and AC induction driving motor are also the same. For the most part, we describe only differences in design and performance. The barrel of the new rotor was made of an aluminum alloy 7068 T6 (Kaiser Aluminum) with 35% higher yield strength than alloy 7075 T6 in Ref. 35 and its length, from the axis of rotation to the nozzle exit aperture, was increased from 9.9 cm to 14.9 cm. The barrel with 1/8 ID is tapered in six steps; from thick to thin, the diameters of the six cylindrical segments are as follows: 0.625, 0.492, 0.412, 0.352, 0.300, and 0.260 in. Their lengths are as follows: 3.231, 2.145, 1.100, 0.700, 0.600, and 1.525 in. These dimensions, determined from computations analyzing the centrifugal forces,[124] maximize the peripheral velocity at which the rotor should break; this theoretical limit is 633 m/s. The exit aperture, made from aluminum, located 2.5 mm from the tip of the barrel, was enlarged from a pinhole of diameter 0.1 mm to a conical shape of length 3 mm, cone angle 30°, and orifice diameter 0.4 mm.

The beam gas is fed into the spinning rotor via a stationary tube, which inserts into a steel stinger whose inner diameter (1.65 mm) is slightly larger than the outer diameter of the feed

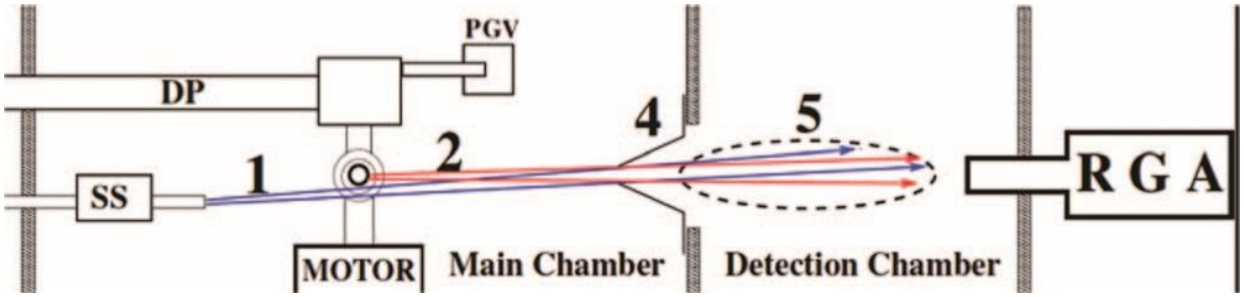

FIG. 2. Schematic (side view, not to scale) showing path of beam **1** (from stationary source, SS) directed at slight angle relative to beam **2** (in the vertical plane) in order to pass below (by ∼3 mm) the rotor orbit, yet pass through the skimmer **4** (3 mm dia orifice) along with beam **2** so both beams overlap almost completely in the observation zone **5**. The "slight angle" is only about arctan(0.3/13) ∼1.3◦, and the angular beam widths transmitted by the skimmer are about $\theta \sim {}^{1}\circ$. Shutter and PMT are not visible in this projection.

tube. The sting (6.4 mm o.d.) is press-fitted into a hole in the topside of the rotor barrel, centered on the rotation axis. As in Ref. 35, we used a feed tube (i.d. 0.75 mm) of PEEK, PolyEtherEtherKetone, which has flexibility and low friction similar to Teflon, but is more robust. The intrinsic leaking that occurs was rendered insignificant by adding a small differentially pumped auxiliary vacuum chamber to house the gas feed. As shown in Figure 3, the sting extends into the auxiliary chamber via a snug hole (6.5 mm dia) in a washer-shaped seal made of PEEK. There is very little leaking through this seal because the auxiliary chamber exhausts to a rotary pump. The PEEK tubing and washer need to be replaced periodically, after about 50 hours of operation. This input system has proved adequate to feed gas at pressures up to 1.5 bars without appreciably affecting the vacuum in the rotor chamber.

The rotating source, in its original version[8] and in that at Freiburg,[50] emits the input gas in a continuous 360° spray, from which only a thin slice passes through a skimmer to become a collimated molecular beam. Such profligacy overburdens conventional pumping. As well as allowing deleteriously high background in the rotor and detector chambers, it lowers the tolerable level of input gas pressure and thereby the quality of the supersonic expansion. These drawbacks led us to introduce a pulsed valve in the rotor gas inlet (indicated by "**PGV**" in Figure 1) and a shutter (**3** in Figure 1) in front of the skimmer (**4** in Figure 1) that gives entry to the detector chamber. For PGV we have used either a standard Parker Series 9 valve for non-aggressive gases, or Parker Series 2 valve for corrosive gases like NO_2, controlled by IOTA-ONE Solenoid Valve Controller by Parker or by a custom made controller. The use of custom made controllers helps significantly to reduce the price, taking into account that we operate up to four valves and shutter. Our custom made controllers produce rectangular voltage pulses with adjustable amplitude up to 300 V,

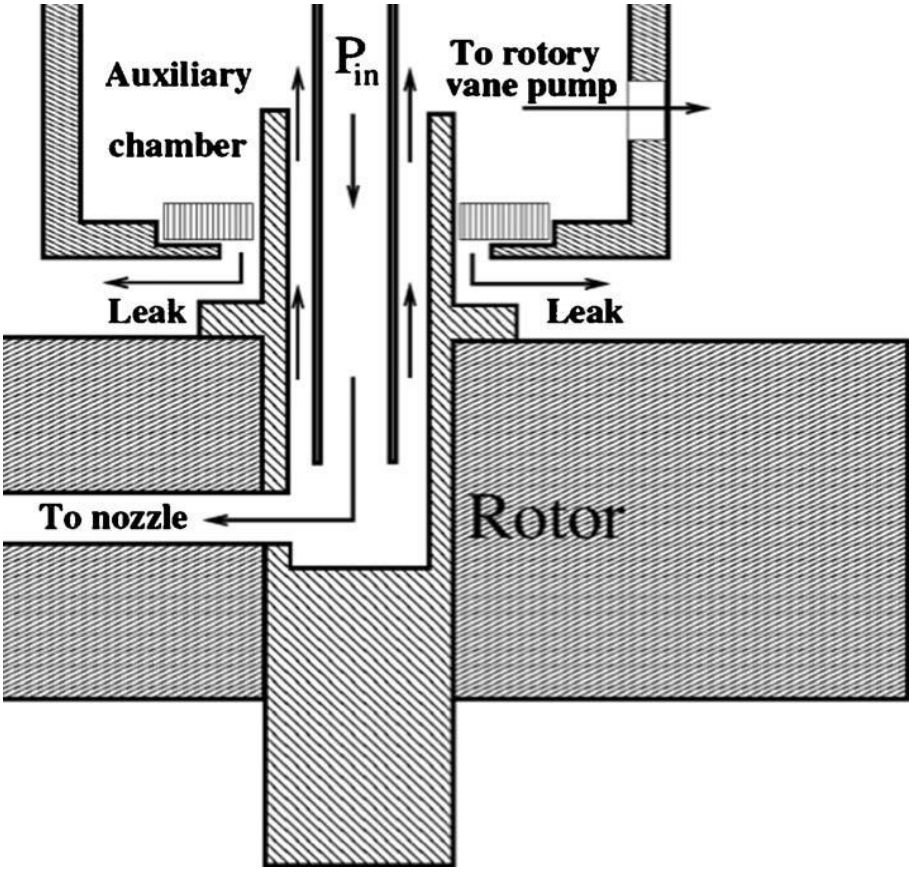

FIG. 3. Schematic (side view) showing how gas is fed from stationary reservoir at pressure P_{in} into spinning rotor (for beam **2** in Figs. 1 and 2). The coupling between the stationary feed tube and the stainless steel inlet to the rotor barrel is housed in an auxiliary chamber that is pumped independently of the main chamber. Cross-section of PEEK washer encircling spigot from rotor is shown as rectangles patterned with vertical lines.

duration (0.1 ms and up) and time delay. Design of such circuits is described in detail in the standard electronics handbook.[125] The time required to open Parker Series 9 can be as short as 0.1 ms. The duration that the PGV is open can be adjusted, typically between 1 ms and 20 ms. The shutter, guarding entry to the skimmer, is also controlled by a custom made controller similar to those used to control the input valves. We designed two types: a solenoid device with open close cycle as short as 2 ms duration, and a hard drive based device about tenfold faster; the latter is very useful for creating short beam pulses and monitoring time-of-flight. The rotor position is monitored by an induction proximity sensor, to provide a time-zero for control of the PGV and the shutter, as well as for time-of-flight measurements. As the inlet gas pulses are much longer than the rotational period of the source, the output that reaches the detector when the shutter is open is a sequence of gas pulses spaced by the rotational period. Closing the shutter in synchrony with the rotor enables isolating a single gas pulse. Figure 4 shows typical raw time-profile data for a krypton beam, (a) with the shutter open and (b) with the shutter operated to transmit only one of the sequences of pulses. The pulses persist for times much longer than the valve open time. This is because the pulsed valve allows gas to fill the rotor, which then leaks out of the nozzle over significantly longer period of time.

Installing the pulsed inlet valve and gated shutter system much enhanced operation of the rotating source. In our apparatus, the main chamber wherein the rotor resides is pumped by a 6000 l/s oil diffusion pump and the detector chamber by a 500 l/s pump, both backed by rotary vane pumps. When the gas input is shut off, the ambient pressure in the rotor chamber is about 2×10^{-7} Torr and in the detector chamber 2×10^{-8} Torr. The two chambers communicate only by the skimmer orifice (3 mm dia). Previously, in our apparatus as well as

that of Ref. 35, when the rotor was continuously spraying gas, if the input pressure into the rotor reached 100 Torr, the pressure in the rotor chamber rose to nearly 10^{-4} Torr and in the detector chamber to 5×10^{-6} Torr. Such high background in the rotor chamber severely scatters slow molecules; e.g., it is estimated that more than 90% of Xe atoms slower than 70 m/s would be scattered from a beam while traveling the 10 cm from rotor to skimmer.[8] When operating in the pulsed mode, with the input pressure into the rotor as high as 1.5 bars, we find that the pressures in the rotor and detector chambers surge to about 5×10^{-5} Torr and 2×10^{-7} Torr, respectively, during the 20 ms–40 ms "shooting" time that delivers the pulses. After the surge, the pressures, as indicated by ion gauges, subside within a few minutes to the pre-shot levels.

The detector chamber contains a residual gas analyzer (RGA-100, Stanford Research System) to monitor the parent beams. The RGA is fitted with an electron multiplier and ion counter and, in one of several modes, can detect a selected species via a quadrupole mass-spectrometer with time resolution of about 0.01 ms. Signals from the RGA electron multiplier are amplified by a custom made current amplifier with filter and subsequently by a voltage amplifier. The design of the current amplifier is similar to that described in standard electronics handbooks [125] tailored to the parameters of our equipment. The amplifier output is processed by a digital acquisition card (PCI-DAS 4020/21, from Measurement and Computing). An analog isolation amplifier is employed between the voltage amplifier and digital acquisition card to isolate the measuring electronics from the computer. LABVIEW software was used to control the RGA and acquire and average signals.

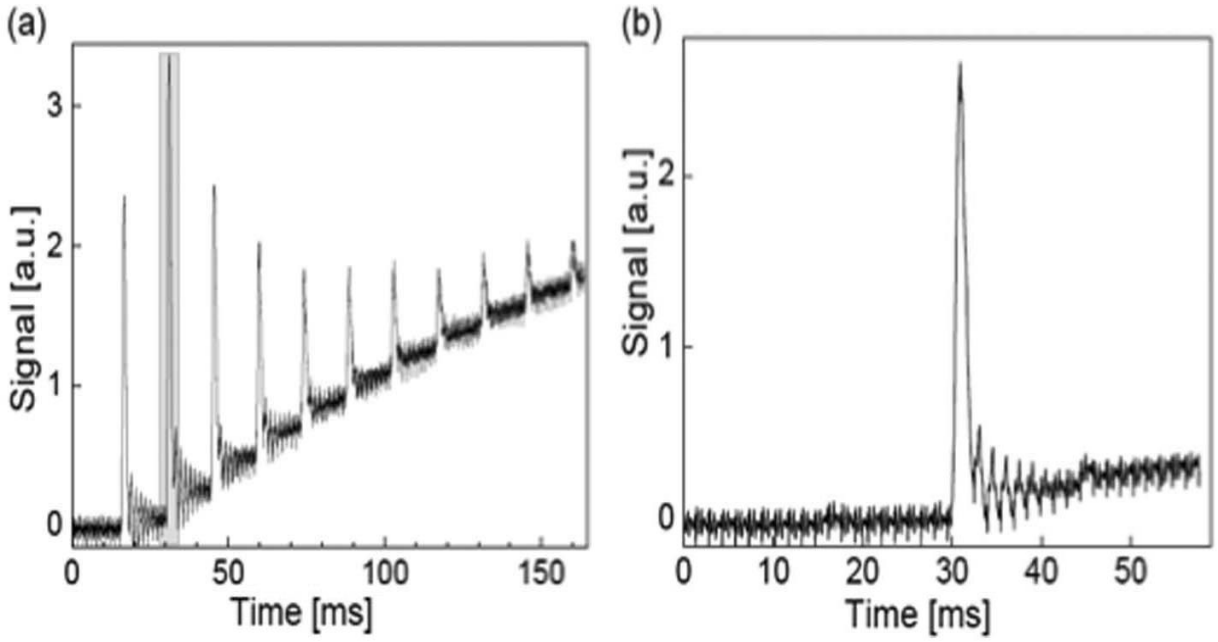

FIG. 4. Raw RGA signals (arbitrary units) vs time (in milliseconds) for pulsed Kr beam, with P_{in} = 300 Torr and rotor spinning at 70 Hz: (a) Sequence of pulses recorded with open shutter; spacing is rotational period of 14 ms, duration of PGV opening was 20 ms. (b) Single pulse [shaded in (a)] was separated from sequence by closing the shutter except during interval from 29 to 33 ms. Growth of background signal in (a) is due to accumulation of gas in detector chamber; closing the shutter suppresses it in (b). The high frequency noise evident in both (a) and (b) is predominantly due to the rectangular pulsed voltage applied to the RGA electron multiplier with frequency 675 Hz; it could be readily filtered out by standard techniques.

Beam Properties

For stationary supersonic beam sources, principles and engineering practice are well established, both for continuous[126] and pulsed versions. For rotating sources, the basic features seem to be the same (although as yet much less thoroughly examined). However, three distinctive features enter. The first is definitely advantageous, the second is compromised by pulsing the gas input, and the third complicates time-of-flight analysis.

(i) As noted already, the rotating source enables scanning the beam velocity without changing the source temperature or seed-to-carrier gas ratio.

(ii) The rotating source acts as a gas centrifuge.[8, 124] For continuous input, this produces a density gradient that increases between the gas inlet at pressure P_{in} on the rotation axis and the exit aperture at R_{out}. If the gas within the rotor remains at thermal equilibrium, the pressure behind the exit aperture, P_0, is governed by

$$P_o = P_{in} e^{\frac{m v_{rot}^2}{2kT}} \qquad (1)$$

where $V_{rot} = 2\pi\omega R_{out}$, with ω the angular velocity of the rotor, m the molecular mass, k_B the Boltzmann constant, T_0 the source temperature. For continuous input, Eq. (1) is expected to be a fair approximation as long as $P_0 A_{out}$ is substantially less than $P_{in} A_{in}$, where the A's denote areas of the exit and inlet apertures. For our apparatus, that condition is satisfied for a wide range with $P_0 > P_{in}$ because $A_{out}/A_{in} = (0.4/3.125)^2 = 0.016$ (orifice diameter 0.4 mm, barrel ID 1/8). For pulsed input, however, the gas flow through the rotor is inherently nonstationary. This is illustrated by data shown in Figure 5, displaying variations in the sequence of pulse amplitudes as the input pressure is raised from P_{in} = 25 to 454 Torr. Note that P_{in} is the initial gas pressure in the mixing chamber

(*cf*. Figure 3) before the PGV is opened to release gas into the rotor. As P_{in} is increased, the pulse with maximum amplitude occurs earlier in the sequence. This indicates that increasing P_{in} boosts how quickly gas fills and drains from the rotor, eventually making the first pulse the largest. Particularly for high P_{in}, the rapid draining renders uncertain the pressure distribution within the rotor, so makes estimates of P_0 from Eq. (1) inapplicable. Although pulsing the gas input allows use of considerably higher P_{in} than does continuous input, there remains the limitation imposed by formation of dimers and higher clusters. Criteria based on empirical results[126] indicate that for Kr and Xe, the carrier gases we most use, P_0 should not exceed ~500 Torr, to keep dimerization below ~1%.

(iii) Because molecular beams have appreciable angular width, for a rotating source the range of "shooting positions" that allow beam molecules to pass through the skimmer is much broader than for a stationary source. Figure 6 indicates this range, which is determined by the ratio of the skimmer aperture to the length of the rotor between the gas inlet and the exit orifice. The range is $\varphi_{max} = \pm 11.5^{\circ}$ for our current rotor and skimmer set-up. Molecules emitted from the rotor at position $\varphi = -11.5^{\circ}$ travel further than those emitted at $\varphi = +11.5^{\circ}$; the difference is $\Delta z = 2R_{out} \sin \varphi_{max} = 6$ cm. The molecules emitted with different φ actually have the same spread in speed. In a TOF measurement, however, the disparity in travel distances introduces an apparent spread, ΔV_{app}. That can become much larger than the actual spread, as V_{app}/V is at least comparable to the ratio of z to the distance between the nozzle exit aperture at the $\varphi = 0$ position and the detector, which is 6/45 = 0.13 in our apparatus. Hence TOF data does not give realistic velocity spreads unless carefully deconvoluted.[7, 8, 50] For slower beams, formed at high rotation

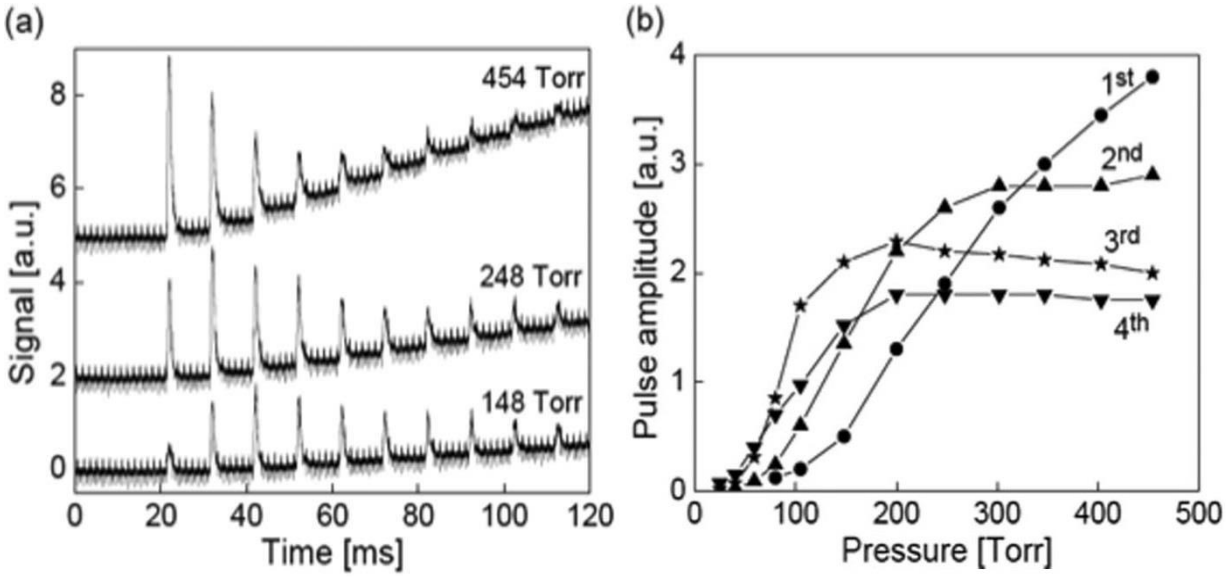

FIG. 5. Comparison of sequences of pulse amplitudes (raw RGA data obtained with open shutter, cf. Figure 4) for pulsed Kr beam with rotor spinning at 100 Hz (corresponding to $V_{rot} = -94$ m/s and $V_{mp} = 305$ m/s); the open PGV duration was held at 20 ms but input pressures ranged from P_{in} = 25 to 454 Torr. (a) Pulses, spaced by $1/\omega$ = 10 ms, for P_{in} = 148, 248=, and454 Torr; for these, the maximum pulse amplitude occurs for the third, second, and first pulse, respectively. (b) Variation of amplitudes of first, second, third, and fourth pulses (at 22, 32, 42, 52 ms, respectively) with input pressure, over range P_{in} = 25 to 454 Torr.

frequencies, TOF analysis is further complicated by "wrap-around" because then spreads in travel time become longer than intervals between pulses.

These complications and partial remedies are more fully discussed elsewhere, from the perspective of the original but conflicting aims of attaining beams both intense and slow enough to trap.[7, 8, 50] As now we intend to use the rotating source in merged beam collision experiments, slowing is no longer a major concern. Here we want to illustrate aspects most pertinent for the merging approach. These are the velocity scanning capability and how much the increase in input pressure enabled by pulsed operation can enhance the beam intensity and narrow its velocity spread. As a basis for assessment, we consider estimates obtained from standard approximate formulas for supersonic beams.[126]

For the rotating source, the velocity distribution of molecular flux obtained on transforming into the laboratory frame [8, 127] is given by

$$F(V) = V^2(V - V_{rot})e^{-\frac{(V-w)}{\Delta v^2}} \qquad (2)$$

aside from normalization; V_{rot} is the peripheral velocity of the rotor, $w = u + V_{rot}$ is the flow velocity along the centerline of the beam in the laboratory frame, u the flow velocity relative to the rotating exit nozzle. In the slowing mode, when the rotor spins contrary to the beam exit flow, $V_{rot} < 0$; in the speeding mode, $V_{rot} > 0$. The velocity spread is governed by

$$\Delta v = \sqrt{\frac{2kT_{\parallel}}{m}} \qquad (3)$$

The parallel (also designated longitudinal) temperature of the expansion, T, describes the molecular translational motion with respect to the flow velocity. According to the thermal conduction model,[26] $T_{\parallel}/T_o$ is proportional to $(P_o d)^{-\beta}$, with d the nozzle diameter and the

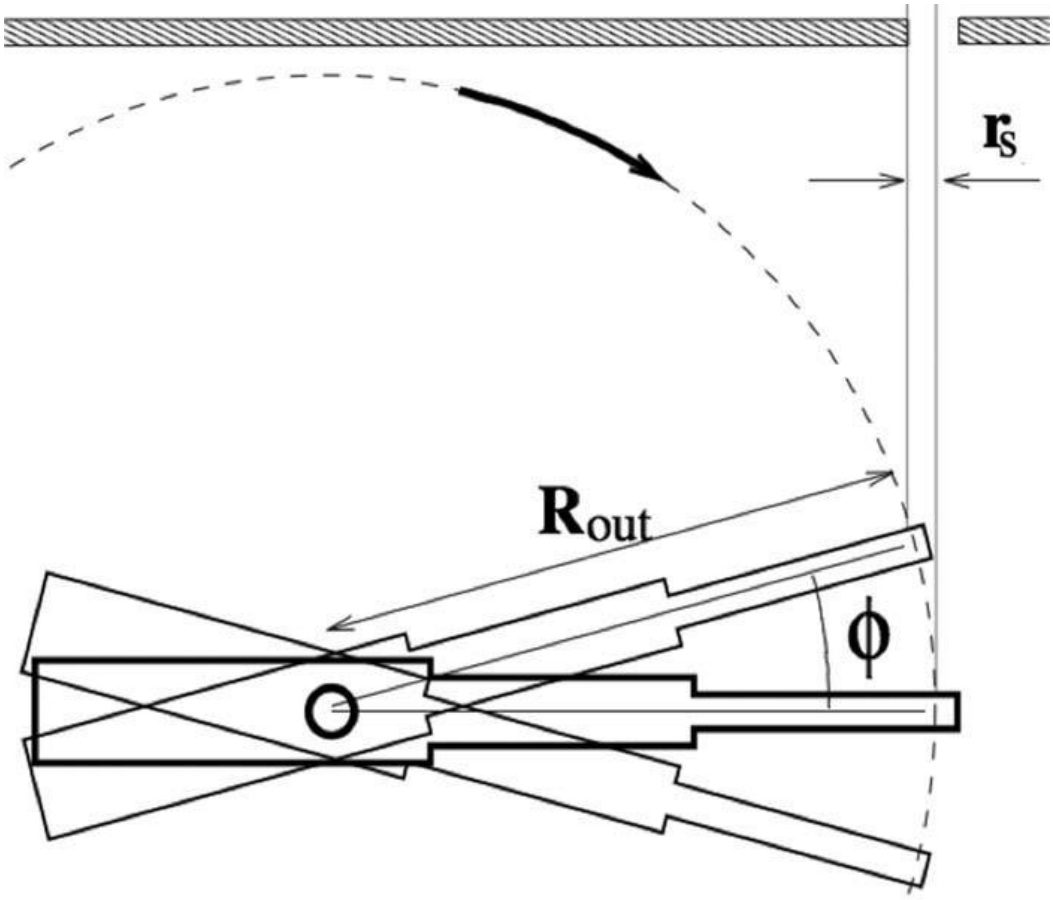

FIG. 6. Spread in "shooting positions" that permit molecules emitted from the rotating source to pass through the skimmer. The maximum angle φ in the plane of the rotor orbit for which molecules can still enter the skimmer is $\varphi_{max} = \cos -1[1 - r_s/R_{out}]$, where r_s is the radius of the skimmer entrance aperture and R_{out} is the length of the rotor barrel between the gas inlet and the exit orifice.

exponent $\beta = 6(\gamma - 1)/(\gamma + 2)$, with $\gamma = C_P/C_V$ the heat capacity ratio. Likewise, the flow velocity involves both $T_{\parallel}/T_0$ and γ:

$$u = \sqrt{\left(\frac{2kT_o}{m}\right)\left(\frac{\gamma}{\gamma-1}\right)\left(1 - \frac{T_{\parallel}}{T_o}\right)} \qquad (4)$$

The intensity delivered to the skimmer is proportional to P_0d.[98] It can be determined by relating the integral of Eq. (2) over all velocities to the centerline intensity when the rotor is stationary, which can be obtained from familiar expressions [126] involving as well T_0, m, γ , and apparatus geometry as described in Refs. 35 and 36. The calculated total beam intensity for $P_0d \sim 1$ is of the order of 10^{18} molecules/sr/s, a typical magnitude. Our RGA calibration proved extremely fickle, so did not provide a satisfactory confirmation. However, comparisons with experimental results of Ref. 35 are consistent with the calculated intensity. The corresponding estimated intensity per pulse, again for $P_0d \sim 1$, is about 10^{15} molecules. Figure 7 displays the variation with V_{rot} and P_0d (Ref. 2) of the number of molecules/sec predicted to arrive at the observation zone. Data points with curve (a) were obtained with our pulsed source; for (b) from Ref. 35 and for (c) from Ref. 37. The shape of the curves, calculated as described in Ref. 35, is governed chiefly by V_{rot}. To illustrate the dependence on P_0d,[98] we shifted the curves for (a) and (c) relative to the curve (b), according to the values P_0 and d. Curve (b) is taken from Figure 10 of Ref. 35. Even for the Xe beam of curve (b), the centrifugal effect of Eq. (1) made only a minor contribution; as it would be much smaller for the Kr beam of (a) and Ar beam of (c), in Figure 7 we have omitted it for all three curves. Thus, we took $P_0 = P_{in}$. For the slowing mode the data points droop below the calculated curves, increasingly so as the lab velocity decreases (V_{rot} more negative). For (b), a correction for attenuation by scattering by background gas, which becomes much more

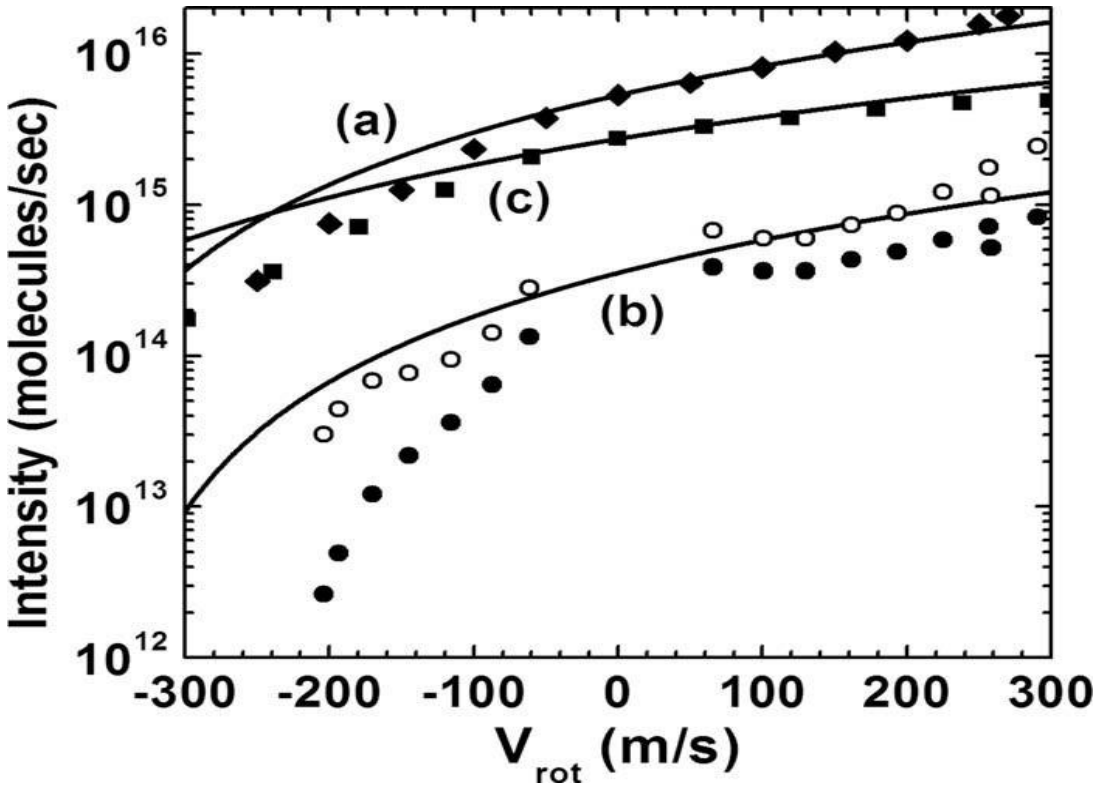

FIG. 7. Variation of intensity with V_{rot} and backing pressure within rotating supersonic nozzle. Curves were calculated from integral of Eq. (2) as described in Ref. 35; the centrifugal contribution of Eq. (1) was not included. Shape of curves depends on the flow velocity u, speed spread v/u and V_{rot}/u; intensity magnitude is proportional to P_0d [98] otherwise involves mostly apparatus factors. Accompanying data points are from: (a) our pulsed source for Kr beam () with P_{in} = 450 Torr; (b) Harvard for Xe beam (●) with P_{in} = 30 Torr; (c) Freiburg for Ar beam () with P_{in} = 220 Torr. All three used the same nozzle exit diameter, d = 0.01 cm. For (b) open points (o) have been obtained by correcting experimental data (●) with estimates of attenuation by scattering from background gas. Nominal spread was v/u = 0.1 and flow velocities used were u = 400, 350, and 550 m/s for (a), (b), (c), respectively.

serious for slow molecules, was applied (open points). For (a) and (c), the background pressure is at least tenfold lower than in (b), and the droop is much less pronounced, but suggests some attenuation may still occur.

Figure 8 shows velocity distributions obtained from Eqs. (2) - (4) to illustrate that the width v narrows as P_0d is increased. That can occur either by increasing P_{in} or by the centrifugal enhancement given by Eq. (1). When operative, the centrifugal effect can decrease the parallel temperature T below that for a stationary source by tenfold or more, so narrow v more than threefold, as confirmed by experimental data presented in Ref. 35. The relation between T and P_0d given by the thermal conduction model has likewise been confirmed for rotating sources, both in Ref. 35 and Ref. 37. Another aspect exhibited in Figure 8 is that a decrease in the Poisson ratio, $\gamma = C_p/C_v$, results in less efficient cooling as the backing pressure is increased. This is evident in comparing the widths for Kr ($\gamma = 5/3$) and NO_2 ($\gamma = 1.282$). Often "inverse" seeding (light seed, heavy carrier), is used to slow supersonic beams. For light molecules, that is done even with a rotating source to lower the range of V_{rot} required. We note this because $T_{\|}$ should be lower for the light seed molecule than the carrier gas, according to theory[126] found consistent with experimental results.[7, 8] This offers a means, e.g., by seeding NO_2 in Xe, to offset the penalty imposed on Δv by a smaller value of the Poisson ratio. The cost of that strategy, however, is a much lower centerline intensity of the seed gas, because of its small mole fraction and mass defocusing. We have adjusted the peak positions in Figure 8 to 420 m/s, to illustrate in (a) the upward effect of "slip" for H atoms seeded in Kr, and in (b) the downward shift provided by the counter rotating source.

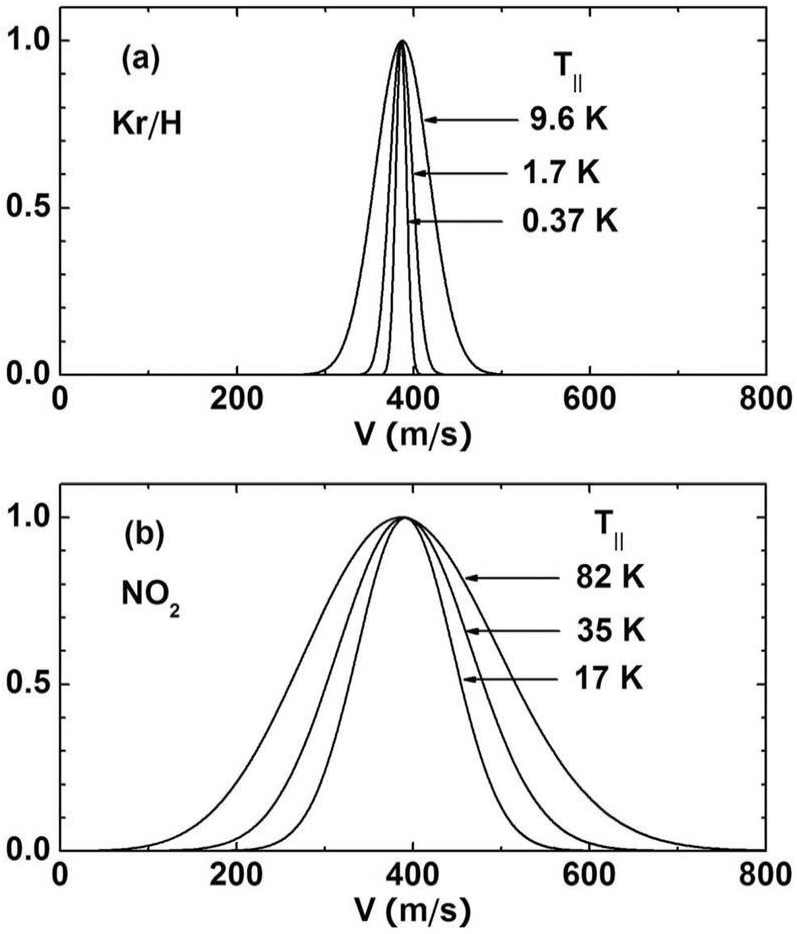

FIG. 8. Velocity distributions for supersonic beams, computed from Eqn. (2) - (4). Panel (a) pertains to stationary source of beam with a few percent H seeded in Kr; peak position is adjusted upward (from u ~ 385 m/s) to 420 m/s, to account for estimated velocity "slip" of H component. Panel (b) for NO_2 beam from counter-rotating source has peak position shifted downwards to 420 m/s (from u ~ 600 – 680 m/s). Longitudinal temperatures T associate with narrowing of width v with increase in backing pressure P_0 behind nozzle exit orifice. Curves are shown for three values of P_0d (in Torrcm); widths obtained from $T||/T_0 = B(P_0d)^{-\beta}$, with T_0 = 300 K; B = 0.0320, β = 1.09 for Kr; B = 0.27, β = 0.52 for NO_2.

Merged-Beams for Slow Collision Experiments

Returning to Figures 1 and 2, which depict a merged beam experiment underway in our laboratory, we provide some details that serve to illustrate characteristic aspects. The distance from the stationary pulsed beam source **1** to the observation zone (OZ) is ~23 cm, and that from our pulsed counter-rotating source **2** at the rotor exit when in the nominal "shooting" position is ~13 cm. Our specimen reaction is $H + NO_2 \rightarrow OH + NO$. It has been much studied, both in "warm" beams[128-135] as well as other kinetic experiments and theory.[136] The beam **1** reactant is atomic H (or D), seeded in Kr and allowing for "slip" in the supersonic expansion,[126] we estimate the most probable beam velocity is $V_1 \sim 420$ m/s, spread $\Delta v_1 \sim 35$ m/s. The beam **2** reactant is NO_2 (without carrier gas); by adjusting the rotor speed (which can be done to within ~1 m/s), we can obtain the same velocity, $V_2 \sim 420$ m/s, with estimated spread $\Delta v_2 \sim 50$ m/s. Use of the rotating source for NO_2 bestows an incidental bonus. In order to avoid appreciable dimerization to form N_2O_4, it is necessary to keep the gas within the source warm and the pressure modest (e.g., 300 K or above, 2 Torr or less). That is a severe constraint for experiments that require the ability to shift the velocity distribution substantially. Simply adjusting the rotor speed enables large shifts in the lab velocity of the beam with no change in the temperature and pressure within the source.

The transit time from source to OZ is considerably longer for beam **1** (nominal $t_1 = 0.66$ ms, spread 0.60–0.73 ms) than for beam **2** (nominal $t_2 = 0.37$ ms, spread 0.33-0.43 ms). Accordingly, the H beam exit valve is opened about 0.3 ms before the rotor reaches its "shooting" position, to ensure that H and NO_2 traveling at the nominal velocity arrive at about the same time at the OZ. High precision in the timing is not required. Complete spatial overlapping of the reactant beams in the OZ actually results simply because the pulse

durations of both beams are long enough to allow long streams of molecules to issue forth. The H exit valve is open longer than 1 ms, so the emitted beam pulse extends beyond 35 cm; likewise, at the rotor speed needed to produce a lab beam velocity of ~420 m/s, the pulse of NO_2 sent through the skimmer lasts longer than ~0.6 ms, so extends beyond 20 cm.

From the top view (Figure 1), it would appear that a traffic problem occurs, since beam **1** would intersect the rotor when it reached the "shooting" position. However, as shown in the side view depicted in Figure 2, beam **1** actually passes below the rotor (by about 3 mm). The rotor tip is made quite small (it only has to house the 0.4 mm exit orifice), so there is sufficient clearance to ensure that only minor scattering occurs from the upper edge of beam **1** as it passes under the rotor. Such scattering is insignificant because only reactive collisions occurring in the OZ are detected.

The small angular spread imposed by the skimmer limits the intensity of the beams arriving at the OZ, although there is some compensation because the reactant beams merge in a pencil-like volume rather than cross perpendicularly. We have estimated from the pressures within the beam sources, exit and skimmer orifice diameters, and distances from the OZ, that in the OZ the density of our H beam is $n_1 \sim 10^{11}$ cm^{-3} and that of our NO_2 beam $n_2 \sim 10^{12}$ cm^{-3}. Estimates for a typical "warm" crossed-beam study, obtained in the same way (as reported in Ref. 47), are of the same order as ours for H but much larger for NO_2. If it proves necessary, by replacing our current rotor (radius 15 cm) by a smaller one (radius 5 cm), we could shrink distances sufficiently to increase n_1 nearly threefold and n_2 about tenfold at the OZ. The overall rate of formation of OH + NO (in various vibrational and rotational states) is given by $n_1 n_2 \langle k(E_R) \rangle = n_1 n_2 \langle V_R \sigma(E_R) \rangle$, where $k(E_R)$ is the reaction rate coefficient, V_R the relative collision velocity, and $\sigma(E_R)$ the total reaction cross section. Brackets $\langle \cdots \rangle$ indicate an

average over both internal states and the spread in E_R. We will detect OH by means of laser induced fluorescence (LIF), as in warm experiments.[129, 131-133, 135]

The extensive application of merged-beams in high energy experiments emphasizes and documents a favorable kinematic effect. It has enabled well-collimated beams with keV lab energies to be merged over interaction distances of tens of cm to study collisions at relative kinetic energies below 1 eV with high resolution.[122] In the center-of-mass system, contributions to the relative kinetic energy from the spreads in lab speeds of the beam particles are markedly "deamplified" by a kinematic factor proportional to the *difference* in the most probable lab beam speeds. This is readily demonstrated when the spreads are small fractions of the most probable speeds for both beams. For beams with lab speeds V_1 and V_2 intersecting at an angle θ, the relative kinetic energy is

$$E_R = \frac{1}{2}\mu(V_1^2 + V_2^2 - 2V_1V_2\cos\theta) \qquad (5)$$

with $\mu = m_1m_2/(m_1 + m_2)$ the reduced mass. For perfectly merged beams, with $V_1 = V_2$ and $\theta = 0$, the relative kinetic energy would be zero (and no collisions could occur). If the spreads in speeds, Δv_1 and Δv_2 are very small, in first-order their contributions to E_R are simply proportional to $|V_1 - V_2|$ and thus strongly deamplified when the most probable beam speeds, V_1 and V_2, are nearly equal. That occurs in many applications using high-energy beams, as the fractional spreads, v/V, are often only 0.1% or less.[122] For supersonic molecular beams, these spreads are typically 10% or more, so deamplification is less dramatic yet still pronounced.

We have computed the average relative kinetic energy, $\langle E_R \rangle$, for merged supersonic beams with fixed θ, using for both beams the flux velocity distribution for a stationary

source, given by F(V) of Eq. (2) with $V_{rot} = 0$ and w = u. The average is obtained in explicit form,

$$\langle E_R \rangle = \frac{1}{2}\mu[u_1^2 f(x_1) + u_2^2 f(x_2) - 2u_1 u_2 g(x_1) g(x_2) \cos\theta] \quad (6)$$

with $x_i = \Delta v_i / u_i$ $(i = 1,2)$ the ratio of velocity spread to flow velocity, specified by the ratio of Eqn. (3) and (4). The following functions f(x) and g(x) are ratios of polynomial form with x-dependent coefficients:

$$f(x) = \langle (V/u)^2 \rangle = P_5(x)/P_3(x), \quad (7)$$

$$g(x) = \langle (V/u)^2 \rangle = P_4(x)/P_3(x), \quad (8)$$

where

$$P_n(x) = \sum_{s=0}^{n} c_s x^s \quad (9)$$

and $c_s = \binom{n}{s} \Gamma(\{s+1\}/2,\ 1/x^2)$, comprised of binomial coefficients weighted by incomplete Gamma functions.

A fuller discussion of merged-beam distributions is given elsewhere,[42] treating further a pair of stationary supersonic beams and also the case of one stationary beam, the other beam from a rotating source with the velocity distribution of Eq. (2). The full distributions, $P(E_R)$, are evaluated, as well as the rms energy spread, $\Delta E_R = |\langle E^2 \rangle - \langle E \rangle^2|^{1/2}$, When the beam velocities are closely matched ($u_1 \approx u_2$ or $u_1 \approx w_2$) the form of $P(E_R)$ is qualitatively Poissonian; whereas, if the velocities become more and more unmatched $P(E_R)$ becomes approximately Gaussian and then Maxwellian. Although for closely matched beams $\langle E_R \rangle$ is minimal, the energy spread then reaches $\Delta E_R = 2^{1/2} \langle E_R \rangle$, its maximal value. For

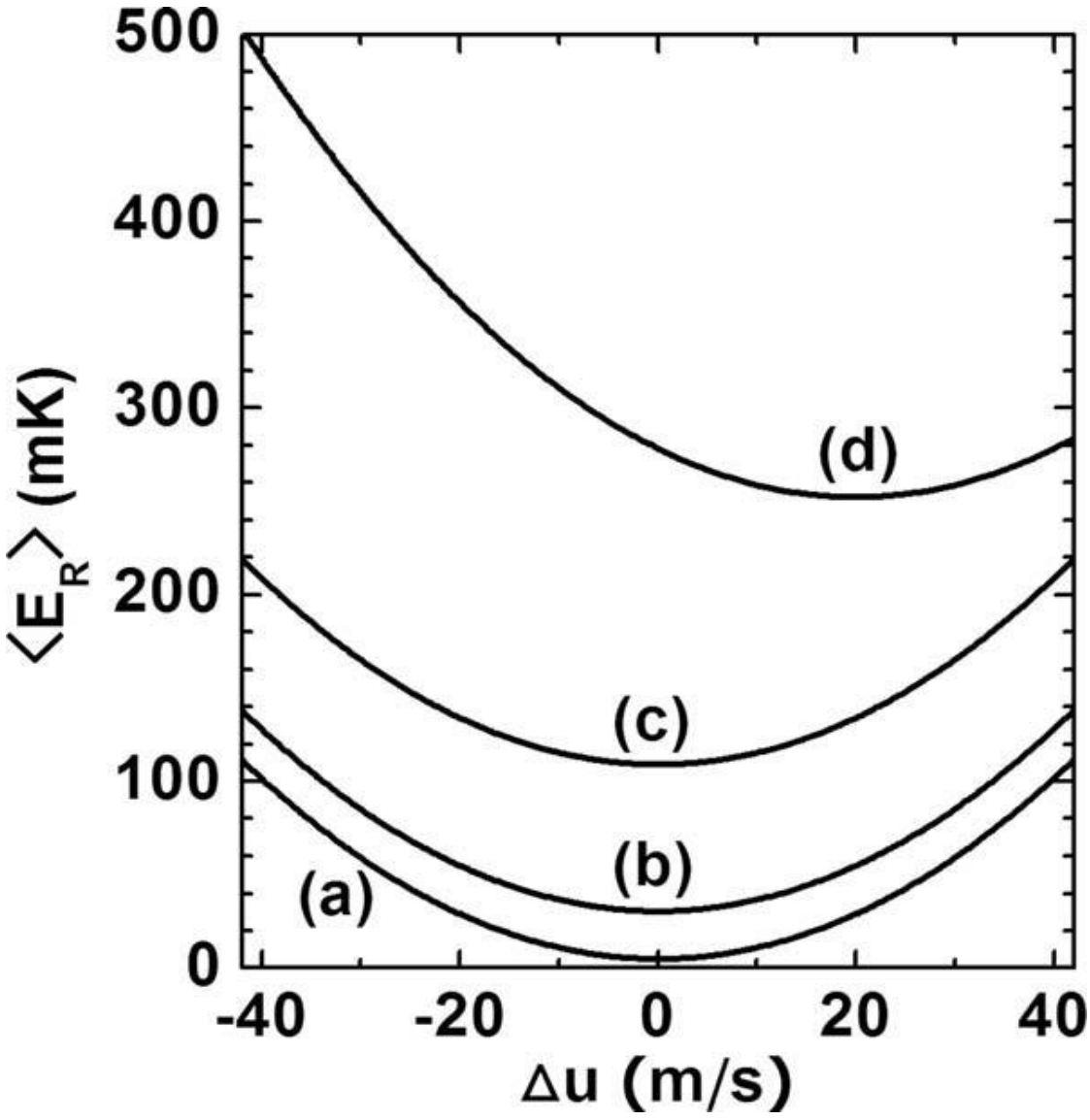

FIG. 9. Relative kinetic energy, $\langle E_R \rangle$, for bimolecular collisions in merged beams, averaged over velocity distributions; cf. Eq. (6). The plot pertains to supersonic beams with the same most probable flow velocities, $u = u_1 = u_2 = 420\ m/s$, reduced mass μ = 1 amu, merging angle $\theta = 1°$; curves shown are for various speed spreads, $\Delta v/u$: (a) 1% for both beams; (b) 5% for both beams; (c) 10% for both beams; (d) 10% for one beam, 20% for the other.

modest unmatching, $\langle E_R \rangle$ increases slowly while E_R shrinks more rapidly.For the conditions anticipated in our current H + NO_2 experiments, $u_1 = u_2 \sim 420$ m/s, $\Delta v_1 \sim 35$ m/s, $\Delta v_2 \sim 50$ m/s, and $\theta \sim 1.5^\circ$, we find $\langle E_R \rangle \sim 110$mK. That is well within the "cold" collision realm (<1 K), although the kinetic energies of the beams are 11 K and 490 K. In $\langle E_R \rangle$, the velocity spreads contribute about 95%; if those were each reduced by 10 m/s, the relative kinetic energy would drop to ~65 mK. Figure 9 shows that $\langle E_R \rangle$ for the $u_1 = u_2$ case can also be reduced substantially by lowering the matched flow velocity. Figure 10 shows how $\langle E_R \rangle$ varies for modest mismatching of the flow velocities. Even a mismatch of ±10% will appreciably increase $\langle E_R \rangle$ when both beams have similar velocity spreads, whereas a small mismatch becomes optimal when the velocity spreads differ considerably. Both Figs. 9 and 10 include curves for four sets of velocity spreads. These range from (a) utopian 1%, achievable for Stark decelerated beams,[110] but at great cost in intensity; to (b) 5%, attainable with a compact velocity selector[137] with acceptable cost in intensity; to (c) 10%, typical for supersonic beams; to (d) 10% + 20%, similar to our current experiment.

Discussion and Outlook

To pursue gas phase "cold chemistry" in the mK range, the prime experimental requisite is sufficient flux of reactant collisions with very low *relative* kinetic energy. That is difficult to attain using either trapped reactants or crossed molecular beams, because then *both* reactants must contribute adequate flux with very low translational energies. Using merged-beams with nearly the same velocity can provide much higher flux with low relative energy because *neither* beam needs to be slow; instead, both can be operated in the usual warm range or not far below it. A rotating supersonic source can readily adjust its beam velocity over a wide range to match that from a stationary partner source. Pulsing both sources enables use of

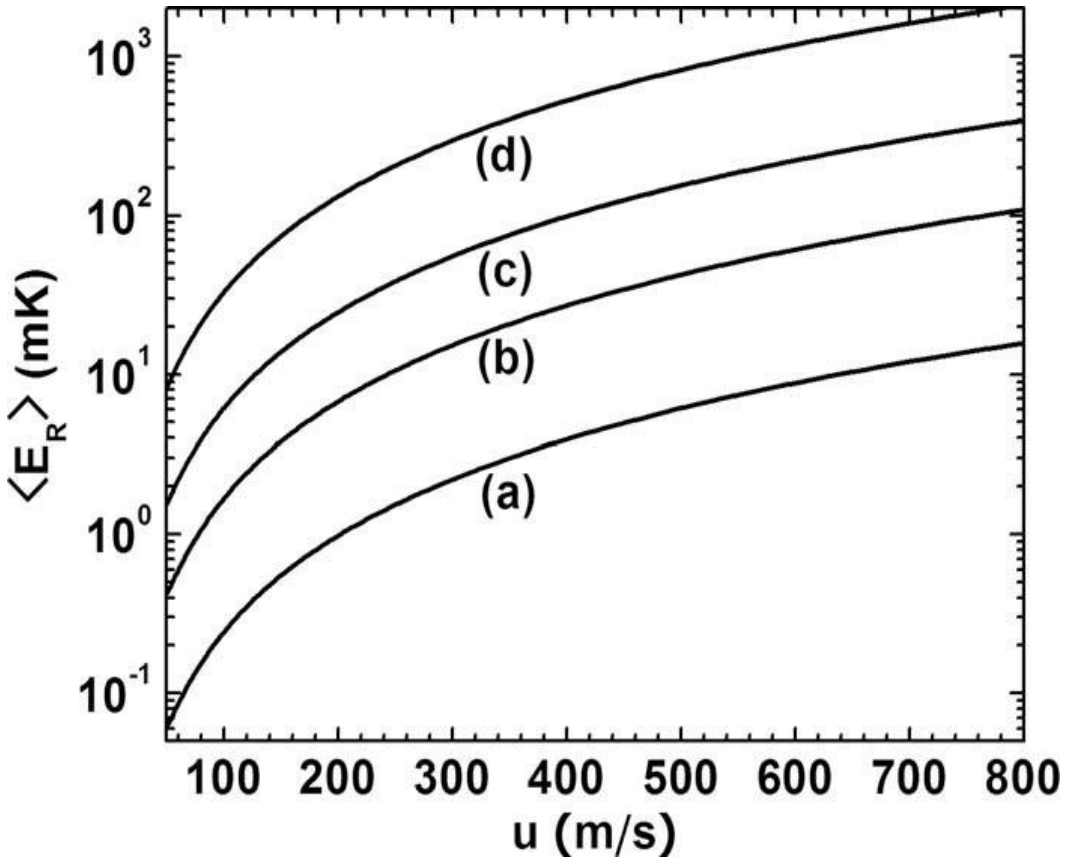

FIG. 10. Relative kinetic energy, $\langle E_R \rangle$, as specified in Figure 9 but for beams with most probable flow velocities that may differ, $\Delta u = u_1 - u_2$, within the range 420 ± 40 m/s. Again, curves shown are for various speed spreads, v/u; in (d) beam **1** has 10% spread, beam **2** has 20%.

higher input pressures and thereby enhances the beam intensities. Also, gaining freedom from the need to produce slow but intense beams much widens chemical scope. The rotor source is suitable for any fairly volatile and docile molecule, whereas the stationary partner provides a complementary capability to generate species that must be produced from precursors, such as hydrogen, oxygen, or halogen atoms or free radicals. For example, with little change, our current apparatus can be used for many reactions of H atoms, including with halogen or halogen halide molecules. With merged beams, candidate reactant molecules need not have properties amenable to manipulation, such as electric or magnetic moments, but it is advantageous to pair reactants that differ greatly in mass, since the relative kinetic energy is proportional to the reduced mass.

In merged-beam reactive collision experiments, the chief observable properties are the total cross section and its dependence on the relative kinetic energy of the reactants. These may be augmented by preparing internal states (electronic, vibrational, and rotational) of the reactants or subjecting them to external fields. Merged-beams are not suited to observing the angular distribution or translational energy of reaction products. However, this situation accords with intrinsic limitations that enter in the slow collision realm.[97] There product angular distributions tend to become isotropic (when s-wave collisions predominate) or nearly so. Also, since reactions accessible in the cold realm are generally exoergic, disposal of energy and angular momentum among product states is virtually the same in cold collisions as in warm collisions. Hence, in cold reactive collisions, usually only reactant interactions can provide new information beyond that better found from experiments in the warm realm.

Another inviting aspect of merged-beam experiments is that they require mostly familiar molecular beam apparatus, not unusually expensive or virtuosic. Although a rotating source is uncommon, our current device has proved simple to assemble and robust in operation. It provides an especially convenient means to match velocities of the reactant beams. Surprisingly, we have found only three previous suggestions, all merely *en passant*, to apply merged beams to study low energy collisions of uncharged molecules.[2, 8, 110] Prospects for merged-beams as a route to cold chemistry seem now to deserve more attention.

Acknowledgements

We are grateful for support of this work by the National Science Foundation (under grant CHE-0809651), by the Norman Hackerman Advanced Research Program (under grant 010366-0039-2007) and by the Robert A. Welch Foundation (under grant A-1688 to Lyuksyutov). Sheffield is a Welch Graduate Fellow. We are also thankful for support provided by Don Naugle, David Lee, and Vladimir Khmelenko. We have enjoyed correspondence with Ronald Phaneuf about merged beams as well as discussions with Manish Gupta about his pioneering rotating beam source. We have benefited from a design by Bretislav Friedrich of a prototype for the differentially pumped gas input (akin to our Figure 3), as well as efforts by Michael Timko to add a pulsed gas feed, and advice from Simon North and Mark Raizen on other experimental aspects. We thank Qi Wei for preparing Figures 7–10.

APPENDIX B

Rotor Construction

Rotor construction begins only after the design program described by Gupta and Herschbach and contained in the appendices of his thesis. This program calculates the diameters and lengths of each of the cylinders that will make up the rotor body. With these dimensions and a 3D computer modeling program a rendering of the rotor can be generated to verify the mass balance and geometric properties. After the design is finalized, construction follows these simple steps:

1. Part off the 0.75" diameter Al-7078 rod to 10" and face each side using a lathe. Measure the length precisely as the central hole will penetrate to within 0.1" of the end. Use a starter drill bit on each end for use with a live center.
2. Drill the central hole using a lathe and generous amounts of cutting fluid. The alloy is harder than pure aluminum but not as hard as stainless steel. A short drill bit should be used at first and there should be several different length drill bits available. Step up the size as the hole gets deeper. The 10" drill bit is the largest used and is in Figure 11b. Do not remove the rod from the lathe during this process as it will destroy any alignment. Verify appropriate cutting speed is used for the hardened alloy of aluminum. This step is critical because if the drill bit walks in any direction at an early stage of drilling, within the first 4 inches, the offset will propagate through the entire rod and most likely break a drill bit. If it does not break the drill bit the final rotor will be have a mass inbalance.
3. Cut the cylinders onto the rotor using a lathe and the dimensions of the finalized design. The live center should be used to maintain alignment of the piece during this

step and all dimensions should be made as precisely as possible with the equipment utilized. This step is seen in Figure 11c. The final product is shown in Figure 11d.

4. Now the rod/rotor is mounted horizontally on an indexing head as is seen in Figure 11e and the holes for the nozzle and rotor stem are drilled. Both of these holes should be predrilled with a smaller drill bit and then a precision reamer should be used as a final cut to ensure the appropriate hole dimensions. The indexing head is rotated 90 degrees in transitioning from one hole to the next and the distance between the two holes is the nozzle length described in Section 2.2. Verify the nozzle hole and the 0.125" hole drilled through the center of the rotor are aligned by inserting the drill bit through the central hole. This is seen in Figure 11g
5. Machine the outer nozzle dimensions into the aluminum alloy used for the rotor shaft. This is shown in Figure 11h. Several of these should be produced simultaneously and the best chosen for use in the rotor. To minimize the potential for failure the side hole and the nozzle cone should be drilled first. The small drill bit used for the nozzle throat will then be much less prone to breaking due to the shorter distance it will have to penetrate. Figure 12b shows the final nozzle design held by the drill bit that is used for the nozzle throat.
6. Clean the rotor and nozzle for use in a high vacuum system and then press the nozzle into the rotor shaft. This is shown in Figure 12c. Verify orientation of the cross drilled hole that feeds gas into the nozzle and remember to use a vacuum grease help seal the nozzle into place.

7. Clean the rotor again thoroughly by flushing deionized water and alcohol through the nozzle. If beads will be used in the rotor they can be cleaned and introduced into the rotor at this point in time.
8. Machine the rotor stem from a high performance stainless steel alloy. This should be rather straightforward however special attention should be paid to the dimensions of the stem where the rotor will be. If this diameter is too small the rotor will not sufficiently engage on the stem. If it is too tight the rotor stem will bend during the pressing proceedure and need to be replaced.
9. Construct a set of holders that will allow the stem to be press fit into the rotor shaft. These should maximize the alignment and minimize the force placed on the rotor stem. The contact between the rotor and the stem should be enough to transfer the force of the motor but not so tight to deform the stem itself. Finally, press the rotor shaft into place remembering to utilize vacuum grease to help reduce binding.
10. If the rotor is cut too short the secondary pieces pieces must be constructed and mounted onto the back end of the rotor. These are shown in Figure 12g. They must contain a setscrew which controls the fine adjustments of the rotor balance. The extra mass limits the rotational frequency of the rotor because it is held on by 8-32 threads and not the actual structure of the rotor. For this reason Rotor 3 was balanced using a lathe and a file so that no balancing setscrew was needed.
11. Prior to utilizing the rotor it should be recleaned, the balance reverified, and the stem should be checked to be sure it runs true. The nozzle should be inspected under a microscope for the presence of burs.

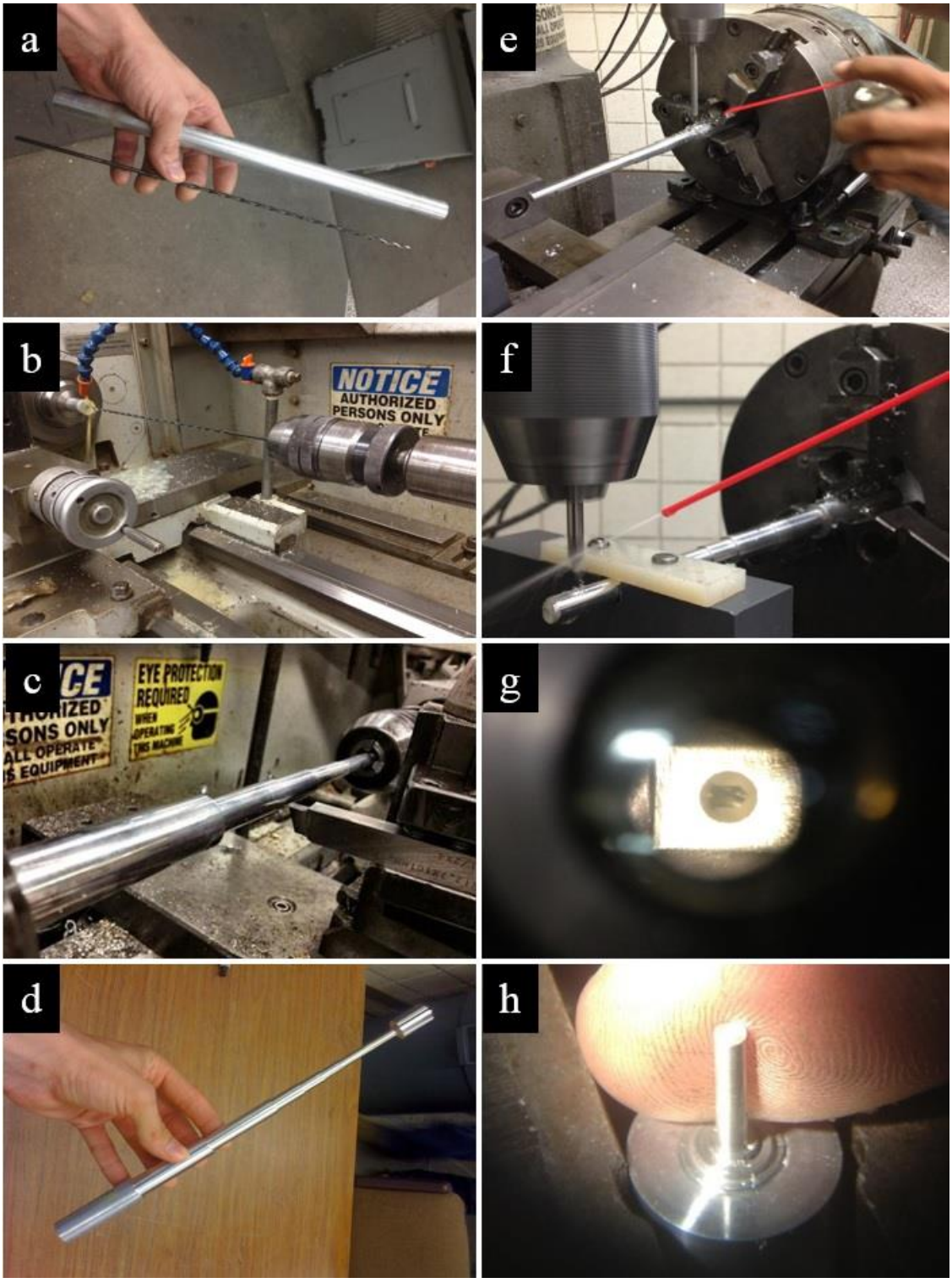
a
e
b
NOTICE
AUTHORIZED
PERSONS ONLY
f
c
EYE PROTECTION
REQUIRED
g
d
h

Figure 11

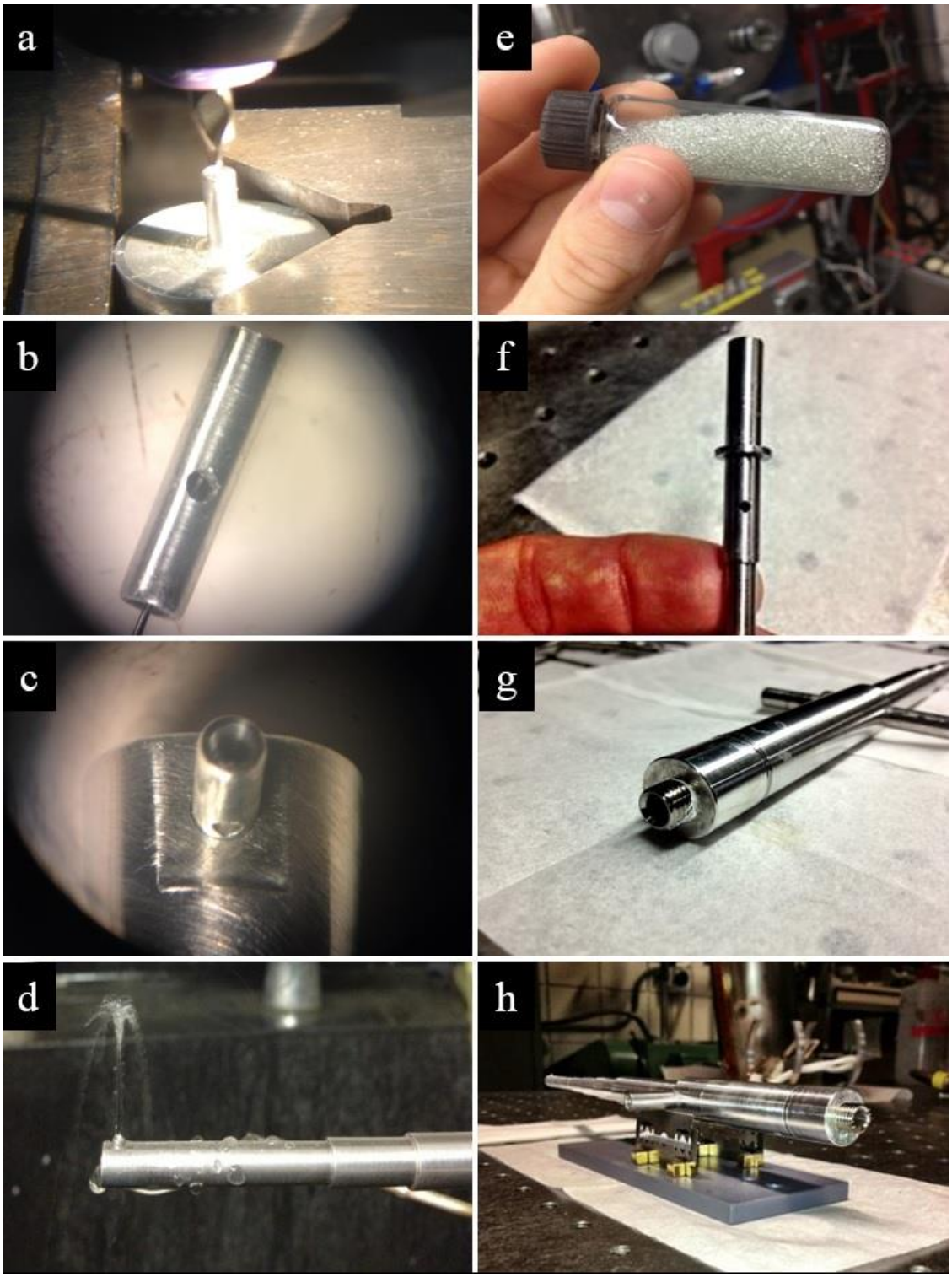

Figure 12

APPENDIX C

Numerical Integration Programs

This appendix describes how the intensity integrals for effusive snd supersonic beams are numerically evaluated in Section 2. Where x is the beam velocity, a is the rotor velocity, and b is the velocity spread. The integral:

$$\int x^2(x-a)e^{-\left(\frac{x-a}{b}\right)^2}dx \tag{5.1}$$

Evaluated utilizing WolframAlpha.org. The output in plaintext is used to define the function g. This is the first step to evaluating this integral using Mathematica 10. The comments below are contained within (* *) style brackets which prevents the notebook from considering it an input.

```
g[x_]:= -(b^2 (E^((2 a x)/b^2) (b^2 + x^2) - a b E^((a^2 + x^2)/b^2) Sqrt[Pi] Erf[(-a +
x)/b]))/(2 E^((a^2 + x^2)/b^2))

(*Evaluate the integrating term, x, at the limits defined by the definite integration. This
results in an analytic equation in terms of a and b. This will be performed for each of the
different integration limits. For the constant integral in the denominator of C the lower limit
is defined as V_min = 0, and this integral is named f. For the intensity integral in the
forward direction, named g in the program, the lower limit is defined as V_min = V_rot = a.
For the intensity integral in the backward direction, named h in the program, the lower limit
is defined as V_min = 0.03V_rot = (3 * a/100).*)

f[a_,b_]:=g[infinity]-g[0];

h[a_,b_]:=g[infinity]-g[a];
```

i[a_,b_]:=g[infinity]-g[(3*a/100)];

(*The functions f, h, and i all depend on the remaining dynamic variables a and b. For an effusive beam the velocity dispersion is the most probable velocity of the gas in the reservoir. For Xenon at 300 Kelvin the velocity spread is b=195 m/s. For the constant integral in the denominator of C the rotor is stationary and the function f is evaluated for a=0. For the integrals in the forward and backwards direction the dependence on rotor velocity is maintained and the velocity spread is $b = 195$. This is accomplished by defining 3 more functions f1, h1, and i1 as follows*)

f1=f[0,195];

h1[a_]:=h[a,195];

i1[a_]:=i[a,195];

(*The value returned by f1 is 7.23E8 and this is used to calculate the constant C found in the intensity calculations of Section 2. Now the functions are turned into plots and the outputs are suppressed by the semi colon*)

Ploth=Plot[h1[a],{a,-300,300}];

Ploti=Plot[i1[a],{a,-300,300}];

(*Now these two plots can be used to generate a two column array that contains the x and y values from the plots. In this case the x value is the rotor velocity and the y value is the intensity from the appropriate numerically evaluated integral*)

Pointsh=Cases[ploth, Line[{x__}]→x, Infinity];

Pointsi=Cases[ploti, Line[{x__}]→x, Infinity];

(*Exporting the data points into files that are appropriately named*)

Export[“Intensity-Eff-FWD.dat”, pointsh];

Export[“Intensity-Eff-BWD.dat”, pointsi];

(*To remember which directory the files are saved on use the following line*)

ExpandFileName[“Intensity-Eff-FWD.dat”]

This section describes how the intensity integrals for a supersonic beam are numerically evaluated in Section 2. Where x is the beam velocity, a is the rotor velocity, and b is the velocity spread. The integral:

$$\int x^2(x-a)e^{-\left(\frac{x-305-a}{b}\right)^2}dx \tag{5.2}$$

Evaluated utilizing WolframAlpha.org. The output in plaintext is used to define the function g. This is the first step to evaluating this integral using Mathematica 10. The comments below are contained within (* *) style brackets which prevents the notebook from considering it an input.

g[x_]:=1/4 b e^(-((a+305)^2+x^2)/b^2) (sqrt(pi) (610 a^2+2 a (b^2+186050)+305 (3 b^2+186050)) e^((a^2+610 a+x^2+93025)/b^2) erf((-a+x-305)/b)-2 b e^((2 (a+305) x)/b^2) (305 a+b^2+x^2+305 x+93025));

(*Evaluate the integrating term, x, at the limits defined by the definite integration. This results in an analytic equation in terms of a and b. This will be performed for each of the different integration limits. For the constant integral in the denominator of C the lower limit is defined as $V_{min} = 0$, and this integral is named f1. For the intensity integral in the forward direction, named f2 in the program, the lower limit is defined as $V_{min} = V_{rot} = a$.

For the intensity integral in the backward direction, named f3 in the program, the lower limit is defined as $V_{min} = 0.03V_{rot} = (3 * a/100)$.*)

F1[a_,b_]:=g[infinity]-g[0];

F2[a_,b_]:=g[infinity]-g[a];

F3[a_,b_]:=g[infinity]-g[(3*a/100)];

(*The functions f1,f2, and f3 all depend on the remaining dynamic variables a and b. For a supersonic beam the velocity dispersion is calculated by the thermal conduction model and is 12.7 m/s. For the constant integral in the denominator of C the rotor is stationary and the function f1 is evaluated for a=0. For the integrals in the forward and backwards direction the dependence on rotor velocity is maintained and the velocity spread is defined. This is accomplished by defining 3 more functions S1, S2, and S3 as follows*)

S1=f1[0,12.7];

S2[a_]:=f2[a,12.7];

S3[a_]:=f3[a,12.7];

(*The value returned by S1 is 3.2E8 and this is used to calculate the constant C found in the intensity calculations of Section 2. The output of S2 and S3 are plotted at this point to verify the performance as a function of rotor velocity. The x-axis is the rotor velocity and the y-axis represents the beam intensity although it must be scaled appropriately*)

LogPlot[{S2[a],S3[a]},{a,-300,500}]

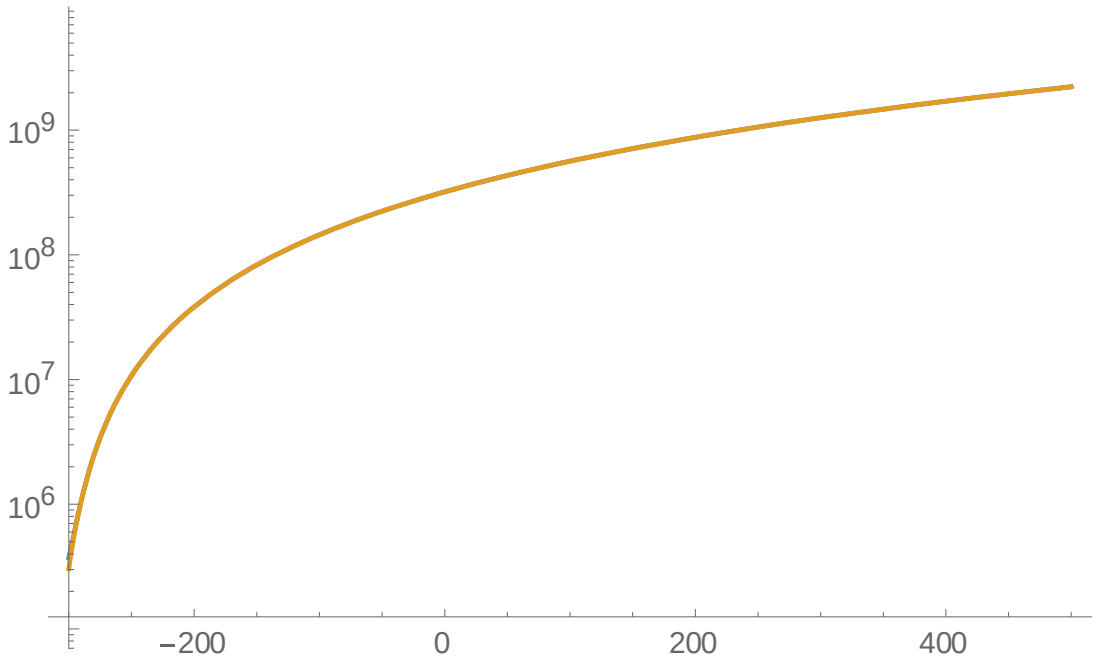

(*S2 and S3 appear to behave as expected in the logplot. To convert this output to a form usable by OriginPro each of the functions are plotted individually and saved as Plot2 and Plot3 for S2 and S3 respectively*)

Plot2=Plot[S2[a],{a,-300,500}]

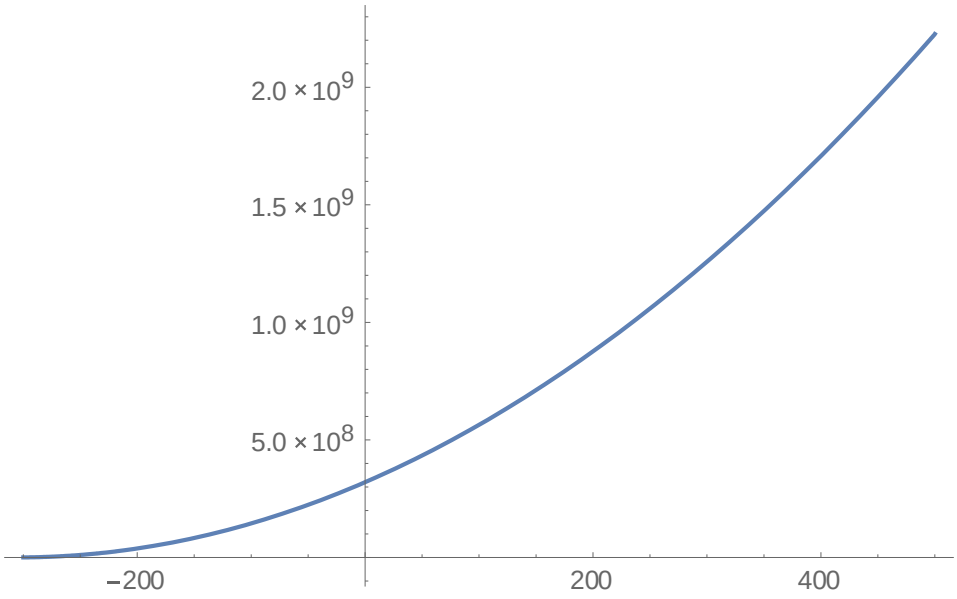

Plot3=Plot[S3[a],{a,-300,500}]

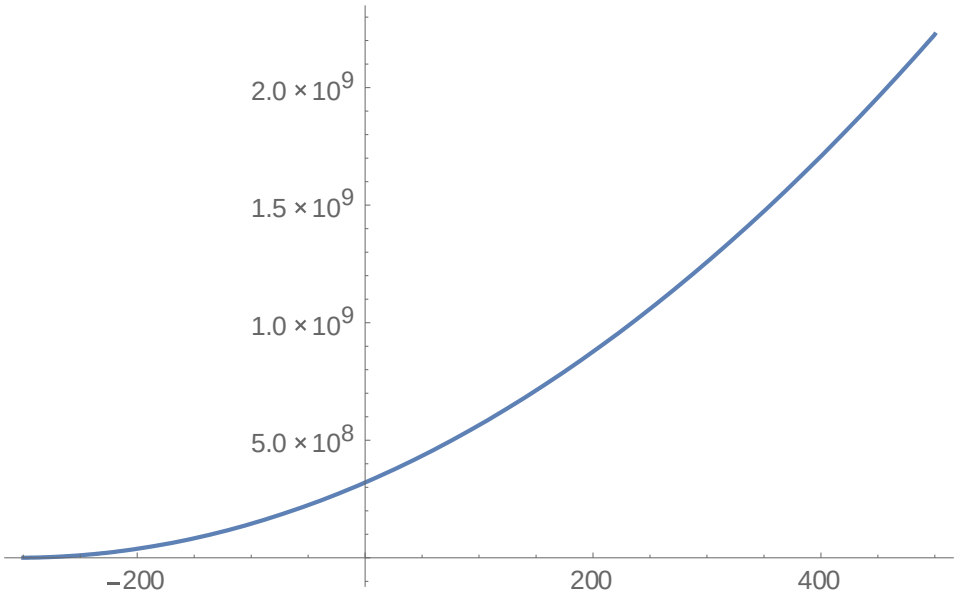

(*Now these two plots can be used to generate a two column array that contains the x and y values from the plots. In this case the x value is the rotor velocity and the y value is the intensity from the appropriate numerically evaluated integral*)

Points2=Cases[plot2, Line[{x__}]→x, Infinity];

Points3=Cases[plot3, Line[{x__}]→x, Infinity];

(*Exporting the data points into files that are appropriately named*)

Export[“IntensityFWD.dat”, points2];

Export[“IntensityBWD.dat”, points3];

(*To remember which directory the files are saved on use the following line*)

ExpandFileName[“IntensityFWD.dat”]

(*This appendix describes how the scattering coefficients for a velocity augmented beam are numerically evaluated in Section 2. Where x is the final beam velocity, a is the product of the path length and background gas density. The integral:

$$\int e^{y^2} dy \tag{5.3}$$

Evaluated utilizing WolframAlpha.org. The output in plaintext is used to define function g.*)

```
g[x_]:= (Sqrt[Pi] Erf[x])/2;

(*Evaluate the integrating term, x, at the limits defined by the definite integration.*)

g[u/195]-g[0];

(*Where 195 is the most probable velocity of the xenon background gas at room temperature
and u is the final velocity of the beam. The relative velocity term is defined in the function h
as *)

h[x_]:=(((((x+195)^3)-((Abs[x-195])^3)))/((1170*x)));

(*To verify the structure of the equation use the traditionalform subfunction in
Mathematica*)

TraditionalForm[h[x]]
```

$$\frac{(x+195)^3 - |x-195|^3}{1170x}$$

```
(*The cross section is defined in the function i as*)

i[x_]:=(3.77*(((8.55*10^-44))/((((((x+195)^3)-((Abs[x-195])^3)))/((1170*x)))))^(2/5))
```

TraditionalForm[i[x]]

$$3.77 \times 10^{-16} \left(\frac{x}{(x+195)^3 - |x-195|^3} \right)^{2/5}$$

(*Verify the form of the relative velocity term by plotting. Both the x axis and y axis are in units m/s. The x axis is the final velocity of the beam and the y axis is the relative velocity between the background xenon gas and the velocity augmented beam*)

plot=Plot[h[x],{x,0,195}]

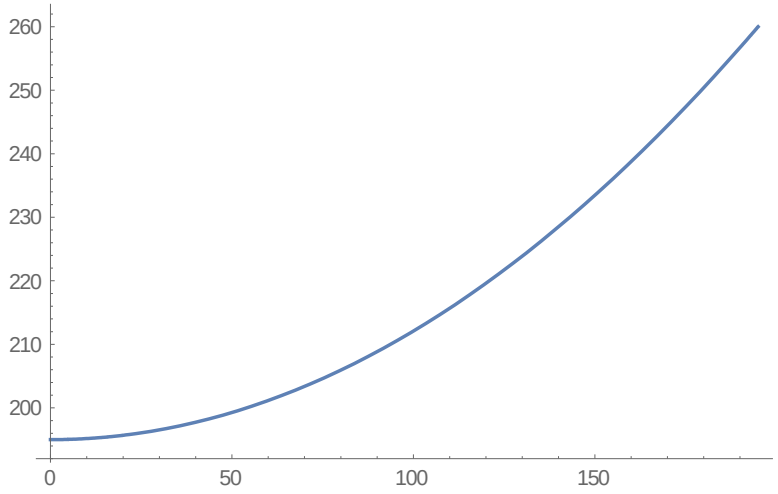

(*Verify the form of the mutual collision cross section by plotting. The y axis is in units m^{-2} and the x axis is the final velocity of the beam.*)

plot=Plot[i[x],{x,0,195}]

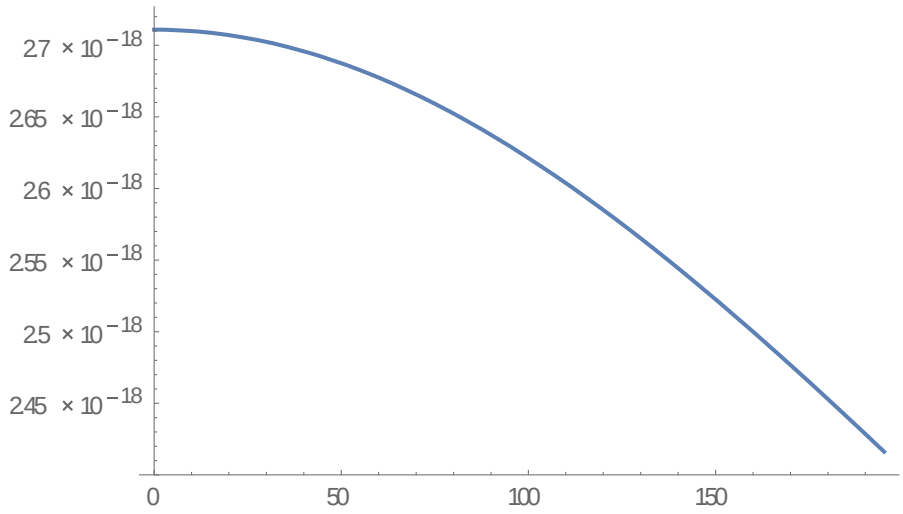

(*Using the previous equations to define the fraction of molecules left in the beam after traveling to the detector. This function j is a function of x, the final beam velocity, and a function of a, the background pressure in the beam path *)

j[x_,a_]:=Exp[-(4.225*10^17)*(a/x)*(3.77*(((8.55*10^-44)/((((((x+195)^3)-((Abs[x-195])^3)))/((1170*x)))))^(2/5))(Exp[-(x/195)^2]+((2 x/195)+(195/x))*1/2 √π Erf[x/195])]

(*To verify the structure of the equation use the traditionalform subfunction in Mathematica*)

TraditionalForm[j[x]]

$$\exp\left(-\frac{159.3a\left(\frac{x}{(x+195)^3-|x-195|^3}\right)^{2/5}\left(\frac{1}{2}\sqrt{\pi}\left(\frac{2x}{195}+\frac{195}{x}\right)erf\left(\frac{x}{195}\right)+e^{-\frac{x^2}{38025}}\right)}{x}\right)$$

(*The constants have all been evaluated except for the term a. For a=0.1, 1, 10 the background pressure is 10^{-5} Torr, 10^{-6} Torr, 10^{-7} Torr respectively. The behavior is verified by plotting below. The units of the y axis are a percentage of the original number density,

and the units of the x axis are m/s and represent the final velocity of the velocity augmented beam *)

```
plot=Plot[{j[x,10], j[x,1], j[x,0.1]}, {x,0,500}, PlotRange -> Full]
```

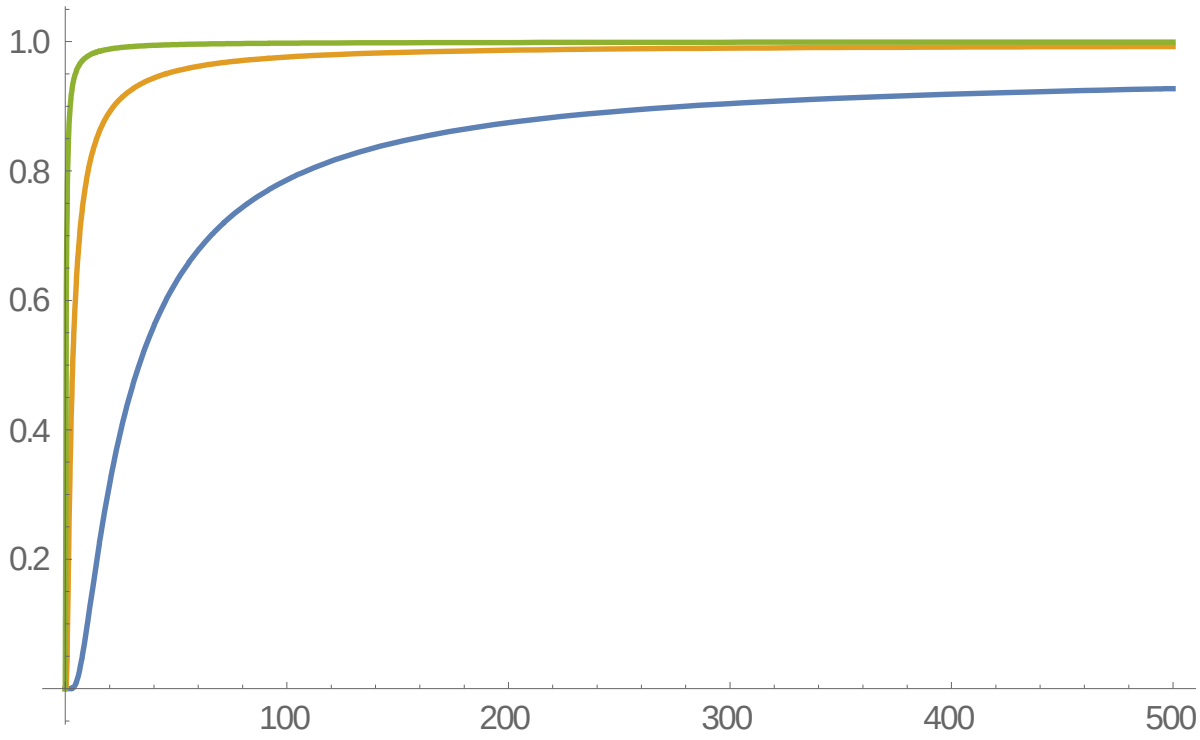


```
(*To export this data first generate a plot for each data set*)

plot1=Plot[j[x,10],{x,0,500},PlotRange-> Full];

plot2=Plot[j[x,1],{x,0,500},PlotRange-> Full];

plot3=Plot[j[x,0.1],{x,0,500},PlotRange-> Full];

(*Next convert the plot to a series of (x,y) coordinates*)

points1=Cases[plot1,Line[{x__}]-> x,Infinity];

points2=Cases[plot2,Line[{x__}]-> x,Infinity];
```

```
points3=Cases[plot3,Line[{x__}]-> x,Infinity];

(*Finally export the points to a set of files on the computer named for the value of
background gas pressure in the beam path.*)

Export["Scattering1E5bk.dat",points1];

Export["Scattering1E6bk.dat",points2];

Export["Scattering1E7bk.dat",points3];
```